Laser desorption/ionization mass spectrometry for direct profiling and imaging of small molecules from raw biological materials

by

Sangwon Cha

A dissertation submitted to the graduate faculty

in partial fulfillment of the requirements for the degree of

DOCTOR OF PHILOSOPHY

Major: Analytical Chemistry

Program of Study Committee:
Edward S.Yeung, Major Professor
Robert S. Houk
Srdija Jeftinija
Victor S.-Y. Lin
Basil J. Nikolau
Hans Stauffer

Iowa State University

Ames, Iowa

2008

INFORMATION TO USERS

The quality of this reproduction is dependent upon the quality of the copy submitted. Broken or indistinct print, colored or poor quality illustrations and photographs, print bleed-through, substandard margins, and improper alignment can adversely affect reproduction.

In the unlikely event that the author did not send a complete manuscript and there are missing pages, these will be noted. Also, if unauthorized copyright material had to be removed, a note will indicate the deletion.

ProQuest LLC
789 East Eisenhower Parkway
P.O. Box 1346
Ann Arbor, MI 48106-1346

To My Families and Friends

TABLE OF CONTENTS

ABSTRACT

Matrix-assisted laser desorption/ionization(MALDI) mass spectrometry(MS) has been widely used for analysis of biological molecules, especially macromolecules such as proteins. However, MALDI MS has a problem in small molecule (less than 1 kDa) analysis because of the signal saturation by organic matrixes in the low mass region. In imaging MS (IMS), inhomogeneous surface formation due to the co-crystallization process by organic MALDI matrixes limits the spatial resolution of the mass spectral image. Therefore, to make laser desorption/ionization (LDI) MS more suitable for mass spectral profiling and imaging of small molecules directly from raw biological tissues, LDI MS protocols with various alternative assisting materials were developed and applied to many biological systems of interest.

Colloidal graphite was used as a matrix for IMS of small molecules for the first time and methodologies for analyses of small metabolites in rat brain tissues, fruits, and plant tissues were developed. With rat brain tissues, the signal enhancement for cerebroside species by colloidal graphite was observed and images of cerebrosides were successfully generated by IMS. In addition, separation of isobaric lipid ions was performed by imaging tandem MS. Directly from Arabidopsis flowers, flavonoids were successfully profiled and heterogeneous distribution of flavonoids in petals was observed for the first time by graphite-assisted LDI(GALDI) IMS.

Aqueous-based colloidal silver solution was also investigated as an alternative matrix for IMS application. For *Arabidopsis thaliana* wild-type and its *cer*2 mutant flowers, direct profiling and imaging of cuticular wax compounds by silver LDI MS and gas chromatography (GC) - MS were carried out for the first time and cuticular wax metabolites of them were compared for predicting the function of *cer*2 gene products. Results from silver LDI MS showed a good agreement with those from traditional GC-MS analysis and we

propose that *cer*2 gene mutation mainly affects the conversion from C_{30} fatty acid to C_{29} alkane in wax biosynthesis pathway. We also applied silver LDI MS to probe cholesterol, which is the major component of lipid raft domains, from the *Astrocyte* cell monolayer. With colloidal silver, cholesterol was readily detected with high sensitivity and cholesterol level changes on cell monolayer by methyl β-cyclodextrin treatment were successfully assayed by introducing relative intensity profiling. Results from more rapid, and simpler silver-LDI MS cholesterol assay method also showed a good agreement with those from traditional enzymatic fluorometry cholesterol assay method.

CHAPTER 1. GENERAL INTRODUCTION

Dissertation Organization

This dissertation begins with a general introduction of small molecule analysis by laser desorption/ionization (LDI) mass spectrometry (MS) and imaging mass spectrometry (IMS). The following four chapters are organized with published papers and a manuscript to be submitted. Chapters two and three are comprehensive studies of LDI MS and IMS of small metabolites in intact animal and plant tissues by using colloidal graphite as a matrix. Chapters four and five are projects related to LDI MS and IMS of small metabolites in plant tissues and cell monolayer by using colloidal silver as a matrix. Tables, cited literature, and figures for each chapter were placed at the end of each chapter. Chapter six includes summary of work and the general conclusions. The following three appendixes include the extended work related to chapter two and supporting information for chapter two and three.

Laser Desorption Ionization Mass Spectrometry

Since the concept of the mass spectrometry was introduced by J.J Thomson's cathode ray tube experiment, mass spectrometry has been developed over 100 years by innovative researchers and has become one of the most important analysis techniques in almost every field of natural sciences. Mass spectrometry is the analytical technique measuring mass and charge state of the analyte. In mass spectrometry (MS), the most important step is the ionization step because this step makes neutral molecules detectable by converting them to charged ions. Ionization can be done through various mechanisms such as protonation, deprotonation, cationization, electron ejection, and electron capture. To achieve ionization through one or more mechanisms above, many ionization techniques have been developed.

Electron ionization (EI) is the classical ionization technique for MS had and has been used as the primary ionization techniques in the early stage of MS. EI is based on the

interaction between emitted electrons and neutral analytes. In 1960 and 1970's various ionization methods such as chemical ionization[1], electrospray ionization[2], field desorption ionization[3], plasma desorption ionization[4] and atmospheric pressure chemical ionization[5] techniques were developed for MS. In early 1980's, inductively coupled plasma was introduced as an ion source for MS[6] and fast atom bombardment technique has also developed for an ion source.[7]

Laser sources were demonstrated as a fast surface heating source for generating atom ions from solid samples[8] a few years after discovery of lasing in 1960. Since then, laser-induced desorption/ionization techniques have been thoroughly investigated as ion sources for MS. In 1978, polar, nonvolatile organic molecules were ionized and detected by using submicrosecond pulsed laser.[9] Those molecules were ionized through cationization and detected as sodium or potassium adduct ions.[9] In the 1980's, ultra fine metal powder (UFMP) which had been used for alloy production was introduced as an assisting material for laser desorption.[10] Compared to bulk material, UFMP has much smaller dimensions which are in the range of the long light wavelength. Therefore, UFMP could absorb energy more efficiently from the light source without loss or dispersion of heat and high temperature required for intact molecule desorption could be achieved by using UFMP as an assisting material.[10] With UFMP, intact polyethylene glycols were detected with very little fragmentations.[11] The use of UFMP for LDI MS was further developed by Tanaka. He used a UFMP suspension in glycerin as an assisting material for LDI MS, and macromolecules over 100 kDa were observed without fragmentation by this method.[12] Inspired by UFMP suspension matrix for LDI MS, Karas and Hillenkamp further optimized this methodology for macromolecule analysis[13, 14]. By using nicotinic acid as a matrix, they observed several proteins including lysozyme, trypsin, and albumin in the form of molecular ion (MH^+).[13] LDI MS with organic acids as matrixes is referred to as matrix-assisted laser desorption/ionization mass spectrometry, MALDI MS. With elctrospray ionization (ESI) technique[15], MALDI MS

has become the most widely-used soft-ionization technique for macromolecule analysis, especially proteins.

Laser Desorption Ionization Mass Spectrometry of Small Molecules

Application of MALDI to small molecule analysis (<1000 Da) seems to be problematic because of a high degree of signal suppression in the low mass region by dominant matrix ion signals. However, MALDI MS is still attractive in small molecule analysis because of the direct sampling capability from complex mixtures and the tolerance for contaminants. With successes in interfacing between MALDI sampling part and a variety of mass analyzers, the instrumental capability of LDI mass spectrometers such as mass spectral resolution and tandem MS capability is no longer a limiting factor any more in small molecule analysis. In addition, great achievements in alternative sample preparation methods for LDI MS allow us to detect small molecules with less severe matrix interference and/or sample inhomogeneity.

First, organic matrixes which have relatively large molecular weights and therefore there was no interference present in the low mass region were used. For example, *meso*-tetrakis(pentafluorophenyl) porhyrin (MW. 974.46) was used as a matrix to analyze low molecular weight alkylphenol ethoxylates which range from *m/z* 300 to *m/z* 800.[16] Second, alternative inorganic matrixes such as cobalt powder[12], silver colloids[17], gold nanoparticles[18] and carbon particles were used to analyze small molecules. Among those, carbon particles including graphite, carbon powder, and carbon nanotubes showed relatively clean background which is suitable for small molecule analysis. Examples of small molecule analysis by using carbon materials are reviewed briefly in this dissertation at the introduction part in Chapter 2. Recently, 30nm-sized silicon nanoparticles were used as a matrix to analyze various drug, small peptide, and pesticide molecules.[19] Interestingly, much lower laser fluence was required for the silicon nanoparticle matrix compared to conventional

MALDI matrixes.[19] Third, electrochemically etched porous silicon surfaces without any additional matrix were used for small molecule analysis by LDI MS. This technique is referred to as desorption/ionization on silicon MS (DIOS MS).[20] Various classes of small molecules including carbohydrates were analyzed with very low detection limit and with low background.[21-23] Further development on DIOS has been made by utilizing silicon nanowires as sample support and it required much lesser laser fluence than porous silicon surface or conventional MALDI environment.[24] Lastly, nanostructures coated with liquid-phase perfluorinated initiator molecules were used as sample support for both LDI MS and SIMS.[25] This technique is called as 'nanostructure initiator MS (NIMS)'. NIMS showed greater sensitivity (~tens of attomoles) over MALDI and ESI in detecting small molecules including lipids and drug molecules.[25]

Imaging Mass Spectrometry of Small Molecules

Pulsed laser-based or energetic particle-based techniques in mass spectrometry have the capability of generating ions directly from the specific location of sample surfaces. This capability of spatial sampling allowed us to investigate chemical spatial distribution by performing serial data collection through sample surfaces. This 'microscope-concept' approach by mass spectrometry is called as 'imaging mass spectrometry (IMS)' or mass spectral imaging'. Major methodologies used for IMS are MALDI MS[26] and secondary ion MS (SIMS)[27]. MALDI IMS was first introduced by Caprioli group.[28] MALDI IMS is advantageous over SIMS in detecting intact large molecules (>1000 Da). However, since the spatial resolution is limited by laser spot size in MALDI IMS, a spatial resolution of MALDI (10 to hundreds of microns) is worse than that of SIMS (~100 nm). To get higher spatial resolution in MALDI IMS, decreasing the laser spot size close to the diffraction limit[29] or using astigmatic optics with a position-sensitive detector[30, 31] were demonstrated. In addition, homogeneous deposition of matrixes is critical in MALDI IMS because all conventional

MALDI matrixes crystallize inhomogeneously on sample surfaces. For homogeneous matrix deposition, finely controlled matrix spraying devices such as acoustic droplet ejection instrument and piezoelectric microdispenser have been developed.[32-34]

Because of the soft-ionization characteristic of MALDI, MALDI IMS has been mainly used for studying protein distribution from tissue sections[35-37]. However, small molecules below 1 kDa such as drug molecules[38, 39] and endogenous primary or secondary metabolites were also spatially investigated from many biological systems by MALDI IMS. Among various primary and secondary metabolites, lipid is the major class of compounds in small molecule imaging by MALDI IMS because of their abundances in tissue samples. However, there are two major challenging issues in IMS of small molecules. First, peaks from conventional MALDI matrixes are dominant in the low mass region and these peaks interfere with or suppress signals from small sample molecules. To overcome this, matrix-free methodology such as IR-MALDI was applied to profile plant metabolites[40], or matrix-embedded surfaces such as clathrate nanostructures[25] and silicon[41] were employed to image small molecules from intact tissues.

Second, several isobaric ions can be associated in one nominal *m/z* value which can cause wrong or overlapped spatial information for a specific compound when generation of mass spectral images was simply based on extracting intensity values from mass spectra. Because of compositional similarities of small metabolites, there are many possible overlaps by several different compounds in the low mass region. To separate distributions of isobaric ions, imaging tandem MS (IMS/MS)[42], high mass resolution MS[36], and ion mobility spectrometry[43] were employed.

In IMS/MS, first generation product ions which were specifically from only one of isobaric ions were chosen for generating chemically selective images. For example, both sodiated phosphatidylcholine 38:6 ions ($[PC\ 38:6 + Na]^+$) and DHB matrix cluster ions contributed the peak intensity at *m/z* 828.[44] But distribution of these two ions were

successfully separated by generating images of their specific product ions at *m/z* 769 (neutral loss of 59 Da, loss of PC headgroup) and at *m/z* 652 (loss of a sodiated DHB molecule).[44] One major disadvantage of IMS/MS is that it is a time-consuming process because a tissue sample needs to be scanned separately for all single *m/z* values which were associated with several isobaric ions.

High mass spectral resolution and accurate mass measurement by using MALDI fourier transform ion cyclotron resonance(FTICR) MS can resolve isobaric ions which cannot be resolved by low-mass resolution TOF or ion-trap mass spectrometers. For example, Images for three peptides within 0.24 Da range at m/z 1293 were successfully obtained from the rat brain tissue.[36] Mass accuracy was 6 ppm in this experiment.[36] However, high mass resolution imaging is also time-consuming process because of longer measuring time by FT-ICR.

Ion mobility spectrometry is a real-time gas phase ion separation technique.[45, 46] Because ion mobility separation was performed prior to mass analysis, detected ions bear the information of ions mobility drift time as well as their *m/z* values. Isobaric ions from different classes can be separated by choosing different drift time region. For example, lipids detected from rat brain tissues showed about 12% longer drift time than isobaric peptides.[47] Therefore, signals from lipids were separated from chemical noises and other isobaric ion signals by choosing a specific mobility drift time.[43] However, acquiring mass and drift time are limited in the current software and hardware instrumentation of ion mobility spectrometry because the allowed data capacity is not enough to process all ions collected from one scanning point.[43, 47]

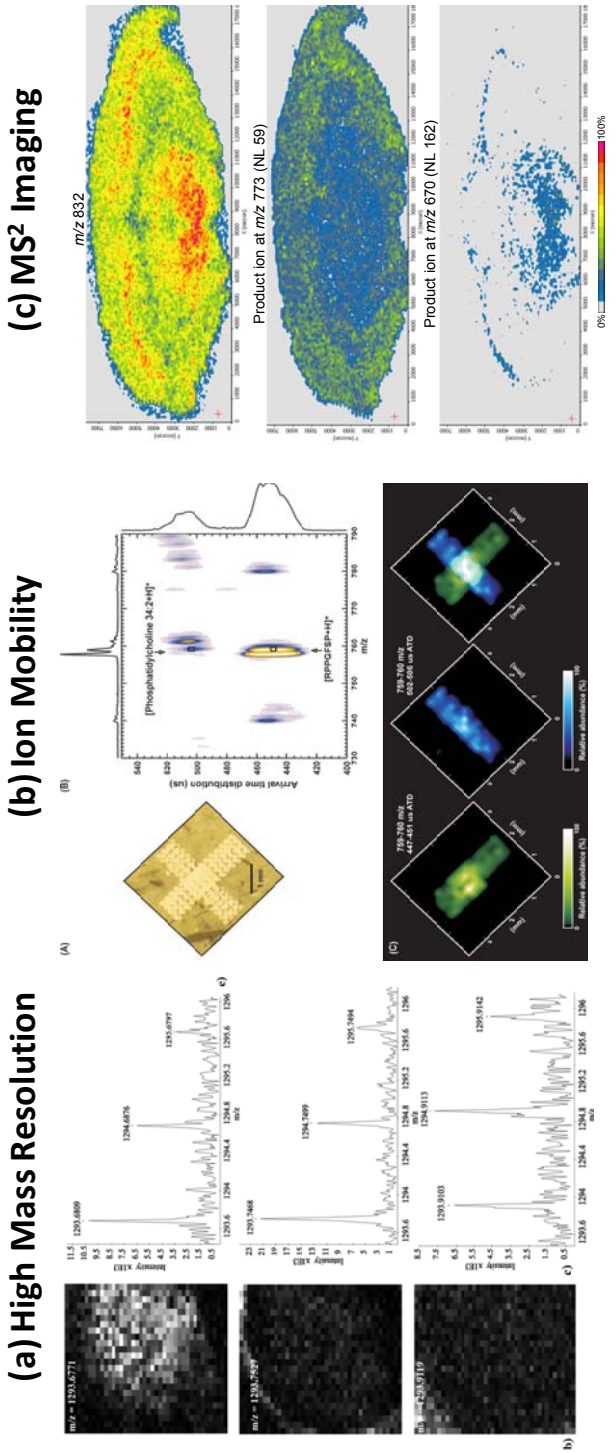

Figure 1. Isobaric ion separations in IMS. Isobaric ions can be separated by (a) high mass spectral resolution MS[36], (b) ion mobility MS[43], (c) tandem MS[42].

References

(1) Munson, M. S. B.; Field, F. H. *Journal of the American Chemical Society* **1966**, *88*, 2621-&.

(2) Dole, M.; Mack, L. L.; Hines, R. L. *Journal of Chemical Physics* **1968**, *49*, 2240-&.

(3) Beckey, H. D. *Angewandte Chemie-International Edition* **1969**, *8*, 623-&.

(4) Macfarlane, R. D.; Torgerson, D. F. *Science* **1976**, *191*, 920-925.

(5) Carroll, D. I.; Dzidic, I.; Stillwell, R. N.; Haegele, K. D.; Horning, E. C. *Analytical Chemistry* **1975**, *47*, 2369-2373.

(6) Houk, R. S.; Fassel, V. A.; Flesch, G. D.; Svec, H. J.; Gray, A. L.; Taylor, C. E. *Analytical Chemistry* **1980**, *52*, 2283-2289.

(7) Barber, M.; Bordoli, R. S.; Sedgwick, R. D.; Tyler, A. N. *Journal of the Chemical Society-Chemical Communications* **1981**, 325-327.

(8) Honig, R. E.; Woolston, J. R. *Applied Physics Letters* **1963**, *2*, 138-139.

(9) Posthumus, M. A.; Kistemaker, P. G.; Meuzelaar, H. L. C.; Tennoeverdebrauw, M. C. *Analytical Chemistry* **1978**, *50*, 985-991.

(10) Tanaka, K. In *Les Prix Nobel, The Nobel Prizes 2002*; Frängsmyr, T., Ed.; Nobel Foundation: Stockholm, 2002, pp 197-217.

(11) Wilkins, C. L.; Weil, D. A.; Yang, C. L. C.; Ijames, C. F. *Analytical Chemistry* **1985**, *57*, 520-524.

(12) Tanaka, K.; Waki, H.; Ido, Y.; Akita, S.; Yoshida, Y.; Yoshida, T.; Matsuo, T. *Rapid Communications in Mass Spectrometry* **1988**, *2*, 151-153.

(13) Karas, M.; Hillenkamp, F. *Analytical Chemistry* **1988**, *60*, 2299-2301.

(14) Karas, M.; Ingendoh, A.; Bahr, U.; Hillenkamp, F. *Biomedical and Environmental Mass Spectrometry* **1989**, *18*, 841-843.

(15) Fenn, J. B.; Mann, M.; Meng, C. K.; Wong, S. F.; Whitehouse, C. M. *Science* **1989**, *246*, 64-71.

(16) F. O. Ayorinde, P. H. T. N. P. Q. L. K., Jr. *Rapid Communications in Mass Spectrometry* **1999**, *13*, 2474-2479.

(17) Sluszny, C.; Yeung, E. S.; Nikolau, B. J. *Journal of the American Society for Mass Spectrometry* **2005**, *16*, 107-115.

(18) McLean, J. A.; Stumpo, K. A.; Russell, D. H. *J. Am. Chem. Soc.* **2005**, *127*, 5304-5305.

(19) Wen, X.; Dagan, S.; Wysocki, V. H. *Anal. Chem.* **2007**, *79*, 434-444.

(20) Wei, J.; Buriak, J. M.; Siuzdak, G. *Nature* **1999**, *399*, 243-246.

(21) Trauger, S. A.; Go, E. P.; Shen, Z. X.; Apon, J. V.; Compton, B. J.; Bouvier, E. S. P.; Finn, M. G.; Siuzdak, G. *Analytical Chemistry* **2004**, *76*, 4484-4489.

(22) Compton, B. J.; Siuzdak, G. *Spectroscopy-an International Journal* **2003**, *17*, 699-713.

(23) Want, E.; Compton, B. J.; Hollenbeck, T.; Siuzdak, G. *Spectroscopy-an International Journal* **2003**, *17*, 681-691.

(24) Go, E. P.; Apon, J. V.; Luo, G.; Saghatelian, A.; Daniels, R. H.; Sahi, V.; Dubrow, R.; Cravatt, B. F.; Vertes, A.; Siuzdak, G. *Analytical Chemistry* **2005**, *77*, 1641-1646.

(25) Northen, T. R.; Yanes, O.; Northen, M. T.; Marrinucci, D.; Uritboonthai, W.; Apon, J.; Golledge, S. L.; Nordstrom, A.; Siuzdak, G. *Nature* **2007**, *449*, 1033-1036.

(26) Cornett, D. S.; Reyzer, M. L.; Chaurand, P.; Caprioli, R. M. *Nature Methods* **2007**, *4*, 828-833.

(27) Heeren, R. M. A.; McDonnell, L. A.; Amstalden, E.; Luxembourg, S. L.; Altelaar, A. F. M.; Piersma, S. R. *Applied Surface Science* **2006**, *252*, 6827-6835.

(28) Caprioli, R. M.; Farmer, T. B.; Gile, J. *Analytical Chemistry* **1997**, *69*, 4751-4760.

(29) Spengler, B.; Hubert, M. *Journal of the American Society for Mass Spectrometry* **2002**, *13*, 735-748.

(30) Luxembourg, S. L.; McDonnell, L. A.; Mize, T. H.; Heeren, R. M. A. *Journal of Proteome Research* **2005**, *4*, 671-673.

(31) Luxembourg, S. L.; Mize, T. H.; McDonnell, L. A.; Heeren, R. M. A. *Analytical Chemistry* **2004**, *76*, 5339-5344.

(32) Aerni, H. R.; Cornett, D. S.; Caprioli, R. M. *Analytical Chemistry* **2006**, *78*, 827-834.

(33) Bogan, M. J.; Agnes, G. R. *Rapid Communications in Mass Spectrometry* **2004**, *18*, 2673-2681.

(34) Stoeckli, M.; Staab, D.; Staufenbiel, M.; Wiederhold, K. H.; Signor, L. *Analytical Biochemistry* **2002**, *311*, 33-39.

(35) DeKeyser, S. S.; Kutz-Naber, K. K.; Schmidt, J. J.; Barrett-Wilt, G. A.; Li, L. J. *Journal of Proteome Research* **2007**, *6*, 1782-1791.

(36) Taban, I. M.; Altelaar, A. F. M.; Van der Burgt, Y. E. M.; McDonnell, L. A.; Heeren, R. M. A.; Fuchser, J.; Baykut, G. *Journal of the American Society for Mass Spectrometry* **2007**, *18*, 145-151.

(37) Verhaert, P. D.; Conaway, M. C. P.; Pekar, T. M.; Miller, K. *International Journal of Mass Spectrometry* **2007**, *260*, 177-184.

(38) Khatib-Shahidi, S.; Andersson, M.; Herman, J. L.; Gillespie, T. A.; Caprioli, R. M. *Analytical Chemistry* **2006**, *78*, 6448-6456.

(39) Hsieh, Y.; Casale, R.; Fukuda, E.; Chen, J. W.; Knemeyer, I.; Wingate, J.; Morrison, R.; Korfmacher, W. *Rapid Communications in Mass Spectrometry* **2006**, *20*, 965-972.

(40) Li, Y.; Shrestha, B.; Vertes, A. *Analytical Chemistry* **2008**, *80*, 407-420.

(41) Liu, Q.; Guo, Z.; He, L. *Analytical Chemistry* **2007**, *79*, 3535-3541.

(42) Cha, S. W.; Yeung, E. S. *Analytical Chemistry* **2007**, *79*, 2373-2385.

(43) McLean, J. A.; Ridenour, W. B.; Caprioli, R. M. *Journal of Mass Spectrometry* **2007**, *42*, 1099-1105.

(44) Garrett, T. J.; Prieto-Conaway, M. C.; Kovtoun, V.; Bui, H.; Izgarian, N.; Stafford, G.; Yost, R. A. *International Journal of Mass Spectrometry* **2007**, *260*, 166-176.

(45) McLean, J. A.; Ruotolo, B. T.; Gillig, K. J.; Russell, D. H. *International Journal of Mass Spectrometry* **2005**, *240*, 301-315.

(46) Vonhelden, G.; Wyttenbach, T.; Bowers, M. T. *Science* **1995**, *267*, 1483-1485.

(47) Jackson, S. N.; Ugarov, M.; Egan, T.; Post, J. D.; Langlais, D.; Schultz, J. A.; Woods, A. S. *Journal of Mass Spectrometry* **2007**, *42*, 1093-1098.

CHAPTER 2. IMAGING OF CEREBROSIDES DIRECTLY FROM RAT BRAIN TISSUE BY COLLOIDAL GRAPHITE-ASSISTED LASER DESORPTION/IONIZATION MASS SPECTROMETRY

A paper published in Analytical Chemistry*

Sangwon Cha and Edward S. Yeung

Abstract

Graphite assisted laser desorption/ionization (GALDI) mass spectrometry (MS) was investigated for analysis of cerebrosides in complex total brain lipids extract. Conventional MALDI MS and graphite GALDI MS were compared regarding lipid analysis by using high-vacuum (HV, $<10^{-6}$ Torr) LDI time-of-flight (TOF) mass spectrometry and intermediate pressure (IP, 0.17 Torr) linear ion trap (LIT) mass spectrometry. Cerebrosides were not detected or detected with low sensitivity in MALDI MS because of other dominant phospholipids. By using GALDI, cerebrosides were detected as intense mass peaks without prior separation from other lipid species while mass peaks corresponding to phosphatidylcholines (PCs) were weak. The signal increase for cerebrosides and the signal decrease for PCs in GALDI MS were more significant in HV than in IP. MS^n experiments of precursor ions corresponding to cerebrosides and PCs in brain lipid extract were performed for identifying the detected species and for distinguishing isobaric ions. 22 cerebroside

---

* Reprint with permission from Analytical Chemistry **2007,** 79(6), 2373-2385.

species were detected by GALDI whereas 8 cerebroside species were detected by MALDI. Sulfatides in brain lipid extract were also easily detected by GALDI MS in the negative ion mode. By forming a colloidal graphite thin film on rat brain tissue, direct lipid profiling by imaging mass spectrometry (IMS) was performed. Chemically-selective images for cerebrosides and sulfatides were successfully obtained. Imaging tandem mass spectrometry (IMS/MS) was performed to generate images of specific product ions from isobaric species.

Introduction

Cerebrosides are one class of glycosphingolipids. A cerebroside is composed of a hexose (galactose or glucose) and a ceramide consisting of a sphingosine or a sphinganine base and an amide-linked long chain fatty acid. Depending on the hexose unit, a cerebroside can be called a galactosylceramide (GalCer) or a glucosylceramide (GlcCer). As mediators, cerebrosides are involved in many biological processes, such as cell adhesion, cell growth, cell morphogenesis, and cell-to-cell communication.[1-3] Cerebrosides also act as receptors or as binding sites for viruses on a cellular membrane.[4] Deficiency of GalCer causes abnormal function and local instability during myelination.[5] Abnormal accumulation of GalCer or GlcCer also results in Krabbe disease or Gaucher's disease, respectively. This increased level of GalCer or GlcCer is caused by a deficiency of galactosylceramidase or glucocerebrosidase.[6] Krabbe disease causes severe mental degeneration because of insufficient development of myelin and Gaucher's disease leads to bone damage, anemia, and enlargement of spleen and liver.[6] In brain tissue, GalCer species are abundant,[7, 8] at up to 40 mol% of the phosphatidylcholines (PCs) in rat brain cortex depending on their locations.[8-10] Among cortex parts, GalCers are 8 to 10 times more enriched in white matter than in gray matter.[3] In addition to GalCers, 2-hydroxy GalCer species are also abundant in mammalian brain tissues and their total amount is about 50% of GalCer species.[3]

Since soft ionization techniques for mass spectrometry (MS) such as matrix-assisted laser desorption/ionization (MALDI) and electrospray ionization (ESI) have been introduced,[11-13] many researchers applied these techniques to analyze lipids. Excellent recent reviews about lipid analysis by using MALDI or ESI technique can be found elsewhere.[10, 14, 15] Lipid analysis with MALDI has the potential advantage over ESI in sample preparation because of the possibility of using raw biological materials such as tissue sections directly (without extraction) to obtain spatial information. MALDI MS, however, has a problem with analyzing lipid mixtures because ionization efficiencies are different according to their head groups. The presence of PCs and sphingomyelines (SMs) which have a quaternary ammonium polar head group has been known to suppress signals of other lipid species in the positive ion mode.[16] For lipid analysis with MALDI MS, the most common organic matrix is 2,5-dihydroxy benzoic acid (DHB).[17-19] Using DHB with the addition of cesium ion (Cs^+) resulted in reducing spectra complexity and enhancing sensitivity.[20, 21] Other matrixes, such as 2,6-dihydroxyacetophenone (DHA), sinapinic acid (SA), α-cyano-4-hydroxycinnamic acid (CHCA), *p*-nitroaniline (PNA), and others, have also been tested,[17, 19-21] PNA generated good profiles of PEs in the presence of PCs and SMs.[20] CHCA and SA, however, suffered from interference signals originated from matrixes. Their low solubility in methanol was also problematic.[14, 17]

Whereas numerous MALDI MS analyses of phospholipids have been reported and many MALDI MS analyses of gangliosides which consists of a glycosphingolipid and one or more sialic acids have been performed,[19, 22-28] relatively little research has been carried out on the analyses of cerebrosides by using MALDI MS despite their biological importance. Harvey examined comprehensively the applicability of MALDI MS to sphingolipids and glycosphingolipids.[18] Analysis of less-polar neutral and acidic cerebrosides' derivatives in monkey brain was performed by MALDI MS after serial chromatographic separations of cerebroside-related compounds.[29] Yurkova and coworkers induced free-radical

fragmentations of cerebrosides by irradiation of γ-ray of cerebroside-containing micelles and analyzed the lipid extracts from these irradiated micelles by MALDI MS.[30] Fujiwaki and coworkers analyzed sphingolipids in tissues and body fluids from patients with Gaucher's disease and found that cerebrosides/SM ratio was elevated in samples from patients with Gaucher's disease.[23, 31] However, all analyses of cerebrosides mentioned above required one or more separation steps for isolating glycosphigolipids from other lipid species before MS analysis.[23, 29, 31] Without separation, it is hard to detect cerebrosides by conventional MALDI MS because phospholipids, especially PCs, are usually dominant in crude extracts from eukaryotes and the *m/z* region of phospholipids in the mass spectra substantially overlaps that of cerebrosides.

Many types of graphite matrices have been suggested as alternative matrices for laser desorption/ionization (LDI) mass spectrometry because they are near blackbody and disperse the energy very effectively. Graphite has been used in forms of suspension in glycerol[32, 33] or 2-propanol,[34] powder[35] and plate.[36-39] These particles or flakes can range from 2 μm to 150 μm. Sunner and coworkers first showed that graphite matrix in glycerol helped the detection of proteolytic digest of cytochrome c and cytochrome c itself.[32] Further development of graphite/liquid matrix was achieved by Dale and coworkers and proteins, oligosaccharides, and synthetic polymers were successfully detected with a glycerol/graphite matrix.[33] The aging of the triterpene in mastic and dammar films was also studied with graphite powder as a matrix.[35] With graphite plate, poly(methylsilsesquioxane)s,[38] fatty acids,[39] and synthetic polymers[36, 37] were analyzed. Peng and coworkers developed an interface for thin-layer chromatography (TLC) plate scanning by atmospheric pressure (AP) LDI MS. They used graphite particle suspension in 2-propanol as a matrix for detecting SMs and PCs directly from the TLC plate.[34] Graphite trapped in silicon polymer was also used for the surface support to facilitate detecting peptides and proteins with desalting effect.[40] Pencil leads, which are mixed forms of graphite, wax, and clay were used as a matrix to analyze

actinide materials and as a calibrant.[41] Activated carbon powder was used for detecting various organic compounds including peptides, prometryn, and hydrochlorothiazide on the TLC plate.[42] Functionalized fullerenes, $C_{60}((CH_2)_2COOH)n$ or $C_{60}(C_{11}H_{23})n$, were also used for the detection of peptides and phospholipids.[43] Recently, carbon nanotubes or oxidized carbon nanotubes were suggested as matrixes for detecting small peptides, small oligosaccharides, and cyclodextrins.[44, 45] Oxidized carbon nanotubes, which have carboxyl groups on oxidized surfaces of carbon nanotubes, have more polar surfaces and increased solubility in aqueous solution.[46, 47]

For imaging mass spectrometry (IMS), several ionization techniques such as matrix enhanced secondary ion mass spectrometry (ME-SIMS)[48], metal-assisted SIMS,[49, 50] MALDI, and cluster SIMS[51] have been used. The advantages and disadvantages of these ionization methods for IMS are well described in the recent review article.[52] Briefly, SIMS has the advantage in spatial resolution but MALDI is more suitable for detecting intact biological macromolecules. MALDI is also advantageous in terms of instrumental simplicity and cost. IMS with MALDI has been applied to biomarker studies and many other pathologically interesting case studies. [53-58]

There are two major issues in MALDI IMS. First, spatial resolution is usually limited by the laser spot size, which usually ranges from 80 μm to 200 μm in diameter. Spengler and coworkers decreased the spot size to about 0.6 μm by modifying the focusing lens.[59] Similarly, Luxembourg and coworkers utilized astigmatic optics and a position-sensitive detector.[60, 61] However, the spatial resolution of 4 μm from this system was determined by the 2D-position sensitive detector and not by the laser spot size.

Second, organic matrices used in conventional MALDI need co-crystallization that can lead to surface inhomogeneity. Luxembourg and coworkers showed different spectral profiles throughout the DHB-spotted surface by ME-SIMS.[62] Spraying a matrix solution electrically or pneumatically, immersing the sample in matrix solution, and dispensing matrix

solution by a piezoelectric microdispenser were suggested for generating homogeneous sample surface with matrixes.[63-65] Recently, Aerni and coworkers used acoustic droplet ejection[66] to generate 180-200 μm matrix droplets reproducibly on tissues. The other solution for generating matrix-sample surface is using ionic matrices. Armstrong and coworkers introduced new ionic liquids, which are basically combinations of acidic MALDI matrixes (e.g., DHB, SA, CHCA and etc.) and basic organic solvents such as pyridine, as MALDI matrixes.[67] Ionic liquid matrixes showed advantages of homogeneity, signal reproducibility, and vacuum-stability.[68-70] Lemaire and coworkers improved the performance of MALDI MS and IMS on rat brain tissue by using solid ionic matrixes such as CHCA/aniline in the negative-ion mode.[71] Recently, imaging tandem mass spectrometry (IMS/MS) of rat brain tissues by using IP-MALDI LIT mass spectrometer has been reported.[72] By doing MS/MS for site-specifically generated ions, separate chemically-selective images of product ions were generated for the isobaric ions at *m/z* 828.6 which could be composed of sodiated PC 38:6, DHB cluster, and phosphatidylethanolamine 38:4 (PE 38:4).[72]

Here we demonstrated a simple approach for GALDI MS by using an aerosol spray which contains 2-propanol-based colloidal graphite. Colloidal GALDI and conventional MALDI mass spectral analyses were performed for standard lipid mixtures which contain various compositions of PCs and GlcCers in high-vacuum (HV, 10^{-6} Torr) and at intermediate pressure (IP, 0.17 Torr). Softer ionization induced by collisional or vibrational cooling in IP-MALDI resulted in less fragmentation for labile molecules including gangliosides.[24, 25] By performing imaging MS of sample spots prepared by DHB matrix, we can derive location-specific mass spectral profiles for PC/GlcCers lipid mixtures as in earlier studies.[62, 73, 74] Total brain lipid extract was chosen as a model of a complex lipid mixture and was analyzed under four different sampling conditions. In addition, GALDI MS^n experiments were performed to identify the ionized species and to examine isobaric ions. We

also investigated the applicability of the colloidal graphite spraying method to direct rat brain tissue analyses and IMS. Finally, overlapping spatial information originating from PC and GalCer isobaric ions were separated from each other by performing IMS/MS.

Experimental Section

1,2-Dipalmitoyl-sn-glycero-3-phosphorylcholine (PC 32:0) and standard GlcCers from bovine buttermilk were purchased from Matreya LLC (Pleasant Gap, PA). Fatty acid composition of GlcCers from bovine buttermilk provided by the manufacturer is 14:0 (trace), 16:0 (15%), 18:0 (3%), 20:0 (2%), 22:0 (31%), 23:0 (28%), 24:0 (17%), and others (4%). Long chain bases for these GlcCers are all C_{18}-sphingosine (d18:1) bases. Brain total lipid extract in chloroform solution (10 mg/ml) was obtained from Avanti Polar Lipids Inc. (Alabaster, AL). DHB from Bruker Daltonics (Billerica, MA) was used. 2-propanol-based colloidal graphite aerosol spray (Aerodag® G) was obtained from Acheson Colloids (Port Huron, MI). All other chemicals were obtained from Fisher Scientific (Fairlawn, NJ).

Rat brain was collected from Spargue-Dawley rats from the College of Veterinary Medicine at Iowa State University and was frozen in liquid N_2 immediately. The frozen rat brain was cryosectioned into 15 μm thick specimens without embedding in the optimum cutting temperature (OCT) compound. Without the OCT compound, mass spectral interference is known to be decreased.[63] A cryostat from International Equipment Co. (Needham Heights, MA) was used for cryosectioning. Sectioned tissues were directly transferred and mounted onto a stainless-steel plate. The prepared tissue sections were stored at –20 °C before mass spectrometric analysis.

HV ($<10^{-6}$ Torr) LDI mass-spectrometric analysis was done with the Biosystems Voyager-DE PRO time-of-flight (TOF) mass spectrometer (Framingham, MA) equipped with a N_2 laser (337 nm, and maximum 180 μJ/pulse). Mass spectra were collected both in positive ion mode and negative ion mode with a ±20 kV accelerating potential. Mass

calibration was performed with lipid standards. An LTQ linear ion trap mass spectrometer equipped with vMALDI source (Thermo Electron, Mountain View, CA) was used for IP (0.17 Torr) LDI mass-spectrometric analysis and imaging MS. A description of the LTQ with vMALDI source can be found elsewhere.[75, 76] The laser source in this mass spectrometer is a fiber-optic guided N_2 laser (337 nm, and maximum 280 μJ/pulse before entering the optical fiber cable). The measured laser spot size is about 100 μm in diameter on the sample plate surface.

For lipid standard mixtures, 1 mg/ml of PC 32:0 and 1 mg/ml of total GlcCers stock solution were prepared in chloroform and in 70% chloroform/ 30% methanol respectively. Two types of lipid standard mixture batches were prepared. One batch contained a constant concentration of PC 32:0 (0.5 mg/ml) and various concentrations of GlcCers (from 0.005 mg/ml to 0.5 mg/ml). In the other batch, the concentration of GlcCers was kept constant (0.5 mg/ml), but the concentration of PC 32:0 were from 0.005 mg/ml to 0.5 mg/ml. The total lipid concentrations in the mixtures thus varied from 0.505 mg/ml to 1 mg/ml. Total brain lipid extract was diluted with chloroform and the final total lipid concentration was 2 mg/ml. 50 mg/ml DHB solution in 70% methanol and 30% water (containing a 0.1% trifluoroacetic acid) was prepared as a conventional MALDI matrix.

For conventional MALDI MS, 1 μl of sample solution was applied to the stainless sample plate followed by 1 μl of DHB matrix solution. For GALDI MS of PC/GlcCer mixtures and brain lipid extracts, colloidal graphite was sprayed directly onto the stainless-steel sample plate by using the aerosol spray can (Aerodag® G). The distance between the nozzle of the spray can and the sample plate was kept at 25 cm. Spraying was performed for 10 to 15 s to form a thin graphite film on the sample plate surface. After spraying, the surface was dried in air at room temperature for 5 min before the application of sample solutions. For the standard lipid mixture or total brain lipids extract, 1 μl of sample solution was applied onto the graphite-coated surface by using a micropipette. For brain tissues, colloidal graphite

was diluted four times with 2-propanol and the diluted solution was loaded into a sample bottle for an airbrush. Double-action airbrush, model "Aztek A470" with a 0.30 mm nozzle from Testor (Rockford, IL), was used. Spraying with 20 psi air pressure was performed 15.4 cm away from the sample plate. This way, the whole rat brain tissue was covered with colloidal graphite without moving either the airbrush or the sample plate. Spraying for 30 to 40 s gave the strongest signals from analytes and the lowest graphite background signals. After spraying, samples were allowed to dry in air for 10 min.

In HV-MALDI MS, mass spectra were recorded from the "big, needle-like crystals" area at the boundary of the sample spot and from the "small crystals" area at the center of the sample spot separately. These two mass spectra were then averaged and the averaged mass spectrum was used for data interpretation. In the case of IP-MALDI MS, rastering over a sample spot was performed. First, for one sample spot, serial optical images were taken every 1 mm-movement of the sample stage in either x- or y-directions. Each segment of the images has a size of 140 pixels by 170 pixels. These segments of optical images were reconstructed as one optical image for one sample spot. Second, a sample spot were rastered with a 100 μm step size. For each spot, a mass spectrum was recorded for desorbed ions by co-adding over five laser shots. For each MALDI sample spot, a mass spectrum constructed by averaging mass spectra from all rastering points was used for data interpretation.

For IMS of rat brain tissue, the number of laser shots for each sample spot was first determined by collecting mass spectra in a small area (usually 10 rastering points) with automatic gain control (AGC, which keeps ion amounts in the trap constant by changing the number of laser shots). Based on the average number of shots per spot with AGC, the number of laser shots was fixed without AGC (usually 5 to 8 shots per spot) when collecting mass spectra over the whole tissue. The tissue sample was rastered with 100 μm steps. In the case of IMS/MS, target precursor ions were first selected based on first generation product ion spectra for the major peaks in the extracted mass spectra and then first generation product ion

spectra of the selected precursor ion were collected with spatial information for all rastering points over the tissue section (instead of collecting full mass profiles). For a 1.8 cm × 0.8 cm tissue sample, about 10,000 mass spectra were collected over 1.7 h for IMS and 3.1 h for IMS/MS, respectively.

Chemically-selective images and extracted mass spectra from specific locations were generated by using the custom software from Thermo (vMALDI Data Browser). Chemically-selective images were plotted as maps using either absolute intensity values or normalized intensity values. The normalized intensity is defined as the fractional peak intensity for the peak of interest compared to the total ion current (TIC) of each mass spectrum. The mass window for generating chemically-selective images was 0.8 Da.

Results and Discussion

Colloidal graphite surface for GALDI MS. The electron microscopic image of the graphite surface generated by colloidal graphite aerosol spray is shown in Figure 1. Graphite particles in the aerosol spray are about 1 μm-sized with flake shapes (Figure 1) and are finer than most other types of preparations. The graphite surface generated in this manner has advantages over other methods of generating graphite surfaces. First, this method is fast and has minimum preparation steps. Only cleaning of the substrate surface (a stainless steel sample plate), spraying colloidal graphite, and drying the plate in the air are needed for MS. It took less than 10 min for the whole preparation. Second, after performing MS, the graphite surface was easily removed by washing with 2-propanol or acetone. The cleaned plate can be reused for either GALDI MS or conventional MALDI MS. Third, because of using conventional stainless steel sample plate as a base, the mechanical stability of the sample plate, which could be an issue when using a pressurized graphite plate, is very good. Last, because the colloidal graphite spray contains thermoplastic resin as a binder, formation of graphite dust is much less problematic than when using a graphite/liquid suspension.

MALDI and GALDI MS of mixtures of PC and GlcCers at different sample chamber pressures. As mentioned before, the presence of PCs and SMs prevents the detection of other lipid species in MALDI MS. To examine whether this phenomenon occurs in GALDI MS, standard batch solutions of various compositions of PC 32:0 and GlcCers were analyzed by MALDI MS and GALDI MS at two different sample chamber pressures. The mass spectra are shown in Figure 2 and mass peak assignments are listed in Table 1 with relative abundances. With DHB matrix, protonated PC ions are dominant at both pressures (Figure 2(a), 2(b), and Table 1). However, with colloidal graphite, the sodiated GlcCer ions were the most intense at both pressures (Figure 2(c), 2(d), and Table 1). The signal intensity ratios among different lipid species were different depending on sample chamber pressures. PC to GlcCer signal intensity ratios were higher in IP than in HV with DHB matrix (Figure 2(a), 2(b), and Table 1). This tendency was even more significant with colloidal graphite (Figure 2(c), 2(d), and Table 1). In other words, the decrease of PC-related mass peaks or the increase of GlcCer-related mass peaks was more distinct in HV than in IP.

To examine the ion signals as a function of lipid concentration and composition, various ratios of PC/GlcCers mixtures were analyzed under the four different conditions. Relative intensities for the major peak of each lipid species are listed in Table 2, and mass spectra for these lipid standard mixtures are shown in Supporting Information Figure S-1, S-2, S-3, and S-4. First, the mass peak corresponding to $[PC\ 32:0 + H]^+$ was dominant in both HV- and IP-MALDI mass spectra even when the concentration of PC 32:0 was tenths of that of total GlcCers (Batch 1). Second, in MALDI, no obvious difference between in IP and in HV was observed in terms of the relative peak intensities. Third, in contrast to HV- and IP-MALDI, significant peak intensity for the mass peak corresponding to $[GlcCer\ 22:0 + Na]^+$ was observed in both HV- and IP-GALDI (Batch 2). Fourth, in GALDI, the peak suppression of PC 32:0 related ions was less in IP than HV (Batch 1) and the peak enhancement for $[GlcCer\ 22:0 + Na]^+$ was higher in HV than IP (Batch 2). In other words, IP-GALDI MS may

be more suitable for the simultaneous analysis of various lipid species in complex mixtures, while HV-GALDI MS may be better for the analysis of cerebrosides in complex lipid mixtures without separation.

Localization of analytes with DHB matrix. Mass spectral studies for elucidating the incorporation of analytes into DHB matrix crystals and the heterogeneity of MALDI samples prepared with DHB matrix have already been reported by many researchers.[62, 73, 74] Because PCs and GlcCers showed very different characteristics in ionization, localization of analytes was examined by LDI imaging MS. Because the size of conventional laser beams at the target plate (80-200 μm) is bigger than those of most crystals, resolving one matrix crystal from another is hard to achieve. However, due to the deposition/drying process, there are two distinct regions which can be macroscopically recognized from the optical image shown as the first image in Figure 3(a). One region is located at the boundary of the sample spot and is mainly composed of "big, needle-like crystals". The other region is at the center of the sample spot and "small crystals" are distributed heterogeneously throughout this region. The subsequent images in Figure 3(a) represent chemically-selective images for the major ions detected from the PC 32:0/GlcCers mixture. As Luxembourg and coworkers pointed out,[62, 73, 74] protonated molecules, $[PC\ 32:0 + H]^+$, showed the most intense peaks at the boundary of the sample which consists of big matrix crystals. However, sodiated molecules, such as $[PC\ 32:0 + Na]^+$, $[GlcCer\ 22:0 + Na]^+$, and $[GlcCer\ 23:0 + Na]^+$ showed much higher peak intensities at the interior of the MALDI sample spot. This phenomenon also can be seen clearly from the mass spectra extracted from the two different regions (Figure 3(b) and 3(c)). This indicates that incorrect mass profiles of lipid mixtures could be generated when spectra was collected and averaged for a certain region but not for the whole sample spot prepared with DHB matrix. In contrast to DHB matrix, colloidal graphite does not involve any crystallization process and are much finer in dimension. Therefore, the surface formed by

colloidal graphite provides uniform signals without hot spots, and is well suited for chemical imaging.

MALDI and GALDI MS and MS^n of total brain lipid extract at different sample chamber pressures. Total brain lipid extract was studied under the various ionization modes because the components and their structures have been relatively well identified or analyzed by several mass spectral techniques. Mass spectral profiles of the brain lipid extract in various ionization environments are shown in Figure 4. First, mass peaks from *m/z* 730 to *m/z* 810 are dominant in MALDI, whereas mass peaks from *m/z* 820 to *m/z* 880 are the major peaks in GALDI. This tendency is similar to that in the PC/GlcCer lipid standard mixtures. Second, for MALDI, no major difference between HV and IP was observed (Figure 4(a) versus 4(b)). Third, for GALDI, the higher mass peak intensities in the region of m/z 820-880 and the lower mass peak intensities in the region of *m/z* 730-810 are more pronounced in HV than in IP (Figure 4(c) versus 4(d)). In other words, lipid species in the region of *m/z* 820-880 were detected more selectively in HV than in IP. This trend is also analogous to that in the mass profiles of PC/GlcCer lipid standard mixtures.

To identify the lipid species detected, MS/MS and MS^3 experiments for most of the major peaks the mass spectra of brain lipid extract (Figure 4(b) and (d)) were performed. Many structural studies of cerebrosides using tandem mass spectrometry have been reported with ESI MS,[3, 10, 77] but not many with LDI MS so far. For example, GALDI 1st generation product ion spectrum of *m/z* 850.66, the most intense peak in Figure 4(d), is shown in Figure 5(a). Neutral loss of 162 Da (NL 162) and NL 180 correspond to the loss of $C_6H_{10}O_5$ and the loss of a galactose unit at the head group position of the sphingosine long chain. NL 18, which corresponds to the loss of water, was also observed. The predominant mass peak at *m/z* 484.50 corresponds to the sodiated C_{18} sphingosine long chain base and *m/z* 512 can be assigned as the sodiated aldehyde form of the C_{18} sphingosine long chain base (see the scheme on Figure 5(a)). The mass peak at *m/z* 850.66 can be assigned as [GalCer

d18:1/24:0h + Na]$^+$. GalCer d18:1/24:0h has been known to be the major hydroxylated cerebroside compound in brain.[3, 78] Both NL 162 and NL 180 are highly characteristic patterns in the first generation product ion spectra for precursor ions of cerebrosides. For all mass peaks assigned as cerebrosides including both standards (data not shown) and the brain lipid extract, these two NLs were always observed in their first generation product ion spectra. In addition, the mass peaks at *m/z* 484 (C_{18} sphingosine long chain base) and at *m/z* 486 (C_{18} sphinganine long chain base) represent also significant mass fragment ions for cerebrosides and one of both was observed in most cerebrosides (Table 3). To verify the structure of the cerebroside further, MS^3 experiments was also performed for the *m/z* 484.50 ion (Figure 5(b)). NL 162 and NL 180 were observed again in the second generation product ion mass spectrum. In addition to these, the loss of NH_3 (NL 17) was also observed. The peaks at *m/z* 203 and *m/z* 185 could be identified as the sodiated galactose ion and subsequent loss of water from it.

Mass peak assignments for cerebrosides and PCs based on the major fragment ions and NLs are listed in Table 3. Only the major ions which have been verified by first generation product ion spectra are listed. Fragment ions and neutral loss patterns of cerebroside species have already been explained with Figure 5. For PCs, the characteristic mass fragment ion m/z 184 (phosphocholine head group), was observed for some PC precursor ions. NL 18(-H_2O), NL 59 (–$N(CH_3)_3$), NL 124(-ethyl phosphate), NL 183(-phosphocholine head group) were observed for PCs. Similar patterns were observed in earlier studies[75, 79-81] and the information was used for identifying PCs. NL 146, NL 162, NL 205 were also observed for some PC precursor ions. NL 146 could correspond to NL of ethyl phosphate with sodium (ethyl phosphate + Na – H) and NL 205 could correspond to NL of phosphocholine head group with sodium (phosphocholine head group + Na – H). NL 162 from PC precursor ions could correspond to NL of ethyl phosphate with potassium (ethyl phosphate + K – H). Note that

there are two neutral losses which have the same decrease of 162 Da but originated from different species; NL 162 from GalCer precursor ions and NL 162 from adduct ions consisting of PC and potassium. The difference between these two neutral losses is that NL 162 from GalCers precursor ions was always observed with NL 180 (-galactose) but NL 162 from PC precursor ions was not. In Table 3, NL 162 from PC precursor ions was annotated as "NL 162k" to distinguish from NL 162 from GalCer precursor ions. As expected from the analysis of the standard lipid mixture, GALDI gives more informative mass profiles for cerebroside species whereas MALDI gives more informative mass profiles for PCs.

In Table 3, note that more than one lipid species can be associated with one *m/z*. There are two possible causes for these isobaric ions in mass spectrum. First, several types of adduct ions can be formed, even if two compounds have quite different monoisotopic masses. In the case of PC 38:4 and PC 36:1, which are present in the brain, their difference in calculated exact mass is 21.98 Da. This is the same as the calculated exact mass difference between H and Na. Therefore, $[PC\ 38:4 + H]^+$ and $[PC\ 36:1 + Na]^+$ can be detected simultaneously at *m/z* 810. Second, if the monoisotopic masses of two or more compounds are too close to each other (less than 0.1 Da difference), they overlap and cannot be selected separately for MS/MS experiments. For example, the monoisotopic masses for GalCer d18:1/24:1 and PC 38:4 are 809.59 Da and 809.67 Da respectively and both compounds are known to be present in the brain. They were observed together in both MALDI and GALDI as listed in Table 3.

However, the ratio of $[GalCer\ d18:1/24:1 + Na]^+$ and $[PC\ 38:4 + Na]^+$ in MALDI MS was different from that in GALDI MS. Figure 6 shows the two first generation product ion spectra of *m/z* 832. Similar fragment patterns were observed but the relative abundances are different in the two modes. The mass peak at *m/z* 773.25 corresponding to NL 59 from PCs is dominant in IP-MALDI product ion spectrum (Figure 6(a)) while the mass peak at *m/z* 670.58 corresponding to NL 162 from cerebrosides is the most intense peak in IP-GALDI

product ion spectrum (Figure 6(b)). Comparison between the two mass spectra confirms that GALDI MS is advantageous when cerebrosides need to be analyzed without separation from the lipid pools, such as crude lipid extracts or tissue samples. In both mass spectra, mass peaks corresponding NL 43 and NL 87 were also observed. NL 87 could correspond to the loss of the $C_3H_5O_2N$ from the phosphatidylserine head group[82] and NL 43 could be the neutral loss of aziridine from phosphatidylethanolamine.[83] This means that many other lipids, such as PE, PS, and PG, can also be incorporated into one m/z for the same reasons.

Detection of sulfatides in negative ion mode by GALDI MS. Sulfatides (STs), one of the derivatives of GalCers, are 3-sulfate esters of GalCers. STs are enriched in brain tissues and mediate several biological processes including cell growth, cell adhesion, and morphogenesis.[84] By using MALDI MS, STs were successfully detected from brain tissue, serum and renal tubule cells in earlier studies.[19, 85, 86] Because ST has a sulfate group (SO_4^-), they are also easily detected in negative ion mode as shown in Figure 7. The hydroxylated forms of STs were also observed. Since C_{24} fatty acids are dominant in the mammalian nervous system,[84] STs and hydroxylated STs which have 24:1 or 24:0 fatty acid composition were observed as the major species here.

IMS and IMS/MS in rat brain tissues by using GALDI MS. To analyze constituents directly from tissue samples, ionization assisting materials need to be coated on top of the tissue. Because extract or other liquid samples were loaded on top of the graphite layer, the thickness of the graphite layer was not critical in extract analysis. In tissue analysis, however, too small an amount of colloidal graphite could give weak signals and too large an amount could generate strong interference signals from the colloidal graphite. To spray more reproducibly, an airbrush was used with the four-times diluted colloidal graphite solution instead of an aerosol spray can. We note that too dilute (over ten times) a solution could not give a firmly-coated surface.

A lipid mass profile in the positive ion mode was generated from a rat brain tissue as shown in Figure 8(b). The lipid profile in negative-ion mode is shown in Supporting Information Figure S-5. To identify lipid species, MS/MS and MS^3 experiments were performed for major peaks in the lipid profile mass spectrum. For example, the mass peak at *m/z* 844.50 in Figure 8(b) could be identified as $[PC\ 38:6\ +K]^+$ and $[PE\ 38:4\ +\ 2K\ –\ H]^+$ based on previous studies[72, 83] and first generation product ion mass spectrum (See Supporting Information Figure S-6). Chemically-selective images for the identified ions are shown in Figure 9. Note that not only the ions listed in Figure 9 but also other isobaric ions could contribute to these chemically selective images as discussed previously. From the images in Figure 9, cerebroside-rich areas and cerebroside-deficient areas can be recognized clearly and the extracted mass spectra from these two regions are shown in Figure 8(c) and 8(d). The mass region of *m/z* 800-880, where most of the cerebrosides were found, is obviously different in Figures 8(c) and 8(d) in terms of mass profiles and relative intensities.

To separate the spatial information of isobaric ions from each other, IMS/MS was performed. The mass peak at *m/z* 832.58 was chosen here because both PC and cerebroside species show this common mass peak from the lipid extract analysis. First product ion spectra of ions at *m/z* 832.58 (data are not shown) from the rat brain tissue have the same fragmentation patterns as those from lipid extracts (Figure 6). Chemically-selective images of the precursor ion at *m/z* 832, the product ion at *m/z* 773, and the product ion at *m/z* 670 are shown in Figure 10. The spatial distribution of product ions at *m/z* 670, which corresponds to NL 162 from $[GalCer\ d18:1/24:1\ +\ Na]^+$, is similar to those of other GalCer species shown in Figure 9. Figure 10 shows that the spatial distribution of the two isobaric ions can be clearly separated by performing IMS/MS.

Conclusions

In this study, a simple and effective method of LDI based on colloidal graphite was developed and was applied to lipid analyses. Comparison between GALDI and MALDI of standard lipid mixtures clearly showed the increase in signal from cerebrosides for the former, making the former more suitable for detection of cerebroside species from lipid pools without separation. With total brain lipid extract, twenty-two cerebroside species were detected as major compounds by IP-GALDI MS and confirmed by MS^n experiments while only eight cerebroside species were verified by IP-MALDI MS and MS^n experiments. From Table 3 and Figure 4(c), we can conclude that the major mass peaks in HV-GALDI mass spectrum correspond to cerebroside species. The peak enhancement for cerebrosides and the peak suppression for PCs were more significant in HV than in IP. Therefore, HV could be more suitable for selective detection of cerebrosides and IP could be more appropriate for profiling various kinds of lipid species in complex lipid mixtures. Negative ion mode of GALDI also showed comparable performance as MALDI for detecting sulfatides in brain lipid extracts. For rat brain tissue, mass profiles and chemically-selective images for lipids were successfully obtained with the modified colloidal graphite spraying technique. Cerebrosides and sulfatides were well detected in tissue analysis as in extract analysis, and the increase in intensities of cerebrosides facilitated the generation of images for cerebrosides. Automated MS/MS experiments over the tissue surface and image processing from these experiments showed the inherent problem of full mass scan data and the need for MS/MS imaging. However, performing MS/MS for even one precursor ion over the tissue surface is already time consuming. Therefore, faster protocols for IMS and further development of IMS/MS are needed. In this work, the issue about sensitivity increase for fragile biomolecules in IP LDI MS due to stabilization of labile bonds by collisional cooling was not discussed. Future studies on the analyses of labile molecules such as gangliosides in HV and IP by using GALDI MS and MS^n would be valuable.

Acknowledgements

E.S.Y. thanks the Robert Allen Wright Endowment for Excellence for support. The Ames Laboratory is operated for the US Department of Energy by Iowa State University under Contract No. W-7405-Eng-82. This work was supported by the Director of Science, Office of Basic Energy Sciences, Divisions of Chemical Sciences and Biosciences.

Appendixes

Supplemental GALDI mass spectra for lipid mixture standards with various ratios and rat brain tissues, and product ion mass spectrum for the *m/z* 844 are listed in Appendix 1. In Appendix 2, a complete scientific paper which describes GALDI MS studies of fruit samples is presented.

Table 1. Mass peak assignments with relative intensities for lipid species in lipid standard mixtures[a] under different sample chamber pressures

Identification	Theoretical m/z (Da)[b]	High-Vacuum		Intermediate Pressure	
		Observed m/z (Relative Intensity[c]) with DHB	Observed m/z (Relative Intensity) with Graphite	Observed m/z (Relative Intensity) with DHB	Observed m/z (Relative Intensity) with Graphite
[GlcCer 16:0+Na]$^+$ [d]	722.55	722.59 (29.4)	722.50 (78.2)	722.66 (12.3)	722.58 (54.8)
[PC 32:0+H]$^+$ [e]	734.57	734.56 (100.0)	—	734.50 (100.0)	734.50 (17.6)
[GlcCer 18:0+Na]$^+$	750.58	750.52 (4.4)	750.53 (13.0)	750.66 (2.6)	750.66 (12.8)
[PC 32:0+Na]$^+$	756.55	756.52 (39.7)	756.57 (6.8)	756.50 (81.2)	756.50 (81.2)
[PC 32:0+K]$^+$	772.53	—	—	—	772.50 (7.8)
[GlcCer 20:0+Na]$^+$	778.62	778.56 (10.1)	778.59 (30.5)	778.66 (5.0)	778.66 (27.3)
[GlcCer 21:0+Na]$^+$	792.63	792.62 (11.0)	792.60 (38.6)	792.66 (5.6)	792.66 (33.7)
[GlcCer 22:0+Na]$^+$	806.65	806.66 (23.6)	806.63 (100.0)	806.66 (16.5)	806.66 (100.0)
[GlcCer 23:0+Na]$^+$	820.66	820.60 (19.6)	820.65 (67.2)	820.66 (13.2)	820.66 (85.1)
[GlcCer 24:0+Na]$^+$	834.68	834.61 (13.1)	834.66 (41.4)	834.75 (8.2)	834.66 (53.8)

[a]Standard lipid mixture contains 0.5mg/ml of PC 32:0 and 0.5mg/ml of total GlcCers.

[b]Masses are monoisotopic.

[c]Relative intensity = [(Intensity of relevant mass peak)/(Intensity of the most intense mass peak in the mass spectrum)] × 100.

[d]All glucosylceramide standards have C_{18} sphingosine (d18:1) base and the numbers m:n correspond to the number of the total carbons (m):number of double bonds (n) in the amide-linked fatty acid.

[e]Number x:y corresponds to the number of the total carbons of fatty acids at sn-1 and sn-2 position (x): number of double bonds (y) of PC.

Table 2. Relative peak intensities of major peaks in lipid standard mixtures with various PC/GlcCers ratios[a]

	Concentration (mg/ml)		Relative Intensity with DHB (%)				Relative Intensity with Graphite (%)			
	PC 32:0	GlcCers	$[PC32:0+H]^+$		$[GlcCer22:0+Na]^+$		$[PC32:0+Na]^+$		$[GlcCer22:0+Na]^+$	
Pressure			**HV**	**IP**	**HV**	**IP**	**HV**	**IP**	**HV**	**IP**
Batch 1	0.25	0.5	346.6	559.3	100		12.4	57.1	100	
	0.125		186.8	311.6			10.1	33.2		
	0.025		115.5	134.1			n.d.	7.6		
	0.005		83.9	112.8			n.d.	5.1		
Batch 2	0.5	0.25	100		9.2	8.3	100		634.5	95.0
		0.125			8.4	6.0			410.3	33.0
		0.025			2.2	4.5			30.5	15.7
		0.005			n.d.	3.4			n.d.	8.3

[a]Mass spectra used for calculation are listed in Supporting Information Figure S-1, S-2, S-3, and S-4.

[b]n.d. represents "not detected".

Table 3. Mass peak assignments for cerebrosides and phosphatidylcholines in brain lipid extract based on MS/MS experiments

IP-GALDI			IP-MALDI	
Observed Product Ions[a] and Neutral Losses (NLs)[b]	**Ions Assigned**	***m/z***	**Ions Assigned**	**Observed Product Ions and Neutral Losses (NLs)**
	Cerebrosides		**Cerebrosides**	
NL 18, NL 162, NL 180	$[GalCer\ d18:1/18:0^{c} + Na]^+$	**750**		
m/z 484, NL 18, NL 162, NL 180	$[GalCer\ d18:1/18:0h^{d} + Na]^+$	**766**		
NL 18, NL 162, NL 180	$[GalCer\ d18:1/22:1 + Na]^+$	**804**		
NL 18, NL 162, NL 180	$[GalCer\ d18:1/22:0 + Na]^+$	**806**	$[GalCer\ d18:1/22:0 + Na]^+$	NL 18, NL 162, NL180
m/z 484, NL 18, NL 162, NL 180	$[GalCer\ d18:0/22:0 + Na]^+$	**808**	$[GalCer\ d18:0/22:0 + Na]^+$	*m/z* 484, NL 18, NL 162, NL180
m/z 484, *m/z* 512, NL 18, NL 162, NL 180	$[GalCer\ d18:1/23:0 + Na]^+$	**820**		
m/z 484, *m/z* 512, NL 18, NL 162, NL 180	$[GalCer\ d18:1/22:0h + Na]^+$	**822**	$[GalCer\ d18:1/22:0h + Na]^+$	*m/z* 484, m/z 512, NL 18, NL 162, NL180
m/z 486, *m/z* 514, NL 18, NL 162, NL 180	$[GalCer\ d18:0/22:0h + Na]^+$	**824**		
NL 18, NL 162, NL 180	$[GalCer\ d18:1/24:1 + Na]^+$	**832**	$[GalCer\ d18:1/24:1 + Na]^+$	NL 18, NL 162, NL180
m/z 484, *m/z* 512, NL 18, NL 162, NL 180	$[GalCer\ d18:1/24:0 + Na]^+$	**834**		
m/z 484, *m/z* 512, NL 18, NL 162, NL 180	$[GalCer\ d18:1/23:0h + Na]^+$	**836**	$[GalCer\ d18:1/23:0h + Na]^+$	*m/z* 484, NL 18, NL 162, NL180
m/z 486, NL 18, NL 162, NL 180	$[GalCer\ d18:0/23:0h + Na]^+$	**838**		
m/z 484, *m/z* 512, NL 18, NL 162, NL 180	$[GalCer\ d18:1/24:1h + Na]^+$ $[GalCer\ d18:1/25:0 + Na]^+$	**848**	$[GalCer\ d18:1/24:1h + Na]^+$ $[GalCer\ d18:1/25:0 + Na]^+$	*m/z* 484, *m/z* 512, NL 18, NL 162, NL180
m/z 484, *m/z* 512, NL 18, NL 162, NL 180	$[GalCer\ d18:1/24:0h + Na]^+$	**850**	$[GalCer\ d18:1/24:0h+Na]^+$	*m/z* 484, *m/z* 512, NL 18, NL 162, NL180
m/z 486, *m/z* 514, NL 18, NL 162, NL 180	$[GalCer\ d18:0/24:0h + Na]^+$	**852**	$[GalCer\ d18:0/24:0h+Na]^+$	*m/z* 486, NL 18, NL 162, NL180
m/z 484, NL 18, NL 162, NL 180	$[GalCer\ d18:1/26:1 + Na]^+$	**860**		
m/z 484, *m/z* 512, NL 18, NL 162, NL 180	$[GalCer\ d18:1/25:1h + Na]^+$	**862**		
m/z 484, *m/z* 512, NL 18, NL 162, NL 180	$[GalCer\ d18:1/25:0h + Na]^+$	**864**		
m/z 486, NL 18, NL 162, NL 180	$[GalCer\ d18:0/25:0h + Na]^+$	**866**		
m/z 484, *m/z* 512, NL 18, NL 162, NL 180	$[GalCer\ d18:1/26:1h + Na]^+$	**876**		
m/z 484, *m/z* 512, NL 18, NL 162, NL 180	$[GalCer\ d18:1/26:0h + Na]^+$	**878**		
m/z 486, *m/z* 514, NL 18, NL 162, NL 180	$[GalCer\ d18:0/26:0h + Na]^+$	**880**		
	Phosphatidylcholines		**Phosphatidylcholines**	
NL 124, NL 146	$[PC\ 34:1 - N(CH_3)_3 + Na]^+$	**723**		
		734	$[PC\ 32:0 + H]^+$	*m/z* 184, NL 59, NL124
NL 124, NL 162k	$[PC\ 34:1 - N(CH_3)_3 + K]^+$	**739**		
NL 124, NL 146	$[PC\ 36:1 - N(CH_3)_3 + Na]^+$	**751**		
NL 59, NL 124, NL146	$[PC\ 32:0 + Na]^+$	**756**	$[PC\ 32:0 + Na]^+$	NL 59, NL 183, NL 205
		760	$[PC\ 34:1 + H]^+$	*m/z* 184, NL 59, NL 124, NL183
		762	$[PC\ 34:0 + H]^+$	*m/z* 184, NL 59
NL 59	$[PC\ 32:0 + K]^+$	**772**	$[PC\ 32:0 + K]^+$	NL 59, NL183
NL 59	$[PC\ 34:1 + Na]^+$	**782**	$[PC\ 34:1 + Na]^+$	NL 59, NL 124, NL 183, NL 205
		784	$[PC\ 34:0 + Na]^+$	NL 59, NL 183, NL 205
		786	$[PC\ 36:2 + H]^+$	NL 59, NL 183
		788	$[PC\ 36:1 + H]^+$	NL 59, NL183
NL 59, NL162k	$[PC\ 34:1 + K]^+$	**798**	$[PC34:1 + K]^+$	NL 59, NL 183
		806	$[PC\ 38:6 + H]^+$	NL 59, NL 124, NL 183
NL 59	$[PC\ 36:2 + Na]^+$	**808**	$[PC\ 36:2 + Na]^+$	NL 59, NL 124, NL 183
NL 59	$[PC\ 36:1 + Na]^+$	**810**	$[PC\ 36:1 + Na]^+$ a/o $[PC\ 38:4 + H]^+$	NL 59, NL 124
NL 59	$[PC\ 38:4 + Na]^+$	**832**	$[PC\ 38:4 + Na]^+$	NL 59, NL 124, NL 183
		836	$[PC\ 38:2 + Na]^+$	NL 59, NL 183

[a,b] See text for assignments of product ions and neutral losses

[c] GalCer A/B corresponds to galactosylceramide sphingoid long chain base (A)/amide-linked fatty acid (B).

[d] h corresponds to the hydroxyl group at the C2 position of the amide-linked fatty acid.

References

(1) Bektas, M.; Spiegel, S. *Glycoconjugate Journal* **2003**, *20*, 39-47.

(2) Tan, R. X.; Chen, J. H. *Natural Product Reports* **2003**, *20*, 509-534.

(3) Han, X. L.; Cheng, H. *Journal of Lipid Research* **2005**, *46*, 163-175.

(4) Lingwood, C. A. *Current Opinion in Chemical Biology* **1998**, *2*, 695-700.

(5) Coetzee, T.; Fujita, N.; Dupree, J.; Shi, R.; Blight, A.; Suzuki, K.; Suzuki, K.; Popko, B. *Cell* **1996**, *86*, 209-219.

(6) Scriver, C. R.*,* 8th ed.; McGraw-Hill: New York, 2001, pp 2641-2692.

(7) Han, X. L.; Holtzman, D. M.; McKeel, D. W.; Kelley, J.; Morris, J. C. *Journal of Neurochemistry* **2002**, *82*, 809-818.

(8) Han, X. L.; Cheng, H.; Fryer, J. D.; Fagan, A. M.; Holtzman, D. M. *Journal of Biological Chemistry* **2003**, *278*, 8043-8051.

(9) Hauser, G. *Journal of Neurochemistry* **1968**, *15*, 1237-1238.

(10) Han, X. L.; Gross, R. W. *Mass Spectrometry Reviews* **2005**, *24*, 367-412.

(11) Whitehouse, C. M.; Dreyer, R. N.; Yamashita, M.; Fenn, J. B. *Analytical Chemistry* **1985**, *57*, 675-679.

(12) Tanaka, K.; Waki, H.; Ido, Y.; Akita, S.; Yoshida, Y.; Yoshida, T.; Matsuo, T. *Rapid Communications in Mass Spectrometry* **1988**, *2*, 151-153.

(13) Karas, M.; Hillenkamp, F. *Analytical Chemistry* **1988**, *60*, 2299-2301.

(14) Schiller, J.; Suss, R.; Arnhold, J.; Fuchs, B.; Lessig, J.; Muller, M.; Petkovic, M.; Spalteholz, H.; Zschornig, O.; Arnold, K. *Progress in Lipid Research* **2004**, *43*, 449-488.

(15) Welti, R.; Wang, X. M. *Current Opinion in Plant Biology* **2004**, *7*, 337-344.

(16) Petkovic, M.; Schiller, J.; Muller, M.; Benard, S.; Reichl, S.; Arnold, K.; Arnhold, J. *Analytical Biochemistry* **2001**, *289*, 202-216.

(17) Harvey, D. J. *Journal of Mass Spectrometry* **1995**, *30*, 1333-1346.

(18) Harvey, D. J. *Journal of Mass Spectrometry* **1995**, *30*, 1311-1324.

(19) Jackson, S. N.; Wang, H. Y. J.; Woods, A. S. *Analytical Chemistry* **2005**, *77*, 4523-4527.

(20) Estrada, R.; Yappert, M. C. *Journal of Mass Spectrometry* **2004**, *39*, 412-422.

(21) Schiller, J.; Subb, R.; Petkovic, M.; Hilbert, N.; Muller, M.; Szchornig, O.; Arnhold, J.; Arnold, K. *Chemistry and Physics of Lipids* **2001**, *113*, 123-131.

(22) Juhasz, P.; Costello, C. E. *Journal of the American Society for Mass Spectrometry* **1992**, *3*, 785-796.

(23) Fujiwaki, T.; Yamaguchi, S.; Sukegawa, K.; Taketomi, T. *Journal of Chromatography B* **1999**, *731*, 45-52.

(24) O'Connor, P. B.; Costello, C. E. *Rapid Communications in Mass Spectrometry* **2001**, *15*, 1862-1868.

(25) O'Connor, P. B.; Mirgorodskaya, E.; Costello, C. E. *Journal of the American Society for Mass Spectrometry* **2002**, *13*, 402-407.

(26) Ivleva, V. B.; Elkin, Y. N.; Budnik, B. A.; Moyer, S. C.; O'Connor, P. B.; Costello, C. E. *Analytical Chemistry* **2004**, *76*, 6484-6491.

(27) Dreisewerd, K.; Muthing, J.; Rohlfing, A.; Meisen, I.; Vukelic, Z.; Peter-Katalinic, J.; Hillenkamp, F.; Berkenkamp, S. *Analytical Chemistry* **2005**, *77*, 4098-4107.

(28) Ivleva, V. B.; Sapp, L. M.; O'Connor, P. B.; Costello, C. E. *Journal of the American Society for Mass Spectrometry* **2005**, *16*, 1552-1560.

(29) Taketomi, T.; Sugiyama, E.; Uemura, K.; Hara, A.; Hidaka, H.; Tozuka, M.; Nakabayashi, T.; Katsuyama, T. *Journal of Lipid Research* **2001**, *42*, 873-885.

(30) Yurkova, I.; Kisel, M.; Arnhold, J.; Shadyro, O. *Chemistry and Physics of Lipids* **2005**, *134*, 41-49.

(31) Fujiwaki, T.; Yamaguchi, S.; Tasaka, M.; Sakura, N.; Taketomi, T. *Journal of Chromatography B-Analytical Technologies in the Biomedical and Life Sciences*

2002, *776*, 115-123.

(32) Sunner, J.; Dratz, E.; Chen, Y. C. *Analytical Chemistry* **1995**, *67*, 4335-4342.

(33) Dale, M. J.; Knochenmuss, R.; Zenobi, R. *Analytical Chemistry* **1996**, *68*, 3321-3329.

(34) Peng, S.; Edler, M.; Ahlmann, N.; Hoffmann, T.; Franzke, J. *Rapid Communications in Mass Spectrometry* **2005**, *19*, 2789-2793.

(35) Zumbuhl, S.; Knochenmuss, R.; Wulfert, S.; Dubois, F.; Dale, M. J.; Zenobi, R. *Analytical Chemistry* **1998**, *70*, 707-715.

(36) Kim, J.; Kang, W. *Bulletin of the Korean Chemical Society* **2000**, *21*, 401-404.

(37) Kim, J.; Paek, K.; Kang, W. *Bulletin of the Korean Chemical Society* **2002**, *23*, 315-319.

(38) Kim, H. J.; Lee, J. K.; Park, S. J.; Ro, H. W.; Yoo, D. Y.; Yoon, D. Y. *Analytical Chemistry* **2000**, *72*, 5673-5678.

(39) Park, K. H.; Kim, H. J. *Rapid Communications in Mass Spectrometry* **2001**, *15*, 1494-1499.

(40) Li, X. P.; Wilm, M.; Franz, T. *Proteomics* **2005**, *5*, 1460-1471.

(41) Black, C.; Poile, C.; Langley, J.; Herniman, J. *Rapid Communications in Mass Spectrometry* **2006**, *20*, 1053-1060.

(42) Chen, Y. C.; Shiea, J.; Sunner, J. *Journal of Chromatography A* **1998**, *826*, 77-86.

(43) Ugarov, M. V.; Egan, T.; Khabashesku, D. V.; Schultz, J. A.; Peng, H. Q.; Khabashesku, V. N.; Furutani, H.; Prather, K. S.; Wang, H. W. J.; Jackson, S. N.; Woods, A. S. *Analytical Chemistry* **2004**, *76*, 6734-6742.

(44) Ren, S. F.; Zhang, L.; Cheng, Z. H.; Guo, Y. L. *Journal of the American Society for Mass Spectrometry* **2005**, *16*, 333-339.

(45) Xu, S. Y.; Li, Y. F.; Zou, H. F.; Qiu, J. S.; Guo, Z.; Guo, B. C. *Analytical Chemistry* **2003**, *75*, 6191-6195.

(46) Ren, S. F.; Guo, Y. L. *Rapid Communications in Mass Spectrometry* **2005**, *19*, 255-

260.

(47) Pan, C. S.; Xu, S. Y.; Hu, L. G.; Su, X. Y.; Ou, J. J.; Zou, H. F.; Guo, Z.; Zhang, Y.; Guo, B. C. *Journal of the American Society for Mass Spectrometry* **2005**, *16*, 883-892.

(48) Wu, K. J.; Odom, R. W. *Analytical Chemistry* **1996**, *68*, 873-882.

(49) Delcorte, A.; Bour, J.; Aubriet, F.; Muller, J. F.; Bertrand, P. *Analytical Chemistry* **2003**, *75*, 6875-6885.

(50) Delcorte, A.; Medard, N.; Bertrand, P. *Analytical Chemistry* **2002**, *74*, 4955-4968.

(51) Sjovall, P.; Lausmaa, J.; Johansson, B. *Analytical Chemistry* **2004**, *76*, 4271-4278.

(52) Heeren, R. M. A.; McDonnell, L. A.; Amstalden, E.; Luxembourg, S. L.; Altelaar, A. F. M.; Piersma, S. R. *Applied Surface Science* **2006**, *252*, 6827-6835.

(53) Caprioli, R. M.; Farmer, T. B.; Gile, J. *Analytical Chemistry* **1997**, *69*, 4751-4760.

(54) Chaurand, P.; DaGue, B. B.; Pearsall, R. S.; Threadgill, D. W.; Caprioli, R. M. *Proteomics* **2001**, *1*, 1320-1326.

(55) Masumori, N.; Thomas, T. Z.; Chaurand, P.; Case, T.; Paul, M.; Kasper, S.; Caprioli, R. M.; Tsukamoto, T.; Shappell, S. B.; Matusik, R. J. *Cancer Research* **2001**, *61*, 2239-2249.

(56) Schwartz, S. A.; Weil, R. J.; Johnson, M. D.; Toms, S. A.; Caprioli, R. M. *Clinical Cancer Research* **2004**, *10*, 981-987.

(57) Chaurand, P.; Cornett, D. S.; Caprioli, R. M. *Current Opinion in Biotechnology* **2006**, *17*, 431-436.

(58) Chaurand, P.; Caprioli, R. M. *Electrophoresis* **2002**, *23*, 3125-3135.

(59) Spengler, B.; Hubert, M. *Journal of the American Society for Mass Spectrometry* **2002**, *13*, 735-748.

(60) Luxembourg, S. L.; McDonnell, L. A.; Mize, T. H.; Heeren, R. M. A. *Journal of Proteome Research* **2005**, *4*, 671-673.

(61) Luxembourg, S. L.; Mize, T. H.; McDonnell, L. A.; Heeren, R. M. A. *Analytical*

Chemistry **2004**, *76*, 5339-5344.

(62) Luxembourg, S. L.; McDonnell, L. A.; Duursma, M. C.; Guo, X. H.; Heeren, R. M. A. *Analytical Chemistry* **2003**, *75*, 2333-2341.

(63) Schwartz, S. A.; Reyzer, M. L.; Caprioli, R. M. *Journal of Mass Spectrometry* **2003**, *38*, 699-708.

(64) Stoeckli, M.; Staab, D.; Staufenbiel, M.; Wiederhold, K. H.; Signor, L. *Analytical Biochemistry* **2002**, *311*, 33-39.

(65) Bogan, M. J.; Agnes, G. R. *Rapid Communications in Mass Spectrometry* **2004**, *18*, 2673-2681.

(66) Aerni, H. R.; Cornett, D. S.; Caprioli, R. M. *Analytical Chemistry* **2006**, *78*, 827-834.

(67) Armstrong, D. W.; Zhang, L. K.; He, L. F.; Gross, M. L. *Analytical Chemistry* **2001**, *73*, 3679-3686.

(68) Tholey, A.; Heinzle, E. *Analytical and Bioanalytical Chemistry* **2006**, *386*, 24-37.

(69) Tholey, A. *Rapid Communications in Mass Spectrometry* **2006**, *20*, 1761-1768.

(70) Mank, M.; Stahl, B.; Boehm, G. *Analytical Chemistry* **2004**, *76*, 2938-2950.

(71) Lemaire, R.; Tabet, J. C.; Ducoroy, P.; Hendra, J. B.; Salzet, M.; Fournier, I. *Analytical Chemistry* **2006**, *78*, 809-819.

(72) Garrett, T. J.; Prieto-Conaway, M. C.; Kovtoun, V.; Bui, H.; Izgarian, N.; Stafford, G.; Yost, R. A. *Int. J. Mass Spectrom.* **2006**, *In Press*, doi:10.1016/j.ijms.2006.1009.1019.

(73) Garden, R. W.; Sweedler, J. V. *Analytical Chemistry* **2000**, *72*, 30-36.

(74) Hanton, S. D.; Clark, P. A. C.; Owens, K. G. *Journal of the American Society for Mass Spectrometry* **1999**, *10*, 104-111.

(75) Garrett, T. J.; Yost, R. A. *Analytical Chemistry* **2006**, *78*, 2465-2469.

(76) Garrett, T. J.; Prieto-Conaway, M. C.; Kovtoun, V.; Bui, H.; Izgarian, N.; Stafford, G.; Yost, R. A. *Int. J. Mass Spectrom.* **2006**, *doi:10.1016/j.ijms.2006.09.019*.

(77) Hsu, F. F.; Turk, J. *Journal of the American Society for Mass Spectrometry* **2001**, *12*, 61-79.

(78) Kaye, E. M.; Ullman, M. D. *Analytical Biochemistry* **1984**, *138*, 380-385.

(79) Ham, B. M.; Jacob, J. T.; Cole, R. B. *Analytical Chemistry* **2005**, *77*, 4439-4447.

(80) Hsu, F. F.; Turk, J. *Journal of the American Society for Mass Spectrometry* **2003**, *14*, 352-363.

(81) Al-Saad, K. A.; Zabrouskov, V.; Siems, W. F.; Knowles, N. R.; Hannan, R. M.; Hill, H. H. *Rapid Communications in Mass Spectrometry* **2003**, *17*, 87-96.

(82) Hsu, F. F.; Turk, J. *Journal of the American Society for Mass Spectrometry* **2005**, *16*, 1510-1522.

(83) Hsu, F. F.; Turk, J. *Journal of Mass Spectrometry* **2000**, *35*, 596-606.

(84) Ishizuka, I. *Progress in Lipid Research* **1997**, *36*, 245-319.

(85) Kyogashima, M.; Tamiya-Koizumi, K.; Ehara, T.; Li, G.; Hu, R.; Hara, A.; Aoyama, T.; Kannagi, R. *Glycobiology* **2006**, *16*, 719-728.

(86) Sugiyama, E.; Hara, A.; Uemura, K. *Analytical Biochemistry* **1999**, *274*, 90-97.

Figure Captions

Figure 1. Scanning electron microscopy image of the colloidal graphite sprayed surface.

Figure 2. LDI mass spectra of the standard lipid mixture under four different conditions, (a) high-vacuum (HV)-MALDI, (b) intermediate pressure (IP)-MALDI, (c) HV-GALDI, and (d) IP-GALDI. The standard lipid mixture contains 0.5mg/ml PC 32:0 and 0.5 mg/ml total GlcCers. Mass peak assignments and relative abundances are listed in Table 1.

Figure 3. (a) On the left is the optical image of the MALDI sample spot consisting of 1 μl of the standard lipid mixture (0.25 mg/ml of PC 32:0 and 0.5 mg/ml of total GlcCers) and 1 μl of 50 mg/ml of DHB matrix solution. The sample spot size is about 2.7 mm by 2.4 mm. Following are four chemically-selective images corresponding to the normalized intensity map (mass peak intensity divided by total ion current of each point) of the major lipid species. (b) IP-MALDI spectrum extracted from the region of "big, needle-like crystals" at the peripheral of the sample spot. (c) IP-MALDI spectrum extracted from the region of "small crystals" at the interior of the sample spot.

Figure 4. LDI mass spectra of total brain lipid extract under different conditions, (a) HV-MALDI, (b) IP-MALDI, (c) HV-GALDI, and (d) IP-GALDI in positive ion mode. Mass peak assignments and corresponding MS/MS data are listed in Table 3.

Figure 5. (A) First generation product ion spectrum of ions detected at *m/z* 850.66 from IP-GALDI mass spectrum of total brain lipid extract (Figure 4(d)). The neutral loss of 18 Da (NL 18) corresponds to the loss of water. NL 162 corresponds to the loss of $C_6H_{10}O_2$ from the sphingosine long chain. NL 180 is the loss of a galactose unit. Mass peaks at *m/z* 484 and at *m/z* 512 correspond to the sodiated C_{18} sphingosine long chain and its aldehyde form as seen in the scheme. (b) First generation product ion spectrum of ions at *m/z* 484.50 which are the first generation product ions of *m/z* 850.66. NL 17 corresponds to the loss of NH_3. NL 162 and NL 180 are the same as those in Figure 5(a). The precursor ion at *m/z* 850.66 can be assigned as $[GalCer\ d18:1/24:0h+Na]^+$.

Figure 6. First generation product ion spectra of ions at *m/z* 832 from (a) IP-MALDI (Figure 4(c)) and (b) IP-GALDI (Figure 4(d)) mass spectra of the total brain lipid extract. NLs of 18, 162, and 180 are the same as those in Figure 5. NL 59, NL 124, and NL183 correspond to losses of trimethylamine ($N(CH_3)_3$), ethyl phosphate from PC, and phosphocholine head group, respectively. NL 87 could correspond to the loss of the $C_3H_5O_2N$ from the phosphatidylserine group. Note that NL 59 from PC is dominant in the MALDI mass spectrum whereas NL 162 and NL 180 from cerebrosides are dominant in the GALDI mass spectrum.

Figure 7. IP-GALDI mass spectrum of total brain lipid extract in the negative ion mode. Sulfatides (STs) were mainly detected. ST m:n(h) represents sulfatide with number of the total carbons (m):number of double bonds (n) in the amide-linked fatty acid (hydroxylated).

Figure 8. (a) Chemically-selective image of ions at *m/z* 810 with grayscale gradation-coded intensities. (b) The mass spectrum is the average of mass spectra at all rastering points on the tissue (10,732 points) in the positive-ion mode. Each mass spectrum in (c) and (d) was extracted from the small specific area (3 × 3 rastering points) as indicated in (a).

Figure 9. Chemically-selective images in the positive-ion and negative-ion modes. Major ionic species identified by MS/MS and MS^3 experiment were listed together with the intensity ranges that correspond to the scale bar at the top center of the figure.

Figure 10. Chemically-selective images of rat brain tissue for (a) the precursor ion at *m/z* 832, (b) the product ion at m/z 773 which represents NL 59 from PCs, and (c) the product ion at 670 which represents NL 162 from cerebrosides. Therefore, the isobaric ions at m/z 832 corresponding to $[\text{GalCer d18:1/24:1} + \text{Na}]^+$ and $[\text{PC 38:4} + \text{Na}]^+$ in (a) can be separated into the image for $[\text{PC 38:4} + \text{Na}]^+$ in (b) and the image for $[\text{GalCer d18:1/24:1} + \text{Na}]^+$ in (c) by performing IMS/MS.

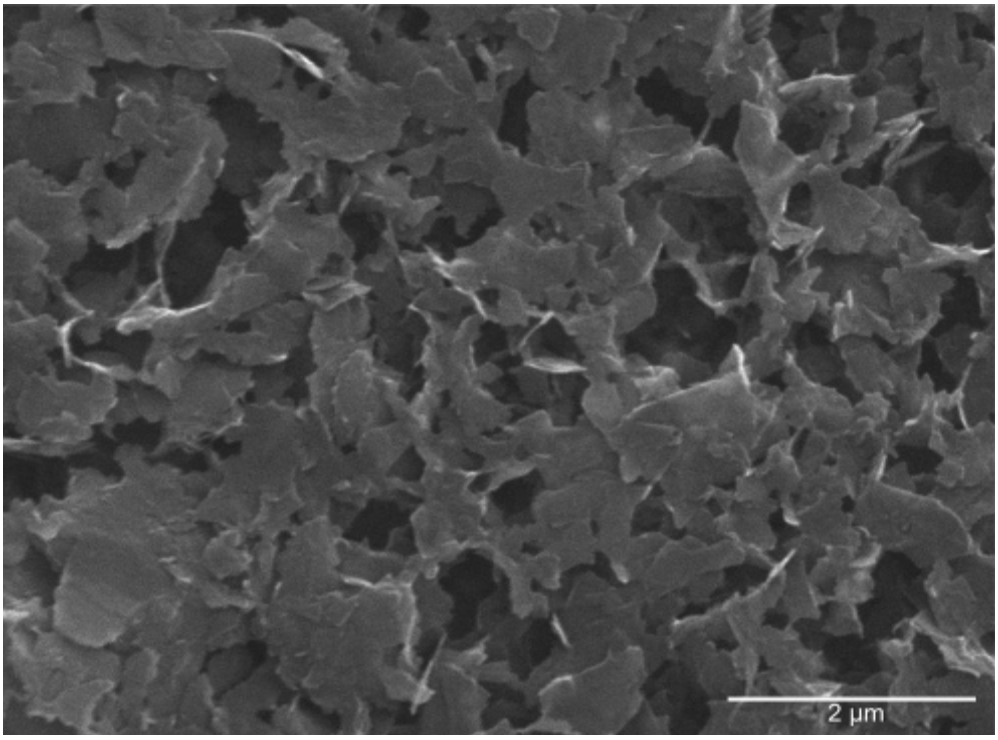

Figure 1.

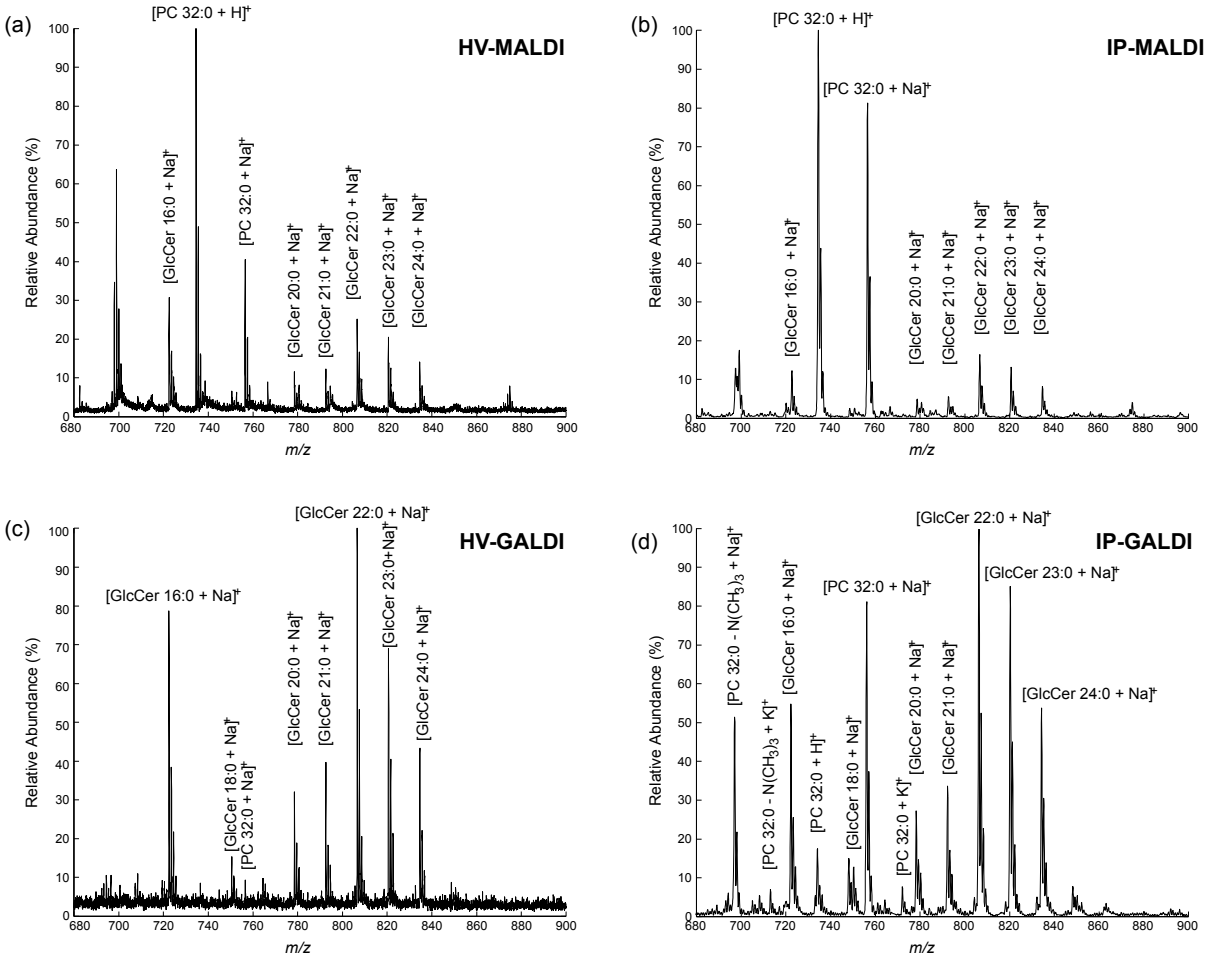
(a)
HV-MALDI
[PC 32:0 + H]+
[GlcCer 16:0 + Na]+
[PC 32:0 + Na]+
[GlcCer 20:0 + Na]+
[GlcCer 21:0 + Na]+
[GlcCer 22:0 + Na]+
[GlcCer 23:0 + Na]+
[GlcCer 24:0 + Na]+
Relative Abundance (%)
m/z
(b)
IP-MALDI
[PC 32:0 + H]+
[PC 32:0 + Na]+
[GlcCer 16:0 + Na]+
[GlcCer 20:0 + Na]+
[GlcCer 21:0 + Na]+
[GlcCer 22:0 + Na]+
[GlcCer 23:0 + Na]+
[GlcCer 24:0 + Na]+
Relative Abundance (%)
m/z
(c)
HV-GALDI
[GlcCer 22:0 + Na]+
[GlcCer 16:0 + Na]+
[GlcCer 18:0 + Na]+
[PC 32:0 + Na]+
[GlcCer 20:0 + Na]+
[GlcCer 21:0 + Na]+
[GlcCer 23:0+Na]+
[GlcCer 24:0 + Na]+
Relative Abundance (%)
m/z
(d)
IP-GALDI
[GlcCer 22:0 + Na]+
[PC 32:0 - N(CH3)3 + Na]+
[GlcCer 23:0 + Na]+
[PC 32:0 + Na]+
[PC 32:0 - N(CH3)3 + K]+
[GlcCer 16:0 + Na]+
[GlcCer 24:0 + Na]+
[PC 32:0 + H]+
[GlcCer 18:0 + Na]+
[PC 32:0 + K]+
[GlcCer 20:0 + Na]+
[GlcCer 21:0 + Na]+
Relative Abundance (%)
m/z

Figure 2.

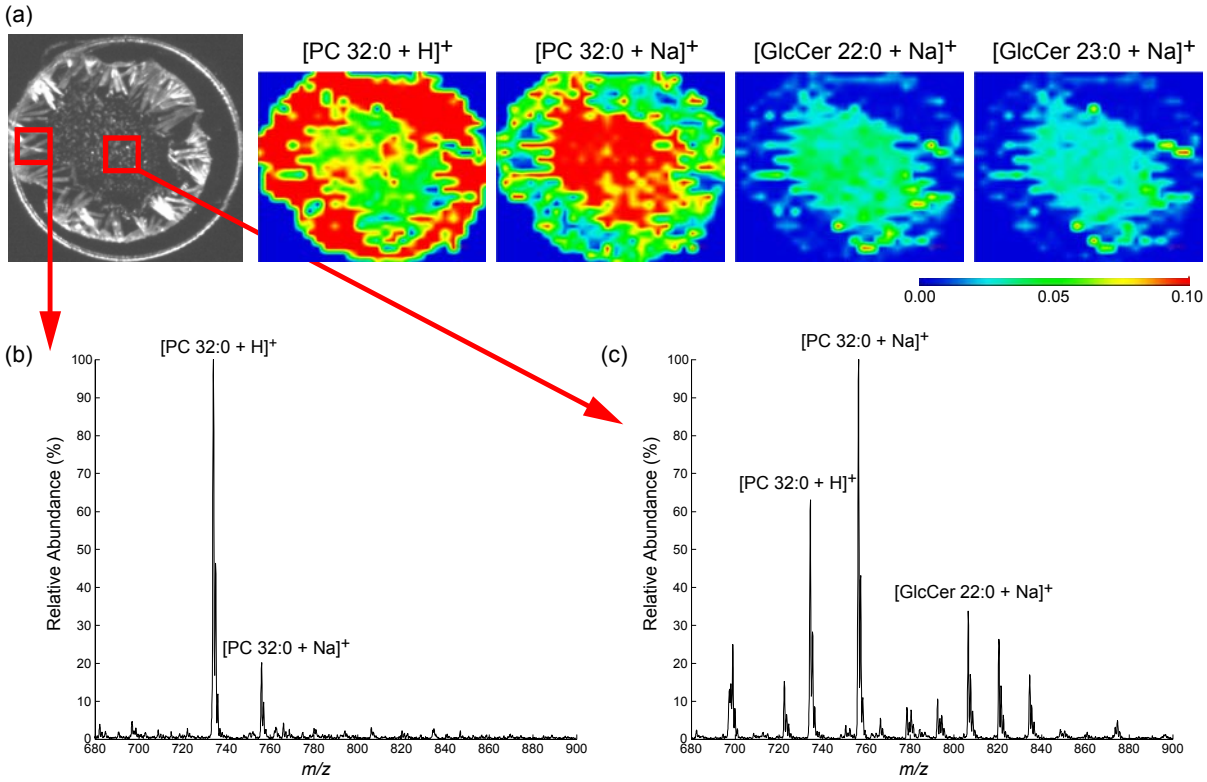
(a)
[PC 32:0 + H]+
[PC 32:0 + Na]+
[GlcCer 22:0 + Na]+
[GlcCer 23:0 + Na]+
0.00
0.05
0.10
(b)
[PC 32:0 + H]+
[PC 32:0 + Na]+
Relative Abundance (%)
m/z
(c)
[PC 32:0 + Na]+
[PC 32:0 + H]+
[GlcCer 22:0 + Na]+
Relative Abundance (%)
m/z

Figure 3.

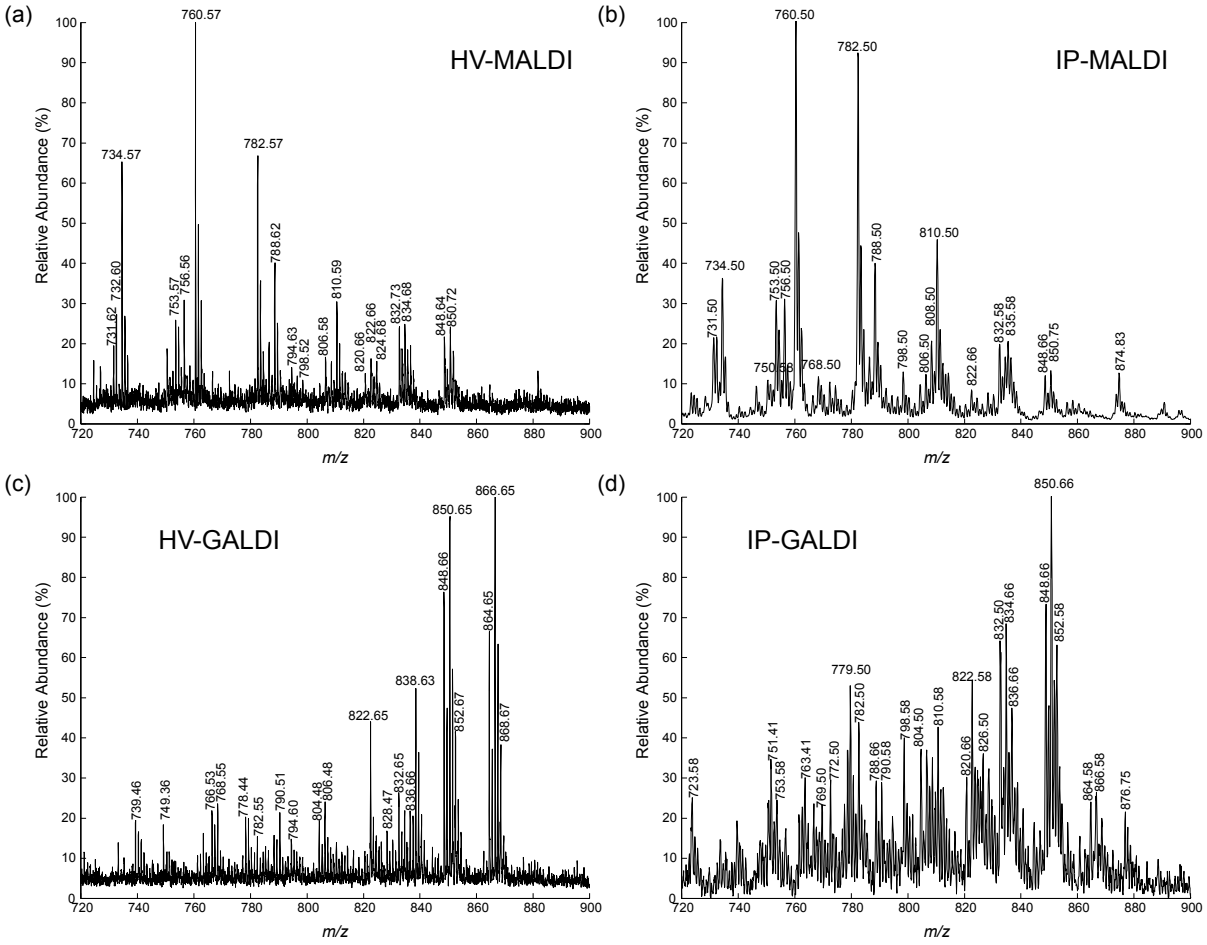
(a)
HV-MALDI
760.57
734.57
782.57
788.62
732.60
731.62
753.57
756.56
810.59
794.63
798.52
806.58
820.66
822.66
824.68
832.73
834.68
848.64
850.72
(b)
IP-MALDI
760.50
782.50
734.50
788.50
810.50
731.50
753.50
756.50
750.38
768.50
798.50
806.50
808.50
822.66
832.58
835.58
848.66
850.75
874.83
(c)
HV-GALDI
866.65
850.65
848.66
864.65
838.63
822.65
852.67
868.67
739.46
749.36
766.53
768.55
778.44
782.55
790.51
794.60
804.48
806.48
828.47
832.65
836.68
(d)
IP-GALDI
850.66
848.66
832.50
834.66
852.58
779.50
822.58
782.50
836.66
798.58
804.50
810.58
826.50
751.41
763.41
769.50
772.50
788.66
790.58
820.66
723.58
753.58
864.58
866.58
876.75
Relative Abundance (%)
m/z

Figure 4.

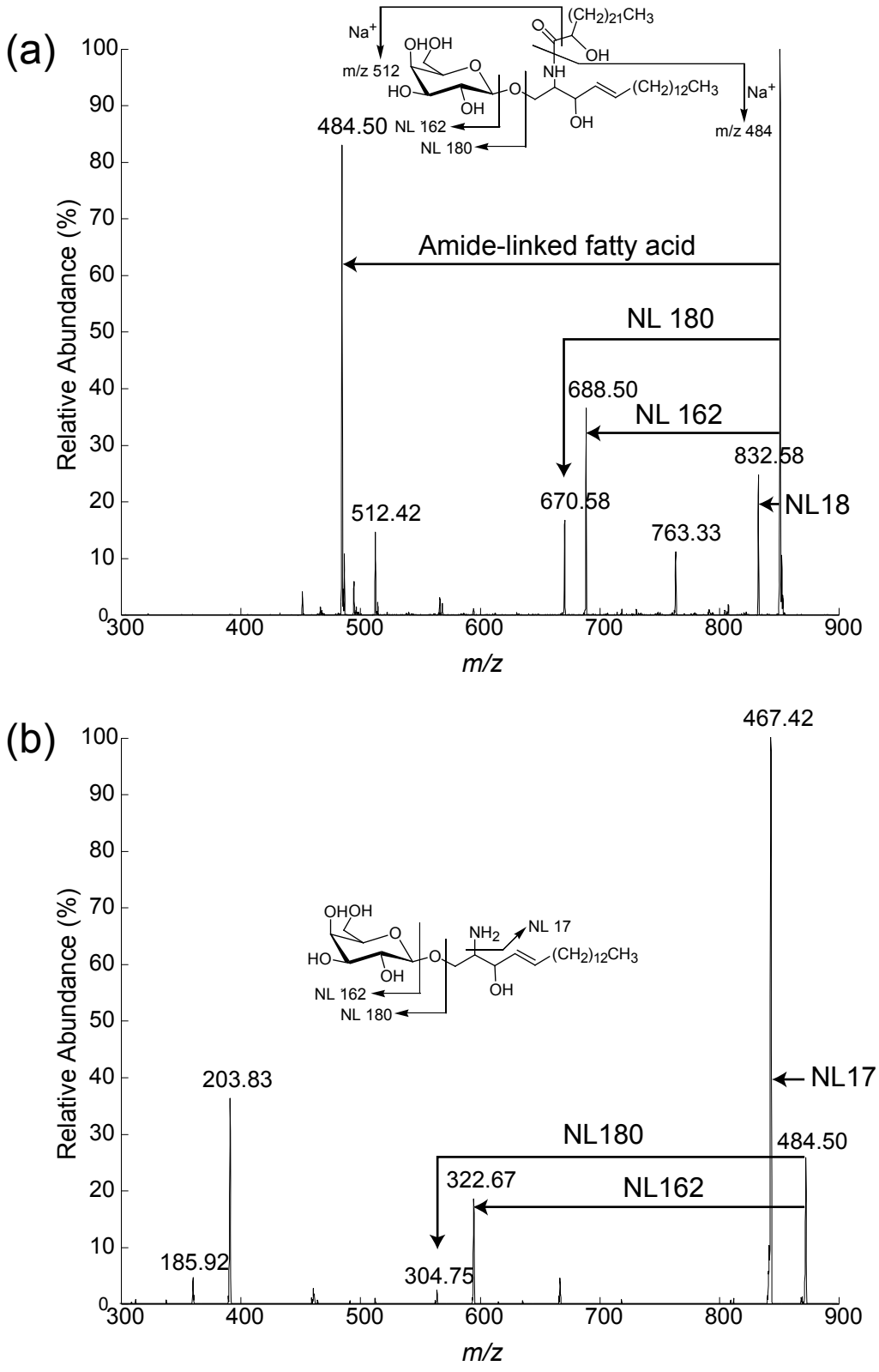
(a)
Relative Abundance (%)
m/z
Amide-linked fatty acid
NL 180
NL 162
NL18
484.50
688.50
832.58
512.42
670.58
763.33
m/z 512
m/z 484
NL 162
NL 180
(b)
Relative Abundance (%)
m/z
467.42
NL17
NL180
NL162
484.50
322.67
203.83
185.92
304.75
NL 17
NL 162
NL 180

Figure 5.

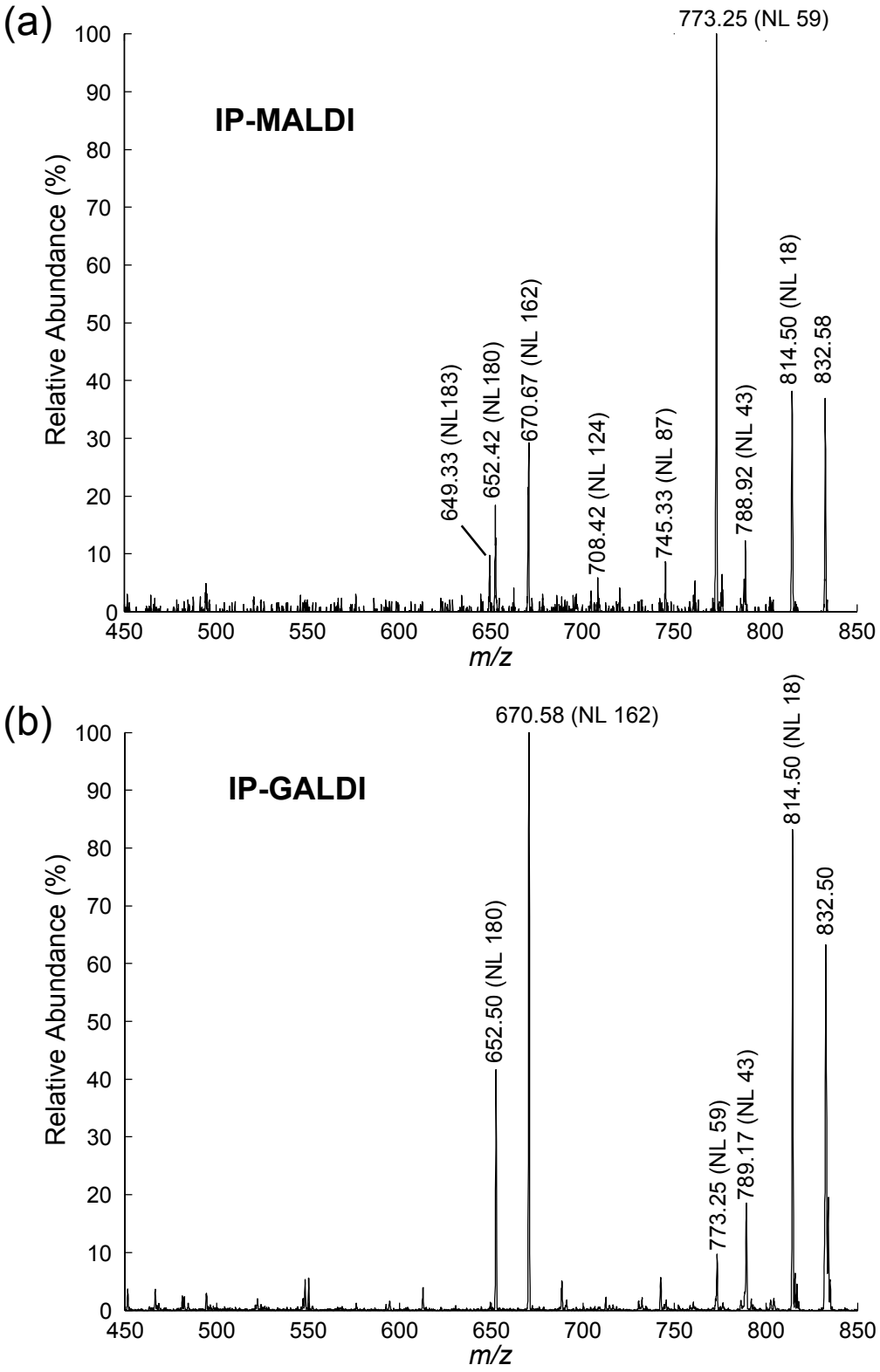
(a)
IP-MALDI
Relative Abundance (%)
m/z
773.25 (NL 59)
649.33 (NL183)
652.42 (NL180)
670.67 (NL 162)
708.42 (NL 124)
745.33 (NL 87)
788.92 (NL 43)
814.50 (NL 18)
832.58
(b)
IP-GALDI
Relative Abundance (%)
m/z
670.58 (NL 162)
652.50 (NL 180)
773.25 (NL 59)
789.17 (NL 43)
814.50 (NL 18)
832.50

Figure 6.

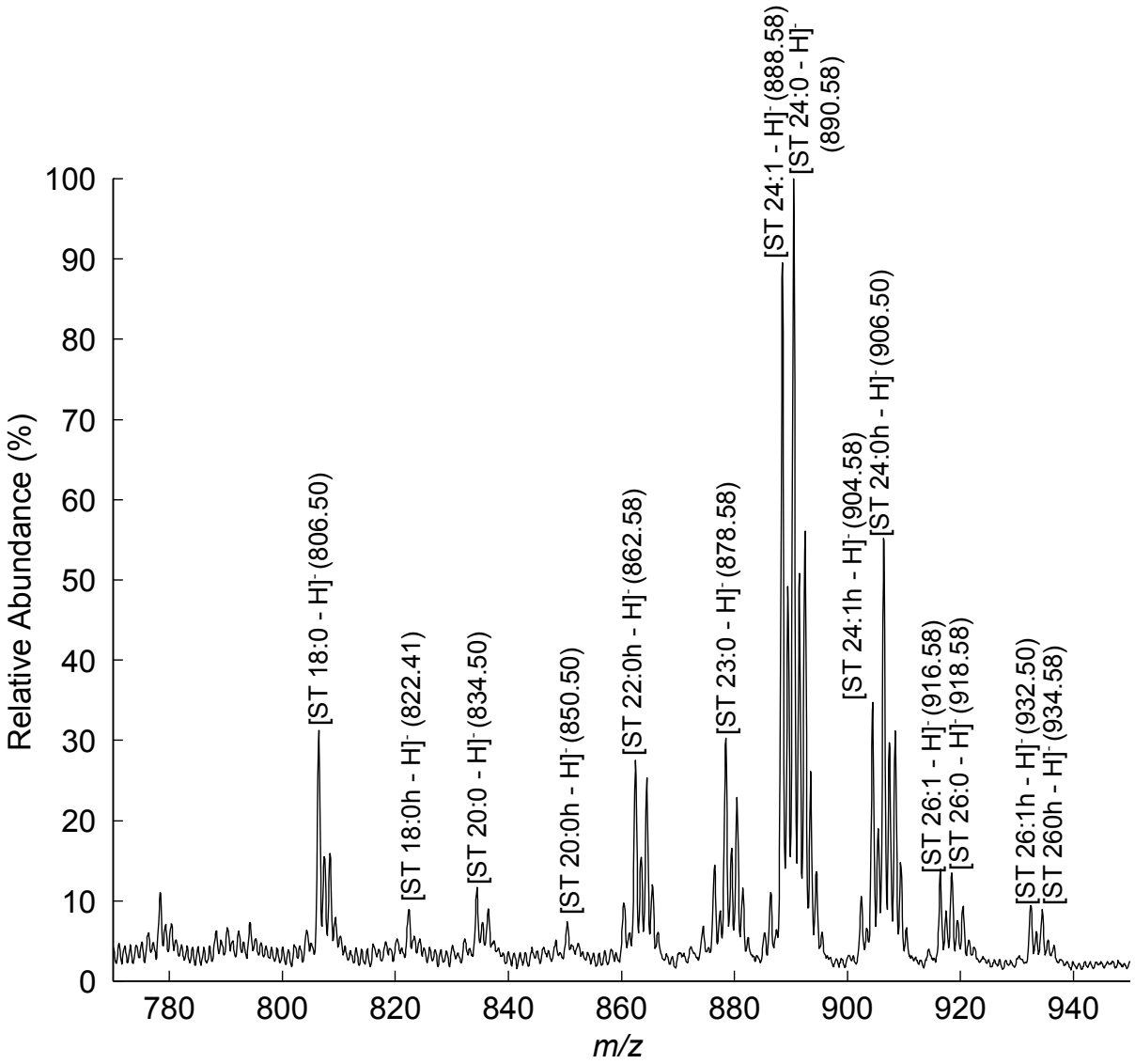
Relative Abundance (%)
m/z
[ST 18:0 - H]- (806.50)
[ST 18:0h - H]- (822.41)
[ST 20:0 - H]- (834.50)
[ST 20:0h - H]- (850.50)
[ST 22:0h - H]- (862.58)
[ST 23:0 - H]- (878.58)
[ST 24:1 - H]- (888.58)
[ST 24:0 - H]- (890.58)
[ST 24:1h - H]- (904.58)
[ST 24:0h - H]- (906.50)
[ST 26:1 - H]- (916.58)
[ST 26:0 - H]- (918.58)
[ST 26:1h - H]- (932.50)
[ST 260h - H]- (934.58)

Figure 7.

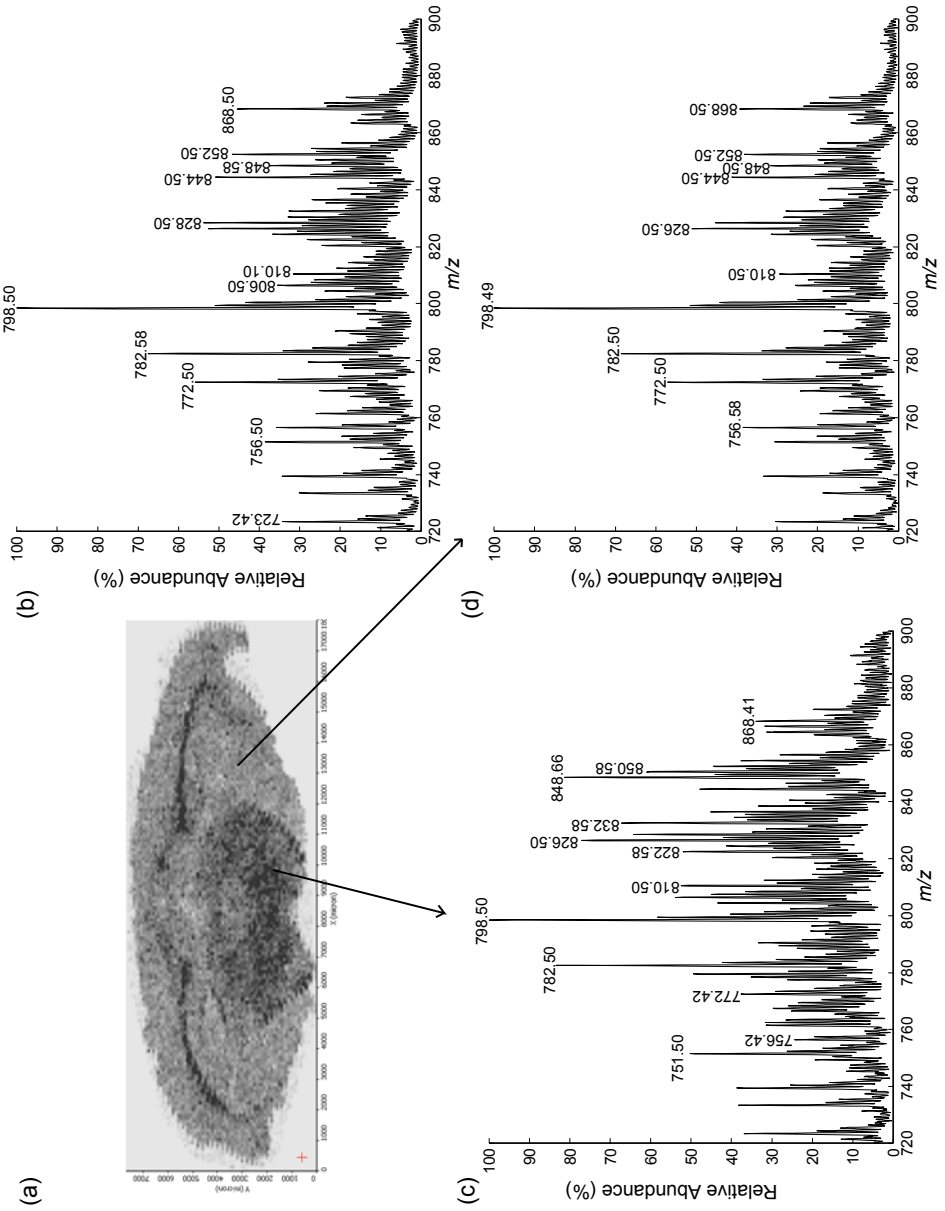
(a)
(b)
(c)
(d)
Relative Abundance (%)
m/z
798.50
782.58
772.50
756.50
723.42
806.50
810.10
828.50
844.50
848.58
852.50
868.50
798.49
782.50
772.50
756.58
810.50
826.50
844.50
848.50
852.50
868.50
798.50
782.50
772.42
756.42
751.50
810.50
822.58
826.50
832.58
848.66
850.58
868.41

Figure 8.

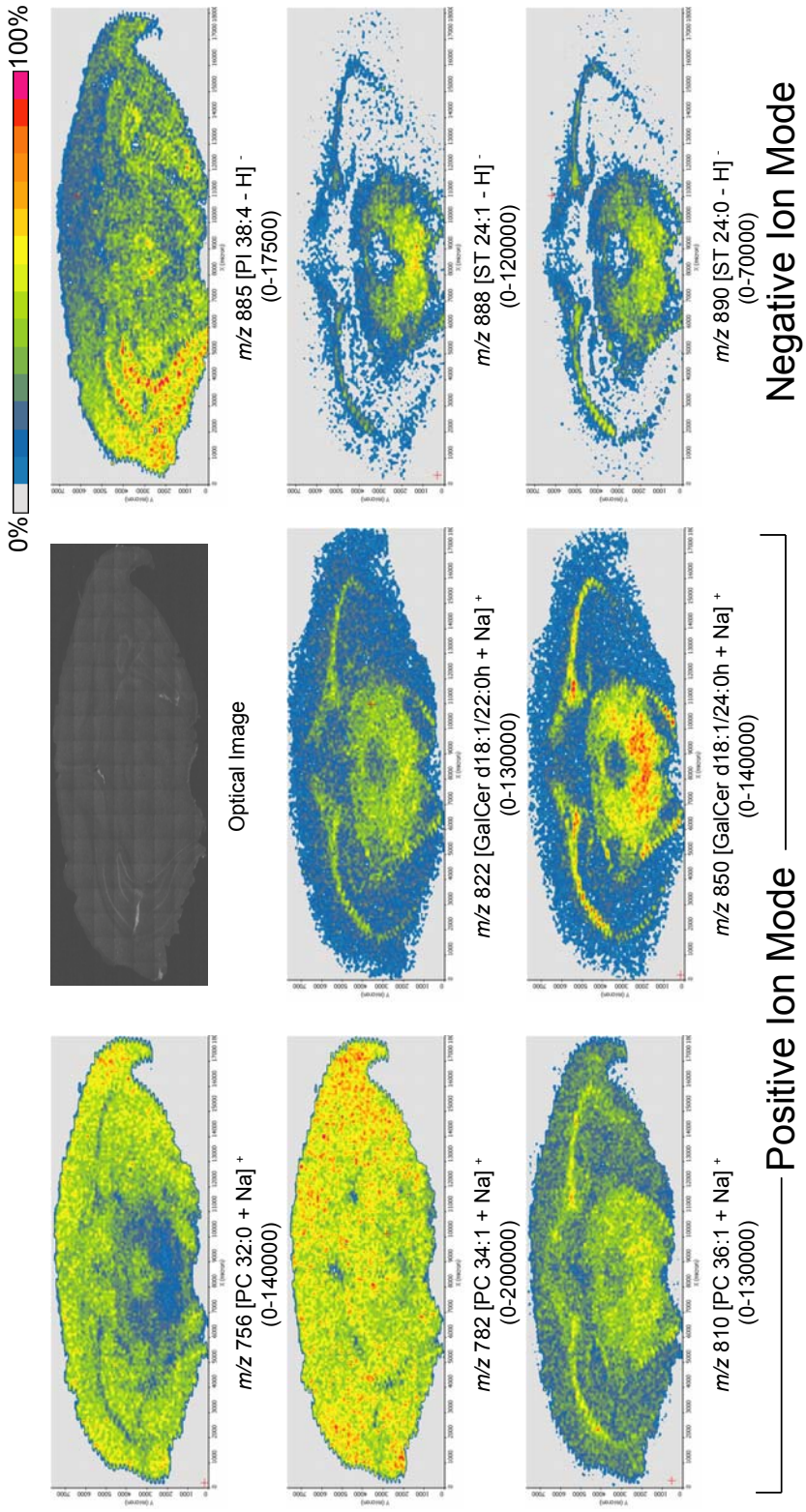
0%
100%
m/z 885 [PI 38:4 - H] -
(0-17500)
m/z 888 [ST 24:1 - H] -
(0-120000)
m/z 890 [ST 24:0 - H] -
(0-70000)
Optical Image
m/z 822 [GalCer d18:1/22:0h + Na] +
(0-130000)
m/z 850 [GalCer d18:1/24:0h + Na] +
(0-140000)
m/z 756 [PC 32:0 + Na] +
(0-140000)
m/z 782 [PC 34:1 + Na] +
(0-200000)
m/z 810 [PC 36:1 + Na] +
(0-130000)
Positive Ion Mode
Negative Ion Mode

Figure 9.

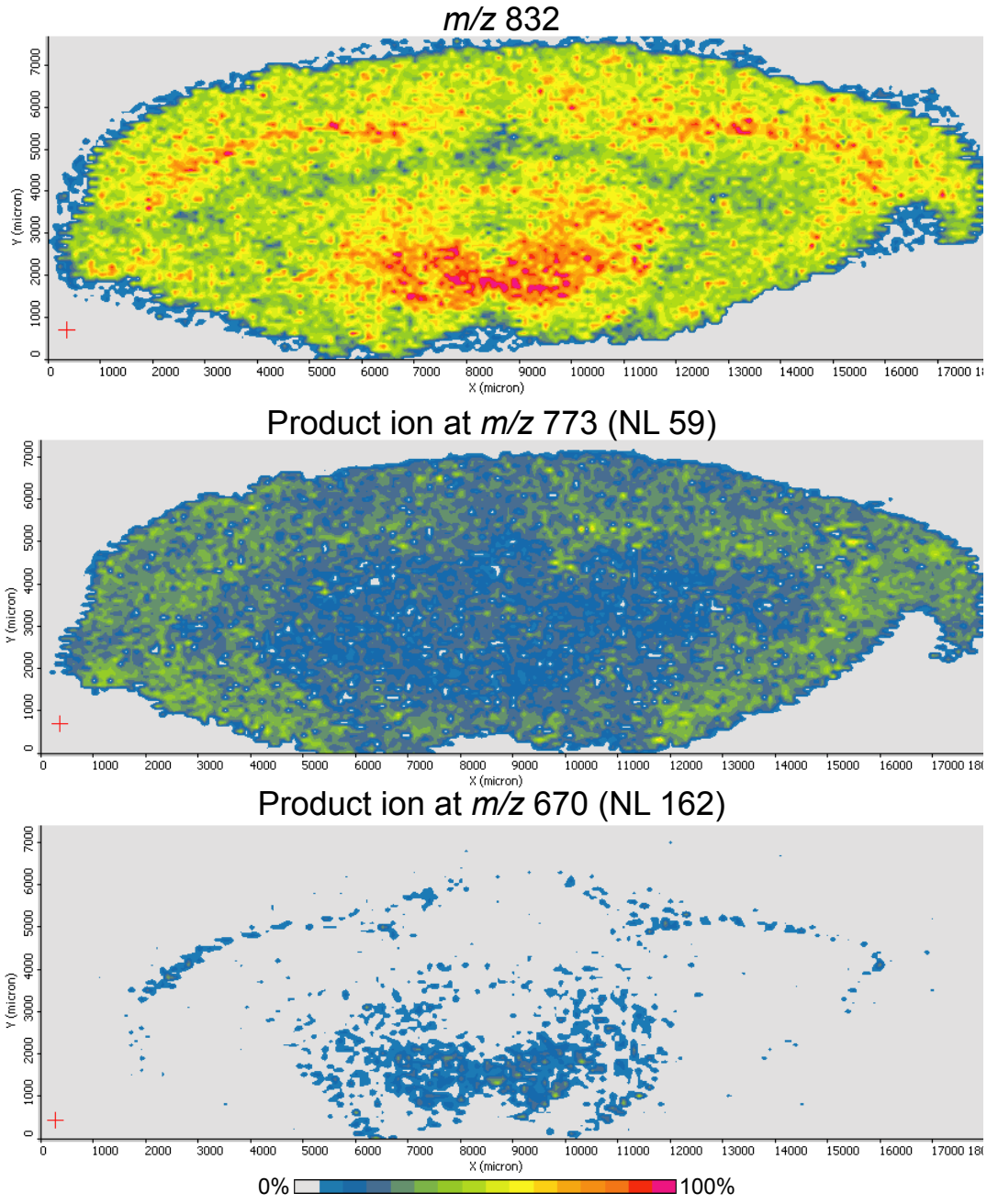
m/z 832
Y (micron)
X (micron)
Product ion at m/z 773 (NL 59)
Y (micron)
X (micron)
Product ion at m/z 670 (NL 162)
Y (micron)
X (micron)
0%
100%

Figure 10.

CHAPTER 3. DIRECT PROFILING AND IMAGING OF PLANT METABOLITES IN INTACT TISSUES BY USING COLLOIDAL GRAPHITE-ASSISTED LASER DESORPTION IONIZATION MASS SPECTROMETRY

A paper accepted for publication in The Plant Journal*

Sangwon Cha, Hui Zhang, Hilal I. Ilarslan, Eve Syrkin Wurtele, Libuse Brachova, Basil J. Nikolau and Edward S. Yeung

Abstract

Laser desorption/ionization (LDI)-based imaging mass spectrometry (MS) has been applied to several biological systems to obtain information about both the identities of the major chemical species and their localization. Colloidal graphite-assisted LDI (GALDI) MS imaging was introduced for imaging of small molecules such as phospholipids, cerebrosides, oligosaccharides, flavonoids, and other secondary metabolites with high spatial homogeneity due to the finely dispersed particles. Mass profiles and images of *Arabidopsis thaliana* were recorded directly from various plant surfaces and cross-sections. The main targeted metabolites were flavonoids and cuticular waxes, both of which are important in many aspects of functional genomics, proteomics, and metabolomics. Mass spectral profiles revealed tissue-specific accumulation of flavonoids in flowers and petals. In addition, many other location-specific ions were observed. The location and the degree of light-induced flavonoid accumulation in stem sections were successfully probed by GALDI MS.

---

* Reprint with permission from The Plant Journal **2008,**

doi: 10.1111/j.1365-313X.2008.03507.x,

Introduction

Because low molecular weight metabolites exhibit a variety of different chemical properties, many analytical methods have been used to assay their structures, abundances, and locations [1, 2]. Among these methods are nuclear magnetic resonance (NMR) spectroscopy [3, 4] for structural analysis of the metabolites, vibrational spectroscopy for metabolic fingerprinting, and mass spectrometry (MS) for metabolite profiling [5]. Gas chromatography-MS (GC-MS) has been extensively used over the last 20 years [1, 6, 7] because it is a relatively well-constructed methodology that has good reproducibility and wide applicability to various classes of metabolites. Moreover, GC-MS has the ability to identify and quantify metabolites. Since the development of electrospray ionization (ESI) techniques [8] and advances in tandem MS technologies, liquid chromatography-MS (LC-MS) is also becoming a workhorse with high throughput and high sensitivity [9].

It is known that metabolic processes in plants are spatially non-uniform. This is readily apparent via microscopic examination of plant organs that reveals considerable heterogeneity in cell morphology and the distribution of pigments (e.g., chlorophylls, anthocyanins) among these cells. At the biochemical level a very good example of this cell-level asymmetry is that of C-4 photosynthesis, which requires a distinct distribution of metabolic processes among mesophyll and the bundle-sheath cells, respectively, to concentrate carbon dioxide at the active site of RuBISCO (ribulose–1,5-biphosphate carboxylase/oxygenase). This discovery required the physical separation of the two cell types before their proteome and/or metabolome could be interrogated. Thus, the development of analytical techniques that can interrogate metabolites in intact tissue and with high-spatial resolution would offer the ability to decipher metabolic processes at the cellular level.

Laser desorption/ionization (LDI) MS and matrix-assisted laser ionization/desorption (MALDI) MS have not been widely used in plant metabolomics mainly because of difficulties in generating ions from the relatively hydrophobic species in plant tissue.

However, the applicability of LDI MS to imaging plant metabolites, including direct profiling of cuticular wax compounds [10], analysis of phosphatidylcholine [11], condensed tannins in bark [12], and profiling of plant carotenoids [13] has been successfully demonstrated. The advantage of LDI MS, over hyphenated techniques (GC-, LC-, and CE- MS) is the ability to sample biochemicals directly without any extraction protocol. Therefore, the spatial distribution of the biochemicals is retained.

In laser desorption, the sampling resolution is governed primarily by the laser spot size. Consequently, the spatial resolution of imaging MS by LDI can be much smaller than that achievable by traditional methods such as dissecting plant materials followed by chemical extraction prior to MS -The effort to achieve smaller sampling size by laser microdissection with traditional GC-MS methods has been reported recently [14]. Location-specific sampling has made it possible for LDI to be employed as a microscope, that is, for "imaging MS" [15]. Imaging MS collects mass spectra consecutively over the sample surface and reconstructs mass spectral data as an image for each specific compound. In addition to LDI, ion beam-induced ionization methods such as secondary ionization (SIMS) [16-21] and beam-induced desorption electrospray ionization (DESI) [22, 23] have also been successfully applied to imaging MS.

In addition to laser spot size, factors that limit the spatial resolution of LDI imaging MS include sensitivity of the mass spectrometer, abundance of a metabolite, and homogeneity of the material added to facilitate ionization. Matrixes in MALDI MS, which require co-crystallization with sample components to be effective, can decrease the spatial resolution because of their irregular crystallization patterns. To overcome this, researchers have introduced alternative matrixes that can be homogeneously distributed on the sample surfaces. Recently, we used colloidal graphite , a sub-micron flake-like material, as an assisting material (GALDI MS) for imaging lipids from rat brain slices and also for imaging secondary metabolites such as flavonoids and organic acids from fruits [24, 25]. The other

advantages of GALDI MS are that graphite is more hydrophobic, making it compatible with plant materials, and is a near-blackbody, making it suitable for irradiation with any wavelength of light. Hence, GALDI MS makes possible to interrogate some classes of compounds that are not detected by conventional MALDI. Recently, Siuzdak's group introduced nanostructure-initiator mass spectrometry (NIMS) where 'initiator' molecules trapped in nanostructures help to ionize intact molecules on their surfaces [26]. NIMS can achieve high spatial resolution because of its structure and it can accept both photon and ion irradiation.

SIMS has been used for imaging studies of metal ions on plant surfaces [27-32]. Recently, localization of phenolic compounds from wood stems has been examined by time-of-flight (TOF) SIMS [33, 34]. However, most studies by LDI MS imaging have been done on animal tissue sections such as rat brain slices. Recently, MS imaging of amino acids, sugars, and phosphorylated metabolites on wheat seeds by using conventional MALDI matrix was reported [35]. IR laser, instead of conventional UV laser, has been used to image several abundant metabolites from fruits [36]. There, the ultimate spatial resolution that can be achieved is compromised because of the wavelength of light.

Elongation of aliphatic fatty acids to form very long chain fatty acids (VLCFAs) is the first step in the biosynthesis of components of the cuticular wax layer. This layer makes plants resistant to external stresses such as insects, pathogens, and water [37-41]. Flavonoids serve as epidermal shields to protect against UV light. In the case of *Arabidopsis thaliana,* the major building blocks of flavonoid are flavonols and flavonol glycosides as shown in Figure 1 [42-44]. Another major class of flavonoids is anthocyanins and proanthocyanidins, end product of flavonoid's biosynthetic pathways [45-47].

Because Arabidopsis is an important model system for plants, and as such the most highly understood, it is important to be able to analyze its metabolome *in situ*. The Arabidopsis plant is small and fragile; therefore its analysis is challenging for sample

handling and MS imaging. For the present imaging MS study, we focused on very long chain fatty acids (VLCFAs) and the flavonoids because we have already demonstrated the ability of GALDI MS to detect members of these classes of compounds [25] and because of the breadth of information on the effects of genetic mutants and environmental perturbations on these metabolites. In addition, we discuss methodological details about MS imaging of surfaces in small-size plants in terms of sample preparation, methods for imaging, and other experimental concerns. Finally, as a model system, we describe spatial probing of flavonoid accumulation from light-treated stem sections.

Experimental Section

Chemicals. Standards such as long-chain fatty acids, flavonoids, and histochemical staining reagents, diphenylboric acid 2-amino-ethyl ester (DPBA) and p-dimethylaminocinnamaldehyde (DMACA), were purchased from Sigma-Aldrich (St. Louis, MO). 2-Propanol-based colloidal graphite aerosol spray (Aerodag G) was obtained from Acheson Colloids (Port Huron, MI).

Plant growth conditions. Seeds of Arabidopsis thaliana Columbia-0 ecotype (Col-0) were surface sterilized for 1 min in 300 µl 50% ethanol, 10 min in 300 µl 50% bleach containing 1% Tween 20, and washed with 3 changes of 300 µl sterile water. Seeds were sown on MS media in Petri plates, and kept at 4 ˚C for 4 days. The plates were then moved to a growth room and seedlings were transferred to pots containing soil (LC1 Sunshine Mix) under continuous illumination (100 µmol m^{-2} s^{-1}) at 23 ˚C.

Light treatment. Plants were grown in a growth room for 40 days under continuous illumination (100 µmol m^{-2} s^{-1}) at 23 ˚C in pots containing soil (LC1 Sunshine Mix). At the time of the experiment, half of the plants (control) were left in this growth room, and the other half were transferred into a second growth room and grown in continuous illumination under high light intensity (750-800 µmol m^{-2} s^{-1}) at 23 ˚C. Fourteen days after transfer, stem

samples were harvested, frozen in liquid nitrogen, and 50-80 μm thick sections were cut on a cryostat (International Equipment Co., Needham Heights, MA).

Flavonoid staining. Cryosectioned stem samples were stained for 15-20 min with saturated 0.25% (wt:vol) DPBA [48] with 0.02% (vol:vol) Triton X-100 and viewed with an epifluorescent microscope (Zeiss AxioPlan II compound fluorescent microscope using an AxioCam MRM camera (for MRC color) and AxioVision software, Carl Zeiss Inc., Thornwood, NY) with a FITC filter (excitation, 450-490 nm; suppression, long pass/515 nm) according to Murphy et al. (2000) and Lazar and Goodman (2006); flavonols (kaempferol and quercetin) stain orange, naringenin stains yellow and chlorophyll autofluorescence is red.

DMACA staining reagent (0.1% DMACA in 6N HCl:95% ethanol, 1:1) [49] was used to detect flavonols (soluble phenols, soluble flavanols and proanthocyanidins) [50]. After staining with this reagent for 5-10 min, cryosectioned stem samples were washed three times with distilled water and observed under the light microscope; flavonols stain blue and purple-brown colors.

Plant sample preparation for mass spectral profiling and imaging. For leaves or flowers, samples were attached to a stainless steel target plate of similar dimensions as a microscopic glass slide using conductive double-sided tape (3M, St. Paul, MN). Any area inadvertently damaged by forceps was excluded when collecting mass profiles. To attach samples firmly onto the target plate, air pressure from a nitrogen gas cylinder was used. After attachment, samples on the target plate were dried for 30 min under moderate vacuum (~50 Torr). In some experiments, the bottom or top halves of fresh Arabidopsis leaves were dipped in chloroform for 30 s or 1 min to remove wax layers.

For stem sections, relocation of compounds due to water condensation is a challenging issue because frozen sections must be thaw-mounted directly onto the stainless steel target plate. To minimize condensation, stem sections on target slides were dried in a semi-sealed box half-filled with desiccant by purging with a flow of dry nitrogen.

Colloidal graphite solution diluted 4X with 2-propanol was used for spraying colloidal graphite onto samples. The spraying device was an airbrush, model Aztek A470 with a 0.30 mm nozzle from Testor (Rockford, IL). Spraying was at 20 psi, 8 cm from the sample plate. Optimized spraying times as determined by mass spectral qualities were 30-40 s for leaves and 20-25 s for flowers and stem sections. Colloidal graphite dried in less than 10 s.

Sample preparation including drying process is a challenging task. We have tried using fresh samples (without drying) for whole organ samples (leaves and whole flowers). By comparing MS profiles from the fresh sample with those from the dried sample, we did not observed any significant difference between them for our targeted metabolites. However, for fresh samples, they shrunk during data collection under the sample chamber pressure (0.17 Torr) even if they were firmly attached, and the chemical images and optical images do not match very well. Therefore, pre-drying under the moderate vacuum pressure (~50 Torr) was needed to prevent this. For stem cryosections, special care was needed to prevent condensation-induced chemical relocation. Other experiments show that without such dry N_2 control, water droplets formed and flavonoids were seen smeared all over the cross section.

Mass spectrometry. Mass spectra were collected with a Thermo Finnigan LTQ linear ion trap mass spectrometer equipped with vMALDI source (Mountain View, CA). In this mass spectrometer, nitrogen laser emission (337 nm, maximum energy of 280 μJ/pulse, and maximum frequency of 20 Hz) was guided through a 200-μm fiber optic cable. After passing through several optical components, 100 μm diameter laser spots were obtained at the sample plate surface. In contrast to high vacuum sampling environments (~10^{-6} Torr) of conventional MALDI TOF instruments, the LTQ mass spectrometer has the intermediate-pressure (0.17 Torr) sampling environment which can lead to softer ionization by vibrational and collisional cooling effects. All mass spectra were collected in the negative-ion mode and the scanning m/z range was set from m/z 150 to m/z 1000. For unknown peaks acquired

directly from plant samples, peak identification were carried out by matching monoisotopic masses of metabolites listed in databases—TAIR (http://www.arabidopsis.org/) and internal GC-MS database—with observed mass values. Identities were confirmed by comparing product ion spectra (up to the third generation) from unknown peaks with those from standards or from literature data.

Mass spectral imaging and image processing of leaves. For untreated leaves, the number of laser shots required was estimated by collecting mass spectra in a small area (usually 5 to 10 rastering points) by turning on automatic gain control (AGC, which keeps the ion amounts in the trap at a similar range by varying the number of laser shots) feature of the mass spectrometer. The optimum number of laser shots was determined and fixed based on the average number of laser shots when collecting mass spectra over the whole sample. For chloroform-dipped leaves, however, mass spectra were collected with AGC because they have several different surface characteristics in one sample which can lead to variations in ion yield. The sample was scanned with a step size which ranged from 100 μm to 150 μm.

Chemically-selective images were processed by using the custom software from Thermo (ImageQuest 1.0). Chemical abundance information was presented using either absolute intensity values or normalized intensity values. The fractional peak intensity for the peak of interest compared to the total ion current (TIC) of each mass spectrum was used for normalized intensity. The mass window was from 0.8 Da to 1.0 Da.

Mass spectral imaging and image processing of flowers and stem sections. 50 μm spacing was used for whole flower imaging and stem section imaging (oversampling). Because of the need of complete ablation for oversampling technique [51], two methods, selective spectra averaging and whole spectra averaging, were applied for MS imaging of Arabidopsis flowers. Images of flowers in this article were processed with whole spectra averaging. Experimental details of selective spectra averaging and comparison between two methods are described in Supporting Information, and chemically-selective images from

Arabidopsis flower by selective spectra averaging is shown in Supporting Information Figure S2.

Whole spectra averaging without complete ablation was designed to generate similar MS images to those with complete ablation. Under our experimental conditions, more than one order of magnitude decrease in normalized intensity of mass spectra was observed after 5 to 8 microscans (one microscan corresponds to getting one mass spectrum from the sample). Therefore, a fixed number of microscans (5 for Arabidopsis flowers) was preset and data were collected for one x,y-coordinate. All microscans were averaged and images were generated by using the custom software from Thermo (ImageQuest 1.0).

Results and Discussion

Mass spectral profiling and imaging of metabolites from Arabidopsis leaves. VLCFAs were readily detected as deprotonated ions ($[M - H]^-$) from the surface of Arabidopsis leaves (Figure 2) using GALDI in the negative-ion mode. Consistent with previous, traditional extraction-based analyses [39, 52, 53], our analyses showed C26, C28, and C30 fatty acids (FAs) as the most abundant such analytes on the surface of Arabidopsis leaves (Figure 2). However, ions from flavonoid compounds were not consistently detected from Arabidopsis leaves. After examination of the leaves used for the MS analysis, we found that ions from flavonoids were readily detected only from the portion of leaves that were damaged during handling when they were attached to the MS sample plate. In contrast, when leaves were attached to the plate using air pressure to avoid damage, no ions from flavonoids were detected (Figure 2). Because flavonoids are typically intracellular metabolites and VLCFAs are constituents of epicuticular waxes, these results indicate that the penetration depth of the laser is shallower than the thickness of the epicuticular wax layer of the leaf.

To confirm this observation, chemically-selective images of the partially chloroform-dipped leaf were collected using GALDI MS. Dipping the leaf in chloroform removes the

surface epicuticular waxes. As shown in Figure 3, ions corresponding to VLCFAs showed high abundance in the area of the leaf that was not dipped in chloroform, especially on the central vein of the leaf, whereas the abundance of these ions was very low in the area of the leaf that was dipped in chloroform. In contrast, ions specific for kaempferol (at *m/z* 285), and kaempferol rhamnoside (at *m/z* 431) were detected mostly from the chloroform-dipped area and from the area in which the intact leaf was grasped with forceps. Thus, minimizing physical stress on the sample surface is critical to avoiding artificial information about the spatial distribution of metabolites.

Intense signals at *m/z* 226, 210, and 194 were observed in the chloroform-dipped area. Mass spectral profiles and chemically selective images for *m/z* 226 and 194 are shown in Supporting Information Figure S1. Images for ions at *m/z* 226 and 194 which are 16 Da away from ions at *m/z* 210 have the same specific pattern that is similar to the venation pattern of the leaf even after chloroform dipping (see Supporting Information, Figure S1). These data indicate that it should be possible to profile internal compounds by the chemical removal of the surface layer from the plant sample while preserving the subsurface spatial information. Such is not possible in conventional imaging MS. Further studies will be needed to verify this observation, since the specific solubility of the targeted compounds and the dipping time are expected to affect their removal and redistribution. Conceptually, depth profiling by serial data collection can probe deeper and deeper into the tissue but additional colloidal graphite sprayings are needed because of the decrease of signal intensities after serial collection. In addition, ablating by laser has much smaller penetration depth than chemical extraction. Therefore, it will take much longer time to access the same depth as that after chemical extraction.

Mass spectral profiling of flavonoids from Arabidopsis flower. Similar to leaves, no flavonoids or only a low apparent abundance flavonols were detected from the surface of flower carpels or sepals. In contrast, flavonoids were easily detected from petals as highly

intense signals. Based on the mass spectral profile from petals and the product ion spectra for the major peaks in this profile, at least 14 flavonoid species could be classified and identified. These ions are listed in Table 1 with possible structural identities, and representative product ion spectra for ions at *m/z* 609 and 623 are shown in Figure 4. These species basically comprised of three different flavonols aglycones-kaempferol (K), quercetin (Q), and isorhamnetin (I)- and their mono-, di- and triglycosides. There are some other observed ions which correspond to other flavonol aglycones. However, in Table 1, we listed only three flavonols and their derivatives that were thoroughly investigated by our own MS^n results and showed reproducible signals through flower by flower, or organ by organ. In GALDI MS, flavonoids were putatively identified as follows: First, MS^n experiments were performed up to the third generation product ion spectra (n=4). Second, fragmentation patterns were comprehensively compared with those from all available standards or with literature data.

Most product ion spectra clearly show the identity of the flavonol aglycone and the composition of sugar moieties. In Figure 4A, for example, fragment ions at m/z 315, which corresponds to the molecular ion of the flavonol isorhamnetin ($[I - H]^-$), were generated after the neutral loss (NL) of 162 Da and of 146 Da which correspond to the elimination of hexose (Hex) residue and rhamnose (Rha) residues from parent ions at *m/z* 623. This series of NLs and fragment ions show that the composition of ions at *m/z* 623 is I-Rha-Hex. Unlike LC-MS and NMR techniques for flavonoid analyses [44, 45, 54-57], direct profiling by LDI MS does not include a separation step. Therefore, there is a possibility of the presence of two or more isobaric species at one *m/z* peak. In the first generation product-ion spectrum for the precursor ions at *m/z* 609 (Figure 4B), the combination of NL(i), NL(iii), and the fragment ion at m/z 285 corresponds to the composition K-Hex-Hex. In contrast, the combination of NL(iii), NL(v), and the fragment ion at m/z 301 corresponds to the composition Q-Rha-Hex. To overcome difficulties associated with isobaric ions, separating isobaric ions by detecting their different specific fragment ions by tandem MS imaging may be needed [24, 25].

Interestingly, mass spectral profiles generated from a single petal changed dramatically depending on the locations where the mass spectra were collected (Figure 5). By matching structural compositions in Table 1 with *m/z* values of the dominant species at the tip of the petal (Figure 5A), kaempferol and its glycosides were found to be much more abundant over the other two flavonols and their derivatives, while the dominant species close to the flower base (Figure 5C) are quercetin (Q), isorhamnetin(I), and their glycosides. The spatial distribution of flavonols and their glycosides are further discussed in the following mass spectral imaging section.

Mass spectral imaging of flavonoids from Arabidopsis flowers. As shown in Figure 5, mass spectral profiles change dramatically within a single flower petal. To confirm this observation that flavonoid accumulation is spatially heterogeneous in petals, chemically-selective images for ions of flavonoid species were generated. As expected, Figure 6 shows the difference in spatial distributions of three flavonols and their sugar moieties. It should be noted that local distributions of flavonols (at *m/z* 285, 301, and 315) shown in Figure 6 are not only from flavonol aglycones themselves but also from their glycosides because favonol glycosides also produce ions corresponding to flavonol aglycones as fragment species by the laser- induced fragmentation. However, the degree of this fragmentation in our sampling environment (0.17 Torr) is usually much lower than in high vacuum environment (~10^{-6} Torr) [58, 59]. In addition, the relative abundances of isobaric ions with different compositions at each *m/z* can be estimated based on the images, although the relative abundances of isomers with the same composition cannot be distinguished by mass spectral images. According to Table 1, isobaric ion species may exist at *m/z* 447 (Q-Rha and K-Hex), 593 (K-Rha-Hex and Q-Rha-Rha), and 609 (Q-Rha-Hex and K-Hex-Hex). By comparing locations with abundant flavonol aglycones with those of isobaric ion species in Figure 6, higher abundances of Q-Rha at *m/z* 447, K-Rha-Hex at *m/z* 593, and Q-Rha-Hex at *m/z* 609 can be expected. Among flavonol glycosides which have the same flavonol aglycone, sub-localization of their

glycosides was observed in one abundant area. The ion species at *m/z* 755, which corresponds to quercetin triglycosides (Q-Rha-Rha-Hex), was observed to be highly localized around the boundary between kaempferol-localized area and quercetin-localized area.

The heterogeneous distribution of flavonoid compounds within a single petal of an Arabidopsis flower has never been reported or visualized in any previous studies. Simultaneously probing metabolite location and chemical composition by using imaging MS makes it possible to expand our understanding of biological synthetic pathways of secondary metabolites in plants. The data presented here can be combined with a series of studies about flower development [60, 61] and biosynthetic pathways of flavonoids [46, 47, 62, 63]. In particular, the spatial distribution of these flavonol compounds suggests that genetic regulation for expressing enzymes involved in flavonoid biosynthesis, such as flavonoid 3′-hydroxylase (F3′H) which converts kaempferol to quercetin by catalyzing the hydroxylation at the 3′ position in the B-ring of the flavonol [43, 64-68] and flavonol glycosyl transferase (FGT) which is responsible for transporting sugar units to the specific hydroxyl groups of the flavonol [47, 69], may be a time-dependant process during maturation of the Arabidopsis flower.

The ability of GALDI MS imaging and profiling shown above can also be applied to rapid screening and metabolite profiling of mutants which are related to the biosynthesis of flavonoids such as the *transparent testa* mutants.[43] Combining the high spatial resolution metabolite imaging with the mutant screening by GALDI MS has the potential to provide a new direction to functional genomics studies.

Figure 7 shows chemically-selective images generated from the whole flower. Higher abundances of flavonols and their glycosides on the petal surface compared to other parts of the flower surface and consistency of the localization of flavonols through petals are clearly depicted. In addition to flavonoids, high abundances of C29 ketone (at *m/z* 421) and C30 FA (at *m/z* 451) were observed in a carpel and a flower pedicle, which is consistent with previous

studies [38-40, 53]. We also found several unknown compounds including ions at *m/z* 978 that were highly localized on the carpel surface. Interestingly, intense signals from ion species at *m/z* 717 were observed at the stigma. This species has not been unambiguously identified, however, its spectra aresimilar to those of condensed tannin compounds [12, 70] based on its fragment ions (*m/z* 602, 339, 311, 309, 291, and 247).

It should be noted that images of those ion species that were found mainly at the carpel and the stigma were processed with normalized intensities instead of absolute intensities. The reason is that the average intensities from the carpel (~10^4) is about 10 times lower than those from petals (~10^5) such that the spatial distribution at the carpel becomes difficult to distinguish from background signals of the petal area if these ions were processed with absolute intensities. This difference in ion yield may come from several inherent factors such as different shape and thickness of flower parts and different surface characteristics due to the different cuticular wax load of each flower part. Therefore, quantitative comparison among different flower organs is limited in the direct profiling of metabolites by LDI MS. Because total ion current is influenced directly by ion yield, normalized intensities by TIC were considered as a reasonable processing approach in this case. In addition, different classes of compounds are difficult to compare quantitatively even if their ions are generated from the same sample surface due to their different ionization efficiencies. In other words, comparing the apparent amounts of flavonoids with those of cuticular wax compounds does not give reliable quantitative estimates.

Light–induced flavonoid accumulation in Arabidopsis stems. Flavonoid accumulation in the stem under the high fluence of photons was chosen as a model system for demonstrating the utility of GALDI MS imaging method. After 14 days of light treatment, stem sections were imaged and compared to images of stem sections from control plants (Figure 8 and 9). As shown in Figure 8, light-treated Arabidopsis stems accumulate anthocyanin pigments and become dark purple in color (Figure 8b). Here we used two

histochemical staining techniques (DMACA and DPBA staining) to determine flavonoid localization in tissue and cells in Arabidopsis stem cross-sections as revealed by bright-field light microscopy and epi-fluorescence microscopy (Figure 8c-8f) [48, 71]. DMACA is highly sensitive and selective for flavonols[50]: a blue to purple-brown color (Figure 8d, shown with black arrows) is produced. The dark-blue DMACA stain showed sieve-tube elements with large amounts of flavanols in vacuoles (black arrows in Figure 8d). Flavonoid accumulation was visualized in vivo by using DPBA histochemical stain via fluorescence (white arrows in Figure 8e and 8f). Thus, although transmission or fluorescence microscopy provides high spatial information concerning the location of 'colored' compounds such as flavonoids, it lacks the ability to decipher chemical identification. On the other hand, the mass spectral images in Figure 9 show obvious areas where kaempferol at *m/z* 285 and their monoglycosides at *m/z* 431 preferentially accumulate in light-treated stem sections as compared to control stem sections. Another interesting observation is that the intense signals at *m/z* 749 and 765 were observed only in light-treated stem sections and their distribution is different from that of kaempferols. Based on fragment ion patterns (data not shown), these may be similar to substructures of the end product, proanthocyanidin (PA). This result suggests that GALDI MS profiling and imaging can simultaneously provide spatial distribution on plant tissue sections like microscopy and chemical identities like LC-MS. However, the current spatial resolution (50-100 μm) is not high enough to differentiate cell by cell in epidermis, and sampling areas with diameters in the low micron range must be developed to achieve cell-to-cell comparison similar to light microscopy techniques.

Acknowledgement

E.S.Y. thanks the Robert Allen Wright Endowment for Excellence for support. H.I.I. thanks the National Science Foundation for support under MCB-0416730 and MCB-0520140. The Ames Laboratory is operated for the U.S. Department of Energy by Iowa State

University under Contract No. DE-AC02-07CH11358. This work was supported by the Director of Science, Office of Basic Energy Sciences, Division of Chemical Sciences.

Appendix

Further experimental consideration about enhancing spatial resolution in mass spectral imaging by ‘Oversampling’ was discussed in Appendix 3.

Table 1. Observed flavonoid compounds by GALDI MS^n from *Arabidopsis thaliana* wild type (Col) flower

***m/z* values [M–H]$^-$**	**Observed major *m/z* values of fragment ions (NLs)**	**Composition[b]**	**Possible structural identities**	**References**
285	151, 179, 229	Kaempferol (K)	Kaempferol	
301	151, 179, 229, 285	Quercetin (Q)	Quercetin	
315	151, 179, 228, 300	Isorhamnetin (I)	Isorhamnetin	72
431	285(146),	K-Rha		
447	285(162), 301(146)	Q-Rha and K-Hex	Quercetin-3-*O* –rhamnoside and Kaempferol-3-*O* – glucoside	55
461	315(146)	I-Rha		
463	301(162)	Q-Hex	Quercetin-3-*O* – glucoside	56
477	315(162)	I-Hex		
577	285, 429, 431(146)	K-Rha-Rha	Kaempferol-3, 7-di-*O* -rhamnoside	44
593	285, 327, 429, 431(162), 447(146)	K-Rha-Hex and Q-Rha-Rha	Kaempferol-3-*O* -glucoside-7-*O*-rhamnoside and Quercetin-di-rhamnoside	44, 54
609	285, 301, 429(180), 447(162), 463(146)	Q-Rha-Hex and K-Hex-Hex	Quercetin-glucoside-rhamnoside	54
623	315, 461(162), 477(146)	I-Rha-Hex		
739[a]	284, 430(309), 447, 593(146)	K-Rha-Rha-Hex	Kaempferol-3-*O* – rhamnoside(1→2)glucoside-7-*O*-rhamnoside	55, 73
755	301, 447, 609(146)	Q-Rha-Rha-Hex	Quercetin- 3-*O* – rhamnoside-glucoside-7-*O*-rhamnoside	57, 74

a: Fragment ions from both 1st generation and 2nd generation (739→593→) product ion spectra were included

b: K: Kaempferol, Q: Quercetin, I:Isorhamnetin, Rha: rhamnoside, and Hex: hexoside (galactose or glucose)

References

(1) Dunn, W. B.; Bailey, N. J. C.; Johnson, H. E. *Analyst* **2005**, *130*, 606-625.

(2) Sumner, L. W.; Mendes, P.; Dixon, R. A. *Phytochemistry* **2003**, *62*, 817-836.

(3) Bligny, R.; Douce, R. *Current Opinion in Plant Biology* **2001**, *4*, 191-196.

(4) Ratcliffe, R. G.; Shachar-Hill, Y. *Annual Review of Plant Physiology and Plant Molecular Biology* **2001**, *52*, 499-526.

(5) Villas-Boas, S. G.; Mas, S.; Akesson, M.; Smedsgaard, J.; Nielsen, J. *Mass Spectrometry Reviews* **2005**, *24*, 613-646.

(6) Fiehn, O.; Kopka, J.; Dormann, P.; Altmann, T.; Trethewey, R. N.; Willmitzer, L. *Nature Biotechnology* **2000**, *18*, 1157-1161.

(7) Roessner, U.; Wagner, C.; Kopka, J.; Trethewey, R. N.; Willmitzer, L. *Plant Journal* **2000**, *23*, 131-142.

(8) Fenn, J. B.; Mann, M.; Meng, C. K.; Wong, S. F.; Whitehouse, C. M. *Science* **1989**, *246*, 64-71.

(9) Glinski, M.; Weckwerth, W. *Mass Spectrometry Reviews* **2006**, *25*, 173-214.

(10) Sluszny, C.; Yeung, E. S.; Nikolau, B. J. *Journal of the American Society for Mass Spectrometry* **2005**, *16*, 107-115.

(11) Zabrouskov, V.; Al-Saad, K. A.; Siems, W. F.; Hill, H. H.; Knowles, N. R. *Rapid Communications in Mass Spectrometry* **2001**, *15*, 935-940.

(12) Ishida, Y.; Kitagawa, K.; Goto, K.; Ohtani, H. *Rapid Communications in Mass Spectrometry* **2005**, *19*, 706-710.

(13) Fraser, P. D.; Enfissi, E. M. A.; Goodfellow, M.; Eguchi, T.; Bramley, P. M. *Plant Journal* **2007**, *49*, 552-564.

(14) Schad, M.; Mungur, R.; Fiehn, O.; Kehr, J. *Plant Methods* **2005**, *1*, 2.

(15) Caprioli, R. M.; Farmer, T. B.; Gile, J. *Analytical Chemistry* **1997**, *69*, 4751-4760.

(16) Wu, K. J.; Odom, R. W. *Analytical Chemistry* **1996**, *68*, 873-882.

(17) Winograd, N. *Applied Surface Science* **2003**, *203*, 13-19.

(18) Sjovall, P.; Lausmaa, J.; Johansson, B. *Analytical Chemistry* **2004**, *76*, 4271-4278.

(19) Parry, S.; Winograd, N. *Analytical Chemistry* **2005**, *77*, 7950-7957.

(20) Eriksson, C.; Borner, K.; Nygren, H.; Ohlson, K.; Bexell, U.; Billerdahl, N.; Johansson, M. *Applied Surface Science* **2006**, *252*, 6757-6760.

(21) Heeren, R. M. A.; McDonnell, L. A.; Amstalden, E.; Luxembourg, S. L.; Altelaar, A. F. M.; Piersma, S. R. *Applied Surface Science* **2006**, *252*, 6827-6835.

(22) Wiseman, J. M.; Ifa, D. R.; Song, Q. Y.; Cooks, R. G. *Angewandte Chemie-International Edition* **2006**, *45*, 7188-7192.

(23) Takats, Z.; Wiseman, J. M.; Gologan, B.; Cooks, R. G. *Science* **2004**, *306*, 471-473.

(24) Cha, S. W.; Yeung, E. S. *Analytical Chemistry* **2007**, *79*, 2373-2385.

(25) Zhang, H.; Cha, S. W.; Yeung, E. S. *Analytical Chemistry* **2007**, *79*, 6575-6584.

(26) Northen, T. R.; Yanes, O.; Northen, M. T.; Marrinucci, D.; Uritboonthai, W.; Apon, J.; Golledge, S. L.; Nordstrom, A.; Siuzdak, G. *Nature* **2007**, *449*, 1033-U1033.

(27) Mangabeira, P. A.; Gavrilov, K. L.; de Almeida, A. A. F.; Oliveira, A. H.; Severo, M. I.; Rosa, T. S.; Silva, D. D.; Labejof, L.; Escaig, F.; Levi-Setti, R.; Mielke, M. S.; Loustalot, F. G.; Galle, P. *Applied Surface Science* **2006**, *252*, 3488-3501.

(28) Gojon, A.; Grignon, N.; Tillard, P.; Massiot, P.; Lefebvre, F.; Thellier, M.; Ripoll, C. *Cellular and Molecular Biology* **1996**, *42*, 351-360.

(29) Gea, L.; Jauneau, A.; Vian, B. *Journal of Trace and Microprobe Techniques* **1994**, *12*, 323-329.

(30) Jauneau, A.; Pariot, C.; Verdus, M. C.; Ripoll, C. *Journal of Trace and Microprobe Techniques* **1994**, *12*, 51-60.

(31) Derue, C.; Gibouin, D.; Demarty, M.; Verdus, M. C.; Lefebvre, F.; Thellier, M.; Ripoll, C. *Microscopy Research and Technique* **2006**, *69*, 53-63.

(32) Heard, P. J.; Feeney, K. A.; Allen, G. C.; Shewry, P. R. *Plant Journal* **2002**, *30*, 237-245.

(33) Imai, T.; Tanabe, K.; Kato, T.; Fukushima, K. *Planta* **2005**, *221*, 549-556.

(34) Saito, K.; Mitsutani, T.; Imai, T.; Matsushita, Y.; Fukushima, K. *Anal. Chem.* **2008**, *80*, 1552-1557.

(35) Burrell, M. M.; Earnshaw, C. J.; Clench, M. R. *J. Exp. Bot.* **2007**, *58*, 757-763.

(36) Li, Y.; Shrestha, B.; Vertes, A. *Analytical Chemistry* **2007**, *79*, 523-532.

(37) Aarts, M. G. M.; Keijzer, C. J.; Stiekema, W. J.; Pereira, A. *Plant Cell* **1995**, *7*, 2115-2127.

(38) Hannoufa, A.; McNevin, J.; Lemieux, B. *Phytochemistry* **1993**, *33*, 851-855.

(39) Jenks, M. A.; Tuttle, H. A.; Eigenbrode, S. D.; Feldmann, K. A. *Plant Physiology* **1995**, *108*, 369-377.

(40) Jenks, M. A.; Tuttle, H. A.; Feldmann, K. A. *Phytochemistry* **1996**, *42*, 29-34.

(41) Podila, G. K.; Rogers, L. M.; Kolattukudy, P. E. *Plant Physiology* **1993**, *103*, 267-272.

(42) Burchard, P.; Bilger, W.; Weissenbock, G. *Plant Cell and Environment* **2000**, *23*, 1373-1380.

(43) Shirley, B. W.; Kubasek, W. L.; Storz, G.; Bruggemann, E.; Koornneef, M.; Ausubel, F. M.; Goodman, H. M. *The Plant Journal* **1995**, *8*, 659-671.

(44) Veit, M.; Pauli, G. F. *Journal of Natural Products* **1999**, *62*, 1301-1303.

(45) Bloor, S. J.; Abrahams, S. *Phytochemistry* **2002**, *59*, 343-346.

(46) Debeaujon, I.; Nesi, N.; Perez, P.; Devic, M.; Grandjean, O.; Caboche, M.; Lepiniec, L. *Plant Cell* **2003**, *15*, 2514-2531.

(47) Jones, P.; Messner, B.; Nakajima, J. I.; Schaffner, A. R.; Saito, K. *Journal of Biological Chemistry* **2003**, *278*, 43910-43918.

(48) Lazar, G.; Goodman, H. M. *Proceedings of the National Academy of Sciences of the United States of America* **2006**, *103*, 472-476.

(49) Sharma, S. B.; Dixon, R. A. *Plant Journal* **2005**, *44*, 62-75.

(50) Abrahams, S.; Tanner, G. J.; Larkin, P. J.; Ashton, A. R. *Plant Physiology* **2002**, *130*, 561-576.

(51) Jurchen, J. C.; Rubakhin, S. S.; Sweedler, J. V. *Journal of the American Society for Mass Spectrometry* **2005**, *16*, 1654-1659.

(52) Millar, A. A.; Clemens, S.; Zachgo, S.; Giblin, E. M.; Taylor, D. C.; Kunst, L. *Plant Cell* **1999**, *11*, 825-838.

(53) Rashotte, A. M.; Jenks, M. A.; Nguyen, T. D.; Feldmann, K. A. *Phytochemistry* **1997**, *45*, 251-255.

(54) Graham, T. L. *Plant Physiology and Biochemistry* **1998**, *36*, 135-144.

(55) Kerhoas, L.; Aouak, D.; Cingoz, A.; Routaboul, J. M.; Lepiniec, L.; Einhorn, J.; Birlirakis, N. *Journal of Agricultural and Food Chemistry* **2006**, *54*, 6603-6612.

(56) Routaboul, J. M.; Kerhoas, L.; Debeaujon, I.; Pourcel, L.; Caboche, M.; Einhorn, J.; Lepiniec, L. *Planta* **2006**, *224*, 96-107.

(57) Tohge, T.; Nishiyama, Y.; Hirai, M. Y.; Yano, M.; Nakajima, J.; Awazuhara, M.; Inoue, E.; Takahashi, H.; Goodenowe, D. B.; Kitayama, M.; Noji, M.; Yamazaki, M.; Saito, K. *Plant Journal* **2005**, *42*, 218-235.

(58) Garrett, T. J.; Prieto-Conaway, M. C.; Kovtoun, V.; Bui, H.; Izgarian, N.; Stafford, G.; Yost, R. A. *International Journal of Mass Spectrometry* **2007**, *260*, 166-176.

(59) Garrett, R.; Grisham, C. *Biochemistry*, 2nd Edition ed., 1999.

(60) Bowman, J. L.; Smyth, D. R.; Meyerowitz, E. M. *Plant Cell* **1989**, *1*, 37-52.

(61) Smyth, D. R.; Bowman, J. L.; Meyerowitz, E. M. *Plant Cell* **1990**, *2*, 755-767.

(62) Kitamura, S.; Shikazono, N.; Tanaka, A. *Plant Journal* **2004**, *37*, 104-114.

(63) Xie, D. Y.; Sharma, S. B.; Paiva, N. L.; Ferreira, D.; Dixon, R. A. *Science* **2003**, *299*, 396-399.

(64) Boss, P. K.; Davies, C.; Robinson, S. P. *Plant Physiology* **1996**, *111*, 1059-1066.

(65) Burbulis, I. E.; Winkel-Shirley, B. *Proceedings of the National Academy of Sciences of the United States of America* **1999**, *96*, 12929-12934.

(66) Holton, T. A.; Brugliera, F.; Lester, D. R.; Tanaka, Y.; Hyland, C. D.; Menting, J. G. T.; Lu, C. Y.; Farcy, E.; Stevenson, T. W.; Cornish, E. C. *Nature* **1993**, *366*, 276-279.

(67) Landry, L. G.; Chapple, C. C. S.; Last, R. L. *Plant Physiology* **1995**, *109*, 1159-1166.

(68) Koornneef, M.; Luiten, W.; de Vlaming, P.; Schram, A. W. *Arabid. Inf. Serv.* **1982**, *19*, 113-115.

(69) Yonekura-Sakakibara, K.; Tohge, T.; Niida, R.; Saito, K. *Journal of Biological Chemistry* **2007**, *282*, 14932-14941.

(70) Behrens, A.; Maie, N.; Knicker, H.; Kogel-Knabner, I. *Phytochemistry* **2003**, *62*, 1159-1170.

(71) Murphy, A.; Peer, W. A.; Taiz, L. *Planta* **2000**, *211*, 315-324.

(72) Wolfender, J. L.; Waridel, P.; Ndjoko, K.; Hobby, K. R.; Major, H. J.; Hostettmann, K. *Analusis* **2000**, *28*, 895-906A.

(73) March, R. E.; Miao, X. S.; Metcalfe, C. D. *Rapid Communications in Mass Spectrometry* **2004**, *18*, 931-934.

(74) Besseau, S.; Hoffmann, L.; Geoffroy, P.; Lapierre, C.; Pollet, B.; Legrand, M. *Plant Cell* **2007**, *19*, 148-162.

Figure Captions

Figure 1. Structures of flavonol aglycones and glycosides. Arrows indicate hydroxyl groups that are modified by glycosylation.

Figure 2. Negative-ion mode GALDI mass spectrum taken from an *Arabidopsis* leaf. Mass spectra from 45 scanning points on the leaf central vein were averaged. VLCFAs which have 24 to 30 carbons were detected. C24, C26, C28, C30 FAs correspond to tetracosanoic, hexacosanoic, octacosanoic, and triacontanoic fatty acids.

Figure 3. An optical image of chloroform-dipped leaf (upper center) and chemically-selective images of major compounds. Dimension of the image is 7600 μm high × 14100 μm wide. The step size for data collection was set to 150 μm for both x and y directions. C26 and C30 fatty acids showed high abundance on untreated area (right column) while kaempferol and its monoglycoside showed high abundance in forcep-grasped area and chloroform-dipped area (left column). Ion species at *m/z* 210 showed very high abundances in the dipped area (lower center). Mass spectral profile of the dipped area is shown in Supporting Information Figure S1. All mass spectral images shown here were presented as normalized intensities and maximum scale values for kaempfeol, kaempferol rhamnoside, ions at *m/z* 210, C26 fatty acid, and C30 fatty acid were set to 2.5%, 3%, 10%, 5%, and 3% of total ion current (TIC) value, respectively. All images were smoothed linearly.

Figure 4. First generation product ion spectra of ions detected at (A) *m/z* 623 and (B) *m/z* 609 from the negative-ion mode GALDI mass spectrum of *Arabidopsis* petal. The neutral loss of 146 Da (NL 146) corresponds to the elimination of a rhamnose moiety and NL 162 corresponds to the elimination of a hexose moiety. The loss of 163 Da corresponds to the elimination of the radical $C_6H_{11}O_5°$. NL 180 corresponds to subsequent water loss after NL 162. Fragment ions at *m/z* 315 and *m/z* 285 correspond to deprotonated ions of isorhamnetin(I) ($[I - H]^-$) and kaempferol(K) ($[K-H]^-$), respectively. Chemical compositions corresponding to ions (A) *m/z* 623 and (B) *m/z* 609 are listed in Table 1.

Figure 5. Mass spectral profiles from three locations in an *Arabidopsis* petal. The optical image on the left side is the image of the whole flower which was attached to the sample plate. The image was taken inside the mass spectrometer before spraying colloidal graphite onto the flower. The image on the right side is the magnified view of the petal. Dimensions are 4900 μm high × 5200 μm wide for the whole flower image and 2822 μm high × 2445 μm wide for the petal image. Three areas annotated with (A), (B), and (C) indicate where the mass spectra were collected. Each area contained 50 rastering points and the plots were the averaged mass spectra of 50 rastering points from each area. Symbol K, Q, and I correspond to the three flavonol aglycones listed in Table 1 and numbers above the major peaks depict nominal *m/z* values listed in Table 1.

Figure 6. Chemically selective images of *Arabidopsis* petals. Petals in these images are the same as in Figure 5. The step size for data collection was set to 50 μm for

both x and y directions. Dimension of the images is 2822 μm high × 2445 μm wide. The nominal value in each image corresponds to the nominal *m/z* value of the corresponding ions. Chemical compositions of corresponding *m/z* values are listed in Table 1. All images were processed with absolute intensity values and intensity scales were adjusted individually for the best presentation. The images were not smoothed.

Figure 7. Chemically selective images of *Arabidopsis* flower. The step size for data collection was set to 50 μm for both x and y directions. Dimension of the images is 4740 μm high × 4600 μm wide. The nominal value in each image corresponds to the nominal *m/z* value of the corresponding ions. Chemical compositions of corresponding *m/z* values were listed in Table 1 except m/z 421(C29 ketone), 451(C30 fatty acid), 978(unknown), and 717(unknown). Four mass images (421,451, 978, and 717) on the first row were processed with normalized intensities and the maximum scale values were shown as a percentage of the total ion current. The other images were processed with absolute intensity values and the maximum scale value was given for each image. All images were smoothed linearly.

Figure 8. Effect of light on flavonoid and anthocyanin content and distribution in the inflorescence stem of Arabidopsis. Left column, grown under normal-light regime; and right column, grown under high-light regime. (a) and (b), Stereomicroscopic images of the inflorescence stem. Anthocyanin accumulation in (b) is shown with stars. Bars: 500 μm. (c) and (d), Bright-field light microscopic view of inflorescence stem cross-sections using DMACA staining to show localization of total soluble phenols, soluble

flavanols and and proanthocyanidins (PAs): the black arrows show blue-brown-purple colored sieve-tube elements of phloem cells. Bars: 20 μm. (e) and (f), DPBA staining viewed by fluorescence microscopy: fluorescence shows mostly selected flavonoid localization in the collenchyma under the epidermis as patchy areas. Orange fluorescence (kaempferol and quercetin); bright-yellow fluorescence (naringenin-chalcone); and chlorophylls red autofluorescence (shown with white arrows). Ph, Phloem; col, collenchyma cells; and Xy, Xylem. Bars: 40 μm.

Figure 9. Chemically selective images of *Arabidopsis* stems grown under normal-light regime as control (top row) and grown under high-light regime (bottom row). Step spacing was set to 50 μm for both x and y directions. Sizes of both stem sections were 1100 ~ 1200 μm in diameter. All images were processed with normalized intensities and maximum scale values were shown as a percentage of the total ion current. The accumulation of kaemperols (*m/z* 285) and its glycosides (*m/z* 431) in light-treated stem section is obvious compared to control stem section. The accumulation of the unknowns at *m/z* 749 and 765 shows a different local distribution from kaempferols. All images were smoothed linearly.

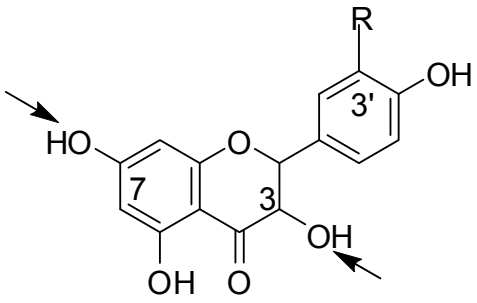

R: H (kaempferol)
OH (quercetin)
OCH_3 (isorhamnetin)

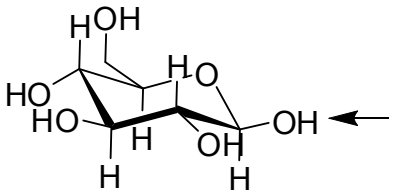

beta-D-glucopyranose

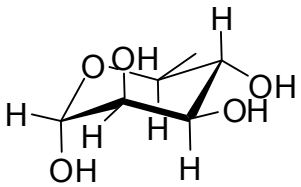

6-deoxy-alpha-L-mannopyranose (Rhamnose)

Figure 1.

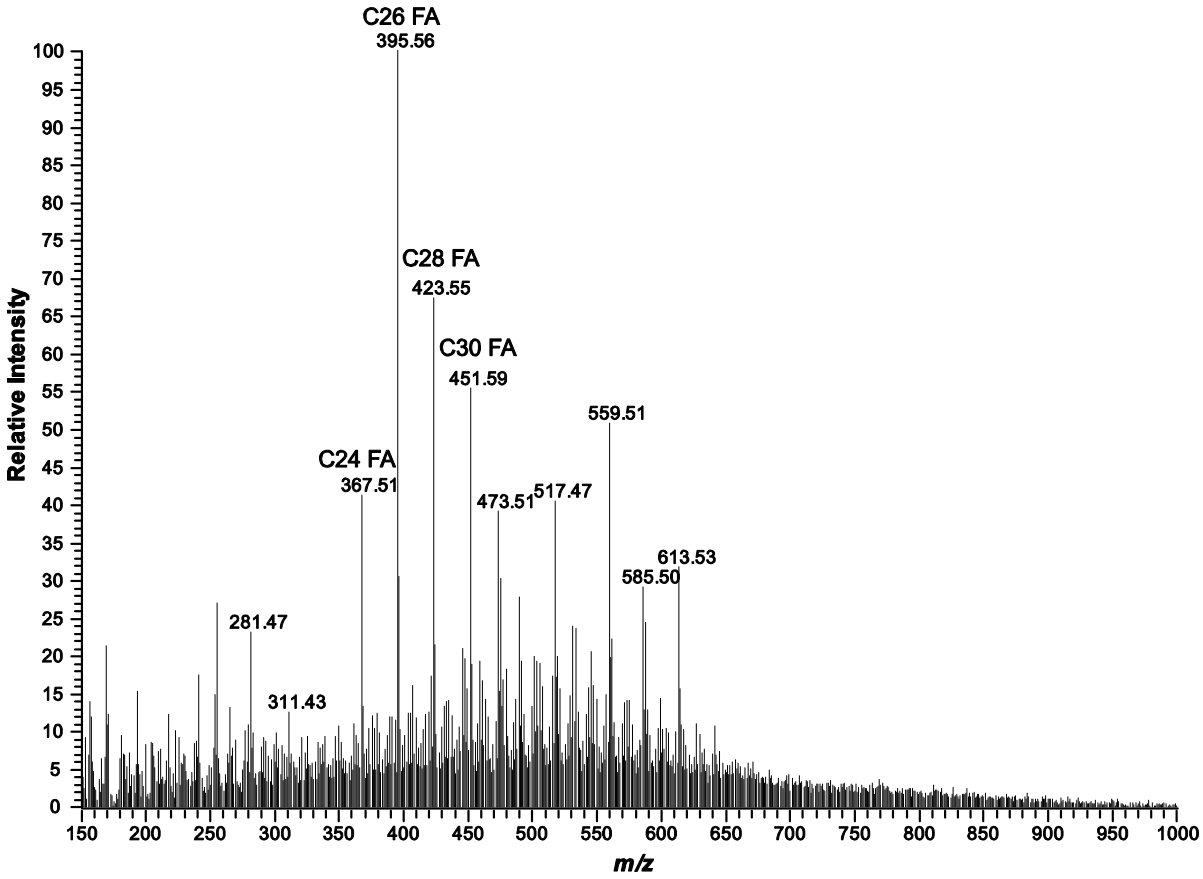
C26 FA
395.56
C28 FA
423.55
C30 FA
451.59
559.51
C24 FA
367.51
473.51
517.47
613.53
585.50
281.47
311.43
Relative Intensity
m/z

Figure 2.

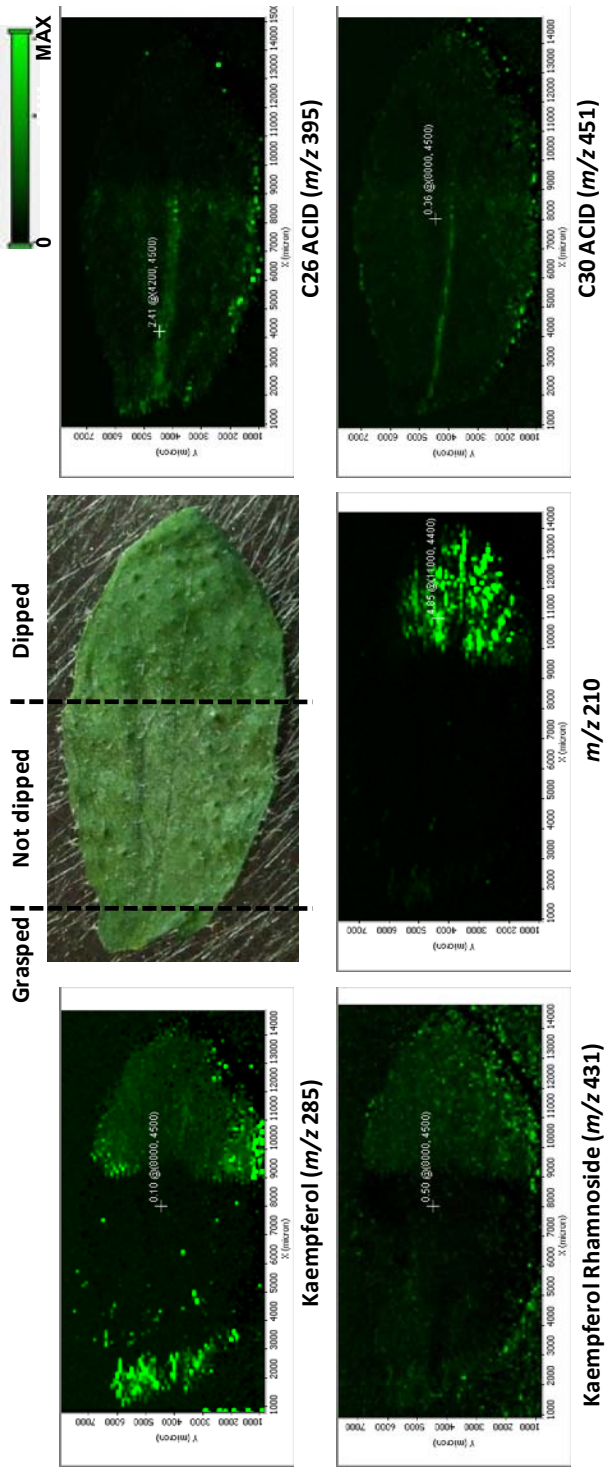
MAX
0
C26 ACID (m/z 395)
C30 ACID (m/z 451)
Dipped
Not dipped
Grasped
m/z 210
Kaempferol (m/z 285)
Kaempferol Rhamnoside (m/z 431)

Figure 3.

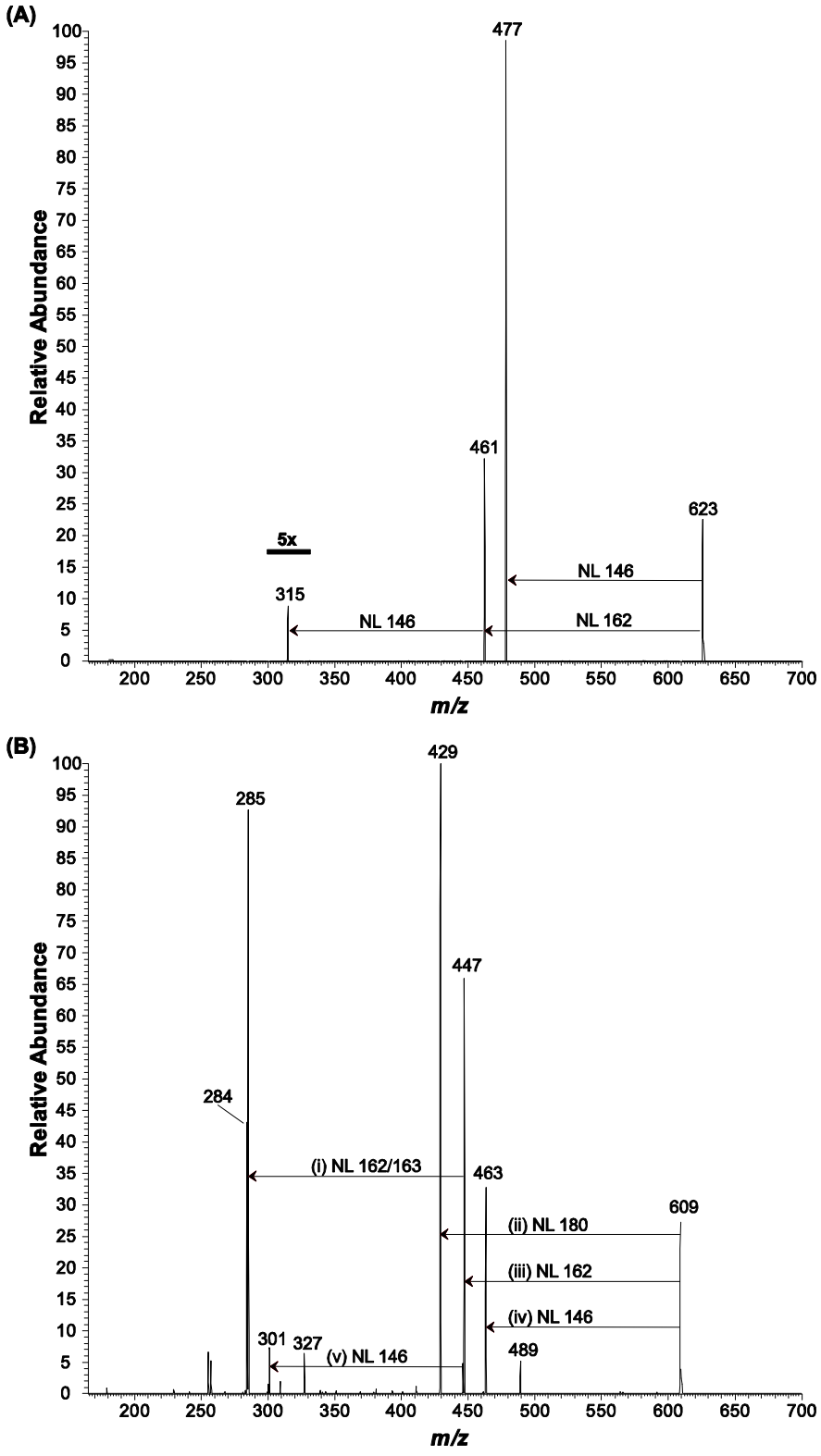
(A)
Relative Abundance
m/z
477
461
623
5x
315
NL 146
NL 146
NL 162
(B)
Relative Abundance
m/z
429
285
447
284
(i) NL 162/163
463
609
(ii) NL 180
(iii) NL 162
(iv) NL 146
301
327
(v) NL 146
489

Figure 4.

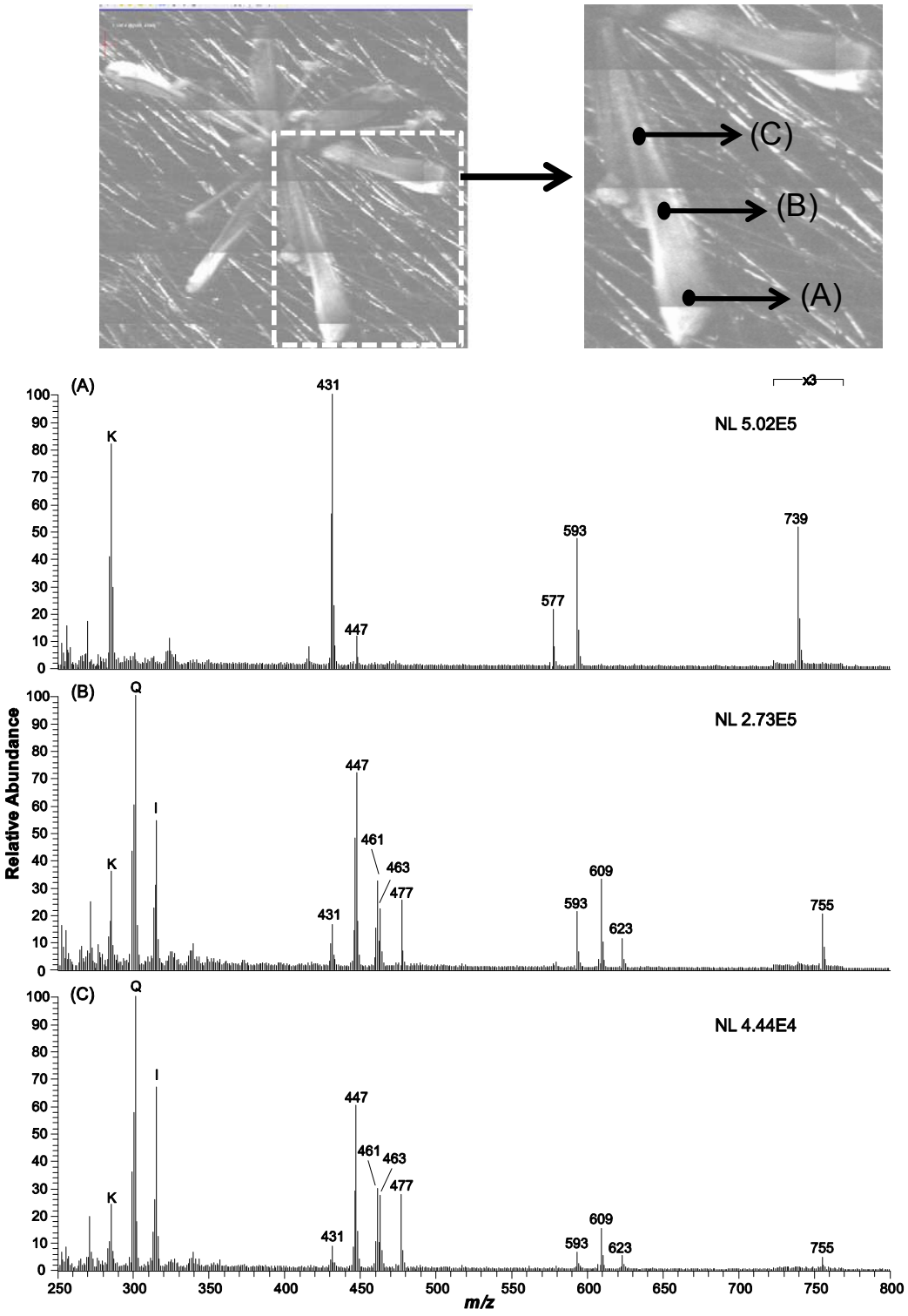
(C)
(B)
(A)
(A)
NL 5.02E5
x3
431
K
593
739
577
447
(B)
NL 2.73E5
Q
447
I
461
463
K
609
477
593
755
431
623
(C)
NL 4.44E4
Q
I
447
461
463
K
477
609
431
593
623
755
Relative Abundance
m/z

Figure 5.

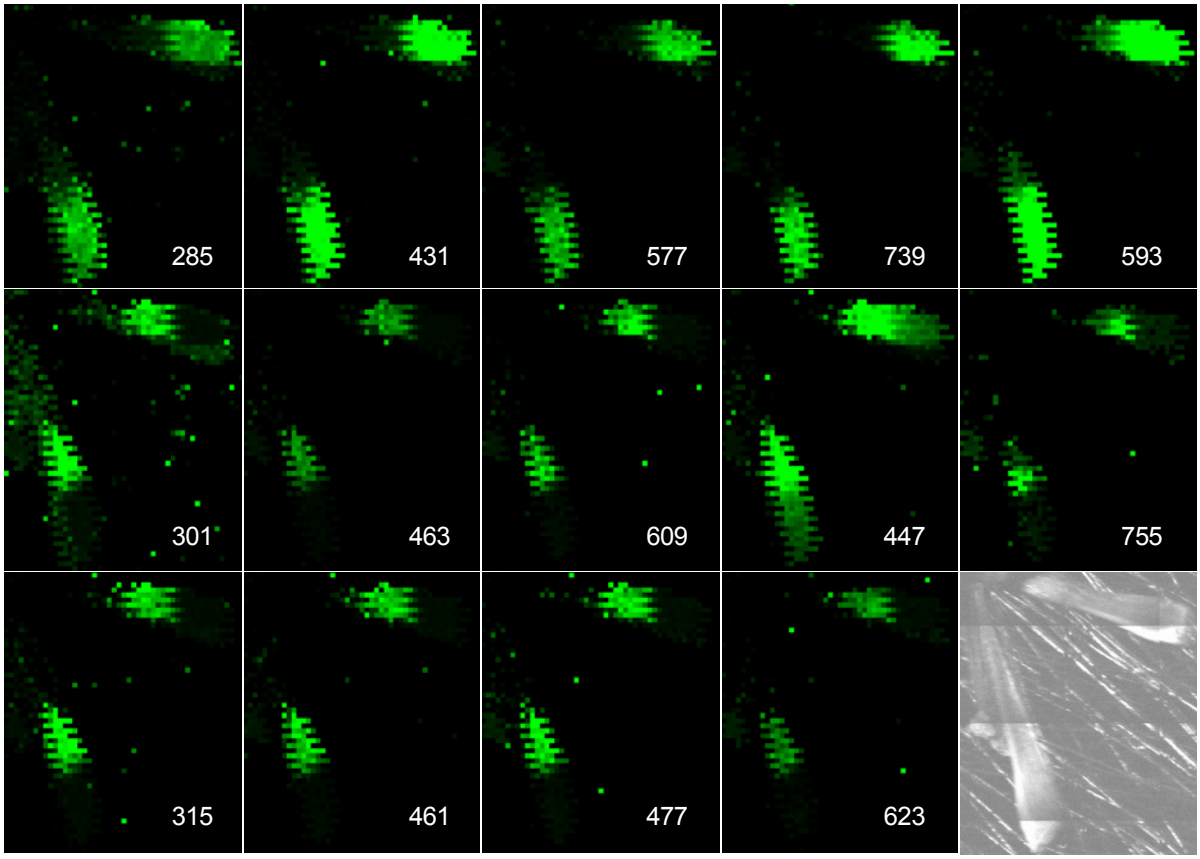

Figure 6.

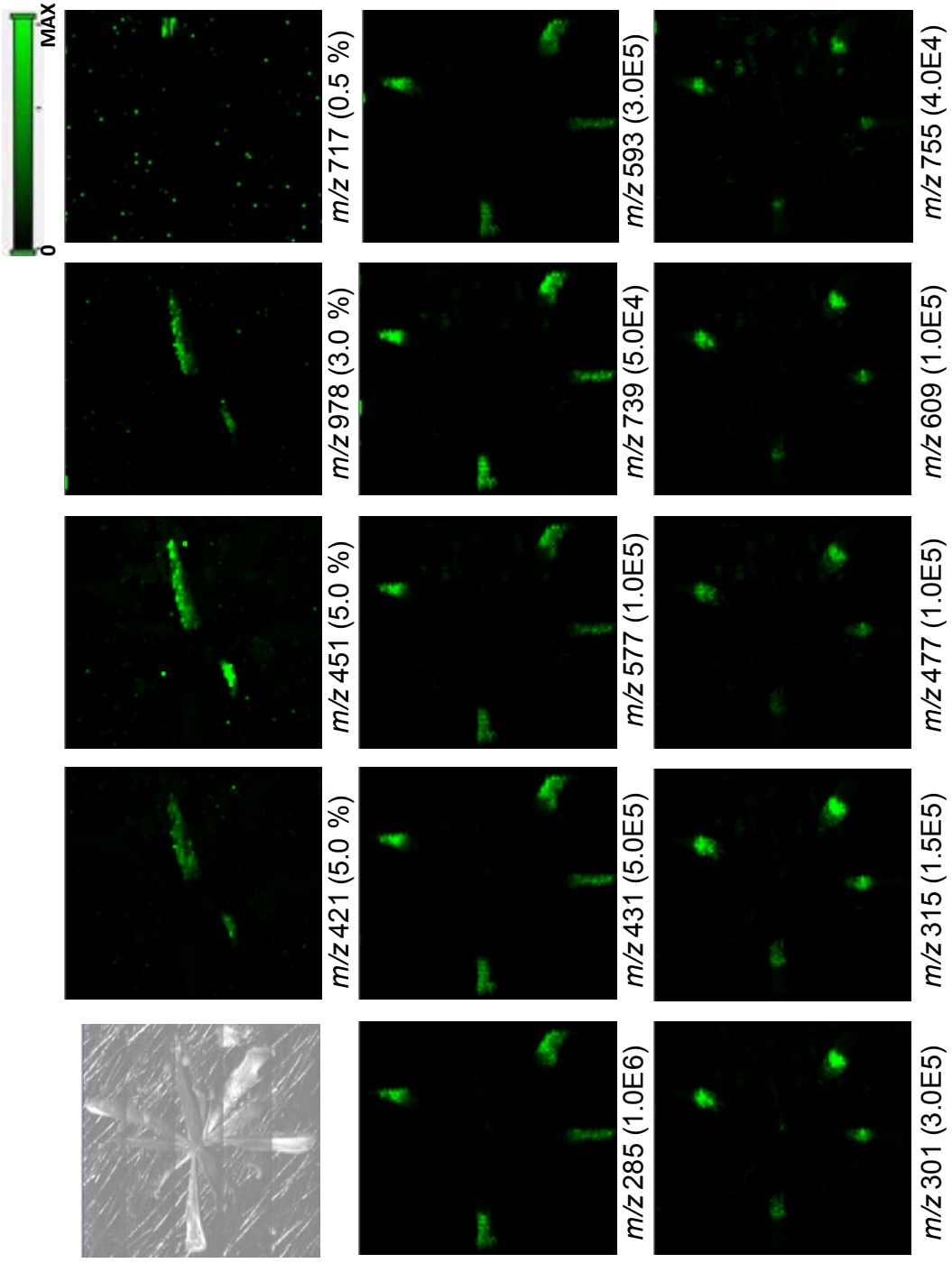
MAX
0
m/z 717 (0.5 %)
m/z 593 (3.0E5)
m/z 755 (4.0E4)
m/z 978 (3.0 %)
m/z 739 (5.0E4)
m/z 609 (1.0E5)
m/z 451 (5.0 %)
m/z 577 (1.0E5)
m/z 477 (1.0E5)
m/z 421 (5.0 %)
m/z 431 (5.0E5)
m/z 315 (1.5E5)
m/z 285 (1.0E6)
m/z 301 (3.0E5)

Figure 7.

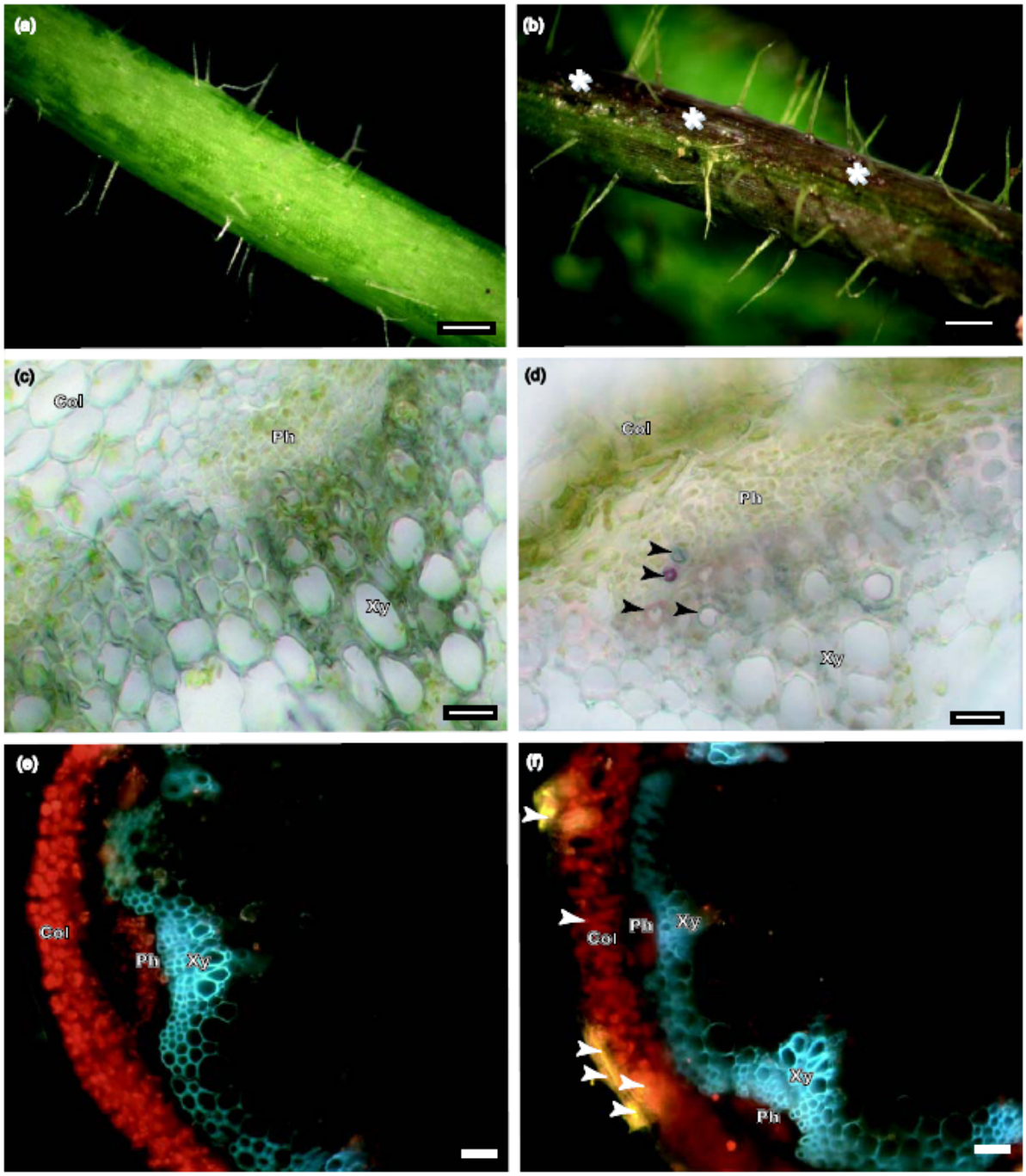

Figure 8.

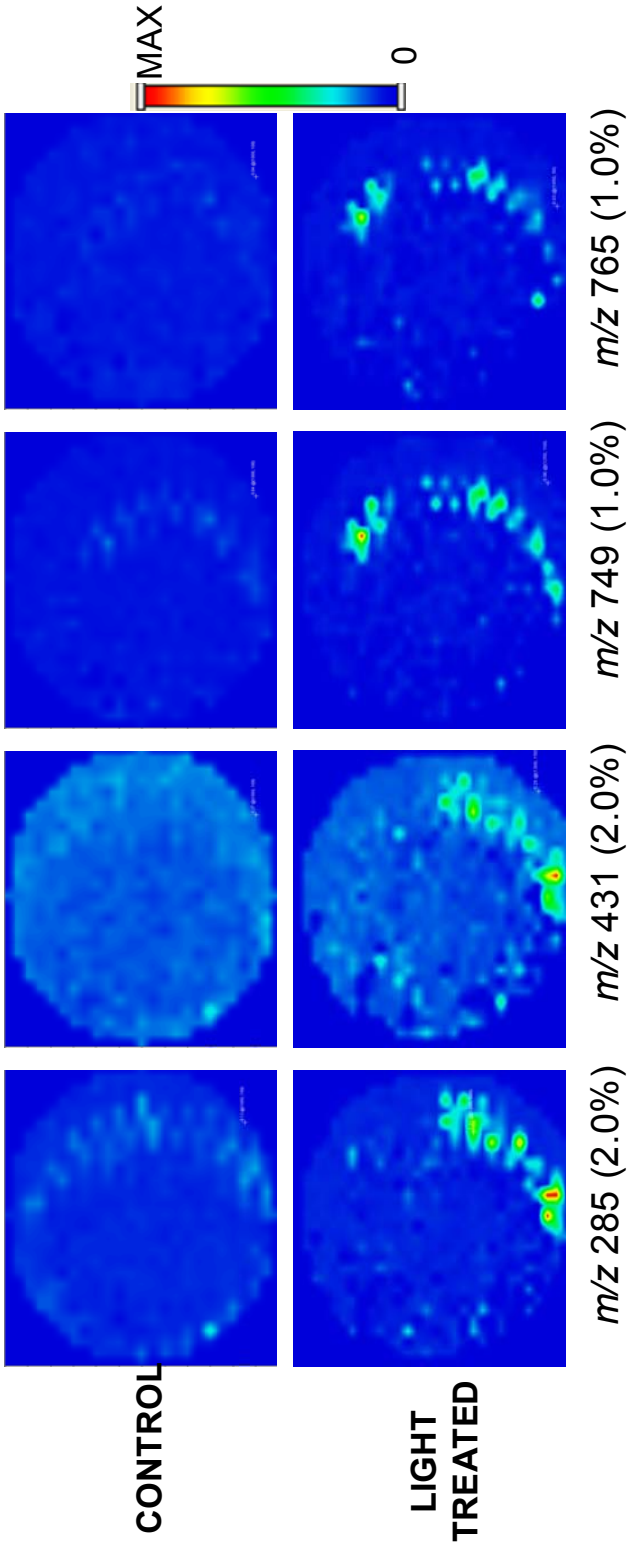
MAX
0
m/z 765 (1.0%)
m/z 749 (1.0%)
m/z 431 (2.0%)
m/z 285 (2.0%)
CONTROL
LIGHT TREATED

Figure 9.

CHAPTER 4. DIRECT PROFILING AND IMAGING OF EPICUTICULAR WAXES ON ARABIDOPSIS THALIANA BY LASER DESORPTION/IONIZATION MASS SPECTROMETRY USING SILVER COLLOID AS A MATRIX

Part of this chapter submitted to The Plant Journal*

Sangwon Cha, Zhihong Song, Wenxu Zhou, Basil J. Nikolau and Edward S. Yeung

Abstract

Colloidal-silver laser desorption/ionization (LDI) mass spectrometry (MS) was employed to profile and image epicuticular wax metabolites in Arabidopsis leaves and flowers. Mass spectral profiles of wax compounds were recorded directly from various plant surfaces. Major wax compounds, very long chain fatty acids and their derivatives including alkanes, primary alcohols, and ketones were successfully detected as silver adduct ions. With the ability of small-area sampling and the excellent sensitivity, surface species of each flower part, carpels, petals, and sepals, were profiled for the first time. In addition, mass spectral profiles and images collected from wild-type and mutants were used for investigating variations of wax products by normalizing the ion intensities to a reference peak, $[^{107}Ag + {}^{109}Ag]^+$. Differences in profiles between wild-type (Ler) and *cer* mutant (*cer*2) by LDI MS were compared with those from GC-MS. We propose that the *cer*2 gene product may be involved in either C_{30} fatty acid to C_{30} aldehyde reduction or C_{30} aldehyde to C_{29} alkane decarbonylation in the wax biosynthesis pathway. It may also have a location specific regulatory function.

Introduction

As a barrier to the abiotic environment, plants produce the cuticle which protects them from external stresses, such as water, insects, and pathogens. The cuticle is composed

of two hydrophobic components, cutin and cuticular waxes [1, 2]. A fatty acid-based polyester, cutin serves as the structural backbone of cuticle and is covered and blended with aliphatic long-chain fatty acids and their derivatives, cuticular wax. Functional genomics and metabolomics studies on cuticular wax biosynthesis pathway and their transport mechanism have been carried out mainly with *Arabidopsis thaliana* and achievements in this field were thoroughly reviewed recently [3].

Several wax-deficient mutants have been screened mainly by visually examining the phenotype, and the mutant loci have been identified for *Arabidopsis thaliana, eceriferum* (*cer*) [4]. In addition to visual screening, a condensed GC method was employed to screen the visually identical mutant lines [5], twenty four *cer* loci have been identified so far. Among CER genes, CER2 gene has been isolated and characterized by Xia *et al.* [6]. And they suggested that CER2 gene encodes a 47 kDa, nuclear localized protein [7]. However, the function of CER2 gene product is still unknown [3].

The wax profiles of *cer* mutants have been analyzed by gas chromatography mass spectrometry (GC-MS) and, based on differences in the carbon-chain lengths and the amounts of wax constituents, the function of *cer* genes and their products that are involved in wax biosynthesis were putatively identified [5, 8-16]. GC-MS methods are always concomitant with chemical extraction of the wax compounds by organic solvents and derivatization with volatile functional groups such as trimethylsilane groups. Therefore, these profiling procedures are labor-intensive and the sample sizes are limited by the extraction protocol and by the sensitivity of GC instrumentation. In addition, chemical extraction cannot be exclusively restricted to epicuticular waxes and the degree of extraction is also ambiguous.

Recently, laser desorption/ionization mass spectrometry (LDI MS) has been employed to analyze various wax compounds and alkane oligomers [17-20]. In these studies, silver-based matrixes yielded adduct ions for alkanes and their derivatives. The other advantage of silver-based matrixes over other transition metal-based matrixes is that the

reactivity of silver to alkanes is lower than that of any other transition metals. Therefore, silver mostly generates intact silver adduct ions without fragmentation [21]. Recently, direct LDI-MS analysis of wax compounds on Arabidopsis stems and leaves by using silver colloid as a matrix was successfully performed [22]. The advantage of colloidal silver over other silver matrixes, such as ultrafine silver powder, silver nitrate, and AgTFA is that colloidal silver solution can be applied more easily and more homogeneously onto hydrophobic surfaces than other silver matrixes. Since it does not form crystals when it dries, good reproducibility of the mass spectral signals can be expected, making it possible to examine localization of the compounds of interest on the plant surface. In other words, colloidal silver is well suited for imaging MS.

Here we extend the application of colloidal silver-LDI MS for the analysis of plant cuticular wax. By rastering over the plant material, mass spectral profiles and chemically-selective images were successfully generated for Arabidopsis leaves and flowers. After normalization of the mass spectra with respect to the reference peak, reliable relative abundance information was obtained that can be compared with traditional GC-MS analysis. Compositional variations between wild-type and *cer*2 mutant flower parts were investigated for the first time by silver-LDI MS and GC-MS analysis of whole-flower wax metabolites was also performed whereas most of the previously reported metabolite profiling were focused on leaf and stem [10, 16].

Experimental Section

Chemicals. Standards such as n-alkanes, alcohols, esters, ketones, and fatty acids, consisting of 13–32 carbon atoms, BSTFA/TMCS (*N*,*O*-Bis(trimethylsilyl)trifluoroacetamide with trimethylchlorosilane), and MS media (Murashige and Skoog basal salt mixture) were obtained form Sigma-Aldrich (St. Louis, MO). A mixture of n-alkanes (C_{12}–C_{60}) was purchased from Supelco (Bellefonte, PA). Water-based colloidal silver (20 ppm) was

purchased from Purest Colloids (Westhampton, NJ). Double-deionized water was used from a MilliQ water purification system (Framington, MA). All other chemicals were purchased from Fisher Scientific (Fairlawn, NJ).

Plant growth conditions. *Arabidopsis thaliana* ecotype Landsberg *erecta* (Ler-0) and its *eceriferum* mutant (*cer*2) seeds were obtained from the ABRC. Seeds were sown on MS media in petri dishes. The dishes were placed in the growth room for 10 days after keeping at 4^{o}C for 4 days. On 15th day the plants were transferred in soil for continuous growth. Leaves were collected on 26th days, and flowers were collected on 34th days. Growth room was at 24°C with an illumination at 85 μE $m^{-2}s^{-1}$ and 100% relative humidity.

Plant sample preparation for LDI mass spectral profiling and imaging. After collecting samples from plants, plant materials were attached onto a stainless steel target plate of similar dimensions as a microscope glass slide using a conductive double-sided tape (3M, St. Paul, MN). To avoid damage to the plant sample surface, contact area by forceps was minimized and air pressure from a nitrogen gas cylinder was used for attaching samples firmly onto the sample plate. All samples were dried in moderate vacuum (approximately ~50 Torr) for 30–60 min. As shown in Figure 1, carpels, petals, and sepals were separated and attached individually for metabolite profiling of flower parts. Three replicates of leaves and whole flowers, and five replicates of flower parts for each genetic type were prepared.

The spraying device for colloidal silver solution was composed of a computer-controlled syringe pump with a 500 μL syringe (Kloehm LTD., Las *Vegas*, NV), MicroFlow PFA-ST nebulizer (Elemental Scientific Inc., Omaha, NE) with a 0.25 mm i.d. sample uptake capillary, and a helium gas cylinder. Spraying time and speed was programmed by the software "WinPump®" which is provided by Kloehm. To obtain a homogeneous coverage of silver particles, several intervals of spraying with a small volume of colloidal silver solution were more desirable than one-time spraying with a large volume because silver particles tend to aggregate when they are dried. Therefore, the parameters for spraying were optimized as

100 μL/min flow rate with 12.5 μL of spraying volume, and 8 sets of spraying and air-drying were performed for each plant sample. The distance between the nebulizer tip and the sample was 12.4 cm and the area covered by colloidal silver on the sample plate was 4.5 cm^2. Spraying onto the leaf was performed without moving the sample plate because leaf sizes are much smaller than the spray area.

Plant sample preparation for gas chromatography-mass spectrometry. Twenty five flowers or whole leaves of a plant were collected and weighed. An aliquot of internal standard hexadecane was added to the surface of the plant material. The plant material was completely immersed in chloroform for 60 s. The cuticular wax was extracted and dried under nitrogen gas. Samples were derivatized using BSTFA/TCMS (65˚C, 30 min) for GC/MS analysis. 3 replicates of leaves and flowers were prepared.

Mass spectrometry. For LDI mass spectral profiling and imaging, a Thermo Finnigan LTQ linear ion trap mass spectrometer equipped with vMALDI source (Mountain View, CA) was used. Fiber-optic guided nitrogen laser (337 nm, maximum energy of 280 μJ/pulse, and maximum frequency of 20 Hz) was used as a laser source. The laser spot size was 100 μm at the target plate surface. The intermediate-pressure (0.17 Torr) sampling environment was kept by nitrogen gas flow control and this allows softer ionization compared to high vacuum environments (~10^{-6} Torr). All mass spectra were collected in the positive-ion mode and the scanning range was set to *m/z* 200 to *m/z* 1000.

For unknown peaks acquired directly from plant samples, peak identification was carried out by matching monoisotopic masses with those detected from GC-MS experiment. For overlapped peaks due to two stable silver isotopes and similar monoisotopic masses, the major compounds detected were determined by comparing the first generation product ion spectra from unknown peaks with those from standards or from literature data.

GC-MS analysis was performed with an Agilent 6890 GC interfaced to a 5973 mass spectrometer (Agilent Technologies). A HP-5ms column (30 m x 0.25 mm i.d. coated with a

0.25 μm film, Agilent Technologies) was used, and temperature gradient was programmed from 80 to 320 °C at 5°C/min with He flow rate at 2.2 mL/min. Operating parameters were set to 70 eV (electron ionization) for ionization voltage and 280 °C for interface temperature. The GC-MS data files were deconvoluted by NIST AMDIS software, and searched against our laboratory's standard compounds library and the NIST compounds library.

LDI Mass spectra collection for profiling and imaging. For leaves and flower parts, the number of laser shots and the laser intensity scale were examined by collecting mass spectra in a small area (usually 5 to 10 rastering points) by turning on the automatic gain control feature (AGC, which keeps the ion amounts in the trap at a similar range by varying the number of laser shots) of the mass spectrometer. After optimizing the laser parameters, a fixed number of laser shots without AGC was used for collecting mass spectra over the whole sample. For whole flower imaging, however, varying numbers of laser shots that were controlled by AGC were applied because each flower part has different surface characteristics and wax loads which can affect ion yields. The sample was scanned with a step size which ranged from 50 μm to 100 μm.

Mass spectral images for whole flowers were processed by using the custom software from Thermo (ImageQuest 1.0). The normalized intensity value which is defined as the fractional peak intensity compared to the total ion current (TIC) of each mass spectrum was used for presentation of chemical abundance information. The mass window was set to 0.8 Da – 1.0 Da. For comparing relative abundances among samples, intensities relative to the peak intensity at *m/z* 215.8 ($[^{107}Ag + {}^{109}Ag]^+$) were used.

Results and Discussion

Silver-LDI mass spectral profiling of metabolites from Arabidopsis leaves. Figure 2 shows the averaged silver-LDI mass spectrum taken from an *Arabidopsis thaliana* wild type (Ler) leaf surface. As shown in the inset of Figure 2, the Ag_2^+ ion at *m/z* 215.8

corresponding to $[^{107}Ag + ^{109}Ag]^+$ showed the highest intensity, and this was consistent through all mass spectra collected under our experimental conditions. Therefore, the relative intensity with respect to the peak intensity at *m/z* 215.8 was used as the intensity scale for quantification purposes in interpreting the mass spectra of wax compounds.

Because two stable isotopes of silver are present with similar abundances (^{107}Ag: 51.839 % and ^{109}Ag: 48.161 %), each hydrocarbon compound produces a quartet of silver adduct peaks. This quartet pattern helped to distinguish sample peaks from noise, but the multiple peaks induced spectral complexity due to the overlap of compounds different by 2 Da in molecular weight. As shown in Figure 2, peaks with odd nominal masses were the major peaks for the cuticular wax compounds because intensities of the two other isotopic peaks (due to either ^{13}C or ^{2}H) were much smaller in the mass range where cuticular wax compounds were detected. Therefore, only peaks with odd nominal masses will be discussed in this article to simplify the interpretation of the mass spectra. From the mass spectra collected from *Arabidopsis* plants, it was hard to identify individual quartet peaks directly due to overlap, but the *m/z* ranges which have signals from cuticular wax compounds were easily grouped as shown in Table 1.

In Table 1, it is obvious that wax load amounts from parallel GC-MS analysis and the sum of relative intensities from silver-LDI mass spectra according to *m/z* ranges have a similar tendency but are not in direct proportion. There are several reasons for this phenomenon. One of the main reason is the sampling depth by LDI is shallower than that by the current chemical extraction protocol for GC-MS analysis. Therefore, the silver-LDI mass spectral profile directly from cuticular wax surfaces does not represent all the cuticular wax compounds. The shallower sampling depth by LDI may bear the possibility of serial profiling of cuticular wax compounds according to the depth of the wax layer. For example, plant sterols and triterpenoids were extracted and constituted about 6 % (~1.5 μmol/g per fresh weight) of the total wax load. With colloidal silver, plant sterol standards were detected with

a very low detection limit, ~200 amol/10000 μm^2 (sampling area of the laser). However, there was no sterol species detected in the LDI mass profiles obtained directly from leaf surfaces. This indicates that there may be no plant sterols at the outermost epicuticular wax surface. In addition, as previously reported [22], there are differences in ionization efficiencies of the wax compounds depending on their functional groups. Therefore, it is difficult to relate observed intensities directly to actual amounts of wax compounds. In silver-LDI MS, wax standards which have 18 - 32 carbons showed good peak reproducibility in terms of intensities but compounds which have smaller carbon number, such as C_{16} fatty acid, showed relative intensity variations depending on laser intensities and concentrations. Similar to the previous report [22], alkanes showed the smallest ionization yields and fatty acids showed the highest ionization yields for the same molar amount. This observation seems to be consistent in the wax compound profile. In Table 1, the relative amounts were higher in LDI than those in GC for *m/z* regions which contain fatty acid species such as *m/z* 475 - 477, 503 - 505 and 557 - 561, and the relative abundances were much lower in LDI than those in GC for *m/z* regions where major alkanes are present, such as *m/z* 515-519 and 543-547. Finally, the relative extraction efficiencies for the different classes of compounds in the GC-MS protocol are not constant.

Despite overlaps due to silver isotopes and similar molecular weights, many of the wax compounds in Table 1 can be recognized independently by focusing on one of two silver isotope adduct ion peaks. In the *m/z* range of 571-575, for example, C_{33} alkane and C_{32} alcohol ion species overlapped each other at m/z 573 as [C_{33} alkane $+ {}^{109}Ag]^+$ and [C_{32} alcohol + $^{107}Ag]^+$, but each was uniquely detected at *m/z* 571 as [C_{33} alkane $+ {}^{107}Ag]^+$ and at *m/z* 575 as [C_{32} alcohol + $^{109}Ag]^+$, respectively. However, isobaric ions such as C_{29} alkane and C_{28} aldehyde cannot be distinguished under the current experimental conditions and the major compounds found in LDI MS among isobaric ions need to be identified putatively by examining fragmentation patterns in their first generation product ion mass spectra. There,

for ion species which contain long chain fatty acids such as *m/z* 503, 559 and 587 or 589, losses of water (18 Da) and formic acid (46 Da) were always observed predominantly with very similar ratios to those observed from fatty acid standards. This may be because of the high ionization efficiency of fatty acids, but it may also suggest that fatty acids are localized at the outer cuticular wax layer. For the ion species at *m/z* 515 and 543 which contain major alkanes, the fragmentation patterns matched well with those of alkane standards. In spite of the low ionization efficiency of alkanes, they can be easily detected because the molar amounts of alkanes in the GC-MS analysis are about 20 to 30 fold higher than isobaric aldehydes. However, the inability to detect aldehydes separately under the current experimental conditions (because the reduction steps from fatty acids to aldehydes cannot be traced by this method) is the main limitation of the silver-LDI MS method. Accurate mass measurement with high mass resolution could be the solution for this problem. Also, as indicated in Table 1, unidentified contaminants showed peaks at *m/z* 533-537. Therefore, abundance information of C_{28} fatty acid could not be extracted unambiguously from silver-LDI mass spectra.

Finally, there were several unknown wax compounds detected in *m/z* 585 – 673. Two groups of unknown ion species were found in this *m/z* range (annotated as 'Unk-A' and 'Unk-B' in Table 1). Unk-A was detected at *m/z* 585, 613, 641, and 669 as ^{107}Ag adduct ions and Unk-B was detected at *m/z* 597, 625, and 653. Ions in each group are 28 Da away from each other and this difference corresponds to a C_2H_4 group. For Unk-B, losses of multiples of 42 Da, which could correspond to propene, were observed and either single loss or quadruple loss of 42 Da was found as a major fragment ion. For Unk-A, the product ion spectra were very complicated due to overlap with minor unknown ions.

Comparison of leaf cuticular waxes between wild-type (Ler) and *cer*2 mutant. Based on parallel GC-MS cuticular wax results and putative identification of the major contributing compounds within overlapped isobaric species by tandem MS experiments, wax

metabolites that were detected with confidence were summarized in Table 2. For wild-type (Ler) and *cer*2 mutant, the relative intensities by silver-LDI MS and the amounts quantified by GC-MS for corresponding wax metabolites were also shown in Table 2. Ratios of the wax metabolites were calculated and presented as $\log_2$(*cer*2/Ler) values in Figure 3. From Table 2 and Figure 3, several observations could be summarized. First, all alkanes were detected with significantly lower intensities or lower amounts from *cer*2 mutant leaves by both methods. Second, differences in the amounts of primary alcohols between wild-type and *cer*2 mutant were less significant than among other classes of compounds in both methods. Third, from the silver-LDI MS results, C_{24} and C_{26} fatty acids showed significantly smaller intensities in *cer*2 than in wild-type, but longer chain length fatty acids, C_{30} and C_{32} fatty acids, were found as more abundant in *cer*2 than wild-type leaves. In GC-MS analysis, however, all fatty acids showed a small increase in *cer*2 mutant. This may also suggest the possibility of differential integration of fatty acids according to the depth of the cuticular wax layer. Discussions about the function of the *cer*2 gene product are given in the last section by combining the observations above with the results from flower parts.

Silver-LDI mass spectral imaging of Arabidopsis whole flower. For demonstrating mass spectral imaging as a rapid metabolite profiling tool, a flower was chosen among Arabidopsis plant organs because flowers are composed of several sub-parts that have small dimensions, such as carpel, petal, sepal, and stamen. Mass spectral images of wild-type (Ler) flowers are shown in Figure 4. Because different flower organs have different surface characteristics and wax loads, the total ion current (TIC), which is directly affected by ion yields, varies among the flower organs. Therefore, all chemically-selective images for whole flowers were processed as a normalized intensity defined as the fractional peak intensity compared to the TIC of each mass spectrum. In Figure 4, the ion species at *m/z* 529, which mainly corresponds to [C_{29} ketone + $^{107}Ag]^+$, was found as highly localized at the flower stem and the carpel. Major alkane species, such as [C_{29} alkane + $^{107}Ag]^+$ and [C_{31}

alkane + ^{107}Ag]$^{+}$ at *m/z* 515 and 543, respectively, were found at all three organs as the major species but they showed relatively low abundances in the tips of petals. Two major wax compounds, C_{31} alkane and C_{30} alcohol, contribute to mass signals in the *m/z* range 543 – 547. Both wax compounds contributed the intensity at *m/z* 545 as [C_{31} alkane + ^{109}Ag]$^{+}$ and [C_{30} alcohol + ^{107}Ag]$^{+}$. This overlapped image was clearly separated into two images by choosing different silver isotope ions, i.e. [C_{31} alkane + ^{107}Ag]$^{+}$ at *m/z* 543 and [C_{30} alcohol + ^{109}Ag]$^{+}$ at *m/z* 547, as shown in Figure 4. From the images for *m/z* 543 and 547, it is clear that the intensity at the petals and at the center part of the sepals for *m/z* 545 is mainly from C_{31} alkane, not C_{30} alcohol. At the tips of petals, fatty acids ([$C_{18:3}$ fatty acid + ^{107}Ag]$^{+}$ and [C_{26} fatty acid + ^{107}Ag]$^{+}$ at *m/z* 385 and 503, respectively) were found at higher amounts than other wax compounds.

For comparing wax compositions between wild-type (Ler) and *cer*2 mutant, serial mass spectral images were generated with a 0.8 Da mass window and a 2.0 Da step size for the *m/z* ranges where wax compounds were detected, and chemically selective images for four *m/z* values that showed distinct differences between wild-type (Ler) and *cer*2 mutant were shown in Figure 5(A). In figure 5(A), it is obvious that C_{29} alkane and C_{29} ketone ([C_{29} alkane + ^{107}Ag]$^{+}$ and [C_{29} ketone + ^{107}Ag]$^{+}$ at *m/z* 515 and 529, respectively) showed much lower abundances in *cer*2 mutant than in wild-type. In contrast, C_{30} and C_{32} fatty acids ([C_{30} fatty acid + ^{107}Ag]$^{+}$ and [C_{32} fatty acid + ^{109}Ag]$^{+}$ at *m/z* 559 and 589, respectively) showed higher abundances in *cer*2 mutant than in wild-type. Interestingly, as clearly visualized in Figure 5(B), both fatty acids showed high abundances at the tip of the petal, while in the carpel only C_{30} fatty acid was found in high abundance.

Silver-LDI mass spectral profiling of Arabidopsis flower parts. Imaging whole flowers can provide information about wax load variations between wild-type and mutants with localization information in a very short time, but there are also limitations. Even if whole flowers are flattened and attached onto the mass spectrometer sample plate with extra

care, overlaps among flower organs cannot be avoided. In addition, the degree of wax variation between wild-type and mutants was hard to recognize accurately by processing images with normalized intensities. Therefore, profiling wax compounds with individual flower parts and comparing their mass profiles based on relative intensities to the reference peak at m/z 215.8 ($[^{107}Ag + {}^{109}Ag]^+$) were more desirable. Three major parts of Arabidopsis flowers, carpels, petals, and sepals were prepared separately and mass spectra were collected serially from these parts with a 50 μm step movement. The averaged mass spectra for three flower parts of wild-type (Ler) and its *cer*2 mutant are shown in Figure 6 and more detailed peak identifications with abundances for these flower parts are listed in Table 3. In contrast to leaf wax profiling, peak identification was more straightforward because fewer silver adduct ion peaks were observed per flower part. Also, the major silver adduct ion peak pattern was a quartet which corresponds to only one wax compound. As discussed previously, the relative intensities for each class of compounds are different. In particular, intensities corresponding to fatty acids were significantly higher. Therefore, to assess the total wax loads between wild-type and mutants, comparing the sum of intensities from C_{27} or higher alkanes, that are known to be the most abundant wax metabolites [3], is more appropriate than comparing the total intensities from all classes of wax metabolites. As shown in Table 3, the sum of intensities from C_{27}, C_{29}, and C_{31} alkanes was higher in wild-type than in *cer*2 mutant throughout all three flower parts. Therefore, it is obvious that a global reduction of wax loads in *cer*2 mutant exists. However, for carpels and petals, C_{31} alkane showed a higher abundance in *cer*2 mutant than in wild-type.

In the carpel (Figure 6(A) and Table 3(A)), C_{29} alkane at *m/z* 515 and C_{29} ketone at *m/z* 529 were detected as the major wax metabolites in wild-type (Ler), as expected from the whole flower imaging results. However, in *cer*2 mutant, the relative intensities for these metabolites were lower by about 5.5 fold. In contrast, the relative intensity for C_{30} fatty acid at *m/z* 559 was higher by about 4.0 fold in *cer*2 mutant. In the petal (Figure 6(B) and Table

3(B)), peaks corresponding to $C_{18:3}$, C_{24}, C_{26} fatty acids (at *m/z* 385, 475, and 503, respectively) and C_{29} alkane at *m/z* 515 showed high abundances in wild-type (Ler). However, in *cer*2 mutant, the relative intensities for all major peaks in wild-type (Ler) were lower by more than 2.6 fold. In contrast, the longer fatty acids, C_{30} and C_{32} at *m/z* 559 and 589, showed about 4.8 fold higher intensities for *cer*2 mutant. In the sepal, (Figure 6(C) and Table 3(C)), C_{29} and C_{31} alkanes and C_{28} and C_{30} alcohol were detected as major peaks in wild-type (Ler) and the wax metabolite profile was similar to that from the leaf. In the *cer*2 sepal, the major differences from the wild-type sepal were lower intensities for C_{29} alkane (~ 6.5 fold), C_{29} ketone (~ 3.5 fold), and C_{26} fatty acid (~ 5.7 fold). However, C_{30} fatty acid and alcohol showed increases in the *cer*2 sepal. Interestingly, unknown wax metabolites were detected for both wild-type and mutant at the sepal and showed lower abundances in the *cer*2 mutant. GC-MS wax metabolite profiling for the whole flower were performed and results are shown in Figure 7. The major difference from GC-MS wax metabolite profile for leaves was that no aldehydes were detected in whole flower analysis.

It should be noted that at least 75 whole flowers (25 flowers per sample and 3 replicates) were needed to get reproducible wax metabolite profiles from GC-MS, whereas, in silver-LDI MS profiling, only 5 flowers were used for collecting the wax metabolite profiles of each kind of flower part.

To compare the variations of each wax metabolite, ratios of metabolites in wild-type(Ler) and *cer*2 mutant flower parts were presented in Figure 8. Several features from silver-LDI MS could be summarized and compared with GC-MS results. First, C_{30} and C_{32} fatty acids showed higher abundances in *cer*2 mutant than in wild-type for all flower parts. The increase in C_{30} fatty acid was most pronounced in the petal in terms of both intensities and ratios. This increase was also observed in whole-flower analysis by GC-MS. However, similar to the results from leaf analysis, C_{24} and C_{26} fatty acids were lower in amounts from silver-LDI MS for all *cer*2 mutant flower parts whereas they were at about the same level or

even higher amounts from GC-MS of *cer*2 mutant flowers. Second, C_{29} ketone was obviously lower in all *cer*2 mutant flower parts and the decrease was the largest at the carpel in terms of both intensities and ratios. The decrease in C_{29} ketone was also seen in GC-MS results. Third, for primary alcohols, their changes were less obvious than the other classes of wax compounds for flower parts. This was also consistent with GC-MS results. Fourth, C_{27} and C_{29} alkanes were significantly lower in *cer*2 mutant flowers. However, C_{31} alkane showed the smallest decrease in ratio at *cer*2 sepals and even increased in *cer*2 carpels and petals. In GC-MS results, C_{31} alkane showed the smallest change in ratio among alkane species. It should be emphasized that GC-MS results are from whole flower waxes and not from a single organ. Therefore, differential wax load changes from flower part to flower part cannot be recognized by GC-MS experiments.

Prediction of regulation of wax synthesis by *cer*2 gene product. By combining the observations from leaves and flower parts with known cuticular wax biosynthetic pathways for *Arabidopsis thaliana*, we propose that *cer2* mutation may be involved either in the C_{30} fatty acid to C_{30} aldehyde reduction pathway, as had previously suggested for *cer13* by Rashotte *et al.* [16], or in the C_{30} aldehyde to C_{29} alkane decarbonylation pathway. Because aldehydes were not readily detected from flower parts, deciding between the two pathways mentioned above was not possible based only on silver LDI MS profiling. Similar to wax load changes of *cer13* mutant stems ([16], levels of C_{29} products, C_{29} alkane and C_{29} ketone, were lower and levels of C_{30} primary alcohol are higher in *cer2* mutant for all flower parts and leaves. This is also consistent with GC-MS results. . In addition, accumulation of C_{32} fatty acid was observed in petals which may be caused by further elongation of the accumulated C_{30} fatty acid. However, increases of C_{31} alkane amounts were only observed in carpels and petals but not in sepals and leaves. The degrees of increases for C_{30} fatty acid in *cer2* mutants were much larger in carpels (~4 fold) and petals (~4.8 fold) than in leaves (~1.2 fold) and sepals (~1.4 fold), so lower amounts of subsequent elongation from C_{30} to C_{32} fatty

acid can be expected in sepals and leaves. Therefore, the relatively smaller amounts of C_{30} fatty acid in *cer2* sepals and leaves may not compensate for the general wax load reduction in *cer*2 mutants and cause decreases in C_{31} alkanes in *cer2* sepals and leaves. However, there is also the possibility of differential regulation of elongation from C_{30} to C_{32} fatty acid by *cer*2 gene product according to flower parts and leaves that is similar to differential regulation between the stem and the leaf [10].

Conclusions

Wax metabolite profiling by LDI MS with colloidal silver as a matrix has several advantages over GC- MS approaches. First, sample preparation is much simpler because it does not require any extraction and derivatization steps. Second, the amounts of samples required are about 20 to 25 times smaller than those in GC-MS. Third, localization information of cuticular waxes can be preserved because of the direct sampling capability. With the use of homogeneous colloidal silver coating on plant surfaces, wax metabolite distributions on each flower part was successfully profiled for the first time. However, there are still challenging issues in this method. Overlap due to isobaric ions, especially alkanes and aldehydes, needs to be resolved to provide more accurate measurements of changes in wax profiles. It may be solved by employing exact mass measurements with high mass resolution. In addition, different ionization efficiencies for different class compounds make it difficult to compare actual abundances between two different classes of wax metabolites directly from the mass spectra. This may be resolved by systematic studies on response factors as a function of metabolite classes and sizes. Last, because a mass spectral database of metabolites for silver LDI-MS does not exist currently, identification of wax compounds is less certain than GC-MS.

By performing reproducible spraying of colloidal silver solution onto the plant sample surface by the finely-controllable spraying device, homogeneous and constant surface

coverage of colloidal silver particles was achieved. This made it possible to use the intensity of silver dimer ions as a reference to normalize all mass spectra. In this way, comparison of the relative wax abundances between wild-type and mutants was successfully made. Wild-type/mutant wax profile comparisons based on silver-LDI MS results generally showed good agreement with those based on GC-MS results. However, major variance was present between the two methods, especially for C_{26} and smaller fatty acids. It may be because of sampling depth differences and further investigation is needed to identify this bias.

Lastly, a data processing scheme for the rapid comparison between wild-type and mutant can be proposed as shown in Figure 9. The basic idea involves two general rules. First, the two largest peaks in a quartet pattern have about the same intensities because of the similar natural abundances of the two silver isotopes. Second, changes in the two adjacent peaks should be similar if only one metabolite is associated with this change. Figure 9 shows the potential of the silver-LDI MS method as a high-throughput mutant screening tool. Future work would involve verification of this scheme with a larger data set.

Acknowledgement

E.S.Y. thanks the Robert Allen Wright Endowment for Excellence for support. The Ames Laboratory is operated for the U.S. Department of Energy by Iowa State University under Contract No. DE-AC02-07CH11358. This work was supported by the Director of Science, Office of Basic Energy Sciences, Division of Chemical Sciences.

Table 1. Possible wax compounds in *Arabidopsis thaliana* wild type (Ler) leaves according to mass-to-charge ratio ranges where wax compounds were detected by silver-LDI MS

m/z range	Possible ion species [a]	Wax load[c] (nmol/g fresh weight)	LDI Relative Intensity (%)[e]
361-365	$C_{16:1}$ fatty acid (361) $C_{16:0}$ fatty acid (363) Unknown contaminant (363)	245.83 ± 39.88 455.39 ± 108.81 [d]n.a.	[f]4.45 ± 0.53
385-393	$C_{18:3}$ fatty acid (385) $C_{18:2}$ fatty acid (387) $C_{18:1}$ fatty acid (389) $C_{18:0}$ fatty acid (391)	[d]n.d. 87.74 ± 18.10 571.67 ± 102.37 119.34 ± 41.54	14.18 ± 0.36
475-477	C_{24} fatty acid (475)	28.74 ± 3.64	9.85 ± 1.09
487-491	C_{27} alkane (487) C_{26} aldehyde (487) C_{26} alcohol (489)	1141.48 ± 46.00 33.13 ± 2.37 171.47 ± 27.50	15.63 ± 1.41
503-505	C_{26} fatty acid (503) C_{27} iso-alcohol (503)	92.45 ± 19.20 18.88 ± 2.50	20.33 ± 2.19
515-519	C_{29} alkane (515) C_{28} aldehyde (515) C_{28} alcohol (517)	8242.73 ± 148.85 403.24 ± 13.63 412.27 ± 47.53	35.97 ± 1.37
529-535	C_{29} ketone (529) C_{28} fatty Acid (531) C_{29} iso-alcohol (531) Unknown contaminant (533)	19.95 ± 1.69 260.95 ± 18.01 11.53 ± 0.58 n.a.	[f]8.38 ± 0.18
543-547	C_{31} alkane (543) C_{30} aldehyde (543) C_{30} alcohol (545)	9014.37 ± 378.82 313.13 ± 21.62 118.37 ± 22.01	32.79 ± 1.56
559-561	C_{30} fatty acid (559) C_{31} iso-alcohol (559)	12.41 ± 2.52 17.76 ± 1.48	6.07 ± 0.29
571-575	C_{33} alkane (571) C_{32} aldehyde (571) C_{32} alcohol (573)	3420.03 ± 170.57 132.80 ± 13.35 59.83 ± 6.86	20.50 ± 1.33
585-589	Unk-A1(585) C_{32} fatty acid (587)	6.63 ± 1.02	6.28 ± 0.23
597-603	Unk-B1(597)[b] C35 alkane (599) C34 alcohol (601)	n.a. 123.05 ± 17.23 3.79 ± 0.43	14.13 ± 0.77
613-617	Unk-A2 (613) C_{34} fatty acid (615)	n.a. 4.38 ± 0.41	4.56 ± 0.29
625-629	Unk-B2 (625)	n.a.	12.00 ± 1.14
641-645	Unk-A3 (641)	n.a.	5.74 ± 0.01
653-657	Unk-B3 (653)	n.a.	6.14 ± 0.47
669-673	Unk-A4 (669)	n.a.	4.70 ± 0.87

a. Cuticular wax compounds (nominal *m/z* values of ^{107}Ag adduct ions) listed are from identified compounds in parallel GC-MS analysis.
b. Unk: Unknown ion species. Unknown species were grouped by fragmentation patterns in their first generation product ion spectra.
c. Wax load values are from GC-MS for three replicates with ± standard error
d. n.a. : not applicable, n.d.: not detected
e. Relative intensity (%) is defined as the fractional intensity of the intensity at *m/z* 215.8 which corresponds to $[^{107}Ag + ^{109}Ag]^+$, and the values are listed with ± standard error.
f. Due to the overlap with unknown contaminants, only the relative intensity at *m/z* 361 was used for *m/z* 361-365 and only relative intensities at *m/z* 529 and 531 were included for *m/z* 529-535.

Table 2. Major cuticular wax compounds with their abundances in *Arabidopsis thaliana* leaves of wild-type (Ler) and *cer*2 mutant

Class		$[M + Ag]^+$	Major ion species	Silver LDI (R.I., %)[a]		GC (nmol/g fresh weight)[b]	
				Ler	*cer*2	Ler	*cer*2
Alkane	C_{27}	487.3	$[C_{27}$ alkane $+ {}^{107}Ag]^+$	6.38 ± 0.69	2.17 ± 0.23	1141.48 ± 46.00	364.72 ± 23.42
	C_{29}	515.4	$[C_{29}$ alkane $+ {}^{107}Ag]^+$	10.63 ± 0.39	3.48 ± 0.33	8242.73 ± 148.85	1011.67 ± 53.85
	C_{31}	543.4	$[C_{31}$ alkane $+ {}^{107}Ag]^+$	12.65 ± 0.99	7.00 ± 0.28	9014.37 ± 378.82	2202.02 ± 95.96
	C_{33}	571.4	$[C_{33}$ alkane $+ {}^{107}Ag]^+$	7.37 ± 0.66	3.71 ± 0.12	3420.03 ± 170.57	132.70 ± 8.32
	C_{35}	599.4	$[C_{35}$ alkane $+ {}^{107}Ag]^+$	5.47 ± 0.51	3.33 ± 0.02	123.05 ± 17.23	11.10 ± 0.59
Alcohol	C_{26}	491.3	$[C_{26}$ alcohol $+ {}^{109}Ag]^+$	2.63 ± 0.43	2.97 ± 0.60	171.47 ± 27.50	242.22 ± 20.44
	C_{28}	519.4	$[C_{28}$ alcohol $+ {}^{109}Ag]^+$	9.01 ± 1.08	7.24 ± 0.64	412.27 ± 47.53	268.81 ± 46.16
	C_{30}	547.4	$[C_{30}$ alcohol $+ {}^{109}Ag]^+$	5.25 ± 0.33	9.04 ± 0.95	118.37 ± 22.01	132.73 ± 20.22
	C_{32}	575.4	$[C_{32}$ alcohol $+ {}^{109}Ag]^+$	4.01 ± 0.49	5.31 ± 0.44	59.83 ± 6.86	15.69 ± 1.72
	C_{34}	603.4	$[C_{34}$ alcohol $+ {}^{109}Ag]^+$	1.26 ± 0.14	2.39 ± 0.09	3.79 ± 0.43	5.33 ± 0.66
Fatty acid	C_{24}	475.3	$[C_{24}$ fatty acid $+ {}^{107}Ag]^+$	5.35 ± 0.80	2.74 ± 0.16	28.74 ± 3.64	48.11 ± 6.96
	C_{26}	503.3	$[C_{26}$ fatty acid $+ {}^{107}Ag]^+$	10.95 ± 1.62	3.48 ± 0.33	92.45 ± 19.20	223.87 ± 20.64
	C_{30}	559.4	$[C_{30}$ fatty acid $+ {}^{107}Ag]^+$	3.71 ± 0.23	4.67 ± 0.10	12.41 ± 2.52	18.80 ± 2.07
	C_{32}	589.4	$[C_{32}$ fatty acid $+ {}^{109}Ag]^+$	1.16 ± 0.13	2.50 ± 0.10	6.63 ± 1.02	11.04 ± 1.50
Ketone	C_{29}	529.4	$[C_{29}$ ketone $+ {}^{107}Ag]^+$	2.64 ± 0.13	1.42 ± 0.07	19.95 ± 1.69	20.12 ± 2.01

a. Relative intensity (R.I.) (%) is defined as the fractional intensity of the intensity at *m/z* 215.8 which corresponds to $[{}^{107}Ag + {}^{109}Ag]^+$ and the values are listed with ± standard error for three replicates.

b. Wax load values are from GC-MS with ± standard error for three replicates

Table 3. Major cuticular wax metabolites detected for each flower part by silver-LDI MS for *Arabidopsis thaliana* wild-type (Ler) and *cer*2 mutant.

Table 3(A) Carpel

Class		$[M + Ag]^+$	ion species	R. I.(Ler) (%)	R. I.(*cer*2) (%)	Log_2(*cer*2/Ler)
Alkane	C_{29}	515.4	$[C_{29}$ alkane $+ {}^{107}Ag]^+$	16.20 ± 0.31	2.93 ± 0.18	-2.47 ± 0.08
	C_{31}	543.4	$[C_{31}$ alkane $+ {}^{107}Ag]^+$	3.64 ± 0.09	5.84 ± 0.84	0.68 ± 0.18
Alcohol	C_{28}	519.4	$[C_{28}$ alcohol $+ {}^{109}Ag]^+$	3.60 ± 0.17	2.03 ± 0.05	-0.83 ± 0.06
	C_{30}	547.4	$[C_{30}$ alcohol $+ {}^{109}Ag]^+$	2.85 ± 0.17	3.04 ± 0.43	0.09 ± 0.19
	C_{32}	575.4	$[C_{32}$ alcohol $+ {}^{109}Ag]^+$	2.52 ± 0.36	2.19 ± 0.82	-0.20 ± 0.48
Fatty acid	$C_{18:3}$	385.3	$[C_{18:3}$ fatty acid $+ {}^{107}Ag]^+$	3.24 ± 0.18	3.01 ± 0.70	-0.11 ± 0.29
	C_{24}	475.3	$[C_{24}$ fatty acid $+ {}^{107}Ag]^+$	2.60 ± 0.09	1.24 ± 0.12	-1.06 ± 0.12
	C_{30}	559.4	$[C_{30}$ fatty acid $+ {}^{107}Ag]^+$	1.86 ± 0.19	7.37 ± 1.09	1.99 ± 0.22
Ketone	C_{29}	529.4	$[C_{29}$ ketone $+ {}^{107}Ag]^+$	21.48 ± 0.98	4.22 ± 0.67	-2.35 ± 0.20

Table 3(B) Petal

Class		[M + Ag]$^+$	ion species	R. I.(Ler) (%)	R. I.(*cer*2) (%)	Log$_2$(*cer*2/Ler)
Alkane	C_{27}	487.3	[C_{27} alkane + ^{107}Ag]$^+$	2.91 ± 0.20	2.07 ± 0.14	-0.48 ± 0.12
	C_{29}	515.4	[C_{29} alkane + ^{107}Ag]$^+$	15.87 ± 1.03	6.10 ± 0.89	-1.38 ± 0.18
	C_{31}	543.4	[C_{31} alkane + ^{107}Ag]$^+$	6.63 ± 0.37	8.97 ± 0.73	0.44 ± 0.12
Alcohol	C_{26}	491.3	[C_{26} alcohol + ^{109}Ag]$^+$	2.24 ± 0.06	3.07 ± 0.40	0.45 ± 0.16
	C_{28}	519.4	[C_{28} alcohol + ^{109}Ag]$^+$	4.88 ± 0.17	3.48 ± 0.26	-0.49 ± 0.10
	C_{30}	547.4	[C_{30} alcohol + ^{109}Ag]$^+$	2.56 ± 0.39	3.32 ± 0.13	0.38 ± 0.19
	C_{32}	575.4	[C_{32} alcohol + ^{109}Ag]$^+$	1.93 ± 0.36	2.77 ± 0.34	0.52 ±0.26
Fatty acid	$C_{18:3}$	385.3	[$C_{18:3}$ fatty acid + ^{107}Ag]$^+$	30.04 ± 2.24	5.40 ± 0.80	-2.48 ± 0.20
	C_{24}	475.3	[C_{24} fatty acid + ^{107}Ag]$^+$	8.45 ± 0.58	2.99 ± 0.24	-1.50 ± 0.13
	C_{26}	503.3	[C_{26} fatty acid + ^{107}Ag]$^+$	15.63 ± 1.03	4.17 ± 0.48	-1.91 ± 0.16
	C_{30}	559.4	[C_{30} fatty acid + ^{107}Ag]$^+$	3.87 ± 0.22	18.68 ± 2.41	2.27 ± 0.17
	C_{32}	589.4	[C_{32} fatty acid + ^{109}Ag]$^+$	0.80 ± 0.10	4.25 ± 0.68	2.41 ± 0.24
Ketone	C_{29}	529.4	[C_{29} ketone + ^{107}Ag]$^+$	3.38 ± 0.26	2.22 ± 0.05	-0.60 ± 0.10
Unknown		625.5	[Unk-B2 + ^{107}Ag]$^+$	6.42 ± 0.39	3.64 ± 0.79	-0.81 ± 0.27
		669.5	[Unk-A4 + ^{107}Ag]$^+$	3.33 ± 0.29	2.14 ± 0.43	-0.64 ± 0.26

Table 3(C) Sepal

Class		$[M + Ag]^+$	ion species	R. I.(Ler) (%)	R. I.(*cer*2) (%)	Log_2(*cer*2/Ler)
Alkane	C_{27}	487.3	$[C_{27}$ alkane $+ {}^{107}Ag]^+$	1.99 ± 0.16	0.74 ± 0.03	-1.42 ± 0.11
	C_{29}	515.4	$[C_{29}$ alkane $+ {}^{107}Ag]^+$	19.28 ± 1.65	2.98 ± 0.17	-2.69 ± 0.12
	C_{31}	543.4	$[C_{31}$ alkane $+ {}^{107}Ag]^+$	11.25 ± 1.60	6.91 ± 0.14	-0.70 ± 0.17
Alcohol	C_{26}	491.3	$[C_{26}$ alcohol $+ {}^{109}Ag]^+$	1.78 ± 0.13	2.34 ± 0.14	0.39 ± 0.12
	C_{28}	519.4	$[C_{28}$ alcohol $+ {}^{109}Ag]^+$	7.64 ± 0.72	5.82 ± 0.27	-0.39 ± 0.12
	C_{30}	547.4	$[C_{30}$ alcohol $+ {}^{109}Ag]^+$	6.85 ± 0.74	11.93 ± 1.22	0.80 ± 0.18
Fatty acid	$C_{18:3}$	385.3	$[C_{18:3}$ fatty acid $+ {}^{107}Ag]^+$	5.77 ± 2.00	2.45 ± 0.52	-1.23 ± 0.49
	C_{24}	475.3	$[C_{24}$ fatty acid $+ {}^{107}Ag]^+$	2.95 ± 0.56	1.31 ± 0.13	-1.17 ± 0.26
	C_{26}	503.3	$[C_{26}$ fatty acid $+ {}^{107}Ag]^+$	4.39 ± 0.91	0.76 ± 0.05	-2.53 ± 0.26
	C_{30}	559.4	$[C_{30}$ fatty acid $+ {}^{107}Ag]^+$	4.13 ± 0.33	6.54 ± 0.88	0.66 ± 0.19
Ketone	C_{29}	529.4	$[C_{29}$ ketone $+ {}^{107}Ag]^+$	5.07 ± 0.76	1.43 ± 0.29	-1.82 ± 0.30
Unknown		625.5	[Unk-B2 $+ {}^{107}Ag]^+$	4.60 ± 0.96	1.61 ± 0.29	-1.52 ± 0.33
		669.5	[Unk-A4 $+ {}^{107}Ag]^+$	2.21 ± 0.71	0.59 ± 0.13	-1.90 ± 0.47

References

(1) Nawrath, C. *Current Opinion in Plant Biology* **2006**, *9*, 281-287.

(2) Heredia, A. *Biochimica Et Biophysica Acta-General Subjects* **2003**, *1620*, 1-7.

(3) Samuels, L.; Kunst, L.; Jetter, R. *Annual Review of Plant Biology* **2008**, *59*.

(4) Koornneef, M.; Hanhart, C. J.; Thiel, F. *Journal of Heredity* **1989**, *80*, 118-122.

(5) Rashotte, A. M.; Jenks, M. A.; Ross, A. S.; Feldmann, K. A. *Planta* **2004**, *219*, 5-13.

(6) Xia, Y. J.; Nicolau, B. J.; Schnable, P. S. *Plant Cell* **1996**, *8*, 1291-1304.

(7) Xia, Y. J.; Nikolau, B. J.; Schnable, P. S. *Plant Physiology* **1997**, *115*, 925-937.

(8) Hannoufa, A.; McNevin, J.; Lemieux, B. *Phytochemistry* **1993**, *33*, 851-855.

(9) McNevin, J. P.; Woodward, W.; Hannoufa, A.; Feldmann, K. A.; Lemieux, B. *Genome* **1993**, *36*, 610-618.

(10) Jenks, M. A.; Tuttle, H. A.; Eigenbrode, S. D.; Feldmann, K. A. *Plant Physiology* **1995**, *108*, 369-377.

(11) Jenks, M. A.; Rashotte, A. M.; Tuttle, H. A.; Feldmann, K. A. *Plant Physiology* **1996**, *110*, 377-385.

(12) Jenks, M. A.; Tuttle, H. A.; Feldmann, K. A. *Phytochemistry* **1996**, *42*, 29-34.

(13) Rashotte, A. M.; Jenks, M. A.; Nguyen, T. D.; Feldmann, K. A. *Phytochemistry* **1997**, *45*, 251-255.

(14) Lai, C.; Kunst, L.; Jetter, R. *Plant Journal* **2007**, *50*, 189-196.

(15) Goodwin, S. M.; Rashotte, A. M.; Rahman, M.; Feldmann, K. A.; Jenks, M. A. *Phytochemistry* **2005**, *66*, 771-780.

(16) Rashotte, A. M.; Jenks, M. A.; Feldmann, K. A. *Phytochemistry* **2001**, *57*, 115-123.

(17) Dutta, T. K.; Harayama, S. *Analytical Chemistry* **2001**, *73*, 864-869.

(18) Kuhn, G.; Weidner, S.; Just, U.; Hohner, G. *Journal of Chromatography A* **1996**, *732*, 111-117.

(19) Pruns, J. K.; Vietzke, J. P.; Strassner, M.; Rapp, C.; Hintze, U.; Konig, W. A. *Rapid*

Communications in Mass Spectrometry **2002**, *16*, 208-211.

(20) Yalcin, T.; Wallace, W. E.; Guttman, C. M.; Li, L. *Analytical Chemistry* **2002**, *74*, 4750-4756.

(21) Chen, R.; Li, L. *Journal of the American Society for Mass Spectrometry* **2001**, *12*, 367-375.

(22) Sluszny, C.; Yeung, E. S.; Nikolau, B. J. *Journal of the American Society for Mass Spectrometry* **2005**, *16*, 107-115.

Figure Captions

Figure 1. Arabidopsis flower samples prepared on a LDI target plate for silver-LDI mass spectral profiling and imaging.

Figure 2. Positive-ion mode silver-LDI mass spectrum taken from an *Arabidopsis thaliana* wild-type (Ler) leaf. Mass spectra from 12674 scanning points on the leaf were averaged. The inset is the expanded *m/z* range view which includes the groups of Ag_2^+ peaks (triplet around *m/z* 215.8) and Ag_3^+ peaks (quartet around *m/z* 322.8). The peak at *m/z* 215.8 which corresponds to the ion $[^{107}Ag + {}^{109}Ag]^+$ is always the predominant peak through all mass spectra collected under our experimental conditions.

Figure 3. Ratios of targeted cuticular wax metabolites in *Arabidopsis thaliana* wild-type (Ler) and *eceriferum* mutant (*cer*2) leaves. Ratios from silver-LDI MS (left) and GC-MS (right) analyses were scaled as $\log_2$ values. Data points in each colored box correspond to the compound class indicated in a box. The number of carbons is indicated for each data point. Detailed ion species assignments and their relative intensities from silver-LDI MS and amounts from GC-MS are listed in Table 2. Each silver-LDI MS and GC-MS analysis has 3 replicates and error bars correspond to standard errors are shown.

Figure 4. Chemically selective images of *Arabidopsis thaliana* wild-type (Ler) whole flowers. The step size for data collection was set to 50 μm for both x and y directions. Dimension of the image is 5550 μm high × 4960 μm wide. The value in each image corresponds to the nominal *m/z* value of the corresponding ions. All images were processed as normalized intensities and

shown as a percentage of the total ion current. All images were smoothed linearly. Major ions detected at *m/z* 529 correspond to $[C_{29}$ ketone + $^{107}Ag]^+$. Ions detected at *m/z* 515, 543 are mainly silver adduct ions of C_{29} and C_{31} alkanes. Ions at *m/z* 547 are from C_{30} alcohol, and the image for the peak at *m/z* 545 corresponds to the overlapped image of C_{31} alkane and C_{30} alcohol as $[C_{31}$ alkane + $^{109}Ag]^+$ and $[C_{30}$ alcohol + $^{107}Ag]^+$. Images for silver adduct ions of $C_{18:3}$ (at *m/z* 385), C_{26} fatty acids (at *m/z* 503), and an unknown compound (at *m/z* 625) are also shown.

Figure 5. (A) Chemically selective images of *Arabidopsis thaliana* wild-type (Ler*)* and *cer*2 mutant flowers. The step size for data collection was set to 50 μm for both x and y directions. Dimensions of the images for Ler and *cer*2 are 5550 μm high × 4960 μm wide and 4100 μm high × 4770 μm wide, respectively. C_{29} alkane (at *m/z* 515 as $[C_{29}$ alkane + $^{107}Ag]^+$) showed higher abundances mainly at sepals and carpels in the wild-type than in the *cer2* mutant. The localization of C_{29} ketone (at *m/z* 529 as $[C_{29}$ ketone + $^{107}Ag]^+$) at the carpel was easily recognized in the wild-type but not in the *cer2* mutant. Higher abundances of very long chain fatty acids such as C_{30} and C_{32} fatty acids (at *m/z* 559 as $[C_{30}$ fatty acid + $^{107}Ag]^+$ and at *m/z* 589 as $[C_{32}$ fatty acid + $^{109}Ag]^+$) were found in the *cer2* mutant. (B) 3D presentations of the normalized intensities of chemically selective images of C_{30} and C_{32} fatty acids (at *m/z* 559 and at *m/z* 589). The yellow arrows in (A) and (B) are for aligning the viewing angle. Both fatty acids showed high abundances in the tips of petals. C_{30} fatty acid showed high abundance in the carpel but C_{32} fatty acid did not.

Figure 6. Positive-ion mode silver-LDI mass spectrum taken from *Arabidopsis thaliana* wild-type (Ler) and *cer*2 mutant flower parts, (A) carpel, (B) petal, and (C) sepal (right). Each mass spectrum is the average of each flower part. The peak intensities were normalized to the reference peak (*m/z* 215.8 which corresponds to the ion $[^{107}Ag + {}^{109}Ag]^+$).

Figure 7. Whole flower cuticular wax profiles of *Arabidopsis thaliana* wild-type (Ler) and *eceriferum* mutant (*cer*2) by GC-MS. Each bar corresponds to the amount of a specific cuticular wax and the carbon numbers are indicated on x-axis. All values are scaled as nmol/g fresh weight with ± standard error. Because of the relatively high amounts of C_{29} alkane and ketone, they were scaled by a factor of 0.2 and 0.1, respectively. For values that exceed the y-axis range, the actual y-values are indicated adjacent to the corresponding bars.

Figure 8. Ratios of targeted cuticular wax metabolites in *Arabidopsis thaliana* wild-type (Ler) and *eceriferum* mutant (*cer*2) flower parts (carpel, petal, and sepal) by silver-LDI MS and whole flowers by GC-MS. Ratios were scaled as $\log_2$ values. Data points in each colored box correspond to the compound class indicated in the box. The number of carbons is indicated for each data point. Detailed ion species assignments and their relative intensities for the three flower parts were listed in Table 3. Each flower part has 5 replicates and error bars correspond to standard errors. Whole flower analysis by GC-MS has 3 replicates and the error bars correspond to standard errors.

Figure 9. Proposed data processing scheme of silver-LDI MS data for fast, high-throughput mutant screening. Sample plots shown were processed with

cuticular wax mass profiles from *Arabidopsis thaliana* wild-type (Ler) and *eceriferum* mutant (*cer*2) carpels.

Whole Flower Imaging

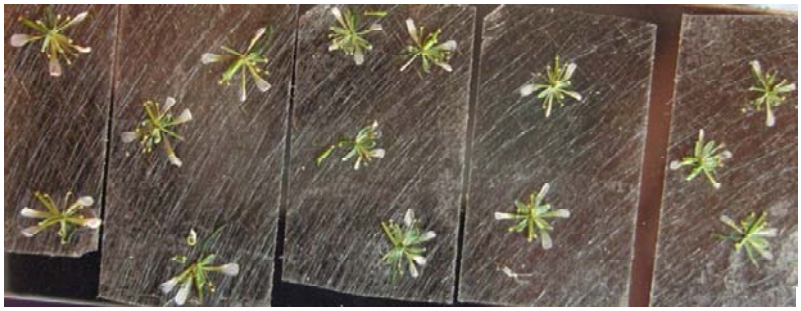

Flower Parts Profiling

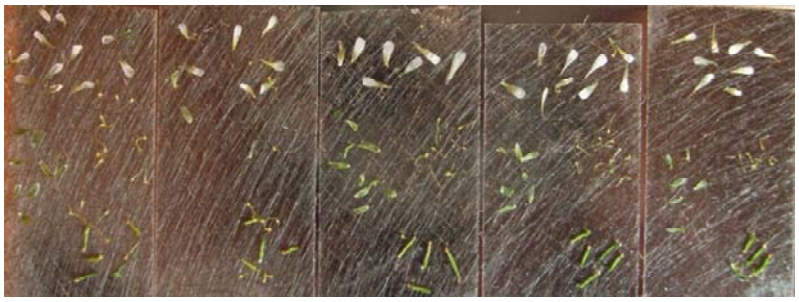

Figure 1.

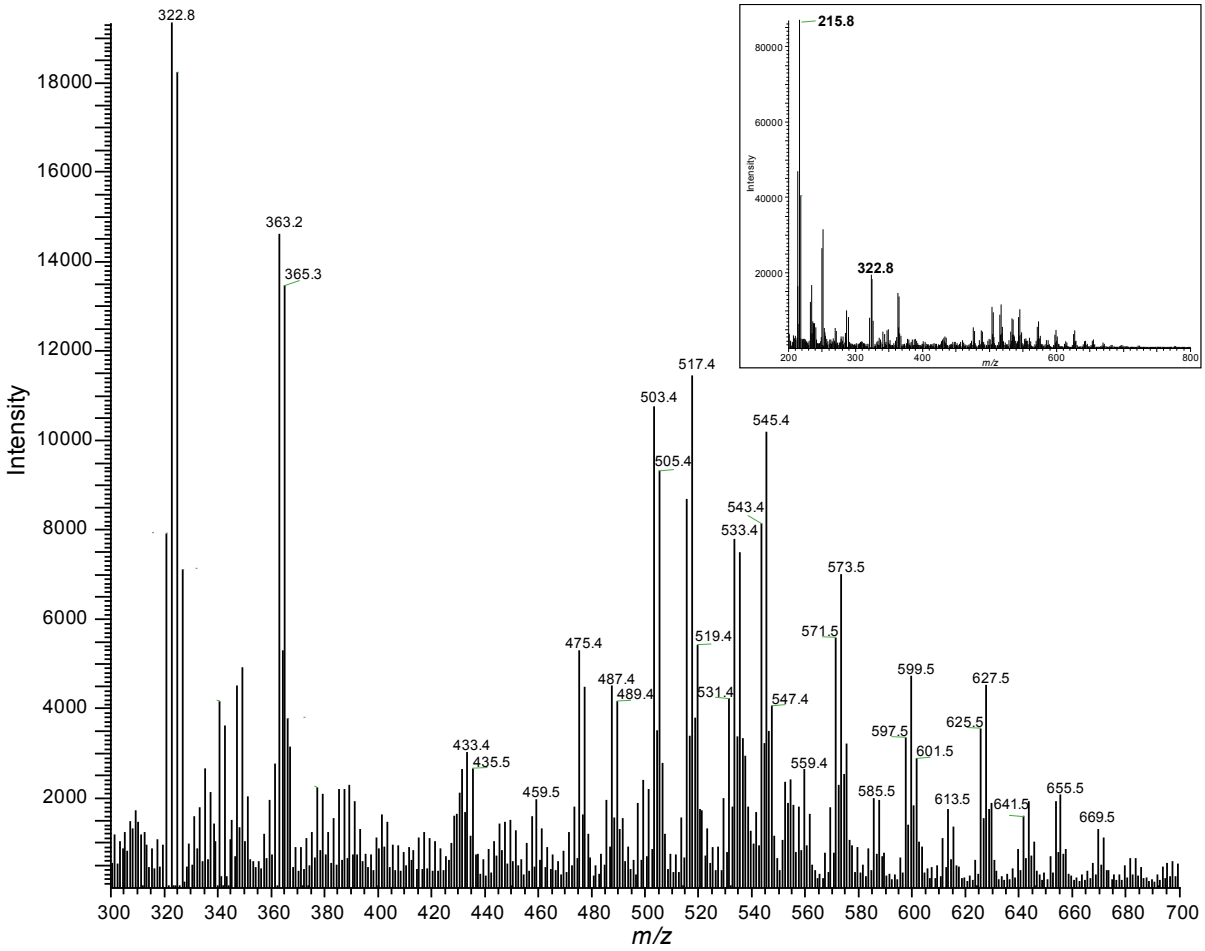
322.8
363.2
365.3
517.4
503.4
545.4
505.4
543.4
533.4
573.5
519.4
571.5
475.4
487.4
489.4
531.4
547.4
599.5
627.5
597.5
625.5
601.5
433.4
435.5
559.4
459.5
585.5
613.5
641.5
655.5
669.5
Intensity
m/z
215.8
322.8
Intensity
m/z

Figure 2.

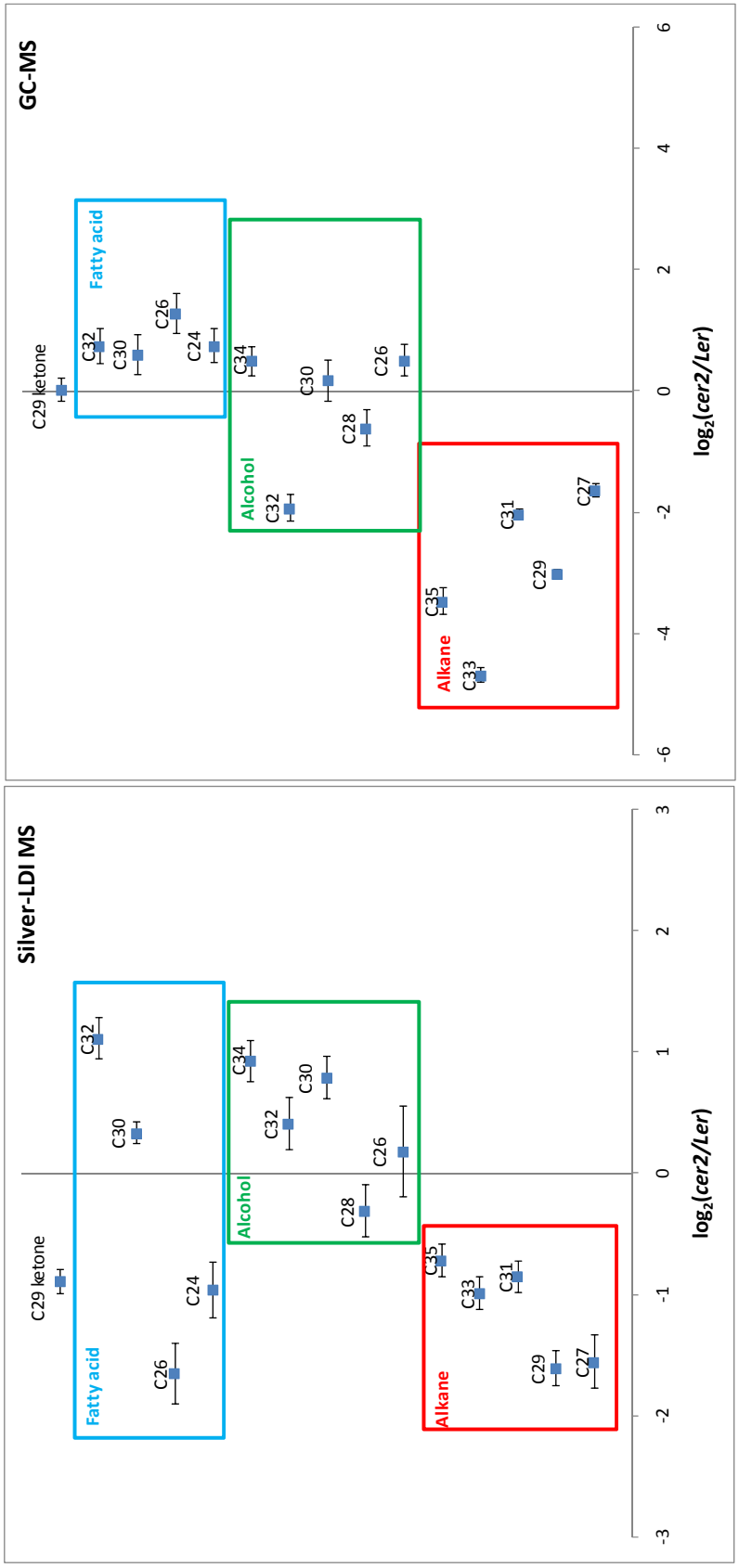
GC-MS
Fatty acid
Alcohol
Alkane
C29 ketone
C32
C30
C26
C24
C34
C28
C31
C27
C29
C35
C33
log2(cer2/Ler)
6
4
2
0
-2
-4
-6
Silver-LDI MS
3
1
-1
-3

Figure 3.

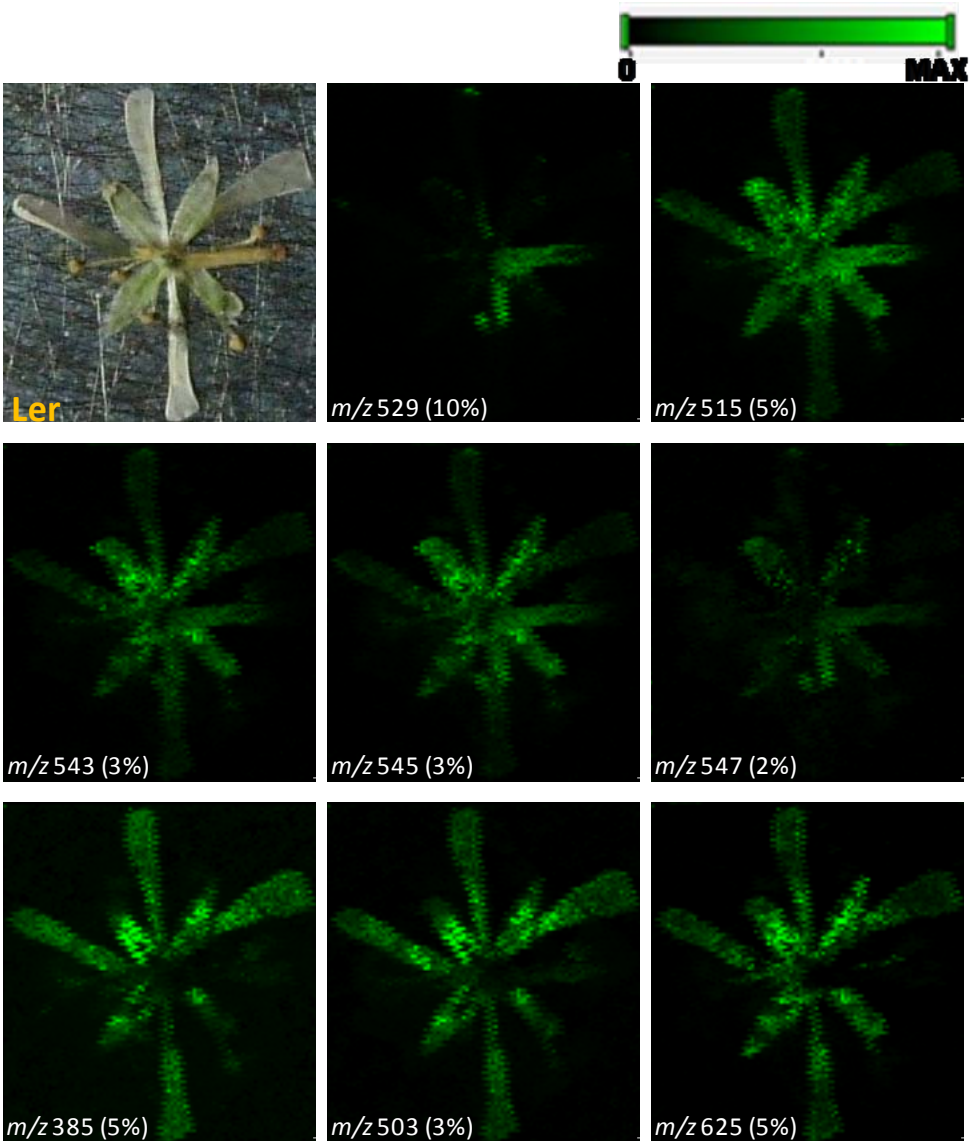
0
MAX
Ler
m/z 529 (10%)
m/z 515 (5%)
m/z 543 (3%)
m/z 545 (3%)
m/z 547 (2%)
m/z 385 (5%)
m/z 503 (3%)
m/z 625 (5%)

Figure 4.

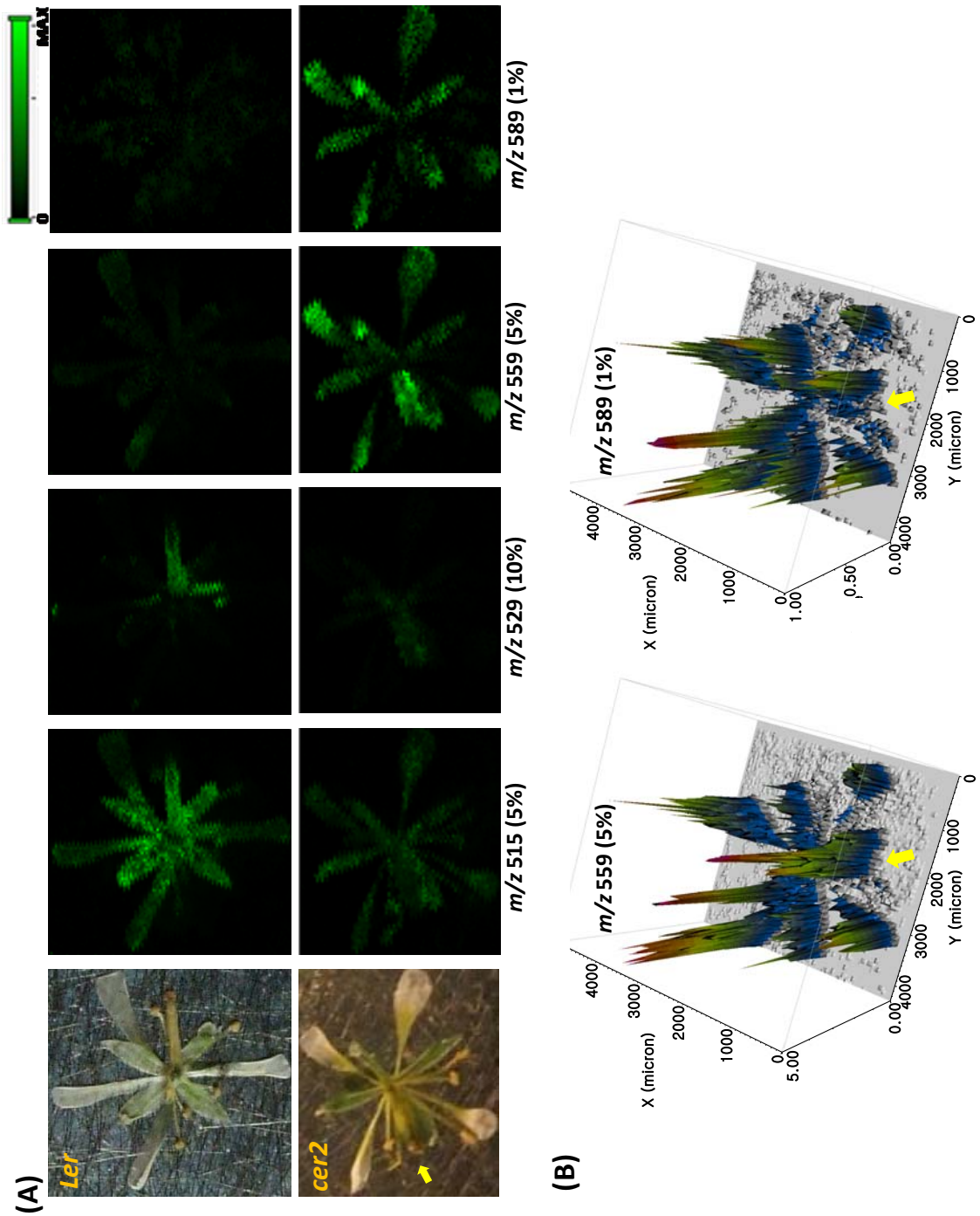
(A)
Ler
cer2
m/z 515 (5%)
m/z 529 (10%)
m/z 559 (5%)
m/z 589 (1%)
MAX
0
(B)
m/z 559 (5%)
m/z 589 (1%)
X (micron)
Y (micron)
0
1000
2000
3000
4000
5.00
1.00
0.50
0.00

Figure 5.

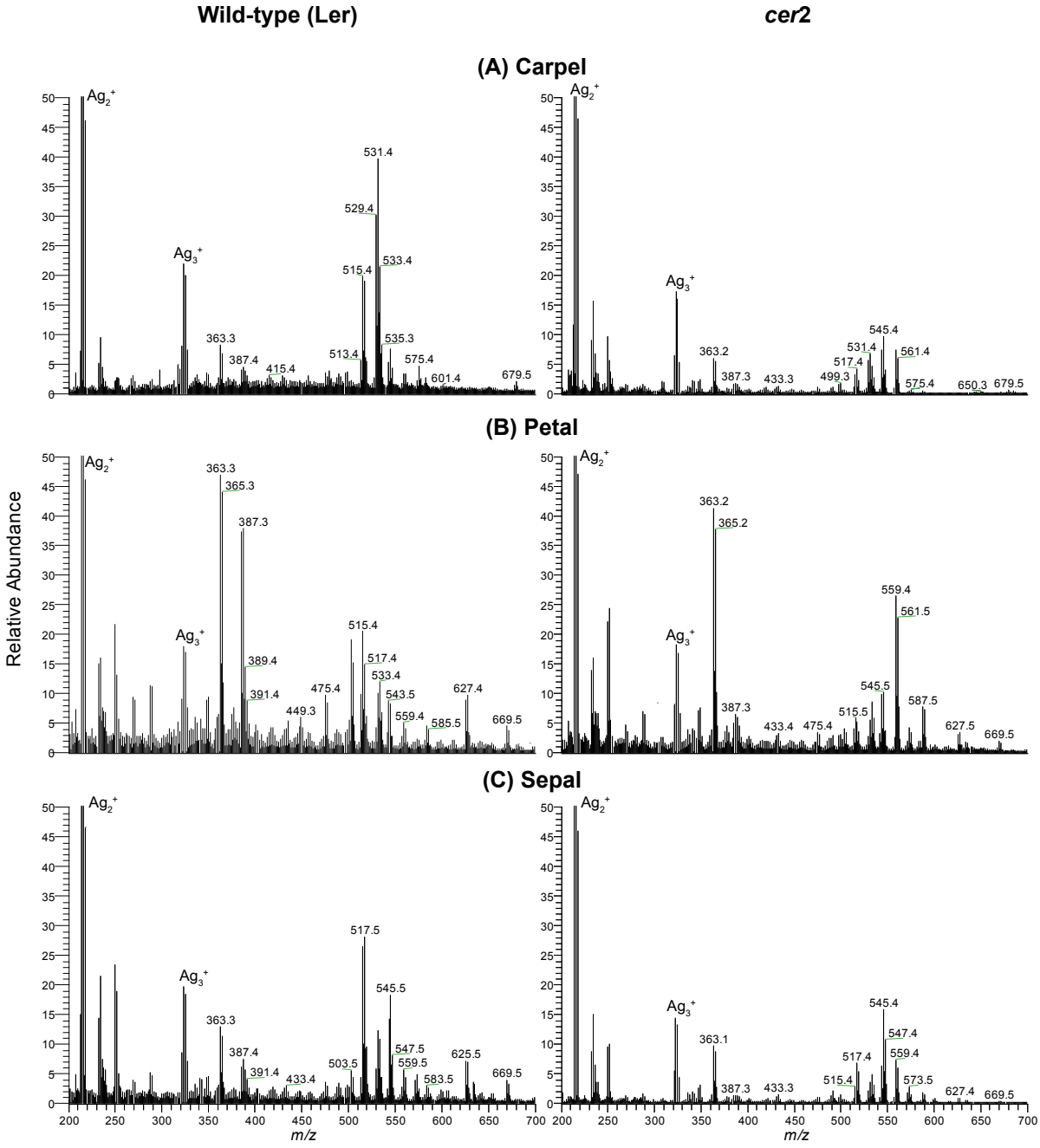
Wild-type (Ler)
cer2
(A) Carpel
(B) Petal
(C) Sepal
Relative Abundance
m/z
Ag2+
Ag3+

Figure 6.

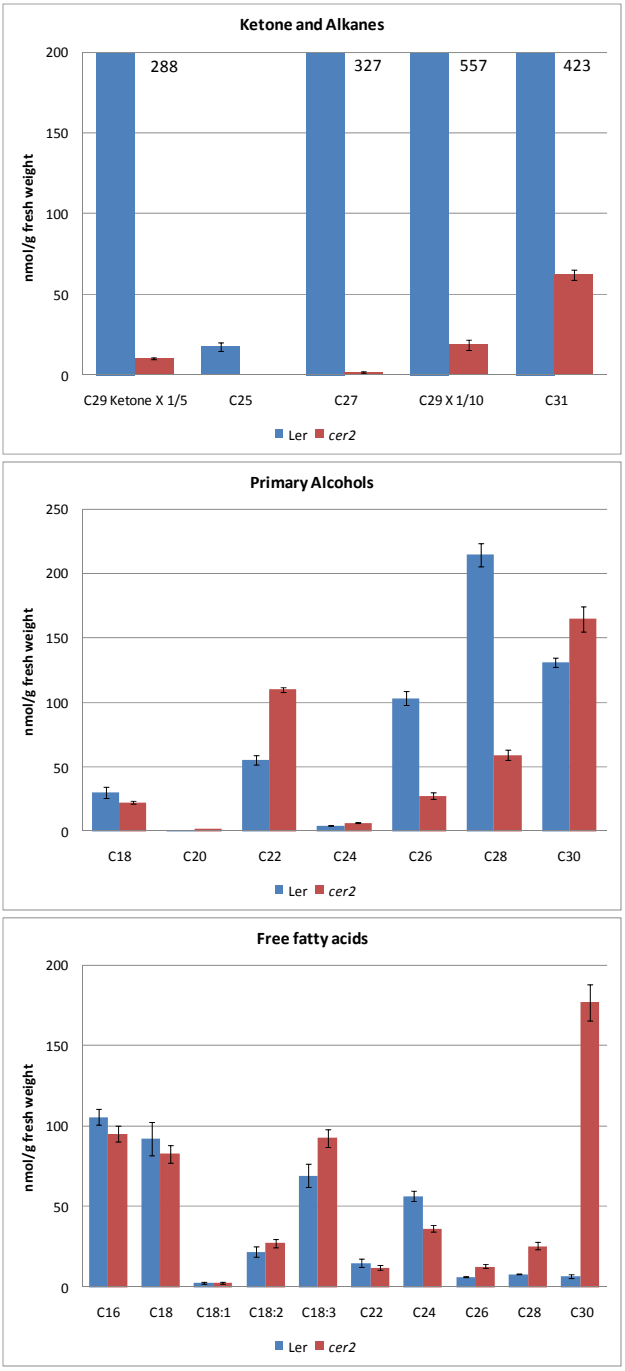
Ketone and Alkanes
nmol/g fresh weight
200
150
100
50
0
288
327
557
423
C29 Ketone X 1/5
C25
C27
C29 X 1/10
C31
Ler
cer2
Primary Alcohols
nmol/g fresh weight
250
200
150
100
50
0
C18
C20
C22
C24
C26
C28
C30
Ler
cer2
Free fatty acids
nmol/g fresh weight
200
150
100
50
0
C16
C18
C18:1
C18:2
C18:3
C22
C24
C26
C28
C30
Ler
cer2

Figure 7.

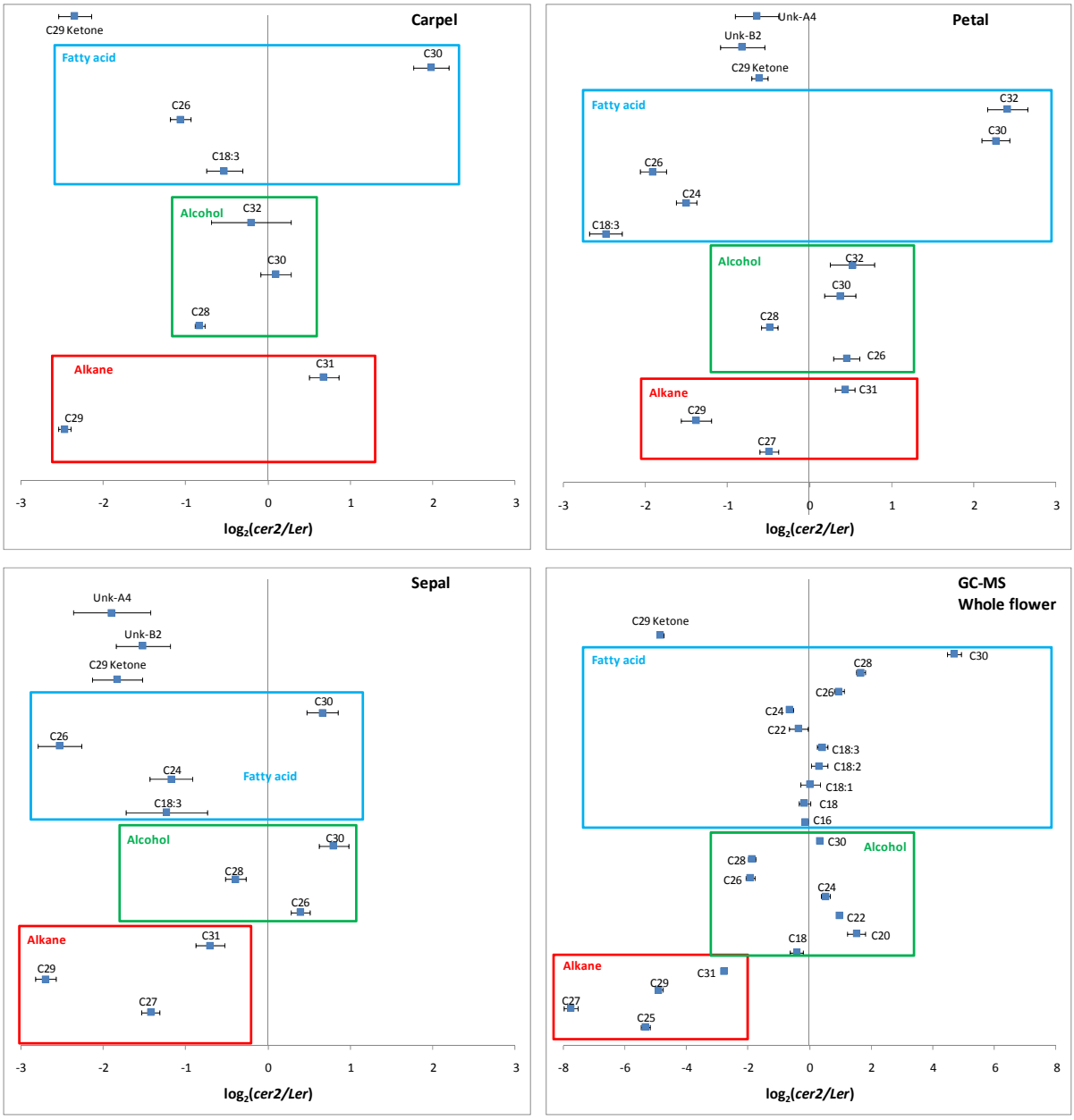
Carpel
C29 Ketone
Fatty acid
C30
C26
C18:3
Alcohol
C32
C30
C28
Alkane
C31
C29
-3 -2 -1 0 1 2 3
log2(cer2/Ler)
Petal
Unk-A4
Unk-B2
C29 Ketone
Fatty acid
C32
C30
C26
C24
C18:3
Alcohol
C32
C30
C28
C26
Alkane
C31
C29
C27
-3 -2 -1 0 1 2 3
log2(cer2/Ler)
Sepal
Unk-A4
Unk-B2
C29 Ketone
C30
C26
C24
Fatty acid
C18:3
Alcohol
C30
C28
C26
Alkane
C31
C29
C27
-3 -2 -1 0 1 2 3
log2(cer2/Ler)
GC-MS
Whole flower
C29 Ketone
Fatty acid
C30
C28
C26
C24
C22
C18:3
C18:2
C18:1
C18
C16
C30
Alcohol
C28
C26
C24
C22
C18
C20
Alkane
C31
C29
C27
C25
-8 -6 -4 -2 0 2 4 6 8
log2(cer2/Ler)

Figure 8.

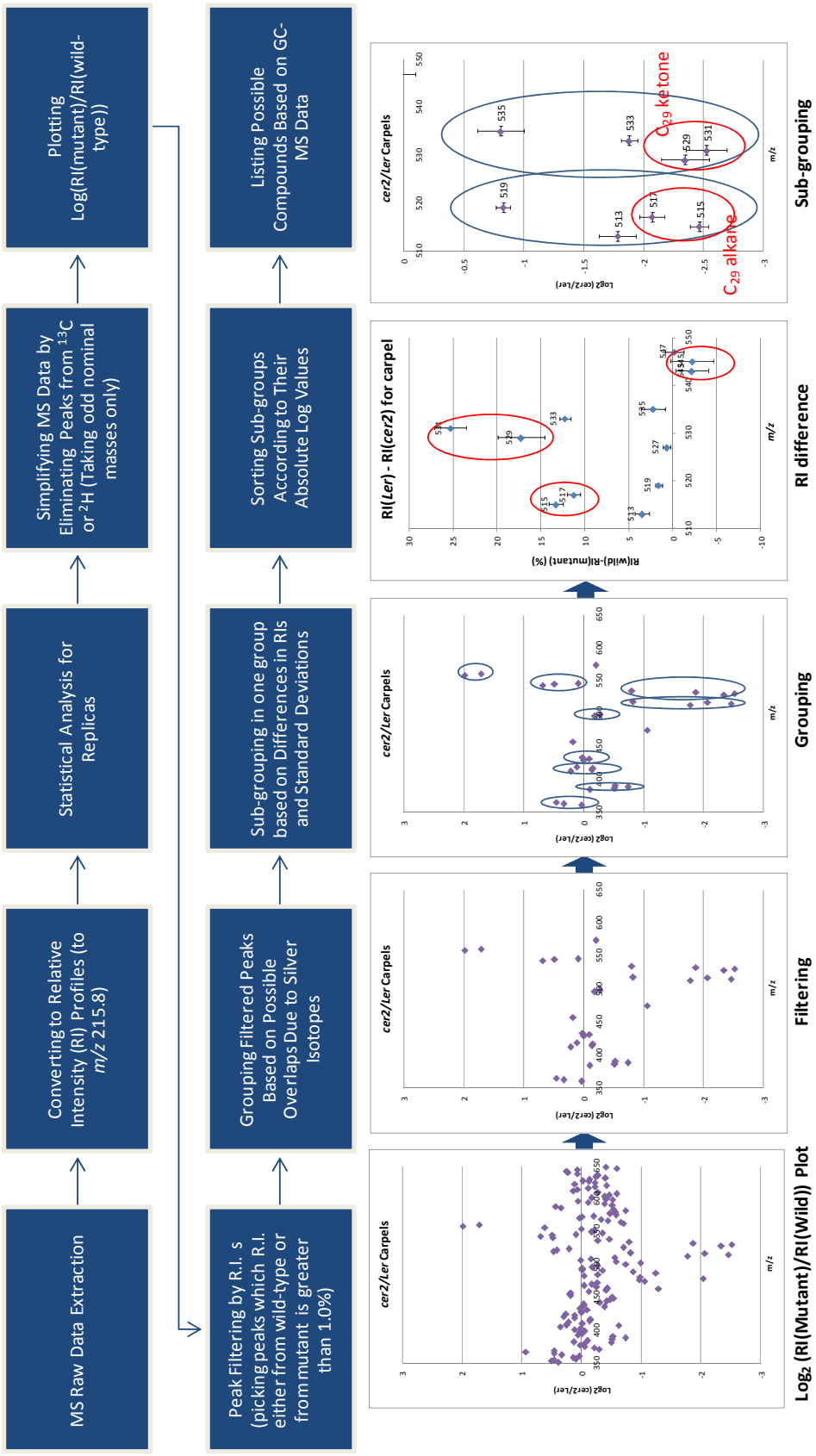
MS Raw Data Extraction
Converting to Relative Intensity (RI) Profiles (to m/z 215.8)
Statistical Analysis for Replicas
Simplifying MS Data by Eliminating Peaks from ^{13}C or ^{2}H (Taking odd nominal masses only)
Plotting Log(RI(mutant)/RI(wild-type))
Peak Filtering by R.I. s (picking peaks which R.I. either from wild-type or from mutant is greater than 1.0%)
Grouping Filtered Peaks Based on Possible Overlaps Due to Silver Isotopes
Sub-grouping in one group based on Differences in RIs and Standard Deviations
Sorting Sub-groups According to Their Absolute Log Values
Listing Possible Compounds Based on GC-MS Data
Log2 (RI(Mutant)/RI(Wild)) Plot
Filtering
Grouping
RI difference
Sub-grouping
cer2/Ler Carpels
RI(Ler) - RI(cer2) for carpel
C29 alkane
C29 ketone

Figure 9.

CHAPTER 5. COLLOIDAL SILVER LASER DESORPTION/IONIZATION MASS SPETROMETRY OF STEROLS AND DIRECT PROBING OF CHOLESTEROL ON ASTROCYTE CELL MONOLAYER

A paper prepared for submission to Rapid Communications in Mass Spectrometry

Sangwon Cha, Ksenija Jeftinija, Srdija Jeftinija, and Edward S. Yeung

Abstract

By using colloidal silver as a matrix, laser desorption/ionization mass spectrometric analysis of sterols was performed. Cholesterol and phytosterols were sensitively detected as silver adduct ions with little or no fragmentation. In-source dehydration difference depending on hydroxyl group orientation was observed. By spraying colloidal silver homogeneously onto the cell monolayer, cholesterol levels were probed directly from the cell monolayer surface. Protocol for assaying relative cholesterol abundances was developed. Based on the protocol, mass spectrometric assay of free cholesterol abundances depending on methyl beta-cyclodextrin(MβCD) treatment time was performed and their results were compared with results by traditional fluorometric cholesterol assay method. LDI MS protocol had simpler sample preparation and assay steps than the traditional method. Both methods showed the same trend of decreases in cholesterol level according to MβCD treatment time, but observed ratios of decreases were higher in silver-LDI protocol than in enzymatic fluorometry.

Introduction

Cholesterol is one of major components in cell membrane and is highly localized at lipid rafts in cell membrane. Cholesterol- and sphingolipids- rich lipid raft microdomains on cell membrane have numerous functions including organization of neurotransmitter signaling.[1] To explore their function and associated proteins, monitoring changes of neurotransmitters after disruption of lipid rafts is the common approach.[2] Disruption of lipid raft domain was mainly performed by inhibition of cholesterol synthesis or chemical removal of cholesterol.[2] Therefore, cholesterol level on cell membrane is a very important factor to understand signal transduction mechanism. For chemical removal of cholesterol, cyclodextrins which are cyclic oligosaccahrides having a lipophilic central cavity were used for capturing cholesterol molecules.[3, 4] Among those, methyl-ß-cyclodextrin (MβCD) has known to be the most effective capturing agent for cholesterol.[5] In addition, unusual cholesterol level in diseases such as Alzheimer's disease[6] and atherosclerosis[7] were found. Therefore, probing cholesterol level on cell membrane is also important to understand diseases.

Free cholesterol and cholesteryl esters from cultured cells are traditionally quantified by enzymatic fluorometry.[8-11] However, this fluorometric assay lacks an internal standard which could cause miscalculation of cholesterol content.[12] In addition, recovery of cholesterol after extracting and redissolving cellular lipids in various solvents was incomplete and the ratio of recovery also varied according to solvent compositions used.[13] Chromatographic separation techniques, such as thin layer chromatography (TLC)[14], gas chromatography(GC) and high performance liquid chromatography (HPLC)[15-19], have been also utilized for measuring cholesterol amounts from cell cultures or human serum.

By combining chromatographic separation techniques with a variety of mass spectrometric methodologies, identification as well as quantification of sterols has become more straightforward. In addition, tandem MS have made it possible to elucidate structures of

sterols. GC coupled with electron impact ionization MS has been used for typical analysis of sterols. GC-MS is sensitive and selective but chemical modification due to high temperature analysis condition and laborious derivatization steps are disadvantageous. HPLC were coupled with several ionization techniques. Among those, HPLC with atmospheric pressure chemical ionization (APCI) MS is the most popular method[20-22] whereas standard electrospray ionization (ESI) method is not efficient ionization methods for sterols[23]. Therefore, derivatization of sterols before spraying[24] and silver ion coordinated spraying[25] were demonstrated for effective ion generation through ESI in analysis of sterols and their esters.

Differently from ionization techniques mentioned above, beam-induced ionization techniques such as matrix-assisted laser desorption/ionization MS (MALDI MS) and seconday ion mass spectrometry (SIMS) have been used off-line for extract analysis. However, sensitivity of sterols in conventional MALDI MS was poor and most of sterols were detected as dehydrated molecules which could cause losses of structural information.[26] Recently, sterols were derivatized with Girad P hydrazine to Girad P hydrazones, and they were readily detected by conventional MALDI using α-cyano-4-hydroxycinammic acid as a matrix.[27] Time-of-flight (TOF)- SIMS was also used for identification of cholesteryl ester from HPLC lipid fractions.[12] Because sample was deposited on pre-etched silver target, cholesteryl esters were detected as silver adduct ions.[12]

However, beam-based techniques also have a capability of direct sampling from intact cells or tissues. Cholesterol in animal tissues or cells was directly detected by TOF-SIMS or MALDI MS[28-31]. In TOF-SIMS, surface metallization (metal enhanced-SIMS) by silver or gold enhanced secondary ion yields and metal adduct ions of cholesterol was predominantly detected in case of silver coating on sample surface.[28, 32] By scanning through cell or animal tissue surfaces, localization information of cholesterol was also obtained by

TOF-SIMS.[28-30] Recently, relative quantification of cholesterol for individual cells was successfully demonstrated by combining TOF-SIMS with *in situ* fluorescence microscopy.[33]

Recently, we first introduced aqueous silver colloidal solution as a matrix for LDI MS of various wax compounds.[34] Here we extend the use of colloidal silver matrix for analysis of sterols inspired by silver metallization in TOF SIMS and Ag^+ coordination ionspray MS. By using a colloidal silver matrix, mass spectral profiles for sterols were obtained and in-source dehydration patterns of them were investigated. In addition, direct probing free cholesterol level on *Astrocyte* cell monolayer was performed. Free cholesterol level on cell surfaces was manipulated by treating cell cultures with methyl-ß-cyclodextrin (MβCD). Relative cholesterol peak intensities to the reference peak ($[^{107}Ag + {}^{109}Ag]^+$) were used for estimating relative abundance of cholesterol on *Astrocyte* cell monolayer and results from LDI MS were compared with those from traditional enzymatic fluorometry.

Experimental Section

Materials and chemicals. Sterol standards were purchased from Steraloids Inc. (Newport, RI) and plant sterol mixture was obtained from Mattrya LLC (Pleasant Gap, PA). Colloidal suspension of silver (20 ppm) was purchased from Purest Colloids (Westhampton, NJ). The Amplex Red Cholesterol Assay Kit was from Molecular Probes (Eugene, OR). Earle's Balanced Salt Solution (EBSS), Dulbecco's Modified Eagle Medium (DMEM) high glucose, fetal bovine serum (FBS), and trypsin (0.25%) were purchased from Invitrogen (Carlsbad, CA). Papain was obtained from Sigma-Aldrich (St. Louis, MO). All other chemicals were obtained from Fisher Scientific (Fairlawn, NJ).

Mass spectrometer. A Thermo Finnigan LTQ linear ion trap mass spectrometer equipped with vMALDI source (Mountain View, CA) was used for mass spectral analysis. nitrogen laser pulses (337 nm, maximum energy of 280 μJ/pulse, and maximum frequency of 20 Hz) were introduced through the fiber optic cable with 200μm in diameter. The laser spot

size on the sample plate surface was about 100 μm in diameter. The pressure of the sampling chamber was kept at 0.17 Torr by nitrogen gas flow. All mass spectra were collected in the positive-ion mode.

Cell culture. Mix neuron-glia cultures from neonatal rat cerebral cortex were established as described. Cortexes from 3 newborn pups (1-3 days old) were freshly dissected and tissues were enzymatically treated in 2 mL of papain solution (1.54 mg/mL in EBSS) for 40 min at 37 °C. After washing tissues with EBSS, tissues were treated with trypsin inhibitor and mechanically dissociated in the DMEM medium (DMEM high glucose : heat-inactivated FBS : penicillin/streptomycin = 89 : 10 : 1 by volume) using pipettes. Cells were plated in the DMEM medium in culture flasks and maintained at 37 °C in a humidified 5% CO_2/95% air atmosphere. The cells were maintained by changing the medium every 2-3 days. The cultures were then shaken overnight (12 hours)at 260 rpm at 37 °C. Cultures enriched in type I astroglia were obtained by trypsinizing the attachedcells for 3 min. Trypsin was inactivated by adding 3 mL of the DMEM medium. Astrocytes were plated on poly-L-lysine (100 g/mL; MW 100,000)-coated glass coverslips or stainless steel plates. All experiments were performed on cells that have been in culture for 1 – 3 days after re-planting.

In vitro fluorometric assay of cholesterol. Astrocyte cells were seeded in a 96-well microplate at a density of 5×10^4 cells per well. Seeded cells were incubated in the DMEM medium for 24 hours. The cells were treated with 100 μL of 10mM MβCD solution with various time periods (0 to 60 minutes). After treatment, cells were washed with KPBS buffer and cellular lipids were extracted from the cells by adding 100 μL of hexane:2-propanol (3:2, v/v) solution. First extracts were transferred to the new 96-well microplate. The cellular lipids were re-extracted with an additional 50 μL of hexane:2-propanol (3:2, v/v) solution and these second extracts were transferred and merged to the first extracts. Solvents in extracts were evaporated under vacuum and cellular lipids were resuspended in 150 μL of phosphate buffer containing 0.1M potassium phosphate, pH 7.4, 50 mM NaCl, 5mM cholic

acid, and 0.1% Triton X-100 for 12 hours with shaking. Cellular free cholesterol content was quantified by using an Amplex Red Cholesterol Assay kit (Molecular Probes, Eugene, OR) without cholesterol esterase. Briefly, cholesterol in the cellular lipid extracts is oxidized by cholesterol oxidase to produce H_2O_2. In the presence of horseradish peroxidase, 10-acetyl-3,7-dihydoxyphenoxazine (Amplex Red) reacts with H_2O_2 and this reaction generates fluorescent resorufin quantitatively. If cholesterol esterase is present, cholesterol esters can be hydrolyzed to cholesterol. Fluorescence was measured with the fluorescence microplate reader (Spectra Max Gemini XS, Molecular Devices, Sunnyvale, CA) using excitation at 538 nm and emission at 590 nm. Cell residues were used for cellular protein quantification by the micro BCA protein assay kit (Pierce, Rockford, IL). The amount of cholesterol was normalized by the amount of cellular protein.

LDI mass spectrometric assay of cholesterol. Astrocyte cells were planted on a poly-L-lysine-coated stainless steel plate. Four spots of cell monolayer were formed on a stainless steel plate (25 mm × 75 mm). Each spot of cell monolayer had about 5×10^4 cells in an area of about 1.5 cm^2. After planting, cells were incubated in the DMEM medium for 24 hours. The cells then were treated with MβCD solution with various time periods (0 to 60 minutes). Immediately after MβCD treatment, all cell monolayers were fixed with 4% of paraformaldehyde solution for 30 min and transferred to KPBS buffer solution. Before spraying colloidal silver, cell monolayers were dried under moderate vacuum (~50 Torr).

Spraying of colloidal silver solution were performed by the home-built spraying device which is the combination of a computer-controlled syringe pump with a 500 μL syringe (Kloehm LTD., Las *Vegas*, NV), MicroFlow PFA-ST nebulizer (Elemental Scientific Inc., Omaha, NE) with a 0.25 mm i.d. sample uptake capillary, and a helium gas cylinder. Spraying action was controlled by the supplied software "WinPump®" by Kloehm. Six sets of spraying-drying processes were performed for each spot of cell monolayer with 100 μL/min flow rate and 12.5 μL of colloidal silver solution per spraying. Because the area

covered by colloidal silver on the sample plate was about 4.5 cm^2 which was larger than the spot of cell monolayer (~1.5 cm^2), spraying action was performed without moving the sample plate.

Based on optical images of cell monolayer spots which were acquired in the mass spectrometer, rastering areas were selected and scanned with a 100 μm movement. Five laser shots were used to obtain the mass spectrum for one scanning point. For one spot of cell monolayer, 485 mass spectra from different scanning points were collected and then averaged. From averaged mass spectra, intensity values of cholesterol silver adduct ion peaks (at *m/z* 493.5 and 495.5) were extracted and normalized as relative intensities to the reference peak at *m/z* 215.8 ($[^{107}Ag + {}^{109}Ag]^+$). These relative intensities were used for calculating abundances of free cholesterol in cell monolayer. Four replicas of cell monolayers were used for each MβCD treatment.

Results and Discussion

Silver-LDI mass spectral profiles of sterols. In silver-LDI MS, cholesterol (5-cholesten-3β-ol) was mostly detected as silver adduct ions at *m/z* 493-496 and showed a quartet of peaks with two major peaks because of the two silver isotopes ($[M + {}^{107}Ag]^+$ at *m/z* 493 and $[M + {}^{109}Ag]^+$ at *m/z* 495). Detection limit for cholesterol was ~ 50 pg per sample spot. However, for high concentration of cholesterol standards (> ~50 ng/sample spot), dehydrated cholesterol silver adduct ions ($[M - H_2O + Ag]^+$) were also detected at *m/z* 475-478 with a constant laser fluence (Figure 1(a)). In Figure 1, one interesting observation was that dehydration ions were not found in the mass spectrum of its isomer, 5-cholesten-3α-ol (Figure 1(b)). In addition, with high laser fluence, dehydroxylated silver adduct ions ($[M - OH + Ag]^+$) were observed for 5-cholesten-3β-ol but not for 5-cholesten-3α-ol. This difference could not be recognized in conventional MALDI MS because only dehydrated ions were observed for both alpha- and beta- hydroxyl group positions. The explanation for

this difference in dehydroxylation or dehydration has not been reported. As shown in Figure 3, an efficient orbital overlap between beta-hydroxy and adjacent alkene group may have stabilizing effects of the intermediates in either dehydroxyation or dehydration (Figure 2). In addition, the other possible explanation is that beta-hydroxy and adjacent alkene group are geometrically aligned well with the hydrogen orbital group at the allylic position and therefore this may facilitate *syn* elimination of water (Figure 2).

Figure 3 shows silver-LDI mass spectrum of major phytosterol mixture. As shown in Figure 3, sterols which are 2 Da different in molecular weight were overlapped due to two stable silver isotopes. In other words, the peak at *m/z* 507 was from both [Brassicasterol + $^{109}Ag]^+$ and [Campesterol + $^{107}Ag]^+$. Similarly, [Stigmasterol + $^{109}Ag]^+$ and [β-Sitosterol + $^{107}Ag]^+$ are associated to the peak at *m/z* 521. However, their intensities could be individually measured by choosing the other silver isotope adduct ion (Figure 3).

LDI mass spectrometric assay of cholesterol on cell monolayer. With colloidal silver spraying on cell monolayer, surface cholesterol was directly probed. Silver-LDI mass spectrum directly taken from an *Astrocyte* cell monolayer spot was shown in Figure 4. As shown in Figure 4, silver adduct ions of cholesterol and dehydrated cholesterol were readily detected at *m/z* 493 - 496 and at *m/z* 475 – 478 directly from an *Astrocyte* cell monolayer spot. For obtaining mass spectral profiles directly from the cell monolayer on poly-L-lysine coated stainless steel surface, about 20 % ~ 30 % higher laser intensity was needed compared to that needed for standard sterol or sterol extract analysis. This may cause higher ratio of dehydrated cholesterol ions. The peak corresponding to the silver dimer ion at *m/z* 215.8 ($[^{107}Ag + ^{109}Ag]^+$) was predominant under our silver spraying condition and this was consistent through mass spectra from all individual scanning points on both control and MβCD-treated cell monolayers. In addition, the relative intensities of cholesterol on one cell monolayer with respect to the peak intensity at *m/z* 215.8 were consistent with a less than 10 % of relative standard deviation. Therefore, the fractional peak intensities for peaks at *m/z*

475, 477, 493, and 495 to the peak intensity at *m/z* 215.8 were extracted from the averaged mass spectrum and summed for comparing relative abundances of cholesterol among cell monolayer spots.

It should be noted that mass spectra from all scanning points showed a variation in terms of total ion current if cell monolayer was prepared on the poly-L-lysine coated cover slip glass. In addition, intensities from cholesterol were also about one order of magnitude lower than those from the cell monolayer on the stainless steel plate even if 50% higher laser intensity was used. Therefore, all cell monolayer spots were prepared on poly-L-lysine coated stainless steel plates for obtaining relative abundance information.

Figure 5 shows relative cholesterol levels of control and MβCD-treated cell monolayer spots which were assayed by both enzymatic fluorometry and silver-LDI MS. From Figure 5, several features from silver-LDI MS could be summarized and compared with enzymatic fluorometry results. First, the silver-LDI MS method successfully probed decreased cholesterol levels on MβCD treated cell monolayer spots by estimating cholesterol abundances with relative peak intensities. In addition, relative peak intensities of cholesterol from four equally-treated cell monolayer spots showed less than 8 % of intensity variations. Second, degrees of decreased cholesterol levels by MβCD treatment were found to be consistent in independently cultured cell batch A and B by both assay methods. Third, the silver-LDI MS method showed the larger decreases of cholesterol levels than the enzymatic fluorometry method in the same treatment. It may be because sampling region by silver-LDI MS is mostly limited to cell surfaces where were affected by MβCD treatment whereas enzymatic fluorometry method probe cholesterol level from total cellular lipid extracts. This observation may suggest that the effect of MβCD treatment on cell monolayer could be underestimated by enzymatic fluorometry method.

Conclusions

LDI MS of sterols using colloidal silver as a matrix were performed and cholesterol levels on cell monolayer spots were demonstrated. With low detection limit, cholesterol and phytosterol standards were mainly detected as intact silver adduct ions, and a difference in in-source dehydration between cholesterol and its isomer was observed which could not be recognized when using conventional MALDI matrixes. By performing homogeneous and reproducible spraying of colloidal silver solution with the micronebulizer-based spraying device, consistent mass spectral profiles could be obtained through surfaces of *Astrocyte* cell monolayer spots. Sample preparation and assay procedure of the silver-LDI MS method was much simpler and faster than the traditional enzymatic fluorometry method because it didn't need any lipid extraction and enzymatic reaction step. Sampling depth by LDI-MS is thought to be limited to the outer cell membrane surface but is still ambiguous. Further investigations on sampling depth according to laser fluence, cell population, and planting surface characteristics are needed.

Ackowledgement

E.S.Y. thanks the Robert Allen Wright Endowment for Excellence for support. The Ames Laboratory is operated for the US Department of Energy by Iowa State University under Contract No. W-7405-Eng-82. This work was supported by the Director of Science, Office of Basic Energy Sciences, Divisions of Chemical Sciences and Biosciences.

References

(1) Tsui-Pierchala, B. A.; Encinas, M.; Milbrandt, J.; Johnson, E. M. *Trends in Neurosciences* **2002**, *25*, 412-417.

(2) Allen, J. A.; Halverson-Tamboli, R. A.; Rasenick, M. M. *Nature Reviews Neuroscience* **2007**, *8*, 128-140.

(3) Wolozin, B. *Proceedings of the National Academy of Sciences of the United States of America* **2001**, *98*, 5371-5373.

(4) Uekama, K.; Hirayama, F.; Irie, T. *Chemical Reviews* **1998**, *98*, 2045-2076.

(5) Abulrob, A.; Tauskela, J. S.; Mealing, G.; Brunette, E.; Faid, K.; Stanimirovic, D. *J Neurochem* **2005**, *92*, 1477-1486.

(6) Simons, K.; Ehehalt, R. *Journal of Clinical Investigation* **2002**, *110*, 597-603.

(7) Lusis, A. J. *Nature* **2000**, *407*, 233-241.

(8) Allain, C. C.; Poon, L. S.; Chan, C. S. G.; Richmond, W.; Fu, P. C. *Clinical Chemistry* **1974**, *20*, 470-475.

(9) Amundson, D. M.; Zhou, M. J. *Journal of Biochemical and Biophysical Methods* **1999**, *38*, 43-52.

(10) Gamble, W.; Vaughan, M.; Kruth, H. S.; Avigan, J. *Journal of Lipid Research* **1978**, *19*, 1068-1070.

(11) Heider, J. G.; Boyett, R. L. *J. Lipid Res.* **1978**, *19*, 514-518.

(12) Cullen, P.; Fobker, M.; Tegelkamp, K.; Meyer, K.; Kannenberg, F.; Cignarella, A.; Benninghoven, A.; Assmann, G. *Journal of Lipid Research* **1997**, *38*, 401-409.

(13) Cullen, P.; Tegelkamp, K.; Fobker, M.; Kannenberg, F.; Assmann, G. *Anal Biochem* **1997**, *251*, 39-44.

(14) Schmitz, G.; Assmann, G.; Bowyer, D. E. *Journal of Chromatography* **1984**, *307*, 65-79.

(15) Araki, N.; Horiuchi, S.; Rahim, A.; Takata, K.; Morino, Y. *Analytical Biochemistry* **1990**, *185*, 339-345.

(16) Contreras, J. A.; Castro, M.; Bocos, C.; Herrera, E.; Lasuncion, M. A. *Journal of Lipid Research* **1992**, *33*, 931-936.

(17) Kuo, J. C.; Yeung, E. S. *Journal of Chromatography* **1982**, *229*, 293-300.

(18) Carroll, R. M.; Rudel, L. L. *J. Lipid Res.* **1981**, *22*, 359-363.

(19) Greenspan, M. D.; Lo, C. Y.; Hanf, D. P.; Yudkovitz, J. B. *J. Lipid Res.* **1988**, *29*, 971-976.

(20) Raith, K.; Brenner, C.; Farwanah, H.; Muller, G.; Eder, K.; Neubert, R. H. H. *Journal of Chromatography A* **2005**, *1067*, 207-211.

(21) Tian, Q.; Failla, M. L.; Bohn, T.; Schwartz, S. J. *Rapid Commun Mass Spectrom* **2006**, *20*, 3056-3060.

(22) Palmgren, J. J.; Toyras, A.; Mauriala, T.; Monkkonen, J.; Auriola, S. *Journal of Chromatography B-Analytical Technologies in the Biomedical and Life Sciences* **2005**, *821*, 144-152.

(23) Chen, B. H.; Chen, Y. C. *Journal of Chromatography A* **1994**, *661*, 127-136.

(24) Griffiths, W. J.; Wang, Y.; Alvelius, G.; Liu, S.; Bodin, K.; Sjovall, J. *J Am Soc Mass Spectrom* **2006**, *17*, 341-362.

(25) Seal, J. R.; Havrilla, C. M.; Porter, N. A.; Hachey, D. L. *Journal of the American Society for Mass Spectrometry* **2003**, *14*, 872-880.

(26) Schiller, J.; Zschornig, O.; Petkovic, M.; Muller, M.; Arnhold, J.; Arnold, K. *Journal of Lipid Research* **2001**, *42*, 1501-1508.

(27) Wang, Y. Q.; Hornshaw, M.; Alvelius, G.; Bodin, K.; Liu, S. Y.; Sjovall, J.; Griffiths, W. J. *Analytical Chemistry* **2006**, *78*, 164-173.

(28) Nygren, H.; Malmberg, P.; Kriegeskotte, C.; Arlinghaus, H. F. *Febs Letters* **2004**, *566*, 291-293.

(29) Nygren, H.; Johansson, B. R.; Malmberg, P. *Microscopy Research and Technique* **2004**, *65*, 282-286.

(30) Altelaar, A. F. M.; Klinkert, I.; Jalink, K.; de Lange, R. P. J.; Adan, R. A. H.; Heeren, R. M. A.; Piersma, S. R. *Analytical Chemistry* **2006**, *78*, 734-742.

(31) Jackson, S. N.; Wang, H. Y. J.; Woods, A. S. *Analytical Chemistry* **2005**, *77*, 4523-4527.

(32) Inoue, M.; Murase, A. *Surface and Interface Analysis* **2005**, *37*, 1111-1114.

(33) Ostrowski, S. G.; Kurczy, M. E.; Roddy, T. P.; Winograd, N.; Ewing, A. G. *Anal. Chem.* **2007**, *79*, 3554-3560.

(34) Sluszny, C.; Yeung, E. S.; Nikolau, B. J. *Journal of the American Society for Mass Spectrometry* **2005**, *16*, 107-115.

(35) Hishiya, T.; Asanuma, H.; Komiyama, M. *J. Am. Chem. Soc.* **2002**, *124*, 570-575.

Figure Captions

Figure 1. Colloidal silver-LDI mass spectra of cholesterol (5-cholesten-3β-ol) and 5-cholesten-3α-ol. Sample loading was 100 ng/spot for both compounds. With the same laser intensity, dehydrated peak $[M - H_2O + Ag]^+$ was observed for 5-cholesten-3β-ol but not for 5-cholesten-3α-ol.

Figure 2. Possible explanation for the difference in in-source dehydration of 5-cholesten-3β-ol and 5-cholesten-3α-ol.

Figure 3. Colloidal silver-LDI mass spectrum of plant sterol mixture solution. Sample loading was 10 ng of total plant sterols/spot. Four sterol compounds were not in equal amount in the mixture. The inset is the enlarged view of the region *m/z* 500-530 where plant sterols were detected with their structures. Peaks with the asterisk are from unknown sample plate contaminants.

Figure 4. Colloidal silver-LDI mass spectral profile directly taken from the *Astrocyte* cell monolayer spot. Silver adduct ions for cholesterol and dehydrated cholesterol were detected at *m/z* 493 - 496 and at *m/z* 475 – 478. Peaks in the *m/z* 220 – 600 were magnified with factor of two. Peaks with the asterisk are from unknown sample plate contaminants.

Figure 5. Effect of MβCD treatment on *Astrocyte* cells which was assayed by both silver- LDI MS and enzymatic fluorometry method. Cholesterol levels in silver-LDI MS were based on sum of relative intensities of peaks from cholesterol and its fragment. Cholesterol levels in enzymatic fluorometry were

based on the cholesterol content which was normalized by protein content in cells. Silver- LDI MS had 4 replicas for each treatment and enzymatic fluorometry had 8 replicas for each treatment. Cholesterol levels were indicated as relative abundances to the cholesterol level of control (without MβCD treatment). Cholesterol assay were performed on two independently cultured batches A and B. Error bars correspond to ± relative standard deviation values.

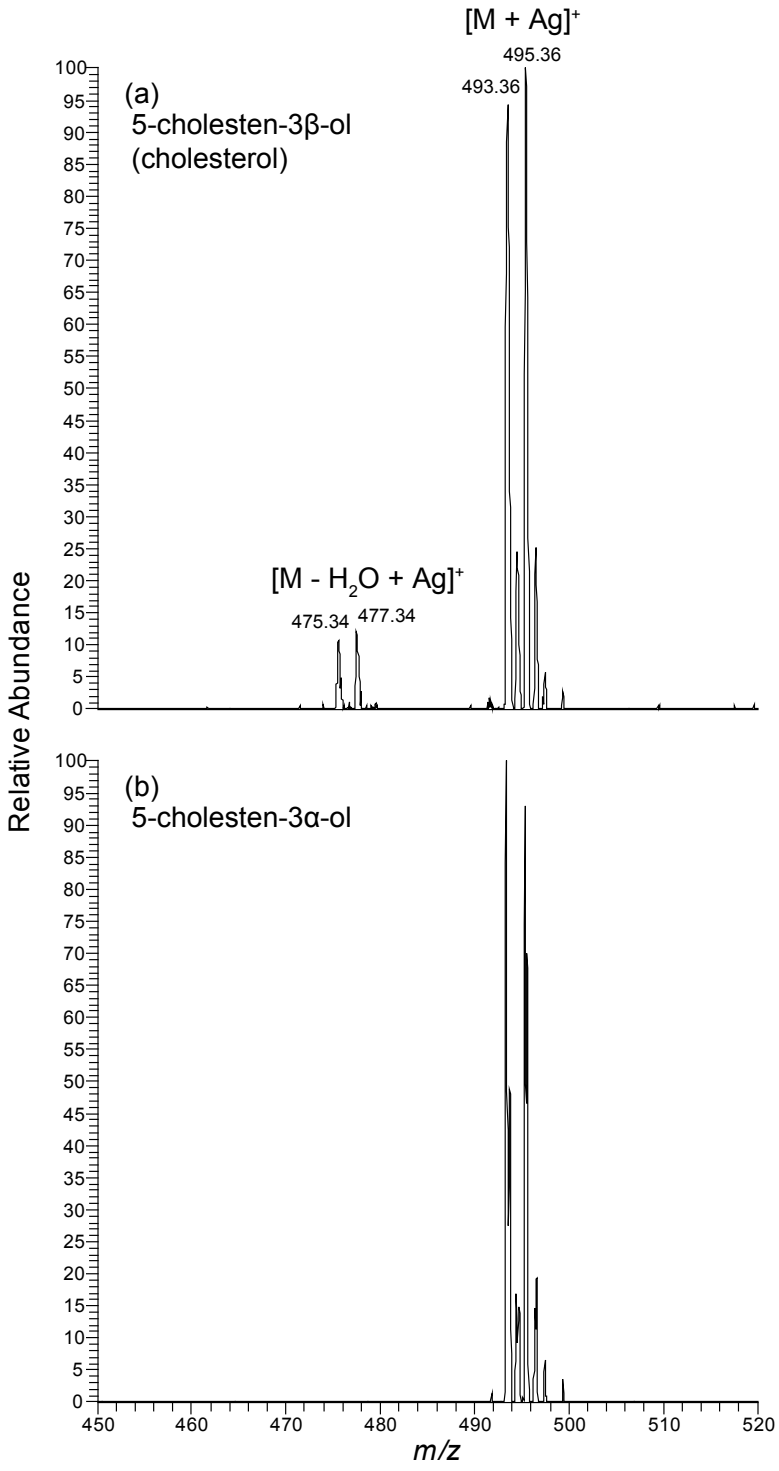
[M + Ag]+
495.36
493.36
(a)
5-cholesten-3β-ol
(cholesterol)
[M - H2O + Ag]+
475.34
477.34
(b)
5-cholesten-3α-ol
Relative Abundance
m/z
100
95
90
85
80
75
70
65
60
55
50
45
40
35
30
25
20
15
10
5
0
450
460
470
480
490
500
510
520

Figure 1.

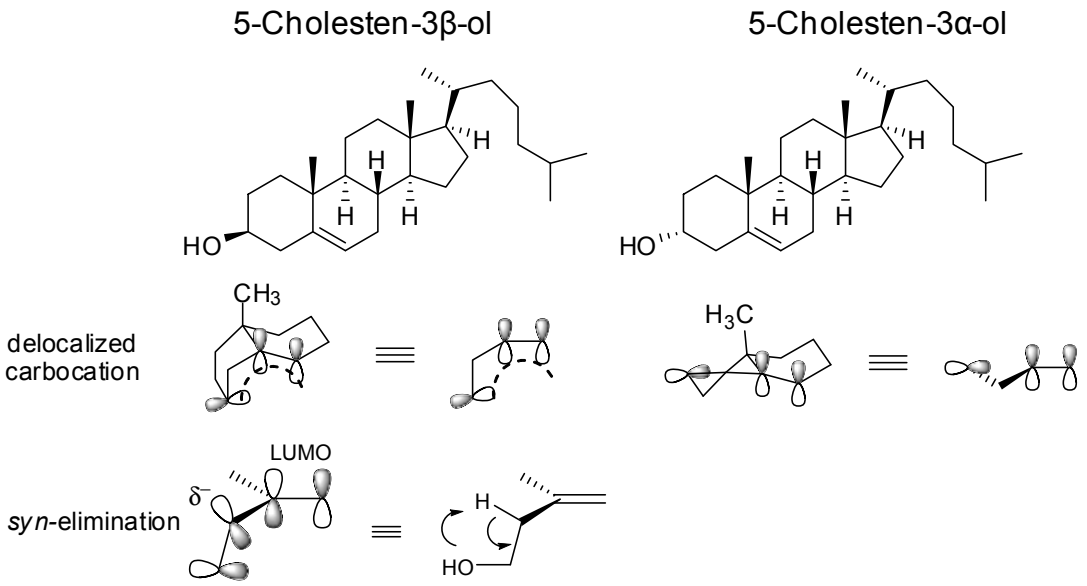
5-Cholesten-3β-ol
5-Cholesten-3α-ol
HO
HO
H
H
H
H
H
H
delocalized
carbocation
CH3
H3C
LUMO
δ−
syn-elimination
H
HO

Figure 2.

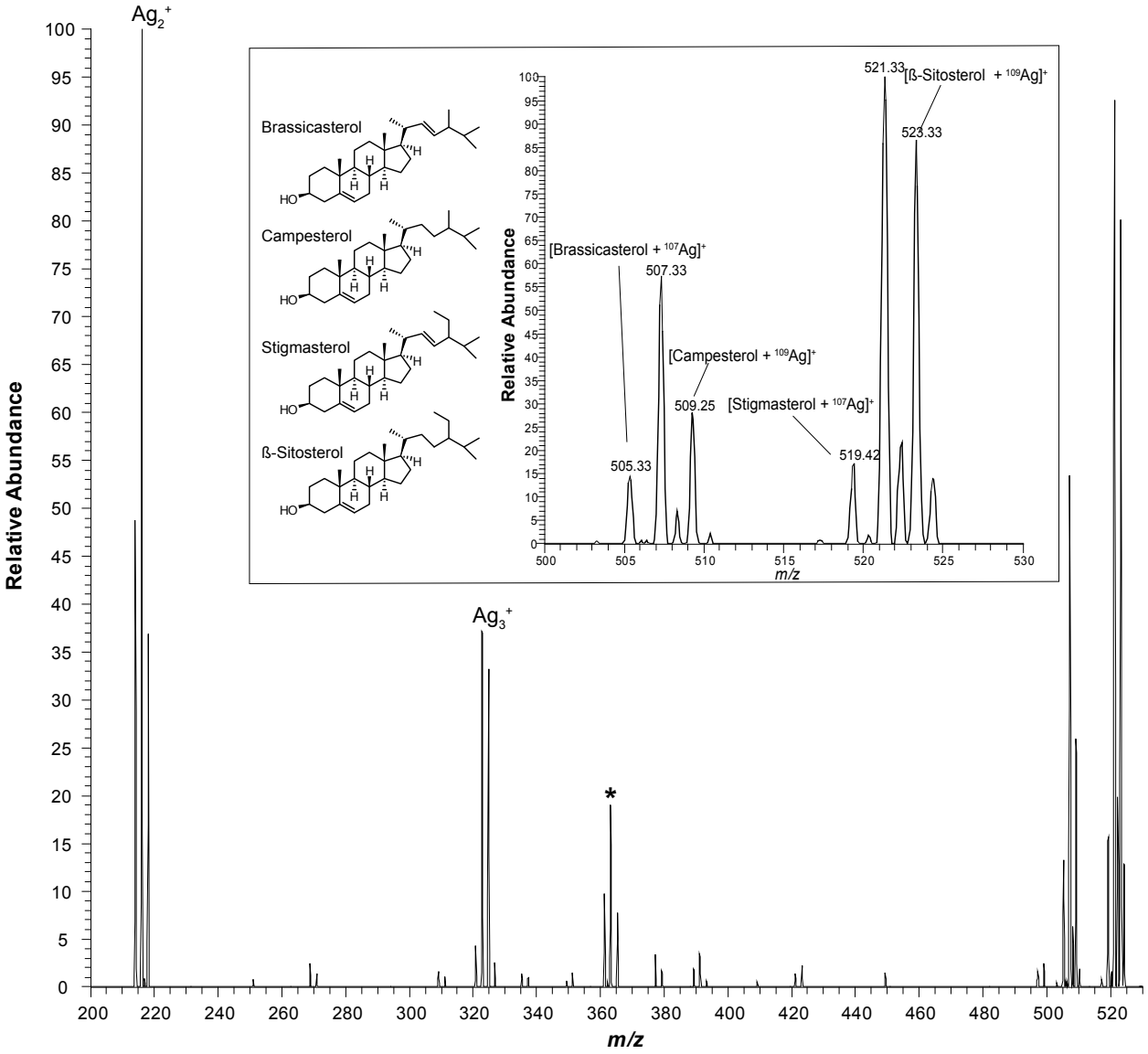
Ag2+
Ag3+
*
Relative Abundance
m/z
Brassicasterol
Campesterol
Stigmasterol
ß-Sitosterol
HO
[Brassicasterol + 107Ag]+
507.33
[Campesterol + 109Ag]+
509.25
[Stigmasterol + 107Ag]+
519.42
505.33
521.33
[ß-Sitosterol + 109Ag]+
523.33

Figure 3.

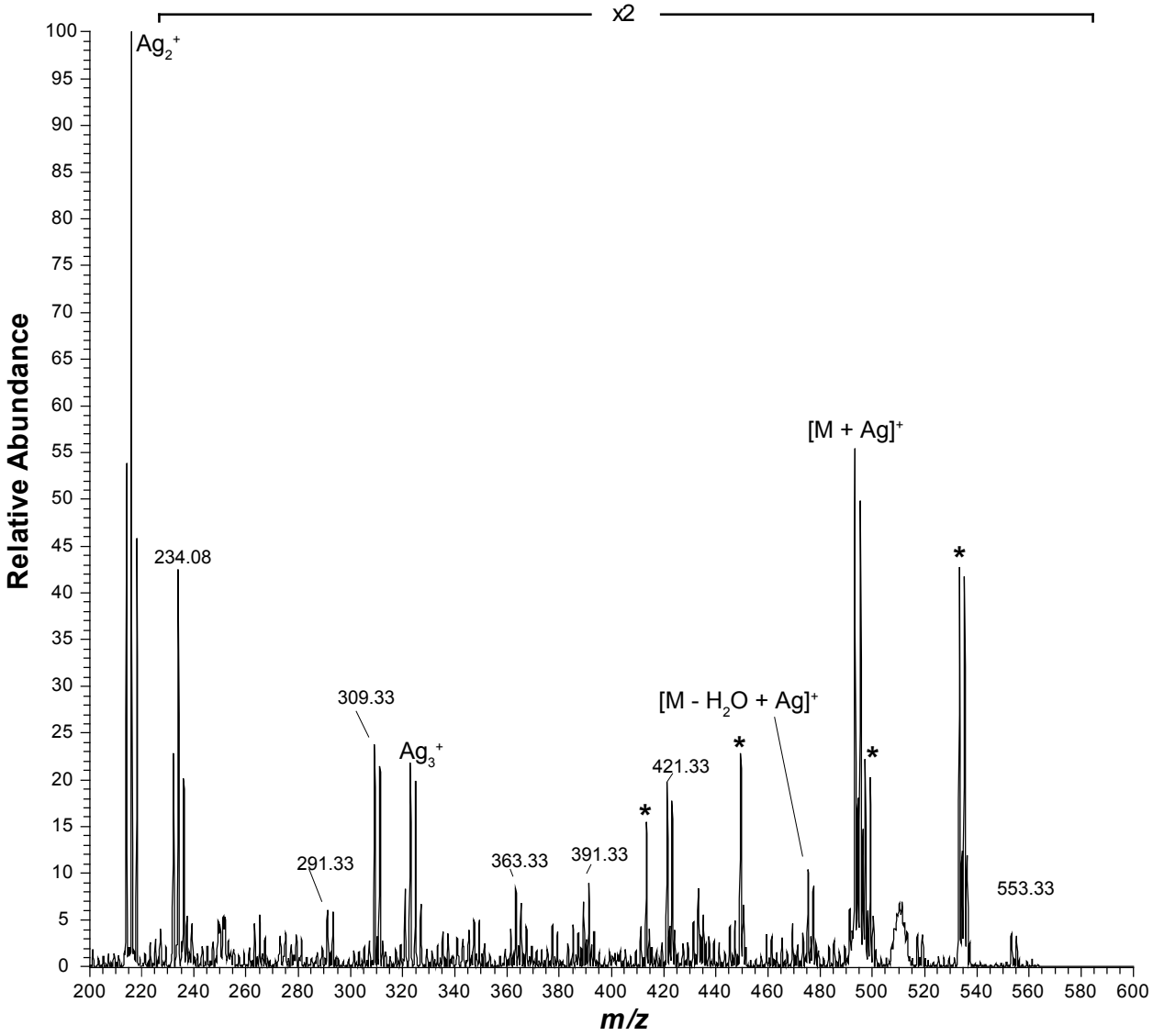
x2
Ag2+
234.08
309.33
Ag3+
291.33
363.33
391.33
421.33
[M - H2O + Ag]+
[M + Ag]+
553.33
*
Relative Abundance
m/z

Figure 4.

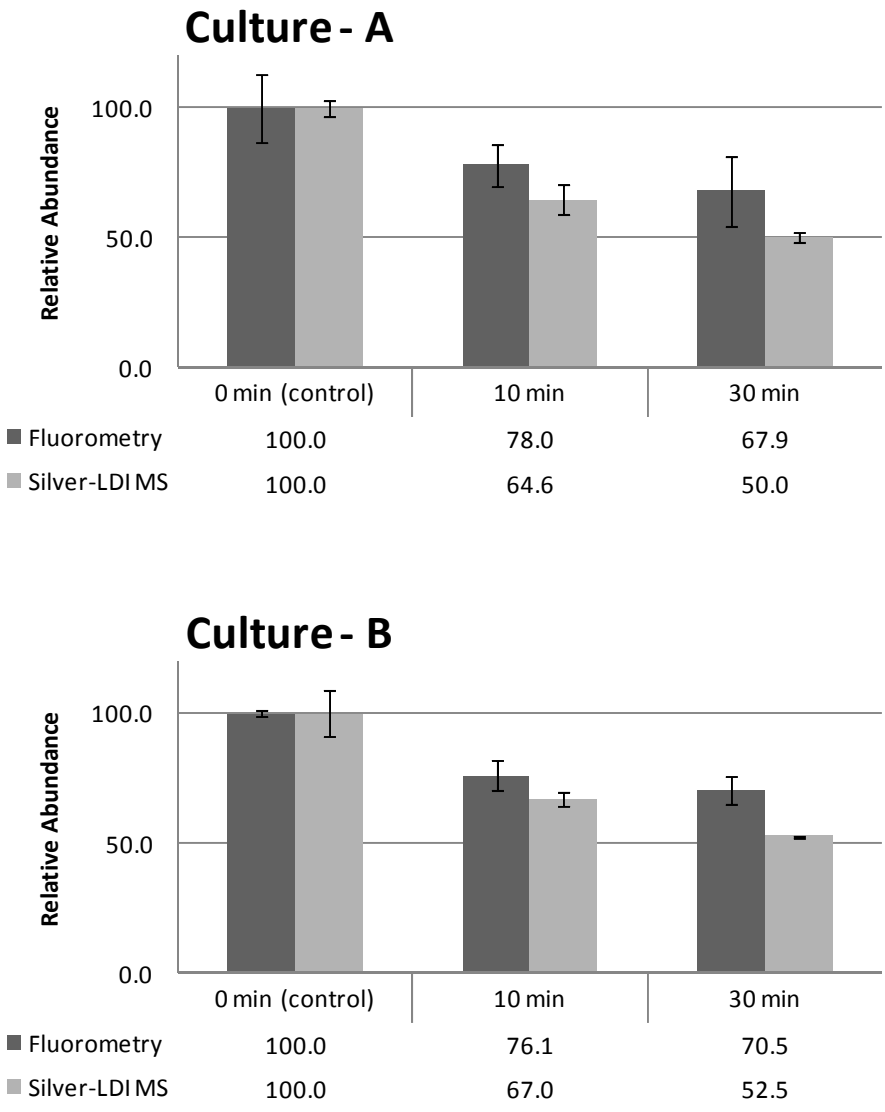
Culture - A
Relative Abundance
100.0
50.0
0.0
0 min (control)
10 min
30 min
Fluorometry
100.0
78.0
67.9
Silver-LDI MS
100.0
64.6
50.0
Culture - B
Relative Abundance
100.0
50.0
0.0
0 min (control)
10 min
30 min
Fluorometry
100.0
76.1
70.5
Silver-LDI MS
100.0
67.0
52.5

Figure 5.

CHAPTER 6. GENERAL CONCLUSIONS

In this dissertation, laser desorption/ionization (LDI) mass spectrometry (MS) and imaging mass spectrometry of small molecules was investigated with various interesting biological systems. With use of alternative matrixes such as colloidal graphite and colloidal silver solution, small molecules which were not detected very well with conventional MALDI method were successfully detected.

With colloidal graphite as a matrix, cerebrosides were readily detected and imaged from rat brain tissues whereas this class of compounds was usually suppressed in conventional MALDI MS spectra of lipid mixture by the signals from phosphatidylcholine species. For isobaric ions present in lipid mass spectral profiles, imaging tandem mass spectrometry was performed and overlapped localization information was successfully separated. In addition, GALDI MS was applied to plant materials such as fruit samples and *Arabidopsis thaliana* plants which is one of the most important plant models. Various classes of secondary metabolites such as small organic acids, oligosaccharides, long chain fatty acids, and flavonoids were detected with high sensitivity. Especially, by imaging of *Arabidopsis* flower petals, the heterogeneous distribution of flavonoid species in a single flower organ was discovered for the first time by GALDI imaging MS. This discovery has a possibility of expanding understandings of functional genomics studies of the flavonoid biosynthetic pathway.

With colloidal silver matrix, cuticular wax compounds were directly profiled and imaged from *Arabidopsis thaliana* flower surfaces. This wax metabolite profiling of flower parts has never been studied by the traditional GC-MS protocol. Reproducible mass profiles from both wild-type and mutants were obtained by using the homogeneous colloidal silver spraying technique. Comparison of relative abundances of wax compounds through wild-type and mutants by silver LDI MS provided the idea of mutant gene product functions in

wax biosynthesis pathway and showed good agreement with traditional GC-MS results. In addition, cholesterol levels were directly probed from *Asctrocyte* cell monolayers by using silver LDI MS.

Overall, alternative matrix-based direct profiling techniques have much simpler sample preparation steps and shorter analysis time than extraction- and separation – based traditional methods. Much smaller sample amount required for the analysis is also the big advantage of direct profiling LDI MS. In addition, compared to organic acid-based MALDI matrixes, alternative matrixes produce generally cleaner background in the low mass region and more homogeneous sample surfaces can be generated which is suitable for imaging MS applications. However, identification of small molecules from complete biosystems by LDI MS is still hard to achieve for some cases and there is a high possibility of isobaric ion overlaps in low mass region profiles. In addition, the sampling depth by LDI MS is thought to be limited to very outer surface but still ambiguous. Therefore, further systematic studies on separating isobaric ions based on tandem MS or high mass resolution MS or ion mobility MS are needed, and investigation of the sampling depth according to matrix application, laser properties, and sample materials is must.

APPENDIX 1. SUPPORTING FIGURES FOR CHAPTER 2

This supporting information is published online at http://pubs.acs.org*

Sangwon Cha and Edward S. Yeung

Figure Captions

Figure S-1. High-vacuum (HV)-MALDI and HV-GALDI mass spectra of standard lipid mixtures of Batch 1. Solutions of Batch 1 are composed of a constant concentration of total glucosylceramides (GlcCers) (0.5 mg/ml) and various concentrations of phosphatidylcholine 32:0 (PC 32:0) (from 0.005 mg/ml to 0.25 mg/ml). Ratios on the right side of the figure represent weight ratios of PC 32:0 to total GlcCers in each mixture. Relative abundances for the major mass peaks are listed in Table 2.

Figure S-2. HV-MALDI and HV-GALDI mass spectra of standard lipid mixtures of Batch 2. Solutions of Batch 2 are composed of a constant concentration of PC 32:0 (0.5 mg/ml) and various concentrations of total GlcCers (from 0.005 mg/ml to 0.25 mg/ml). Ratios on the right side of the figure represent weight ratios of

---

* http://pubs3.acs.org/acs/journals/supporting_information.page?in_manuscript=ac062251h

PC 32:0 and total GlcCers in each mixture. Relative abundances for the major mass peaks are listed in Table 2.

Figure S-3. Intermediate pressure (IP)-MALDI and IP-GALDI mass spectra of standard lipid mixtures of Batch 1. Solutions of Batch 1 are composed of a constant concentration of total GlcCers (0.5 mg/ml) and various concentrations of PC 32:0 (from 0.005 mg/ml to 0.25 mg/ml). Ratios on the right side of the figure represent weight ratios of PC 32:0 to total GlcCers in each mixture. Relative abundances for the major mass peaks are listed in Table 2.

Figure S-4. IP-MALDI and IP-GALDI mass spectra of standard lipid mixtures of Batch 2. Solutions of Batch 2 are composed of the constant concentration of PC 32:0 (0.5 mg/ml) and various concentrations of total GlcCers (from 0.005 mg/ml to 0.25 mg/ml). Ratios on the right side of the figure represent weight ratios of PC 32:0 and total GlcCers in each mixture. Relative abundances for major mass peaks are listed in Table 2.

Figure S-5. Mass spectrum of rat brain tissue in the negative-ion mode. This mass spectrum is the average of mass spectra from all rastering points (10,817 points) on the rat brain tissue.

Figure S-6. First generation product ion spectra of ions at *m/z* 844.50. NL 59, NL 124, NL 183, and NL 256 could correspond to the loss of trimethylamine, ethyl phosphate, phosphocholine head group, and palmitic acid from [PC 38:6 + K]+, respectively. NL 43, NL 284, and NL 304 could correspond to the loss of

aziridine, stearic acid (18:0), and arachidonic acid (20:4) from [PE 38:4 + 2K – H]+, respectively.

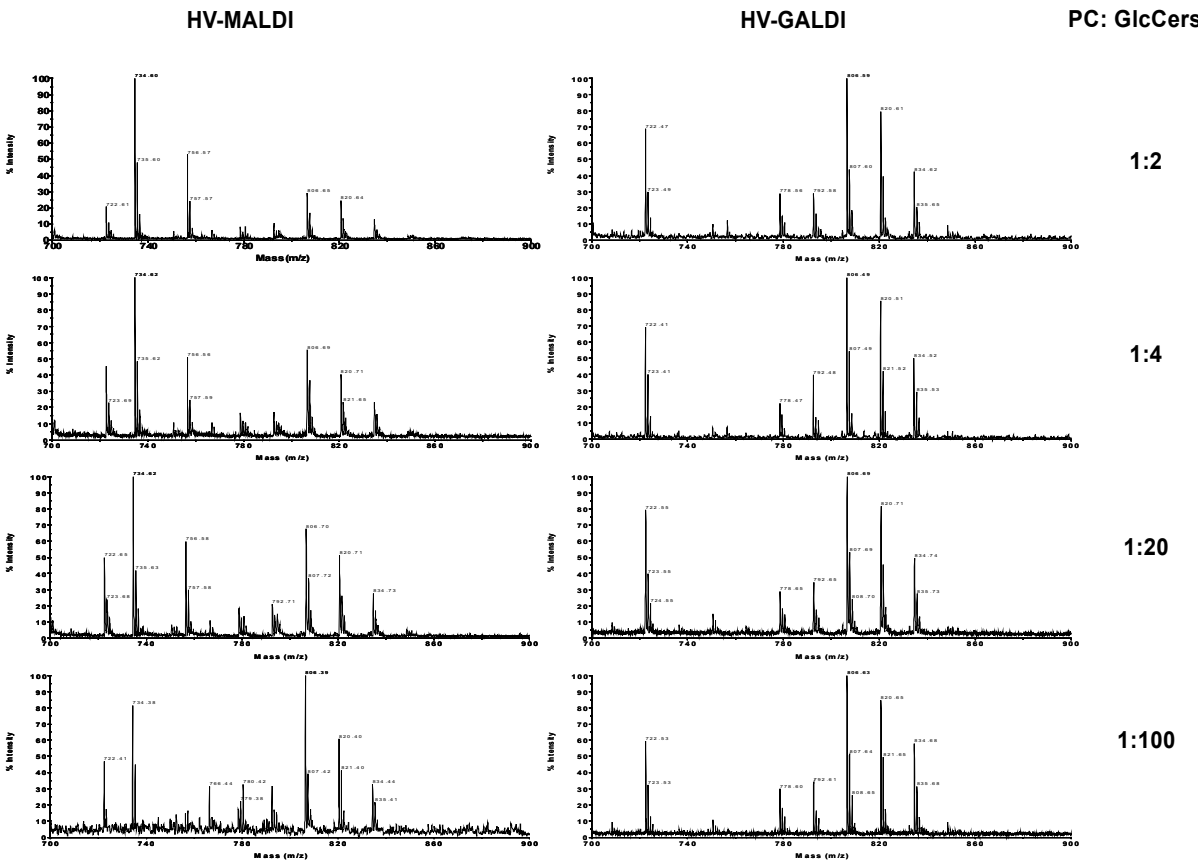

Figure S- 1.

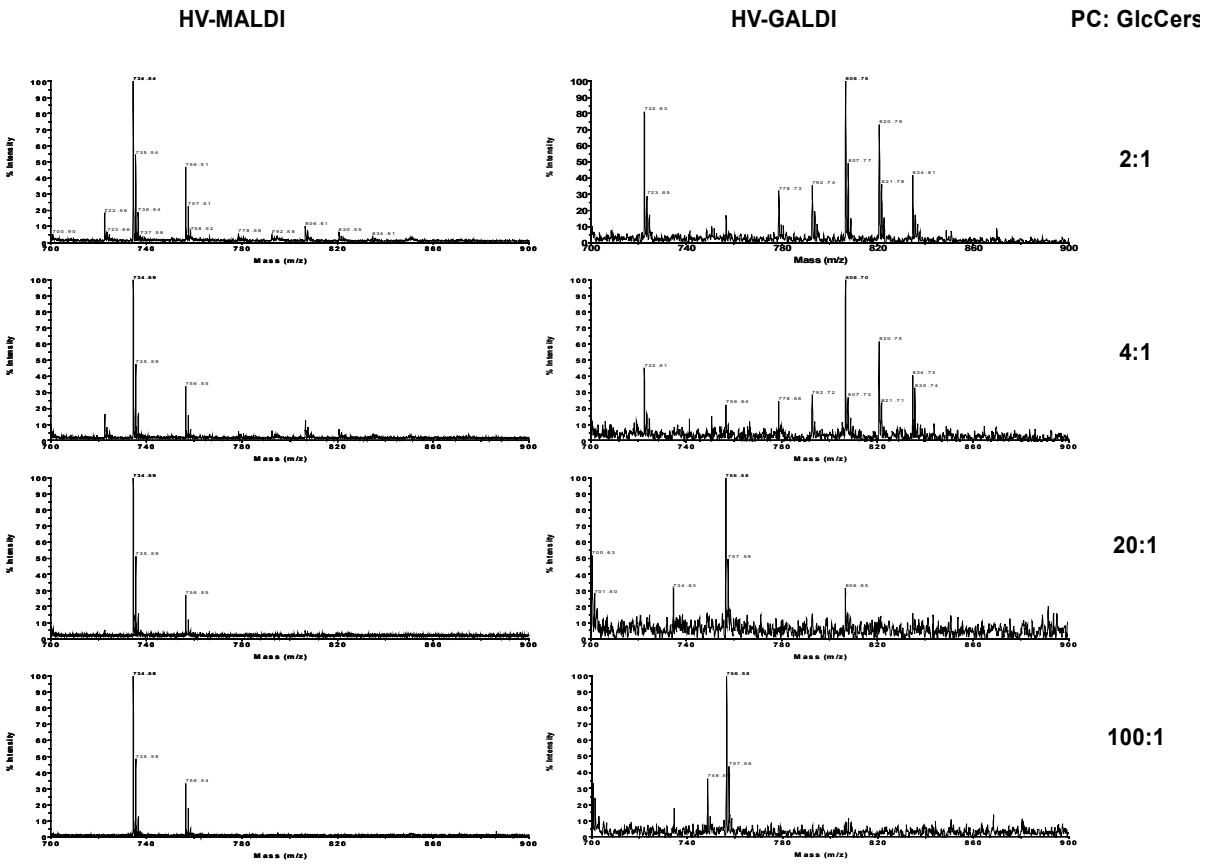

Figure S- 2.

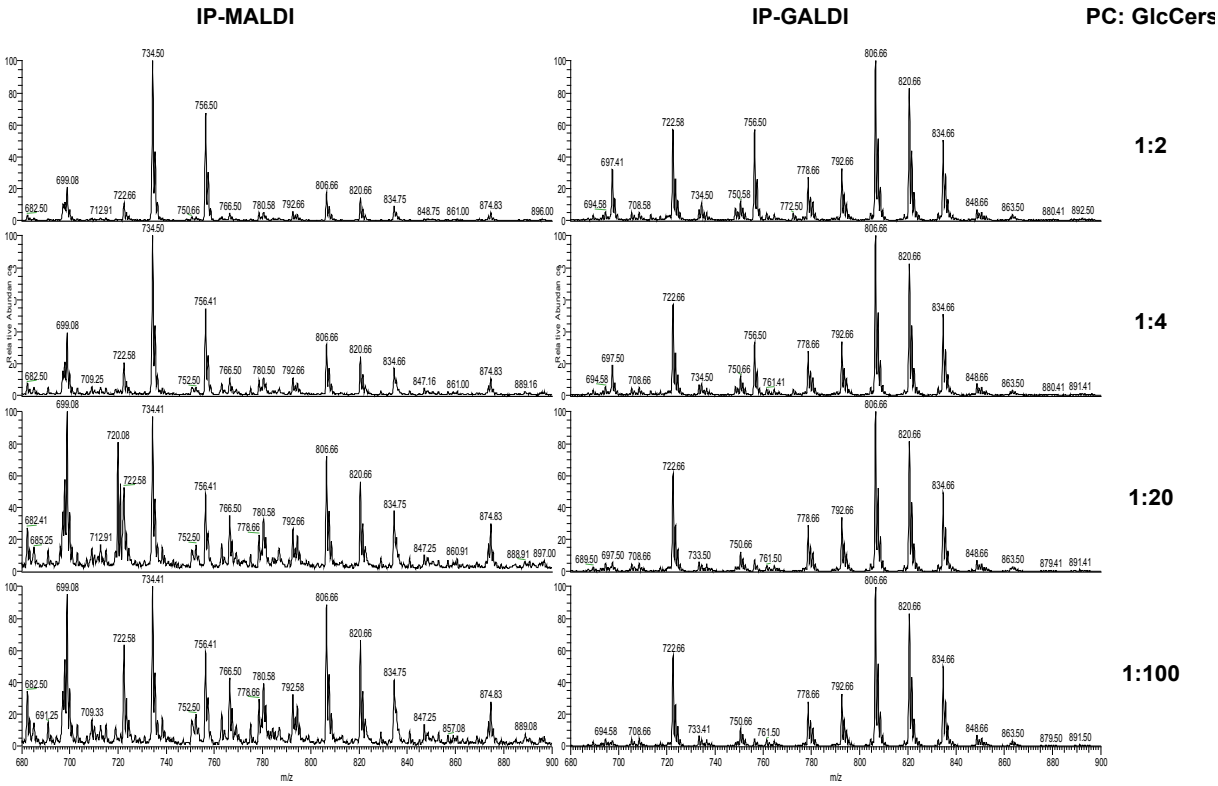

Figure S- 3.

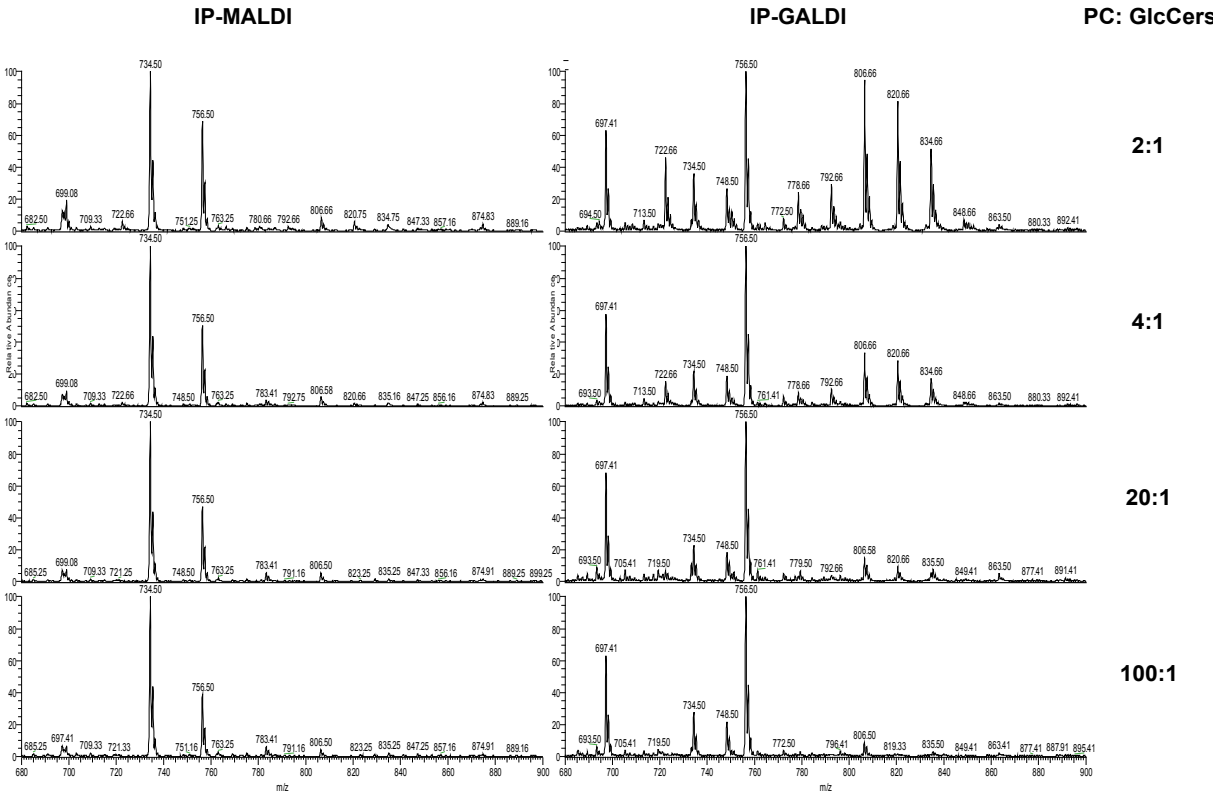
IP-MALDI
IP-GALDI
PC: GlcCers
2:1
4:1
20:1
100:1
Relative Abundance
m/z

Figure S- 4.

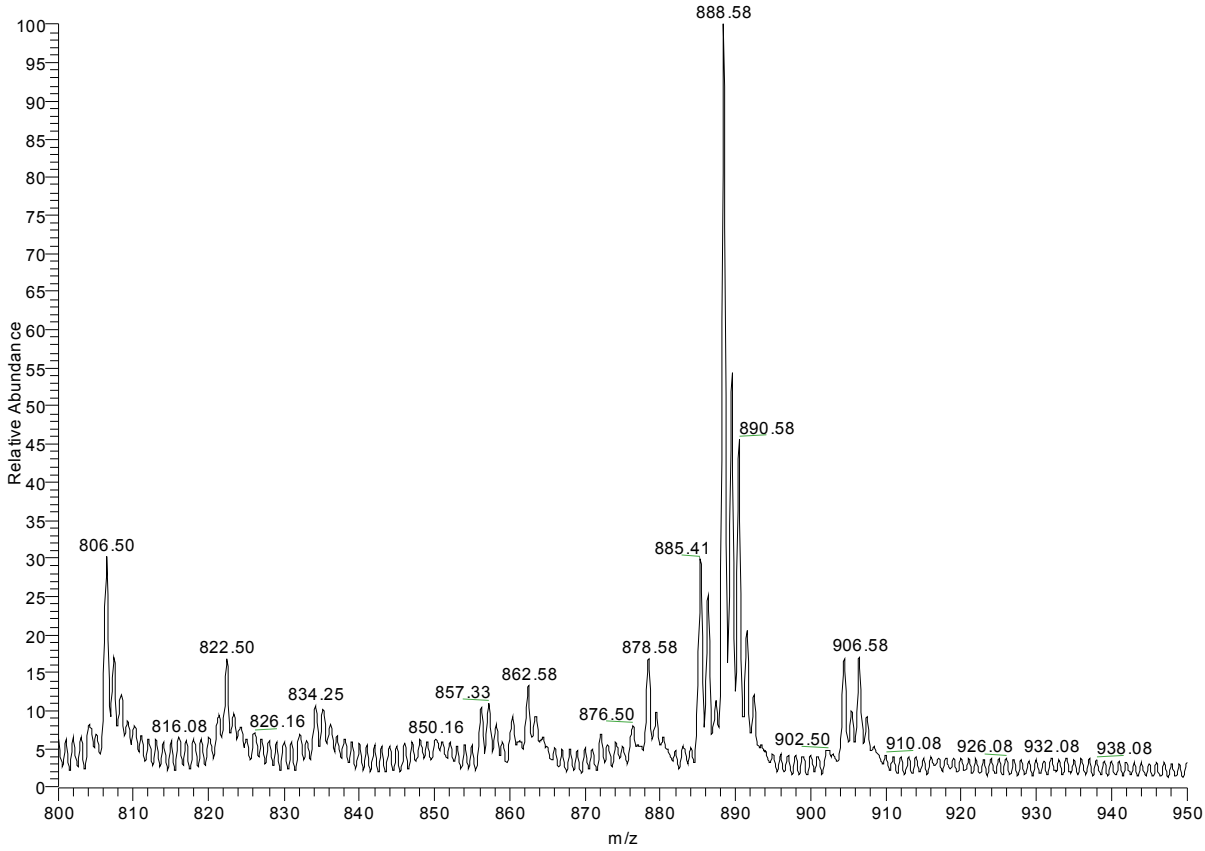
888.58
890.58
806.50
885.41
822.50
878.58
906.58
834.25
862.58
857.33
816.08
826.16
850.16
876.50
902.50
910.08
926.08
932.08
938.08
Relative Abundance
m/z
100
95
90
85
80
75
70
65
60
55
50
45
40
35
30
25
20
15
10
5
0
800
810
820
830
840
850
860
870
880
890
900
910
920
930
940
950

Figure S- 5.

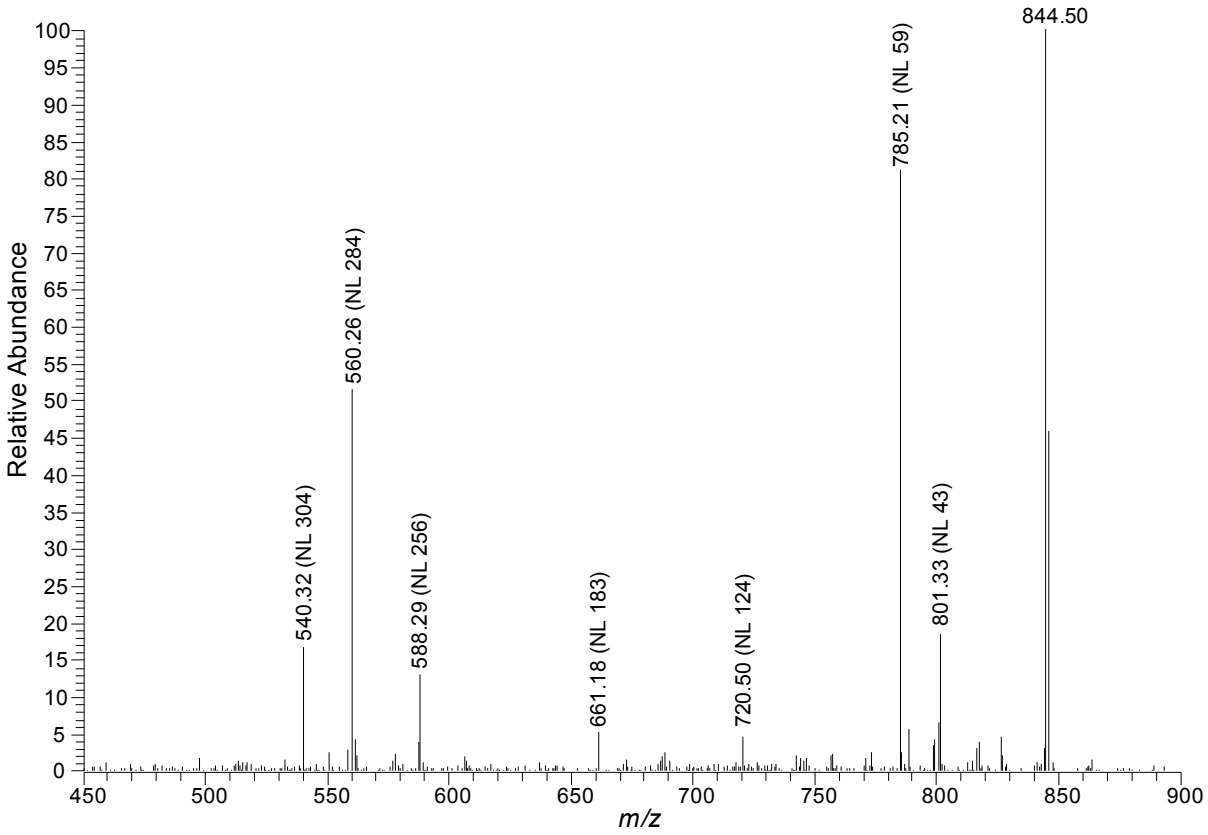
844.50
785.21 (NL 59)
560.26 (NL 284)
540.32 (NL 304)
588.29 (NL 256)
661.18 (NL 183)
720.50 (NL 124)
801.33 (NL 43)
Relative Abundance
m/z
100
95
90
85
80
75
70
65
60
55
50
45
40
35
30
25
20
15
10
5
0
450
500
550
600
650
700
750
800
850
900

Figure S- 6.

APPENDIX 2. DIRECT PROFILING AND MS IMAGING OF SMALL METABOLITES FROM FRUITES BY COLLOIDAL GRAPHITE-ASSISTED LASER DESORPTION/IONIZATION MASS SPECTROMETRY

A paper published in Analytical Chemistry*

Hui Zhang, Sangwon Cha, Edward S. Yeung

Abstract

Due to a high background in the low mass region, conventional MALDI is not as useful for detecting small molecules (molecular weights < 500 Da) as it is for large ones. Also, spatial inhomogeneity that is inherent to crystalline matrixes can degrade resolution in imaging mass spectrometry (IMS). In this study, colloidal graphite was investigated as an alternative matrix for laser desorption/ionization (GALDI) in IMS. We demonstrate its advantages over conventional MALDI in the detection of small molecules such as organic acids, flavonoids and oligosaccharides. GALDI provides good sensitivity for such small molecules. The detection limit of fatty acids and flavonoids in negative ion mode are in low femtomoles range. Molecules were detected directly and identified by comparing the MS and MS/MS spectra with those of standards. Various fruits were chosen to evaluate the practical utility of GALDI since many types of small molecules are present in them. Distribution of these small molecules in the fruit was investigated by using IMS and IMS/MS.

---

* Reprint with permission from Analytical Chemistry 2007, 79(17), 6575-6584.

Introduction

Matrix-assisted laser desorption/ionization mass spectrometry (MALDI MS) has been extensively used for the analysis of large molecules such as proteins[1] and synthetic polymers.[2] The key feature of MALDI MS are its soft ionization characteristic and simplified spectra as mostly singly charged species are generated. Compared to electrospray ionization (ESI) MS, MALDI bears other advantages such as better tolerance to interference from salts and buffers and simpler sample preparation. MALDI has also proven to be very useful for the analysis of medium-size molecules (500-10 kDa) such as peptides,[3] oligonucleotides,[4] and oligo-saccharides.[5] However, the analysis of small molecules (< 500 Da) by conventional MALDI MS is far less successful than that of larger molecules because the analyte ions are strongly interfered with or are suppressed by the matrix-related ions that are predominant at the low *m/z* range.

Different approaches have been employed in MALDI MS to minimize the background in the low mass range. Reports includes derivatization of the analyte molecules to a higher molecular weight[6] or using a matrix with higher molecular weight such as porphyrin (MW 974.6).[7] Extra sample preparation was then needed, thereby limiting the classes of analytes that can be detected. It has been observed that matrix ions can be suppressed dramatically and sometimes complete suppression can be achieved under well controlled conditions.[8, 9] For example, surfactant additives such as cetyltrimethylammonium bromide (CTAB) have been reported to substantially suppress the background from α-cyano-4-hydroxycinnamic acid (CHCA).[10] Laser intensity and the relative molar ratio of matrix to analyte are the major parameters to adjust. However a suitable molar ratio is not always achievable especially for native biological samples.

Many inorganic materials have been tested as matrixes for surface-assisted laser desorption/ionization (SALDI), including different metal powders and metal oxide nanoparticles such as Ag, Au, Co, Al, Mn, Mo, Zn, Sn, W, Fe_3O_4, SnO_2, TiO_2, WO_3, ZnO,

etc.[11-15] Generally, those SALDI MS can provide a cleaner background than conventional MALDI MS as no interference peaks from fragment ions of the organic matrixes were present. Another matrix-free approach for laser desorption/ionization on porous silicon (DIOS) was extensively studied since 1999.[16, 17] Porous silicon surfaces were etched from crystalline silicon chips with hydrofluoric acid and functionalized as the laser desorption/ionization matrix as well as trapping agents for analyte molecules. Small molecules including pharmaceuticals, nucleic acids, carbohydrates, and steroids were successfully detected.[18-20] In a more recent work, commercially available silicon nanoparticles were utilized as an LDI matrix and the silicon powder preparation was optimized for the analysis of small molecules.[21] Different kinds of carbon materials, including graphite particles,[22] graphite plates,[23, 24] graphite suspension in different solvents,[25-27] graphite trapped in silicone polymer,[28] activated carbon powders,[29] functionalized carbon nanotubes[30-33] and fullerenes,[34] and more recently pencil lead,[35-37] have been suggested as alternative matrixes for LDI MS. Many kinds of analyte molecules over a wide mass range (100-6000 Da) have been detected, such as peptides,[20, 26-29, 31, 33-36] phospholipids,[25] oligosaccharides,[30-33, 35] fatty acids,[24, 36] synthetic polymers[7, 23, 26, 31, 32, 35, 37] and other various organic compounds.[7, 15, 22-29, 31, 33-37] A more detailed description of graphite-LDI can be found in our previous paper.[38] Recent reviews about small molecules MALDI MS[39] and matrix-free LDI MS can be found elsewhere.[40]

Imaging mass spectrometry (IMS) has proven to be a powerful technology for direct profiling and imaging of elements and biomolecules in tissue sections. Secondary ion mass spectrometry (SIMS),[41, 42] MALDI[43-47] and direct electrospray ionization (DESI)[48] have been applied as desorption/ionization techniques for the IMS of molecules such as metal elements, peptides, proteins, lipids and other metabolites. SIMS has the best spatial resolution among the three and DESI requires the least sample preparation and allows true *in situ* measurement with the simplest instrumentation.[48] The spatial resolution of MALDI IMS is in between

SIMS and DESI IMS, usually ranging from 80-200 μm in diameter. The diverse choices of lasers and matrixes make MALDI MS suitable for fast, simultaneous and high-throughput analyses of metabolites from tissue samples. MALDI equipped with UV laser has been successfully demonstrated for the imaging of peptides, proteins and lipids.[43-47] Due to the high background problem as discussed earlier there is limited application of UV-MALDI for imaging of small molecules (< 500 Da). Infrared (IR) MALDI was introduced recently as a technique for imaging small metabolites from fruit samples.[49] Water is used as the natural matrix for IR MALDI, but it is inevitable that the sample may dry out during the process of IR irradiation. Different locations will thus give different sensitivities due to inhomogeneous water content. So far, molecules that can be detected by IR MALDI are quite limited, either because of the low desorption/ionization efficiency or low detection sensitivity. Furthermore, the spatial resolution of IR-IMS is inherently worse than that of UV-IMS.

Previously we demonstrated that colloidal graphite was a good LDI matrix for the analysis of molecules in 500-1000 Da range, such as different lipid species.[38] This matrix contains fine particles and is spatially homogeneous, making it suitable for quantitative imaging. The colloidal property also allows it to be easily sprayed to form a layer on top of tissue samples and thus simplifies imaging experiments. In this study, we investigated the applicability of colloidal graphite as an alternative LDI matrix for the analysis of even smaller metabolite molecules. Fruits contain many kinds of small molecules such as long-chain fatty acids, small oligosaccharides, and flavonoids; so they serve as good systems to test the performance. GALDI MS and tandem MS were used to identify the ionized species, while IMS and IMS/MS were utilized to map the distribution of those molecules in fruit slices.

Experimental Section

Standards such as long-chain fatty acids, oligosaccharides and flavonoids were purchased from Sigma-Aldrich (St. Louis, MO). Dihydroxybenzoic acid (DHB) from Bruker Daltonics (Billerica, MA) and CHCA solution from Agilent Technologies (Palo Alto, CA) were used as standard MALDI matrixes. 2-Propanol-based colloidal graphite aerosol spray (Aerodag G) was obtained from Acheson Colloids (Port Huron, MI). Pure water was obtained from a MilliQ water purification system (Billerica, MA). All other chemicals were purchased from Fisher Scientific (Fairlawn, NJ).

Apple and strawberry fruits were purchased from a local grocery store. Apple skin was peeled off by a sharp razor blade and attached to the stainless steel plate by double-sided tape. Apple juice was collected from crushed flesh onto a glass slide, dried and used directly. A cryostat from International Equipment Co. (Needham Heights, MA) was used for cryosectioning. Fruit chunks were dipped in liquid N_2 before they were cryosectioned into about 15-μm thick specimens and stored at –20 °C before mass spectrometric analysis. No optimum cutting temperature (OCT) compounds were used to embed the fruit samples as the interference to mass spectra from OCT compounds is known.[50] Sectioned fruit slices were directly transferred and mounted onto the stainless-steel plate. Before applying colloidal graphite solution, the slices were dried under moderate vacuum (~50 Torr) at room temperature for half an hour.

Long-chain fatty acid standards were prepared by dissolving stearic acid (C18, MW 284.48), pentacosanoic acid (C25, MW 382.66), hexacosanoic acid (C26, MW 396.69), octacosanoic acid(C28, MW 424.74), and melissic acid (C30, MW 452.80) in chloroform to a final concentration of 200 pmole/μl each. For flavonoid standards, quercetin (MW 302.24), kaempferol (MW 286.23), phloretin (MW 274.27), and apigenin (MW 270.24) were dissolved individually in DMSO to give concentration of 5mg/ml of each; then the four standard solution were mixed and further diluted to a final concentration of 200 pmole/μl

each in water/acetonitrile/trifluoroacetic acid (49.95/49.95/0.1). Oligosaccharide standards were prepared by dissolving ribose (MW 150.13), glucose (MW 180.16), sucrose (MW 342.30), N-acetyl-D-lactosamine (LacNAc) (MW 383.35), maltotriose (MW 504.44), and maltotetraose (MW 666.58) in water/acetonitrile/trifluoroacetic acid (49.95/49.95/0.1) to a final concentration of 100 ng/μl each. 20 mg/mL DHB solution in 70% methanol and 30% water (containing a 0.1% trifluoroacetic acid) was prepared. Commercial Agilent CHCA solution at 6 mg/ml in 36/56/8 methanol/acetonitrile/water was purchased and used directly. Four times dilution of colloidal graphite solution with 2-propanol was used for GALDI MS and IMS.

For all mass spectrometric analysis and IMS, an LTQ linear ion trap mass spectrometer equipped with vMALDI source (Thermo Electron, Mountain View, CA) was used. The N_2 laser (337 nm) is guided to the source by a fiber-optic cable and has a maximum output of 280 μJ/pulse (before entering the optical fiber cable). The measured laser spot size is ~100 μm in diameter on the sample plate surface. A more detailed description of the LTQ with vMALDI source has been reported elsewhere.[46]

For conventional MALDI MS, 1 μL of DHB or CHCA matrix solution was applied onto the stainless-steel sample plate and let to dry in air, followed by 1 μL of sample solution on top of the matrix crystals. For GALDI MS of standards, 0.5 μL of diluted colloidal graphite solution was applied onto the stainless-steel sample plate by a micropipette and let to dry in air. Then 1 μL of standard solution was applied on top of the graphite spot. To obtain mass spectra from apple juice with GALDI, 1 μl of fresh apple juice was applied onto a dried (0.5 μl) graphite spot. For apple peels and fruit slices, diluted colloidal graphite solution was applied by a double-action airbrush (Aztek A470 with a 0.30 mm nozzle from Testor, Rockford, IL). The whole fruit slice was covered with colloidal graphite homogeneously by spraying with 20 psi air pressure and 15 cm away from the sample plate

for 30 s. Peak identification was made by comparing both mass and tandem mass spectra with those of standards.

Optical images of fruit slices were taken inside the vMALDI source before IMS. Serial optical images were taken every 1 mm movement of the sample stage in either *x*- or *y*-direction. Each segment of the images has a size of 140 pixels by 170 pixels. These segments of optical images were reconstructed as one optical image for one fruit slice. To collect mass spectra, the same sample plate was rastered with 100 μm steps. For each raster point, a mass spectrum was recorded for desorbed ions and integrated over 3-5 laser shots. In the cases of IMS/MS, target precursor ions (*m/z* 191 or *m/z* 301) were first selected based on the mass spectral profiles of strawberry. Then the first-generation product-ion spectra of the selected precursor ion were collected from all rastering points on the strawberry slice. More laser shots were required for MS^2 experiments and so 9 laser shots were averaged for each raster point.

Custom software "vMALDI data browser" (Version 1.0) was used to extract mass spectra from specific locations and generate chemically selective images. This software was provided by the instrument vendor (Thermo Electron, Mountain View, CA). The mass window for generating images was 0.5 Da. Intensities of the selected ion were normalized by dividing the total ion current of each mass spectrum. Then, chemically selective images were plotted as 3-D maps with the 3rd dimension being the normalized intensity.

Results and Discussion

MALDI and GALDI MS of Standard Mixtures of Fatty Acids, Flavonoids and Oligosaccharides. Different classes of compounds were selected to compare the performance of conventional MALDI and GALDI. Long-chain fatty acids (C18-C30) were selected as one group of standards because of their important roles in many metabolic

pathways of living organisms.[51] Fatty acids can be detected by GC-MS with proper derivatization such as esteritication to reduce the polarity and increase volatility.[52] HPLC-ESI MS can detect native fatty acids in the negative-ion mode through deprotonization.[53] However, the basic pH condition which is required to produce such negative ions is not compatible with most reverse-phase C18 columns that typically require acidic mobile phases. To overcome this problem, judicious derivatization was needed.[54] MALDI MS can eliminate the separation step but conventional MALDI matrixes do not work well for detection due to a high background and ion suppression in that mass region. This is underscored by the fact that none of the selected standard fatty acids were detected with DHB or CHCA in either positive-ion mode or negative-ion mode (data not shown). With GALDI, all five fatty acids (100 ng each) were detected as deprotonated peaks ($[M - H]^-$), as shown in Figure 1. It is noteworthy that the background in the negative-ion mode of GALDI is very clean up to at least *m/z* 1000 without any pretreatment. In fact, there are only a few low number carbon cluster ions, such as C_{12}^--C_{14}^-; and the intensity of such peaks are much lower than those for the analytes. GALDI is very sensitive to detect those fatty acids in negative ion mode. Fig. 2 shows the spectrum of the fatty acid mixture with sample loading of 100fmole of each on a 3mm-in-diameter spot. Such fatty acids can also be detected as potassium adduct ions ($[M + K]^+$) in positive ion mode (data not shown), though the detection sensitivity (detection limit: 50pmole/spot) is not as good as in negative ion mode .

Another group of standards tested were natural phenolic molecules, the flavonoids. It was estimated that 2% of all carbon photosynthesized by plants is converted into flavonoids or related compounds.[55] They have been reported to have antioxidant, antiatherosclerotic and anti-neurodegenerative properties, and are also known to be beneficial for the prevention of chronic diseases like cancer and heart diseases.[56, 57] In the positive-ion mode, quercetin, kaempferol and apigenin were detected as $[M + H]^+$ in both MALDI and GALDI experiments (Fig. 3a-c). $[M + Na]^+$ and $[M + 2Na-H]^+$ ions for these three flavonoids can also

be detected with GALDI. Phloretin was not detected with any of the three matrixes. This suggests that the center ring in the other three flavonoids plays an important role for protonation. However, it was possible to detect phloretin with GALDI in the negative-ion mode (Fig. 3f). Several peaks in the region of *m/z* 150-200 in the spectra were identified as in-source-fragments for the flavonoids by using tandem MS. For example, *m/z* 167 was identified as a fragment of phloretin while *m/z* 151 and *m/z* 179 were fragments of quercetin. Unlike GALDI, which has a clean background, with DHB and CHCA, matrix peaks are predominant and none of the four flavonoid standards were detected in the negative-ion mode (Fig. 3d-e).With GALDI, negative ion mode provides better sensitivity for detection of those flavonoid standards than positive ion mode does, and the detection limit are 50 fmole and 200 fmole/3mm-in-diameter spot, respectively.

The third group of standards selected were oligosaccharides. Due to the lack of acidic or basic groups, they are difficult to be ionized with conventional MALDI. DHB can be used to detect large oligosaccharides (> 1000 Da)[58] but smaller oligosaccharides are strongly interfered with by matrix ions. We tested oligosaccharides between 150-700 Da with DHB (Fig. 4a), CHCA (Fig. 4b), and graphite matrixes (Fig. 5). With CHCA, only larger molecules like LacNAc, maltotriose and maltotetraose can be detected as $[M + Na]^+$ but not the smaller ones such as ribose, glucose and sucrose. DHB works slightly better than CHCA in that the small oligosaccharides such as glucose and sucrose can be detected. However, the intensity of the small saccharide peaks was very low. For example $[ribose + Na]^+$ and $[glucose + Na]^+$ peaks are strongly suppressed as they are very close to matrix peaks $[DHB + Na]^+$ and $[DHB + 2Na – H]^+$ respectively. LacNAc has the highest detection sensitivity among all the oligosaccharides. This may suggest that the N-acetyl group has more affinity for sodium ions than the other moieties of oligosaccharides. In both the CHCA and DHB MALDI mass spectra (Fig. 4a-b), the matrix peaks were predominant and oligosaccharides peaks were strongly interfered with. With GALDI, all six oligosaccharides were detected as

$[M + Na]^+$ with decent signal-to-noise ratios, as shown in Fig. 5. $[M + Na -18]^+$ peaks were also observed for all five oligosaccharides as water loss (Fig. 5). Neutral loss (NL) of 60 are known to result from the major cross-ring cleavage fragments of oligosaccharides with 1,4 linkages.[59] Here, *m/z* 629 and *m/z* 467 were observed as such fragments of maltotetraose and maltotriose respectively. The peak at *m/z* 305 corresponds to the major fragment of LacNAc. All of the above fragments were verified by tandem MS (data not shown). All cross-ring cleavage fragments were marked with asterisks in Fig. 5. That the positive-ion mode of GALDI gave a noisier background compared to the negative-ion mode did not prevent the successful detection of small oligosaccharides. Small oligosaccharides such as hexose (glucose or fructose) and sucrose can also be detected as $[M – H]^-$ under the negative-ion mode peaks, *vide infra*. The detection sensitivity of oligosaccharides with GALDI under positive ion mode is better than with GALDI under negative ion mode. For instance, the detection limit of sucrose is 20pmole and 100pmole/3mm-in-diameter spot, respectively. This can be understood as oligosaccharides have neither carboxyl group as fatty acids, or aromatic rings as flavonoids which can stabilize the deprotonated phenol group.

Direct Detection of Small Metabolite Molecules from Fruit Samples. Because of the sensitivity and background issues, GALDI in the positive-ion mode was used to detect oligosaccharides and the negative-ion mode was used to detect other metabolite molecules from fruit samples. Unlike experiments with the standards, colloidal graphite solution was applied on top of the sample, otherwise the graphite particles may not be accessed by laser irradiation. For imaging purposes, homogeneous coverage over the sample area is a must. The application methodology has been optimized for IMS of mouse brain tissues in our previous work[38] and was used in this study without modification.

A list of small molecules detected directly from apple and strawberry samples were summarized in Table I, with concentration data wherever available.[60-65] All identifications were made by comparing the MS spectra with those of standards. MS/MS data were also

compared with those of standards except those at too low a concentration to give meaningful MS/MS data, as marked with asterisks. Tandem MS data is indispensable to identify isobaric ions, such as *m/z* 191, which were observed from both apple and strawberry. Tandem mass data of *m/z* 191 from apple and strawberry flesh are shown in Fig. 6. Notably, citric acid gave a predominant product ion at *m/z* 111 while quinic acid has specific product ions at *m/z* 85, 93 and 127, as reported previously.[66] By tandem MS it was confirmed that the peaks at *m/z* 191 were from quinic acid in apple while such peak came from citric acid in strawberry.

Fig. 7 shows typical mass spectra taken from different parts of the apple. Fruits in supermarkets were always coated with a thin layer of wax for preservation and for better appearance. Fatty acids are one major class of components of wax and many of those up to C28 fatty acids were detected from apple peel, as shown in Fig. 7a. Other compounds such as sugars or flavonoids were absent from the mass spectrum. The reason may be that such compounds were covered by the wax layer and were not accessible. Fatty acids may be naturally present on the apple peels as well; however, those cannot be discriminated from the species in the artificial wax layer.

As shown in Fig. 7b, fresh apple juice gave malic acid, quinic acid, palmitic acid, and linolenic acid in the negative-ion mode. Hexose (glucose or fructose) and sucrose were detected as deprotonated ions as *m/z* 179 and *m/z* 341, respectively. Quercetin is one of the major flavonoids contained in apple and it was also detected. Fig. 7c shows the spectrum in the positive-ion mode. Sodium adduct ions of hexose and sucrose were detected, as well as potassium adduct ions. According to the USDA nutrient database, fruits usually contain much higher amounts of potassium than sodium (90 mg vs. 0 mg/100 g for apple and 292 mg vs. 37 mg/100 g for strawberry).[64]

Fig. 7d is the representative spectrum taken from the apple core (endocarp). Here, organic acids such as malic acid and quinic acid were still observed, but the relative intensities were not as high as those from juice. On the other hand, higher amounts of

flavonoids such as phloretin and quercetin accumulated in the endocarp region. Apple peel also contains a lot of flavonoids and quercetin was the predominant one found on the inside of apple peel (data not shown).

Fig. 8a and 8b are representative mass spectra taken from strawberry. As reported previously with IR-MALDI,[49] strawberry contains a lot of citric acid. In our study, citric acid (*m/z* 191) was always the most intense peak in the negative-ion mode. GALDI can also detect those compounds which were too low in concentration to be detected by IR-MALDI, such as ascorbic acid and ellagic acid. Quercetin and kaempferol was also detected in the red part of strawberry (more details in IMS data below). Other deprotonated ions include palmitic acid, oleic acid, apigenin, hexose, and sucrose, as marked in Fig. 8a. Similar to the previous report,[49] citric acid and sucrose were barely detected in the seed region, as shown in Fig. 8b. Instead, C16 and unsaturated C18 fatty acids were the major components.

IMS of Metabolites from Apple and Strawberry. IMS in the negative-ion mode was performed to show the detailed distributions of different metabolite molecules on apple and strawberry slices, as Fig. 9 and Fig. 10 respectively. Small molecules such as malic acid, quinic acid, and sucrose distributed relatively evenly over the apple flesh part, as shown in Fig. 9b, c, and e. Long-chain fatty acid such as linoleic acid was detected all over the slice but more accumulated along the core line and bundles, as shown in Fig. 9d. Flavonoids also accumulated more in the core region but not in the flesh, as shown in Fig. 9f-i. Unlike linoleic acid, they seem to be only enriched in the bundles (both sepal and pedal), but not along the core line. Another interesting feature is that flavonoids were found in the *ventral carpellary* bundle (center of the apple slice) except for quercetin.

The images shown in Fig. 10 were scanned from a pie-shaped strawberry slice, with the red skin on the right-hand side and one seed in the middle-right part. Citric acid, apigenin, hexose and sucrose were distributed all over the flesh, while fatty acids such as linolenic and linoleic acids accumulated on the seed. The peak at *m/z* 301.2 was detected all over the

strawberry with a relatively constant concentration in the flesh, but showed higher local intensity on the outside (red part) and the seed areas. The candidates were quercetin (MW 302.24) and ellagic acid (MW 302.20) and the two species could be distinguished in tandem MS. Fig. 11a and 6b show the MS/MS spectra of ellagic acid and quercetin standards. *m/z* 151 and *m/z* 179 were specific fragments of quercetin due to the cleavage of the center ring, as reported previously;[56, 67] while ellagic acid is more rigid and only small fragments such as NL 28 and NL 44 were observed. MS/MS product ion spectra from strawberry flesh were similar to those from ellagic acid (Fig. 11c), while those at *m/z* 301.2 on the edge gave quercetin-like fragments (Fig. 11d). The chemically selective ion image at *m/z* 179 with precursor ions at *m/z* 301.2 is shown in Fig. 11e. The ambiguity in Fig. 10i is thus resolved.

Similarly, both citric acid (MW 192.13) and quinic acid (MW 192.17) were detected as *m/z* 191 with GALDI in the negative-ion mode. IMS/MS (data not shown) with precursor ions at *m/z* 191.2 showed that product ions at *m/z* 111.3 were detected all over the strawberry slice, while no specific fragments of quinic acid (*m/z* 85 or *m/z* 93) were observed. This suggests that all *m/z* 191 ions from strawberry were from citric acid (Fig. 10c).

Acknowledgements

E.S.Y. thanks the Robert Allen Wright Endowment for Excellence for support. The Ames Laboratory is operated for the U.S. Department of Energy by Iowa State University under Contract No. DE-AC02-07CH11358. This work was supported by the Director of Science, Office of Basic Energy Sciences, Divisions of Chemical Sciences and Biosciences.

Table I. List of compounds detected directly from apple and strawberry and their average concentrations from the literature. All species have been checked by *m/z* against standards, and all but those with marked with asterisks have been checked by tandem MS.

	Apple			Strawberry		
	m/z	Peaks assigned	Concentrations g/Kg	m/z	Peaks assigned	Concentrations g/Kg
Organic acids	133 $[M-H]^-$	Malic Acid	4.9 $*10^{-3}$ [60]	175 $[M-H]^-$	Ascorbic Acid*	0.59
	191 $[M-H]^-$	Quinic Acid	0.76 $*10^{-3}$ [60]	191 $[M-H]^-$	Citric Acid	6.9-12.6 [62]
	255 $[M-H]^-$	Palmitic Acid	0.24	255 $[M-H]^-$	Palmitic Acid	0.12
	277 $[M-H]^-$	Linolenic Acid	0.09	277 $[M-H]^-$	Linolenic Acid	0.65
	279 $[M-H]^-$	Linoleic Acid	0.43	279 $[M-H]^-$	Linoleic Acid	0.90
	281 $[M-H]^-$	Oleic Acid	0.07	281 $[M-H]^-$	Oleic Acid	0.42
Phenolics	273 $[M-H]^-$	Phloretin	4.7 $*10^{-3}$ [60]	269 $[M-H]^-$	Apigenin	0.00-0.01
	289 $[M-H]^-$	Epicatechin	47.1 $*10^{-3}$	285 $[M-H]^-$	Kaempferol	4.6 $*10^{-3}$
	301 $[M-H]^-$	Quercetin	45.7 $*10^{-3}$	301 $[M-H]^-$	Ellagic Acid	0.06-0.5 [63]
	435 $[M-H]^-$	Phloridzin*	55.9 $*10^{-3}$ [61]	301 $[M-H]^-$	Quercetin	11.4 $*10^{-3}$
	447 $[M-H]^-$	Quercetin Glucosides*	0.13 [61]	431 $[M-H]^-$	Apigenin Glucosides*	
Oligo-saccharides	179 $[M-H]^-$ 203 $[M+Na]^+$ 219 $[M+K]^+$	Glucose/ Fructose*	83.3	179 $[M-H]^-$ 203 $[M+Na]^+$ 219 $[M+K]^+$	Glucose/ Fructose*	44.3
	341 $[M-H]^-$ 365 $[M+Na]^+$ 381 $[M+K]^+$	Sucrose	20.7	341 $[M-H]^-$ 365 $[M+Na]^+$ 381 $[M+K]^+$	Sucrose	4.7

Except noted, all other concentration data come from (1) See the USDA National Nutrient Database at http://www.nal.usda.gov/fnic/foodcomp/search/, and (2) See the USDA National Nutrient Database at http://www.nal.usda.gov/fnic/foodcomp/Data/Flav/flav.pdf

References

(1) Karas, M.; Hillenkamp, F. *Anal. Chem.* **1988**, *60*, 2299-2301.

(2) Bahr, U.; Deppe, A.; Karas, M.; Hillenkamp, F.; Giessmann, U. *Anal. Chem.* **1992**, *64*, 2866-2869.

(3) Kaufmann, R.; Kirsch, D.; Spengler, B. *Int. J. Mass Spectrom. Ion Processes* **1994**, *131*, 355-385.

(4) Lecchi, P.; Pannell, L. K. *J. Am. Soc. Mass. Spectrom.* **1995**, *6*, 972-975.

(5) Finke, B.; Stahl, B.; Pfenninger, A.; Karas, M.; Daniel, H.; Sawatzki, G. *Anal. Chem.* **1999**, *71*, 3755-3762.

(6) Tholey, A.; Wittmann, C.; Kang, M. J.; Bungert, D.; Hollemeyer, K.; Heinzle, E. *J. Mass Spectrom.* **2002**, *37*, 963-973.

(7) Ayorinde, F. O.; Hambright, P.; Porter, T. N.; Keith, Q. L. *Rapid Commun. Mass Spectrom.* **1999**, *13*, 2474-2479.

(8) Knochenmuss, R.; Dubois, F.; Dale, M. J.; Zenobi, R. *Rapid Commun. Mass Spectrom.* **1996**, *10*, 871-877.

(9) Knochenmuss, R.; Karbach, V.; Wiesli, U.; Breuker, K.; Zenobi, R. *Rapid Commun. Mass Spectrom.* **1998**, *12*, 529-534.

(10) Guo, Z.; Zhang, Q. C.; Zou, H. F.; Guo, B. C.; Ni, J. Y. *Anal. Chem.* **2002**, *74*, 1637-1641.

(11) Sluszny, C.; Yeung, E. S.; Nikolau, B. J. *J. Am. Soc. Mass. Spectrom.* **2005**, *16*, 107-115.

(12) Tanaka, K.; Waki, H.; Ido, Y.; Akita, S.; Yoshida, Y.; Yoshida, T.; Matsuo, T. *Rapid Commun. Mass Spectrom.* **1988**, *2*, 151-153.

(13) McLean, J. A.; Stumpo, K. A.; Russell, D. H. *J. Am. Chem. Soc.* **2005**, *127*, 5304-5305.

(14) Kinumi, T.; Saisu, T.; Takayama, M.; Niwa, H. *J. Mass Spectrom.* **2000**, *35*, 417-422.

(15) Chen, C. T.; Chen, Y. C. *Anal. Chem.* **2005**, *77*, 5912-5919.

(16) Wei, J.; Buriak, J. M.; Siuzdak, G. *Nature* **1999**, *399*, 243-246.

(17) Shen, Z. X.; Thomas, J. J.; Averbuj, C.; Broo, K. M.; Engelhard, M.; Crowell, J. E.; Finn, M. G.; Siuzdak, G. *Anal. Chem.* **2001**, *73*, 612-619.

(18) Pihlainen, K.; Grigoras, K.; Franssila, S.; Ketola, R.; Kotiaho, T.; Kostiainen, R. *J. Mass Spectrom.* **2005**, *40*, 539-545.

(19) Compton, B. J.; Siuzdak, G. *Spectroscopy-an International Journal* **2003**, *17*, 699-713.

(20) Li, Q.; Ricardo, A.; Benner, S. A.; Winefordner, J. D.; Powell, D. H. *Anal. Chem.* **2005**, *77*, 4503-4508.

(21) Wen, X. J.; Dagan, S.; Wysocki, V. H. *Anal. Chem.* **2007**, *79*, 434-444.

(22) Zumbuhl, S.; Knochenmuss, R.; Wulfert, S.; Dubois, F.; Dale, M. J.; Zenobi, R. *Anal. Chem.* **1998**, *70*, 707-715.

(23) Kim, H. J.; Lee, J. K.; Park, S. J.; Ro, H. W.; Yoo, D. Y.; Yoon, D. Y. *Anal. Chem.* **2000**, *72*, 5673-5678.

(24) Park, K. H.; Kim, H. J. *Rapid Commun. Mass Spectrom.* **2001**, *15*, 1494-1499.

(25) Peng, S.; Edler, M.; Ahlmann, N.; Hoffmann, T.; Franzke, J. *Rapid Commun. Mass Spectrom.* **2005**, *19*, 2789-2793.

(26) Dale, M. J.; Knochenmuss, R.; Zenobi, R. *Anal. Chem.* **1996**, *68*, 3321-3329.

(27) Sunner, J.; Dratz, E.; Chen, Y. C. *Anal. Chem.* **1995**, *67*, 4335-4342.

(28) Li, X. P.; Wilm, M.; Franz, T. *Proteomics* **2005**, *5*, 1460-1471.

(29) Chen, Y. C.; Shiea, J.; Sunner, J. *J. Chromatogr. A* **1998**, *826*, 77-86.

(30) Pan, C. S.; Xu, S. Y.; Hu, L. G.; Su, X. Y.; Ou, J. J.; Zou, H. F.; Guo, Z.; Zhang, Y.; Guo, B. C. *J. Am. Soc. Mass. Spectrom.* **2005**, *16*, 883-892.

(31) Ren, S. F.; Guo, Y. L. *Rapid Commun. Mass Spectrom.* **2005**, *19*, 255-260.

(32) Ren, S. F.; Zhang, L.; Cheng, Z. H.; Guo, Y. L. *J. Am. Soc. Mass. Spectrom.* **2005**, *16*, 333-339.

(33) Xu, S. Y.; Li, Y. F.; Zou, H. F.; Qiu, J. S.; Guo, Z.; Guo, B. C. *Anal. Chem.* **2003**, *75*, 6191-6195.

(34) Ugarov, M. V.; Egan, T.; Khabashesku, D. V.; Schultz, J. A.; Peng, H. Q.; Khabashesku, V. N.; Furutani, H.; Prather, K. S.; Wang, H. W. J.; Jackson, S. N.; Woods, A. S. *Anal. Chem.* **2004**, *76*, 6734-6742.

(35) Black, C.; Poile, C.; Langley, J.; Herniman, J. *Rapid Commun. Mass Spectrom.* **2006**, *20*, 1053-1060.

(36) Langley, G. J.; Herniman, J. M.; Townell, M. S. *Rapid Commun. Mass Spectrom.* **2007**, *21*, 180-190.

(37) Berger-Nicoletti, E.; Wurm, F.; Kilbinger, A. F. M.; Frey, H. *Macromolecules* **2007**, *40*, 746-751.

(38) Cha, S.; Yeung, E. S. *Anal. Chem.* **2007**, *79*, 2373-2385.

(39) Cohen, L. H.; Gusev, A. I. *Anal. Bioanal. Chem.* **2002**, *373*, 571-586.

(40) Peterson, D. S. *Mass Spectrom. Rev.* **2007**, *26*, 19-34.

(41) Altelaar, A. F. M.; Klinkert, I.; Jalink, K.; de Lange, R. P. J.; Adan, R. A. H.; Heeren, R. M. A.; Piersma, S. R. *Anal. Chem.* **2006**, *78*, 734-742.

(42) Ostrowski, S. G.; Van Bell, C. T.; Winograd, N.; Ewing, A. G. *Science* **2004**, *305*, 71-73.

(43) Caprioli, R. M.; Farmer, T. B.; Gile, J. *Anal. Chem.* **1997**, *69*, 4751-4760.

(44) Chaurand, P.; Caprioli, R. M. *Electrophoresis* **2002**, *23*, 3125-3135.

(45) Chaurand, P.; Cornett, D. S.; Caprioli, R. M. *Curr. Opin. Biotechnol.* **2006**, *17*, 431-436.

(46) Garrett, T. J.; Prieto-Conaway, M. C.; Kovtoun, V.; Bui, H.; Izgarian, N.; Stafford, G.; Yost, R. A. *Int. J. Mass Spectrom.* **2007**, *260*, 166-176.

(47) Garrett, T. J.; Yost, R. A. *Anal. Chem.* **2006**, *78*, 2465-2469.

(48) Wiseman, J. M.; Ifa, D. R.; Song, Q. Y.; Cooks, R. G. *Angew. Chem. Int. Ed.* **2006**, *45*, 7188-7192.

(49) Li, Y.; Shrestha, B.; Vertes, A. *Anal. Chem.* **2007**, *79*, 523-532.

(50) Schwartz, S. A.; Reyzer, M. L.; Caprioli, R. M. *J. Mass Spectrom.* **2003**, *38*, 699-708.

(51) Claudio, G. A., P.; Simopoulos, E. T. *Effects of fatty acids and lipids in health and disease; Basel: New York* **1994**.

(52) Halket, J. M.; Zaikin, V. G. *Eur. J. Mass Spec.* **2004**, *10*, 1-19.

(53) Nagy, K.; Jakab, A.; Fekete, J.; Vekey, K. *Anal. Chem.* **2004**, *76*, 1935-1941.

(54) Yang, W. C.; Adamec, J.; Regnier, F. E. *Anal. Chem.* **2007**, *ASAP*.

(55) Robards, K.; Antolovich, M. *Analyst* **1997**, *122*, R11-R34.

(56) Seeram, N. P.; Lee, R.; Scheuller, H. S.; Heber, D. *Food Chem.* **2006**, *97*, 1-11.

(57) Törrönen, R. a. M., K. *Acta Hort. (ISHS)* **2002**, 797-803.

(58) Harvey, D. J.; Martin, R. L.; Jackson, K. A.; Sutton, C. W. *Rapid Commun. Mass Spectrom.* **2004**, *18*, 2997-3007.

(59) Asam, M. R.; Glish, G. L. *J. Am. Soc. Mass. Spectrom.* **1997**, *8*, 987-995.

(60) Gokmen, V.; Artik, N.; Acar, J.; Kahraman, N.; Poyrazoglu, E. *Eur. Food Res.Technol.* **2001**, *213*, 194-199.

(61) Lee, K. W.; Kim, Y. J.; Kim, D. O.; Lee, H. J.; Lee, C. Y. *J. Agric. Food. Chem.* **2003**, *51*, 6516-6520.

(62) Skupien, K.; Oszmianski, J. *Eur. Food Res.Technol.* **2004**, *219*, 66-70.

(63) Williner, M. R.; Pirovani, M. E.; Guemes, D. R. *Journal of the Science of Food and Agriculture* **2003**, *83*, 842-845.

(64) *See the USDA National Nutrient Database at http://www.nal.usda.gov/fnic/foodcomp/search/* Accessed on Mar. **2007**.

(65) *See the USDA National Nutrient Database at http://www.nal.usda.gov/fnic/foodcomp/Data/Flav/flav.pdf* Accessed on Mar. **2007**.

(66) Ng, L. K.; Lafontaine, P.; Vanier, M. *J. Agric. Food. Chem.* **2004**, *52*, 7251-7257.

(67) Chen, M. L.; Song, F. R.; Guo, M. Q.; Liu, Z. Q.; Liu, S. Y. *Rapid Commun. Mass Spectrom.* **2002**, *16*, 264-271.

Figure Captions

Figure 1. Mass spectrum of fatty acid standards (C18-C30 fatty acids) with GALDI in the negative-ion mode. Sample loading: 200 pmole of each.

Figure 2. Mass spectrum and detection limit of fatty acid standards (C18-C30 fatty acids) with GALDI in the negative-ion mode. Sample loading: 100 fmole of each.

Figure 3. Comparison of MALDI and GALDI spectra of flavonoid standards: quercetin (MW 302.24), kaempferol (MW 286.23), phloretin (MW 274.27) and apigenin (MW 270.24); Sample loading: 200 pmole of each. Apigenin, kaempferol and quercetin were observed as $[M + H]^+$ with DHB (a) and CHCA (b) in the positive ion mode. With GALDI in the positive-ion mode (c), apigenin, kaempferol and quercetin are detected as $[M + H]^+$ (*m/z* 271, *m/z* 286, and *m/z* 303, respectively), $[M+Na]^+$ (*m/z* 293, *m/z* 309, and *m/z* 325, respectively), and $[M + 2Na - H]^+$ (*m/z* 315, *m/z* 331, and *m/z* 347, respectively). Phloretin was not observed either. None of the four flavonoids can be detected with DHB (d) or CHCA (e) in the negative ion mode; However, all the four flavonoids are detected as $[M - H]^-$ ions with GALDI in the negative-ion mode (f). Fragment from phloretin (*m/z* 167) and fragments from quercetin (*m/z* 151 and *m/z* 179) are observed in the lower mass range as well.

Figure 4. Mass spectrum of oligosaccharide standards with DHB (a) and CHCA (b) in the positive-ion mode. Sample loading: 100 ng of each.

Figure 5. Mass spectrum of oligosaccharide standards with GALDI in the positive-ion mode. Sample loading: 100 ng of each. Peaks with ●: water loss fragments; peaks with *: major ring-cleavage fragments.

Figure 6. Product ion spectra of *m/z* 191 from (a) quinic acid standard; (b) apple flesh; (c) citric acid standard; and (d) strawberry flesh. All spectra were collected in the negative-ion mode.

Figure 7. Representative GALDI-MS spectra from different parts of apple. (a) fatty acids composition on the outside of apple peel, negative-ion mode; (b) fresh apple juice, negative-ion mode; (c) hexose and sucrose from fresh apple juice, positive-ion mode; and (d) apple core, negative-ion mode. See Table I for peak identification in (b) and (d).

Figure 8. Representative GALDI-MS spectra (negative-ion mode) from strawberry (a) flesh; and (b) seed.

Figure 9. Chemically selective images of major ionic species identified from apple endocarp region with GALDI in the negative-ion mode. (a) optical image taken with reversed color; (b) malic acid; (c) quinic acid; (d) linoleic acid; (e) sucrose; (f) phloretin; (g). epicatechin; (h) quercetin; and (i) phloridzin. All peak intensities were normalized by dividing by the total ion current (TIC) of each spectrum.

Figure 10. Chemically selective images of the major ionic species identified from strawberry with GALDI in the negative-ion mode. (a) optical image taken

with reversed color. One seed was present as the darkest dot on the right-hand side; (b) ascorbic acid; (c) citric acid; (d) linoleic acid; (e) hexose; (f) sucrose; (g) apigenin; (h) kaempferol; and (i) *m/z* 301-301.5 ellagic acid + quercetin. All peak intensities were normalized by dividing by the total ion current of each spectrum.

Figure 11. Product ion spectra of *m/z* 301 from (a) ellagic acid standard; (b) strawberry flesh; (c) quercetin standard; (d) edge of strawberry; and (e) chemically selective image for product ion at *m/z* 179 (precursor ion *m/z* 301) of strawberry slice with GALDI. All spectra were collected in the negative-ion mode. The proposed fragment pathways are shown as inserts.[67]

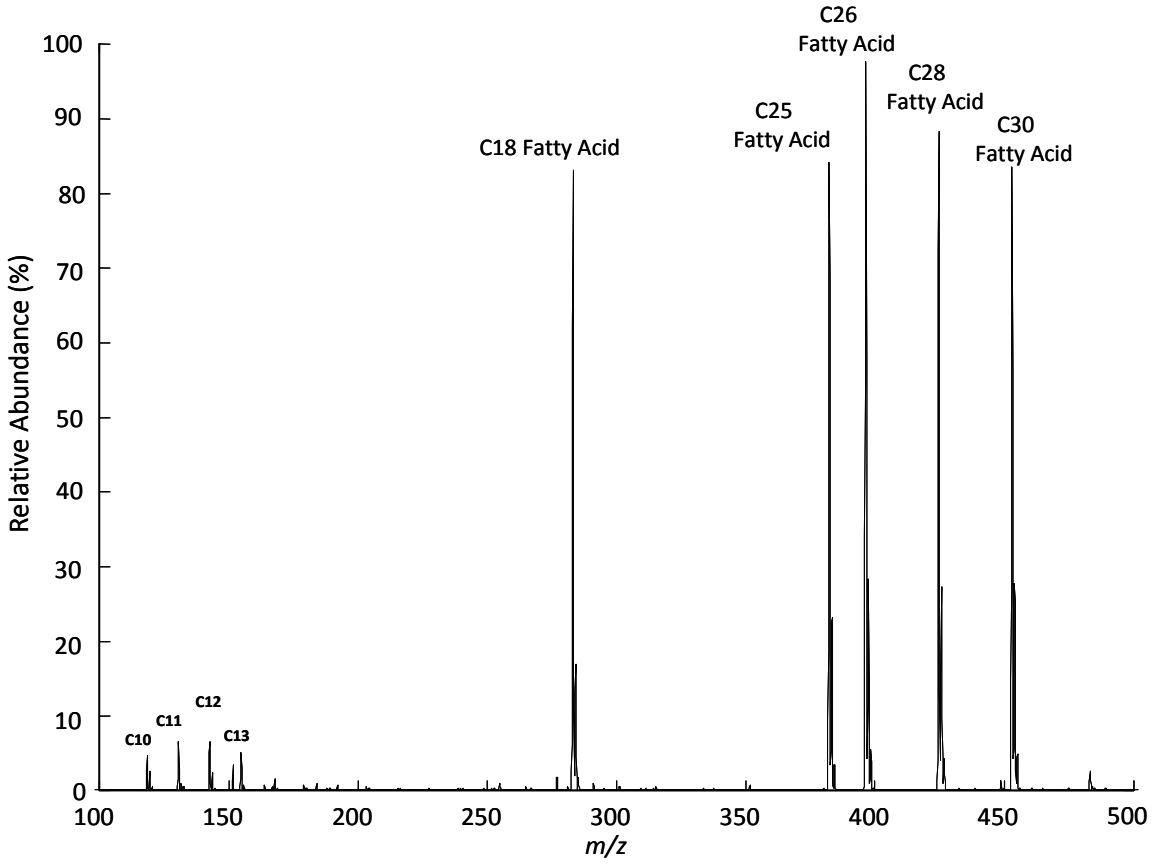
C26
Fatty Acid
C28
Fatty Acid
C25
Fatty Acid
C30
Fatty Acid
C18 Fatty Acid
C10
C11
C12
C13
Relative Abundance (%)
m/z
100
90
80
70
60
50
40
30
20
10
0
100
150
200
250
300
350
400
450
500

Figure 1.

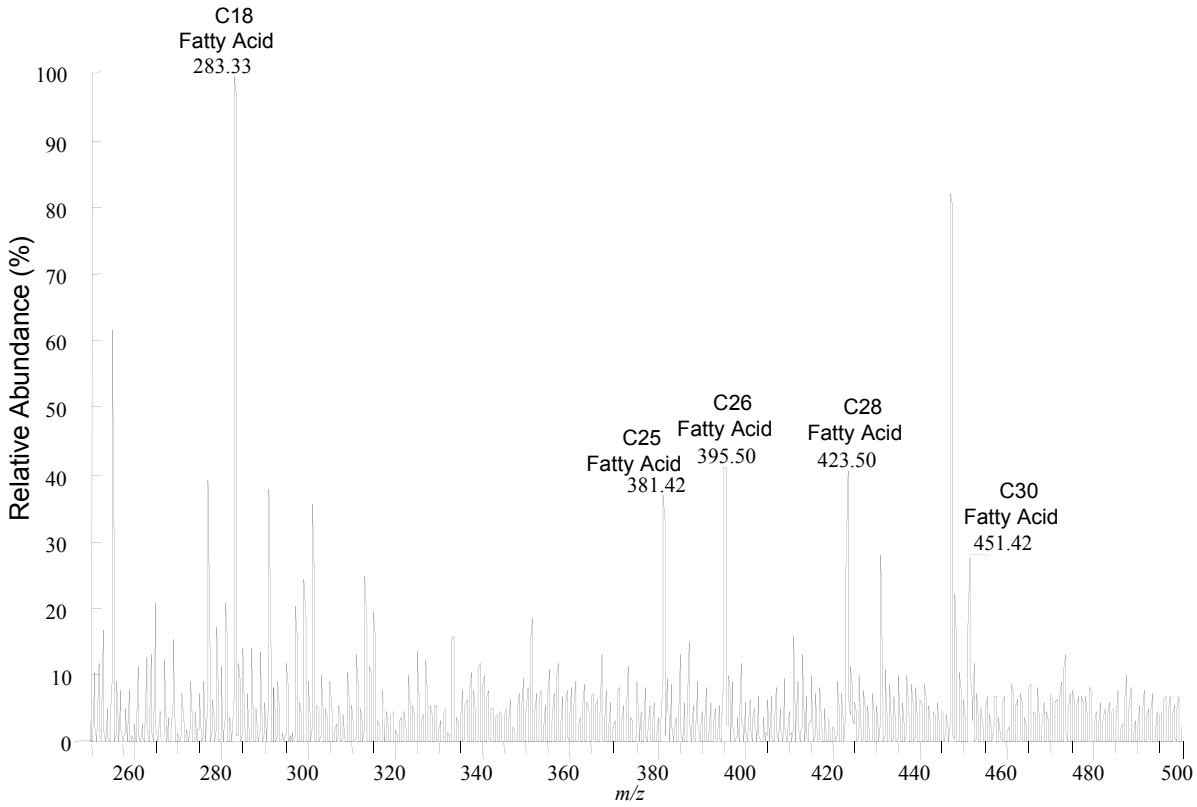
C18
Fatty Acid
283.33
C25
Fatty Acid
381.42
C26
Fatty Acid
395.50
C28
Fatty Acid
423.50
C30
Fatty Acid
451.42
Relative Abundance (%)
m/z
0
10
20
30
40
50
60
70
80
90
100
260
280
300
320
340
360
380
400
420
440
460
480
500

Figure 2.

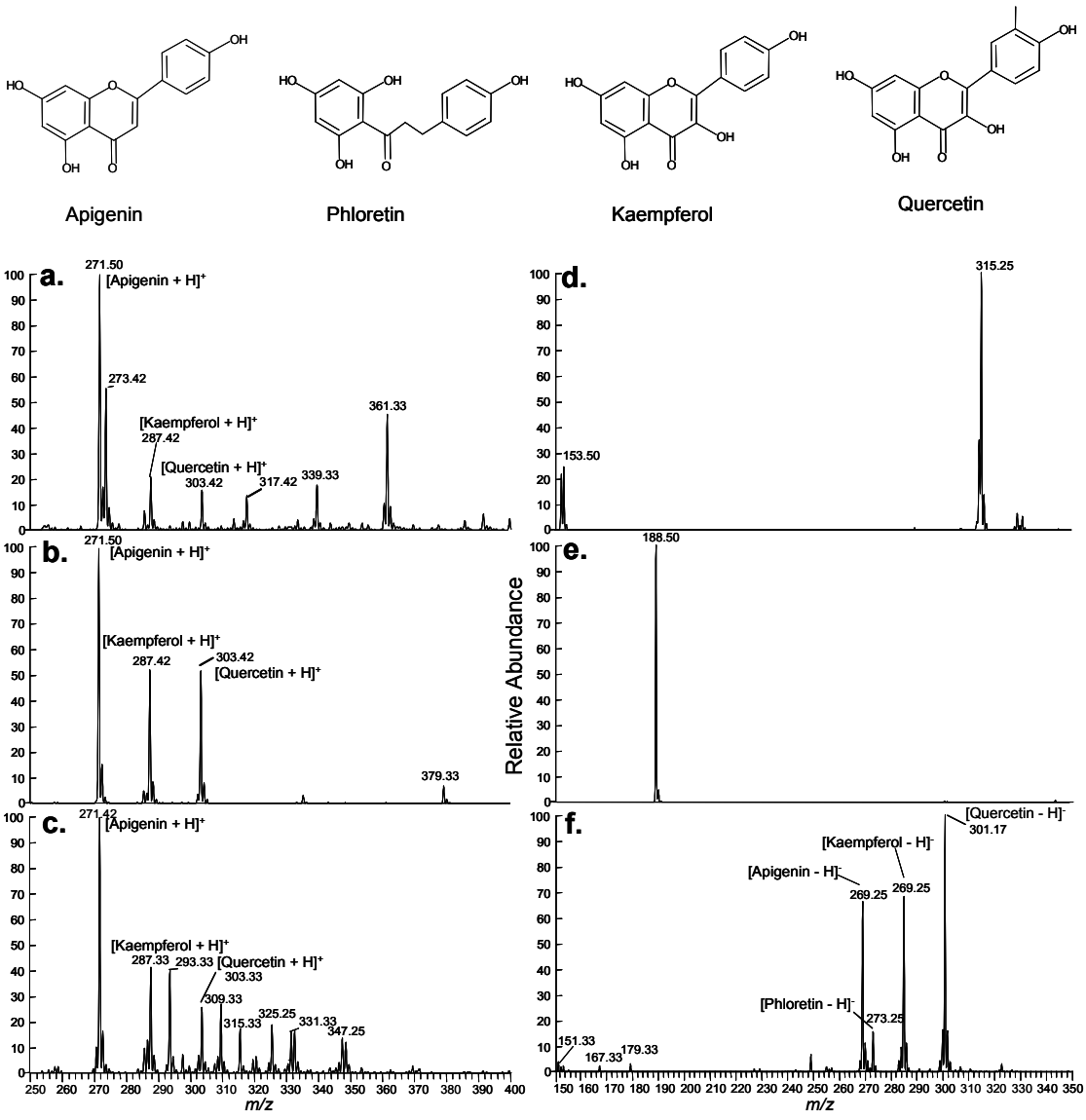
Apigenin
Phloretin
Kaempferol
Quercetin
a.
271.50
[Apigenin + H]+
273.42
[Kaempferol + H]+
287.42
[Quercetin + H]+
303.42
317.42
339.33
361.33
b.
271.50
[Apigenin + H]+
[Kaempferol + H]+
287.42
303.42
[Quercetin + H]+
379.33
c.
271.42
[Apigenin + H]+
[Kaempferol + H]+
287.33
293.33
[Quercetin + H]+
303.33
309.33
315.33
325.25
331.33
347.25
d.
315.25
153.50
e.
188.50
f.
[Quercetin - H]-
301.17
[Kaempferol - H]-
[Apigenin - H]-
269.25
269.25
[Phloretin - H]-
273.25
151.33
167.33
179.33
Relative Abundance
m/z

Figure 3.

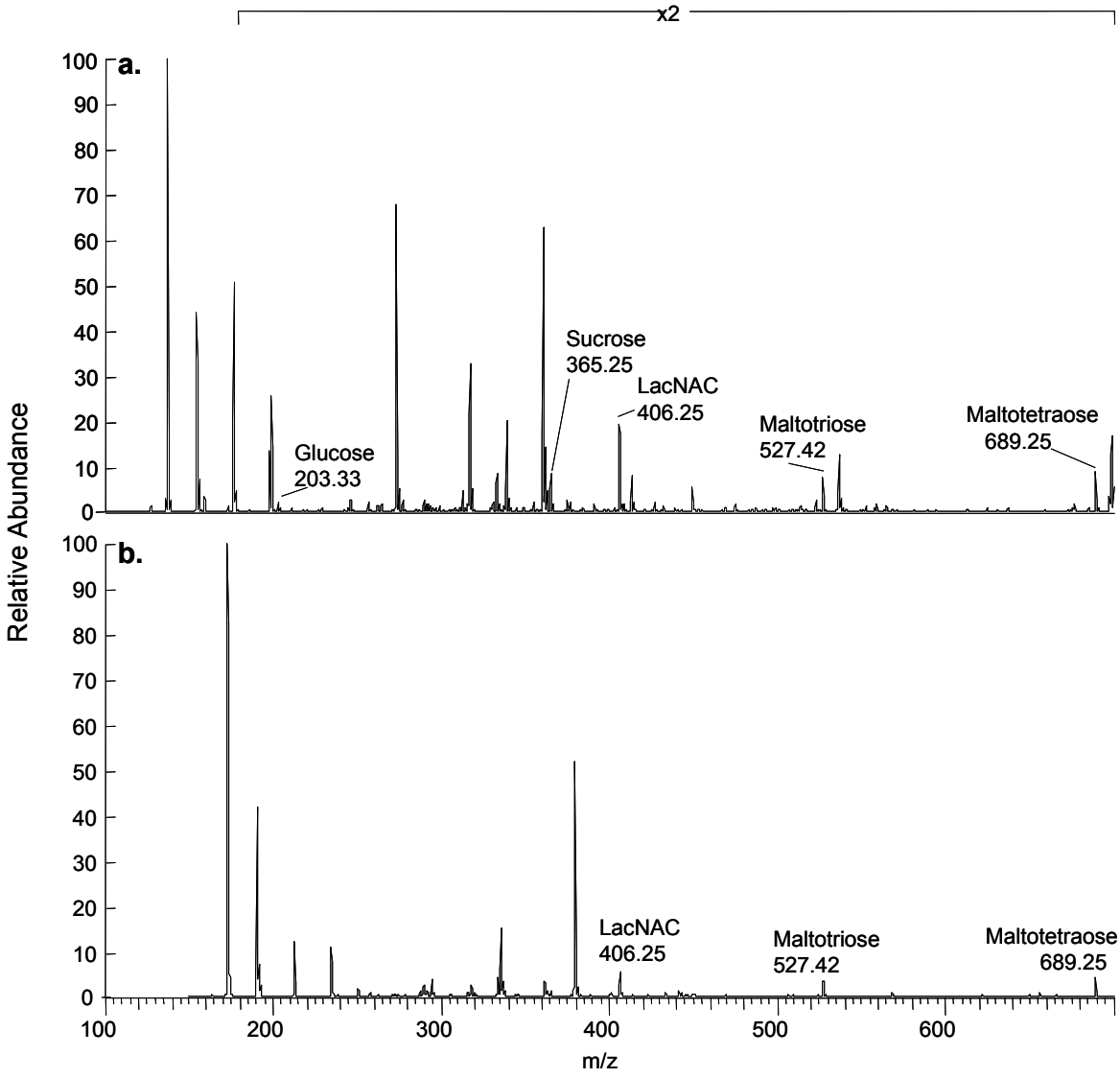
x2
a.
b.
Relative Abundance
Glucose
203.33
Sucrose
365.25
LacNAC
406.25
Maltotriose
527.42
Maltotetraose
689.25
LacNAC
406.25
Maltotriose
527.42
Maltotetraose
689.25
m/z

Figure 4.

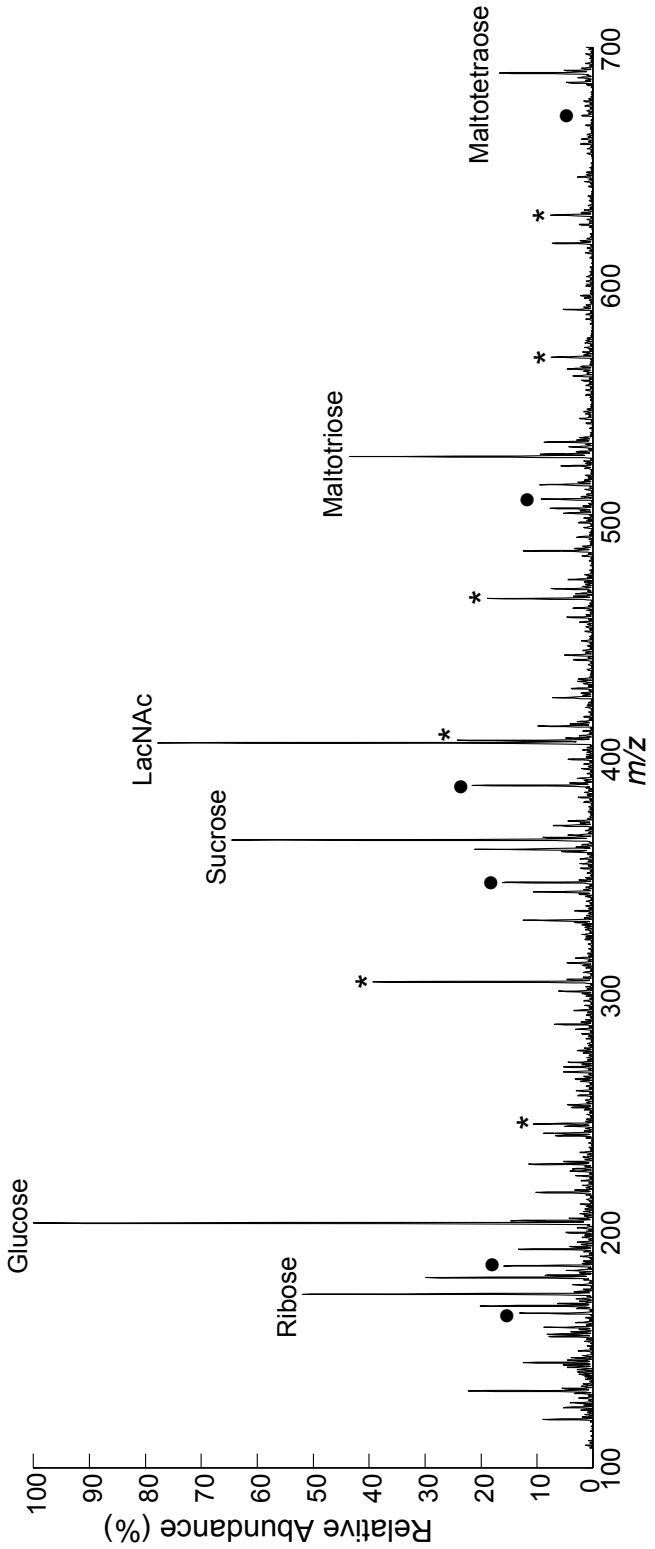
Glucose
Ribose
Sucrose
LacNAc
Maltotriose
Maltotetraose
Relative Abundance (%)
m/z
100
90
80
70
60
50
40
30
20
10
0
100
200
300
400
500
600
700

Figure 5.

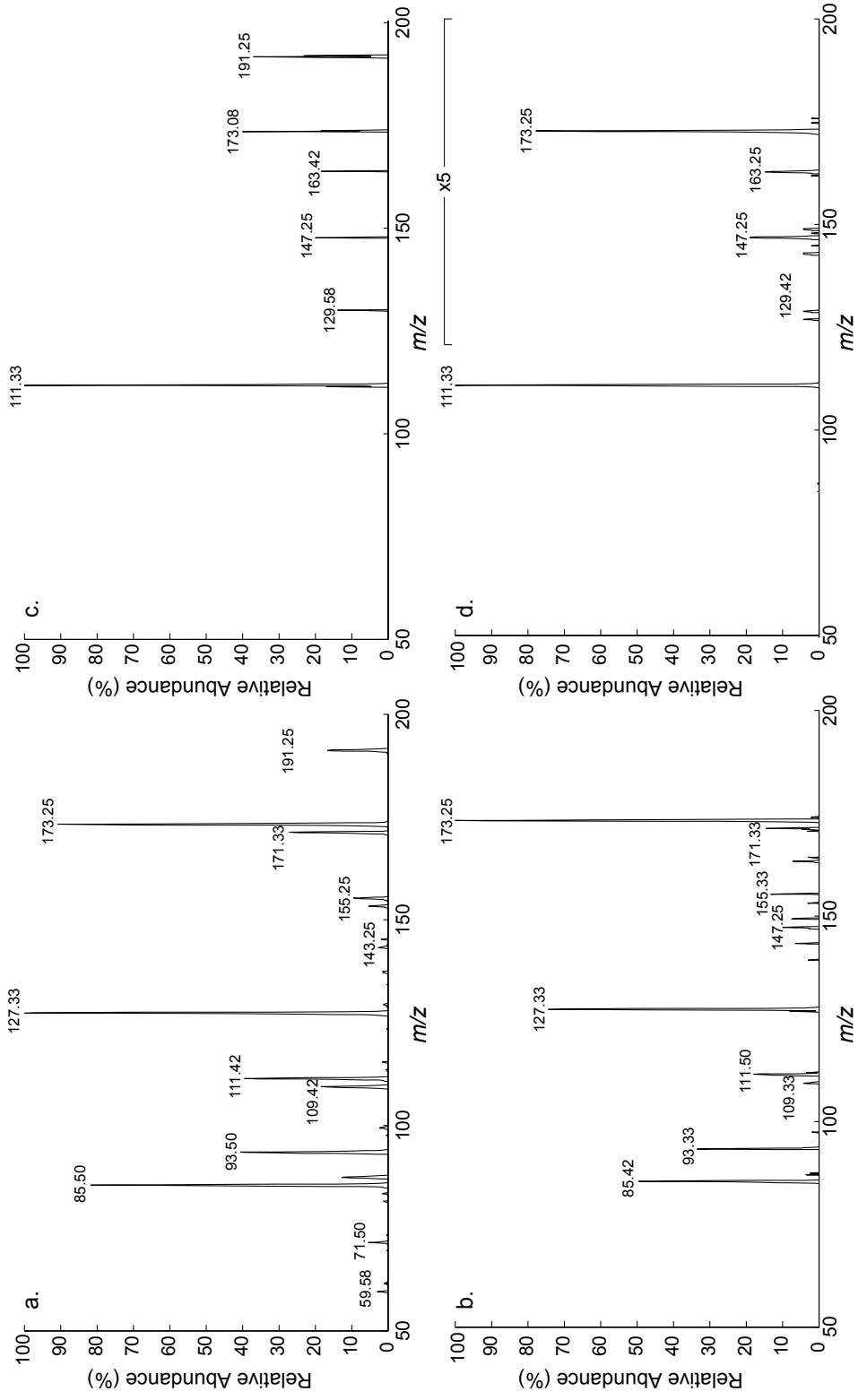
a.
b.
c.
d.
Relative Abundance (%)
m/z
x5
59.58
71.50
85.50
93.50
109.42
111.42
127.33
143.25
155.25
171.33
173.25
191.25
85.42
93.33
109.33
111.50
147.25
155.33
129.58
163.42
111.33
129.42
163.25
173.08

Figure 6.

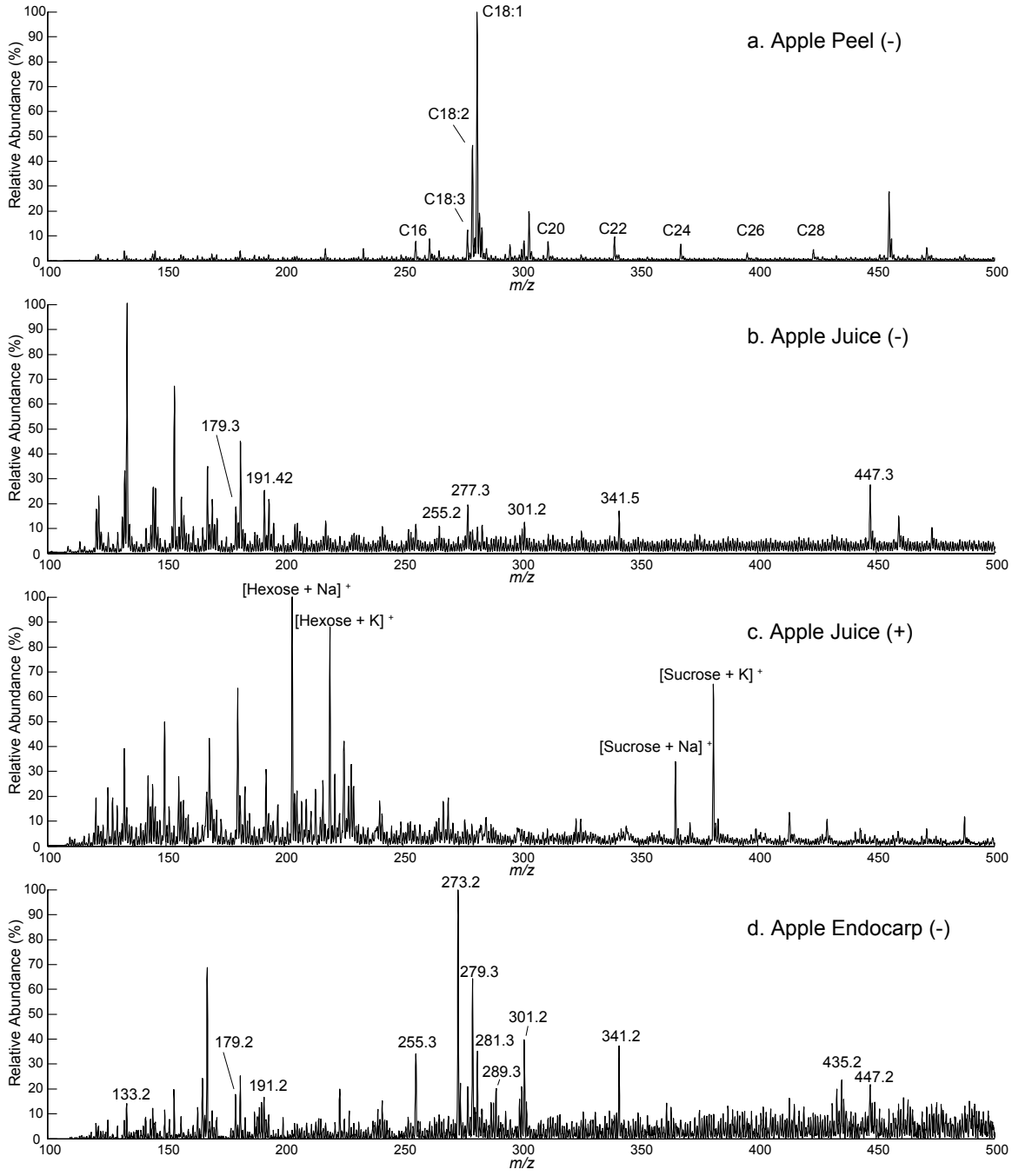
a. Apple Peel (-)
C18:1
C18:2
C18:3
C16
C20
C22
C24
C26
C28
b. Apple Juice (-)
179.3
191.42
277.3
255.2
301.2
341.5
447.3
c. Apple Juice (+)
[Hexose + Na] +
[Hexose + K] +
[Sucrose + K] +
[Sucrose + Na] +
d. Apple Endocarp (-)
273.2
279.3
301.2
179.2
255.3
281.3
341.2
289.3
435.2
447.2
191.2
133.2
Relative Abundance (%)
m/z

Figure 7.

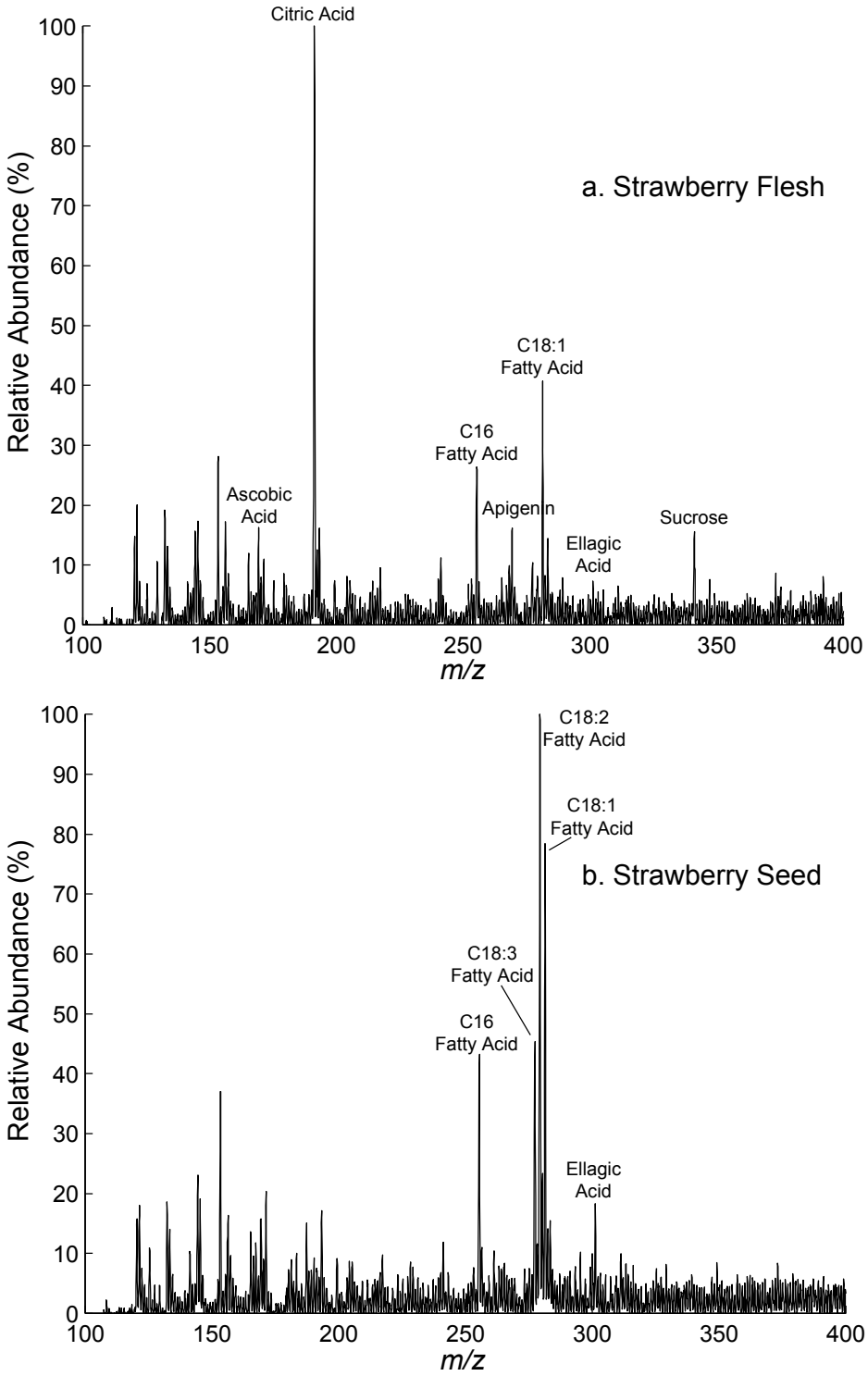
Citric Acid
a. Strawberry Flesh
C18:1
Fatty Acid
C16
Fatty Acid
Ascobic
Acid
Apigenin
Sucrose
Ellagic
Acid
Relative Abundance (%)
m/z
C18:2
Fatty Acid
C18:1
Fatty Acid
b. Strawberry Seed
C18:3
Fatty Acid
C16
Fatty Acid
Ellagic
Acid
Relative Abundance (%)
m/z

Figure 8.

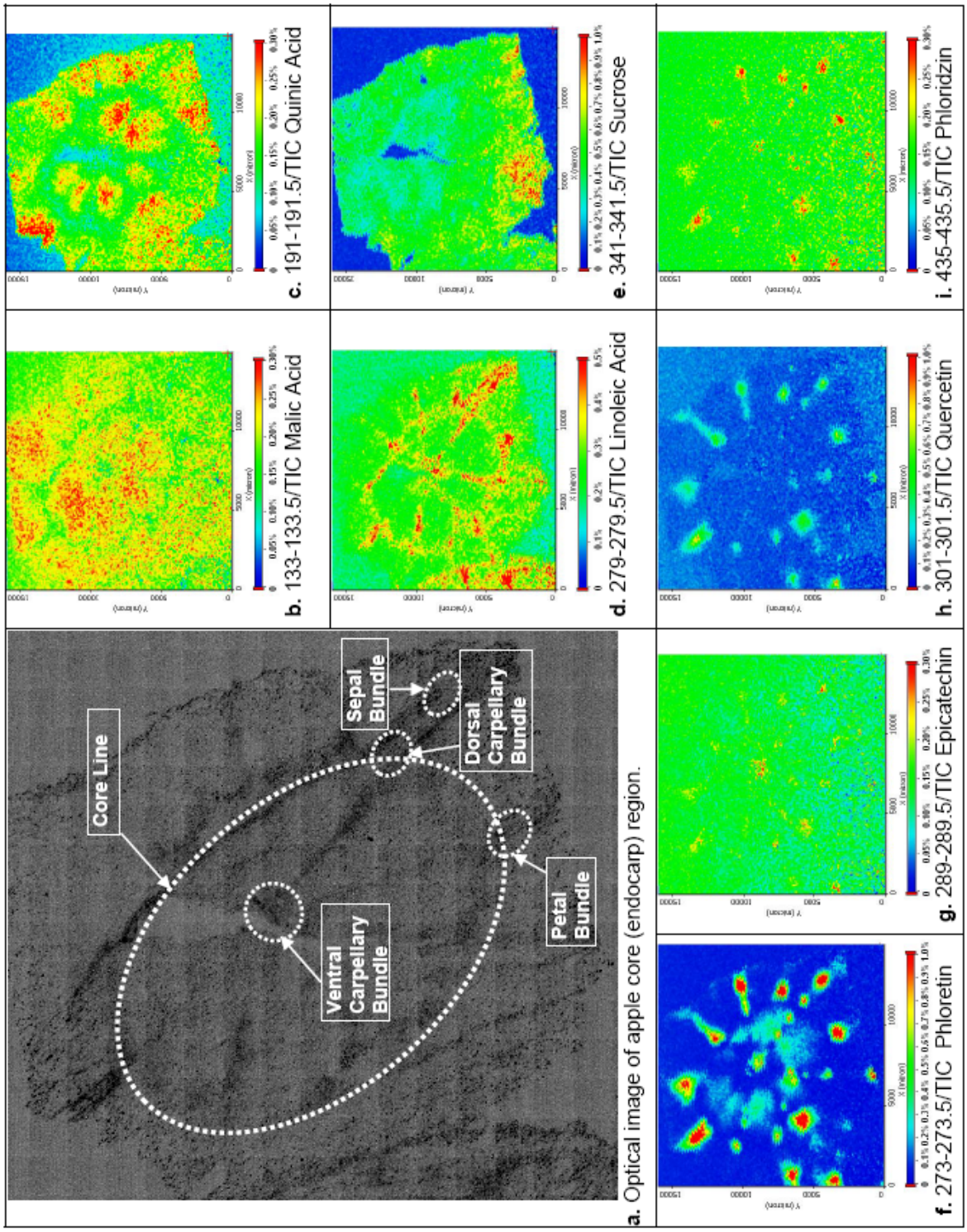
Core Line
Sepal Bundle
Dorsal Carpellary Bundle
Ventral Carpellary Bundle
Petal Bundle
a. Optical image of apple core (endocarp) region.
b. 133-133.5/TIC Malic Acid
c. 191-191.5/TIC Quinic Acid
d. 279-279.5/TIC Linoleic Acid
e. 341-341.5/TIC Sucrose
f. 273-273.5/TIC Phloretin
g. 289-289.5/TIC Epicatechin
h. 301-301.5/TIC Quercetin
i. 435-435.5/TIC Phloridzin

Figure 9.

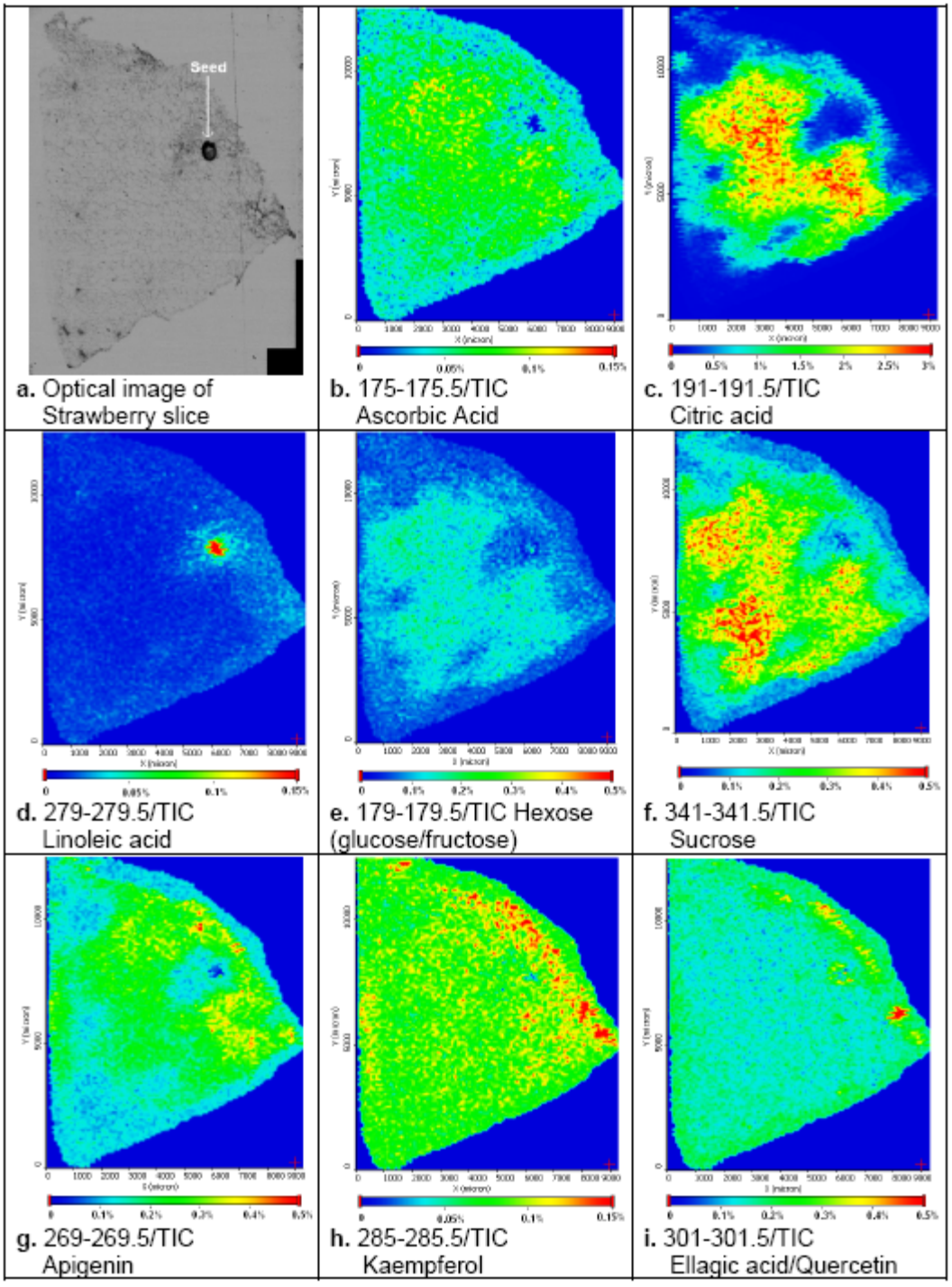
Seed
a. Optical image of Strawberry slice
b. 175-175.5/TIC Ascorbic Acid
c. 191-191.5/TIC Citric acid
d. 279-279.5/TIC Linoleic acid
e. 179-179.5/TIC Hexose (glucose/fructose)
f. 341-341.5/TIC Sucrose
g. 269-269.5/TIC Apigenin
h. 285-285.5/TIC Kaempferol
i. 301-301.5/TIC Ellagic acid/Quercetin

Figure 10.

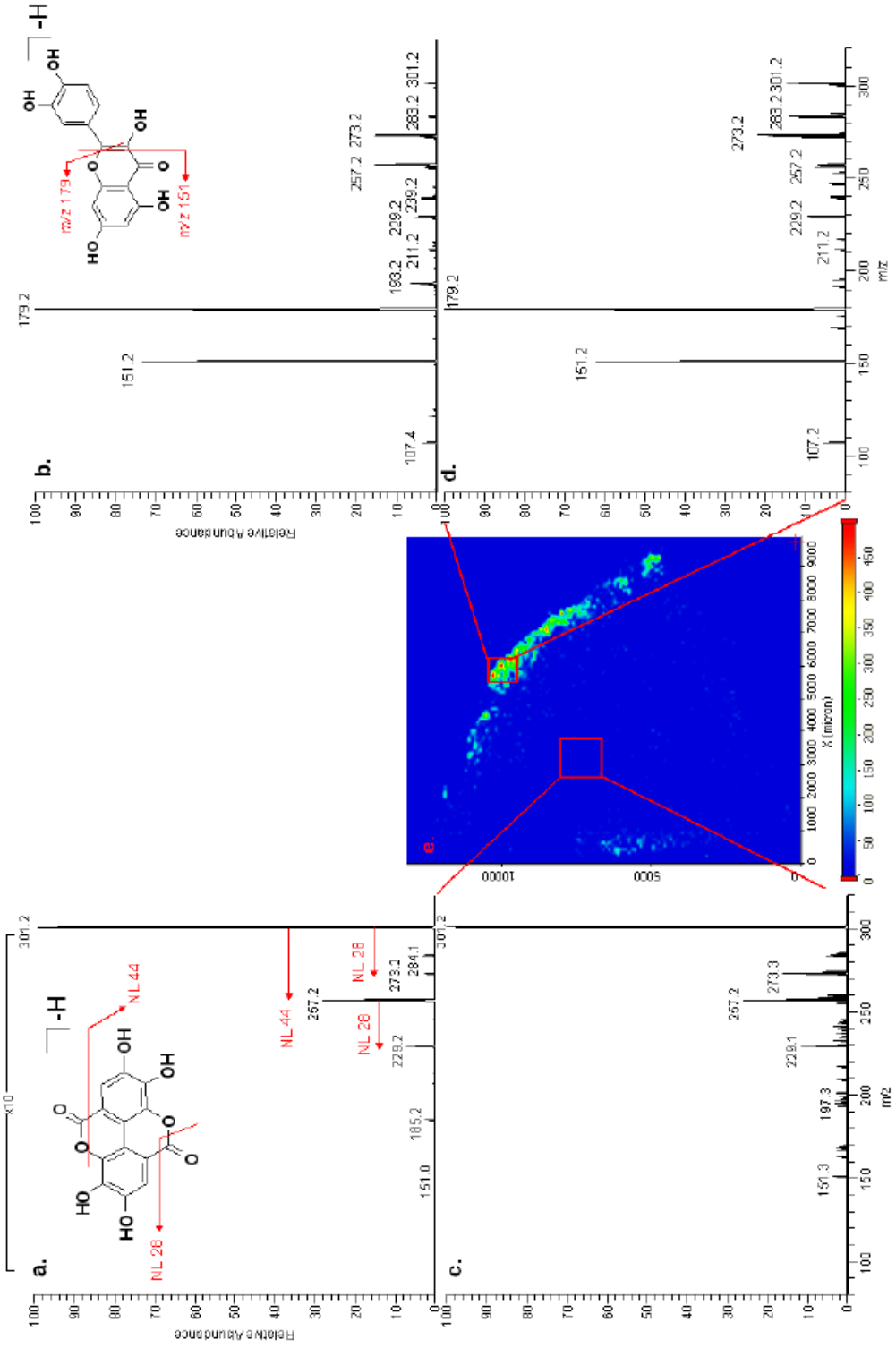
a.
b.
c.
d.
e.
-H
NL 44
NL 28
NL 28
m/z 179
m/z 151
Relative Abundance
m/z
X (micron)

Figure 11.

APPENDIX 3. SUPPORTING INFORMATION FOR CHAPTER 3

Sangwon Cha, Hui Zhang, Hilal I. Ilarslan, Eve Syrkin Wurtele, Libuse Brachova, Basil J. Nikolau and Edward S. Yeung

Enhancing Spatial Resolution in Mass Spectral Imaging by 'Oversampling'

Because 100 μm or 150 μm step size was too big to distinguish flower components—carpels, petals, sepals and so on—and to recognize the boundaries of the flower components, 50 μm spacing was used for flower scanning. Scanning with a spacing which is smaller than laser spot size is called oversampling. This oversampling can enhance the spatial resolution of the chemical selective image without optical adjustments if complete ablation occurs in each scanning spot (Jurchen *et al.*, 2005). If complete ablation is not achieved, oversampling just increases the number of pixels of the processed image but could not provide real spatially-resolved chemical distribution information. The number of laser shots needed for complete ablation was investigated experimentally by counting to when mass spectrum started showing no or negligible signal. However, as Jurchen and coworkers pointed out (Jurchen *et al.*, 2005), the qualities of mass spectra collected near complete ablation point were poor and this leads to poor sensitivities if all mass spectra collected at one point were averaged.

To overcome this issue, 'selective spectra averaging' method with complete ablation for one scanning point and 'whole spectra averaging' method without complete ablation for one scanning point were performed. In selective spectra averaging, a series of mass spectra were collected for the small area (9-16 rastering points on the sample) at one x, y coordinate

on the sample with a fixed number of laser shots per mass spectrum (10 laser shots in this case) until no signal or negligible signal was observed. With an averaged number of microscans (one microscan corresponds to getting one mass spectrum from the sample) until complete ablation, data were collected over the sample surface. Intensity information with x, y-coordinates for interesting *m/z* ranges were extracted by using the custom software from Thermo (vMALDI Data Extract). This data were then separated to individual microscan spectra. Under our experimental condition, 7 to 8 microscans were needed to achieve complete ablation in most cases. For Arabidopsis flowers, averaged intensity values from the first three to five microscans were used to generate chemically-selective images of flavonoids and less than three microscans were averaged for the other classes of compounds. Images from selective spectra averaging were generated by using in-house written Matlab (Mathworks, Natick, MA, USA) program.

By using these two methods, there was no significant difference in terms of qualities of chemical images for flavonoids but the two methods have advantages and disadvantages over each other. Because of the need for complete ablation of graphite materials, 'selective spectra averaging' method usually requires 1.3 to 2 times longer collection time compared to 'whole spectra averaging' method. 'Whole spectra averaging' method can reduce the data collection time but there is a possibility of resulting in poor image quality if the sample contains many different surface properties that can lead to different ion yields, or if interesting molecules have very different ionization characteristics or different abundances. These possible problems can be resolved in 'selective spectra averaging' method by varying number of microscans to be averaged according to different ion species. For example, the ion species at *m/z* 717 on stigma depleted much quicker than flavonoid species. Therefore, if the number of microscans averaged for ions at *m/z* 717 are the same as the number of those for flavonoid species, chemical distribution information of *m/z* 717 becomes indistinguishable from the background. Figure S2 shows chemically-selective images from *Arabidopsis*

thaliana flower by using ‘selective spectra averaging’ method. When comparing chemically selective images for ions at *m/z* 717 (Figure 7 and Figure S2), it is obvious that clearer background was generated by selective spectra averaging method.

Jurchen, J.C., Rubakhin, S.S. and Sweedler, J.V. (2005) MALDI-MS Imaging of Features Smaller than the Size of the Laser Beam. *Journal of the American Society for Mass Spectrometry*, **16**, 1654-1659.

Figure Captions

Figure S-1. Chemically selective images of ions at m/z 194, 210, and 226 and GALDI mass spectrum of chloroform-dipped area. The mass spectrum was averaged from 10 scanning points.

Figure S-2. Chemically-selective images of *Arabidopsis* flowers. Data were collected by 'selective averaging' method described in experimental procedure section. The step size for data collection was set to 50 μm for both x and y directions. Dimension of the images is 4700 μm high × 6700 μm wide. Chemical compositions of corresponding *m/z* values were listed in Table 1. All images were processed with absolute intensity values except the three mass images for m/z 421, 451, and 978, which were processed with normalized intensities. The maximum intensity value is listed under each image. For the image of ions at *m/z* 717, the first two microscans were averaged for image presentation. For the rest of the images, the first five microscans were averaged.

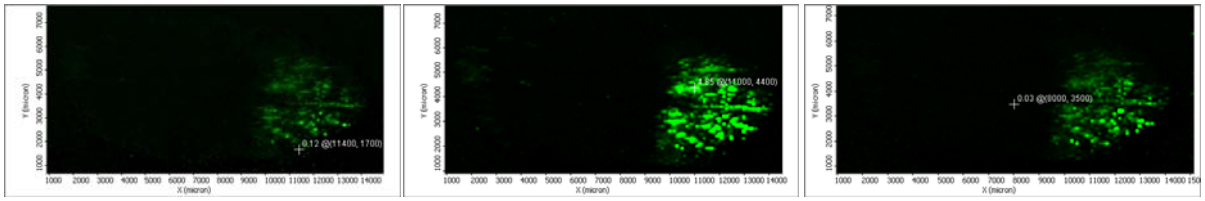

***m/z* 194 (-16)** ***m/z* 210** ***m/z* 226 (+16)**

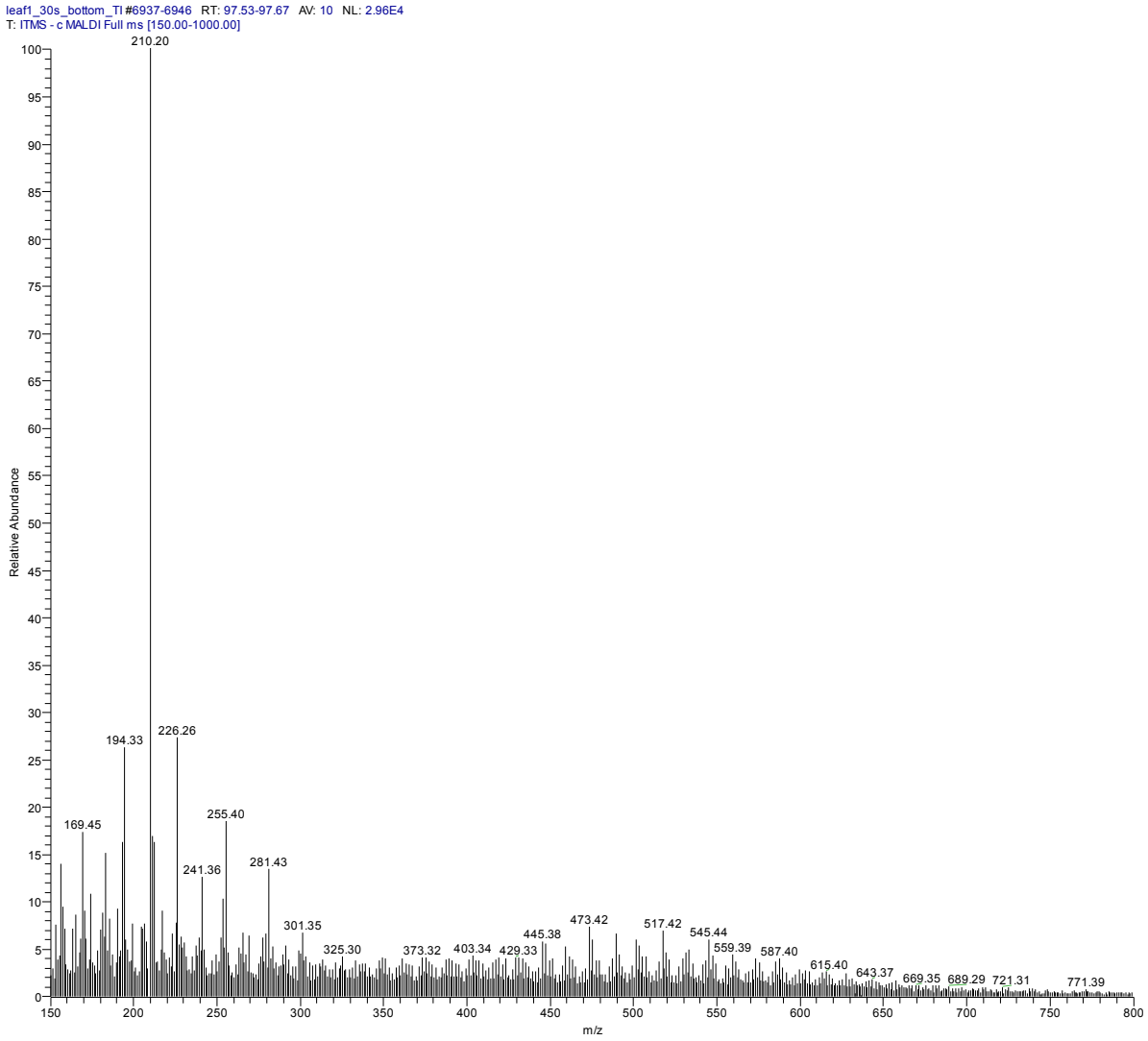

Figure S-1.

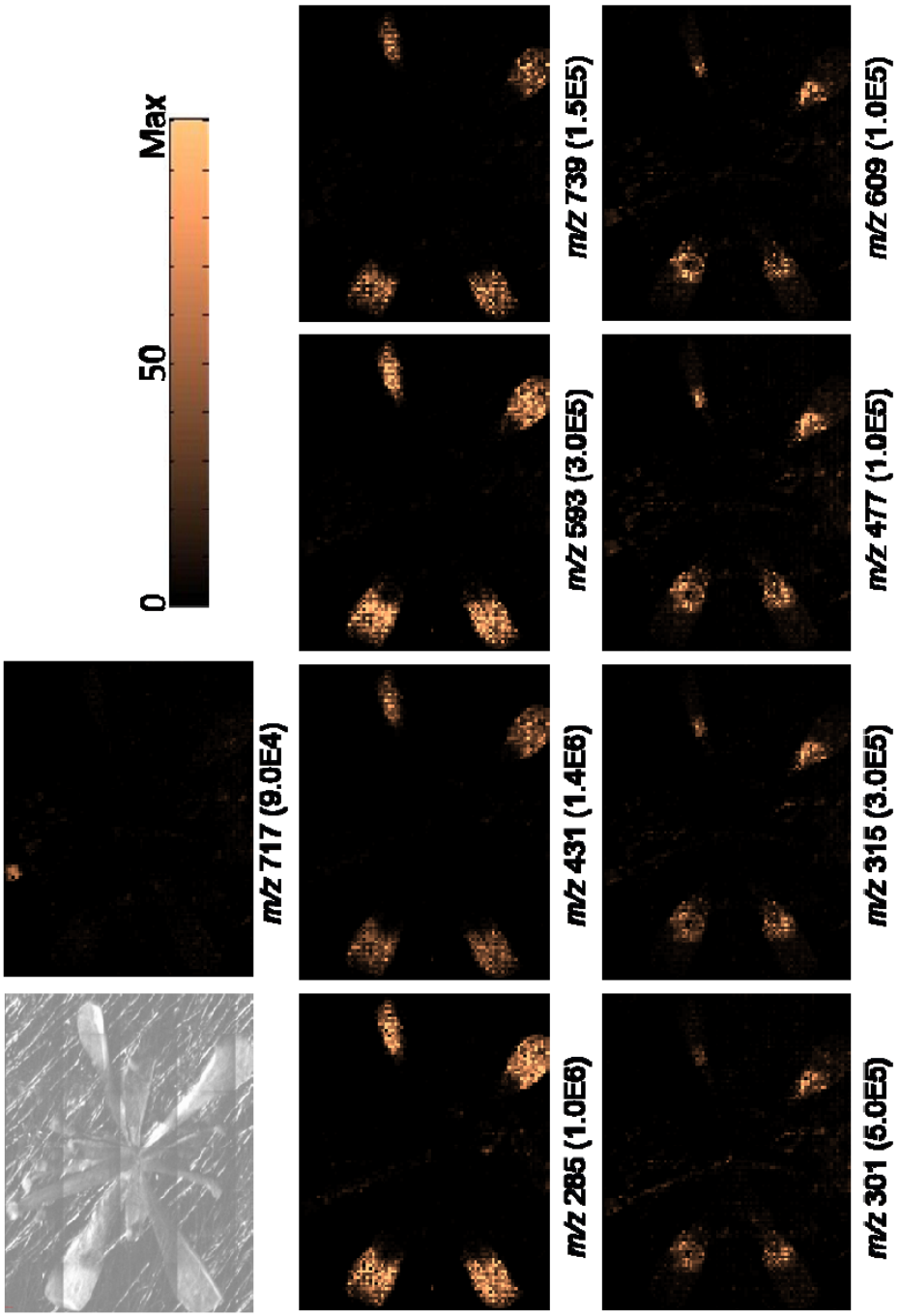
Max
50
0
m/z 739 (1.5E5)
m/z 609 (1.0E5)
m/z 593 (3.0E5)
m/z 477 (1.0E5)
m/z 717 (9.0E4)
m/z 431 (1.4E6)
m/z 315 (3.0E5)
m/z 285 (1.0E6)
m/z 301 (5.0E5)

Figure S-2.

ACKNOWLEDGEMENT

First of all, I would like to thank my advisor, Professor Edward S. Yeung for the generous support through my graduate works. I really enjoyed working with him and I have learned a lot in all aspects. I sincerely admire him for his enthusiasm, dedication, and insight to research. He is a great mentor and scientist.

I am also grateful to my POS committee members, Dr. Robert Houk, Dr. Victor Lin, Dr. Basil Nikolau, Dr. Srdija Jeftinija, and Dr. Hans Stauffer for their precious advices and supports.

I want thank all current and past Dr. Yeung group members for their help, advices, and friendship: Becky Li, Melissa Zhang, Aoshuang Xu, Wei Sun, Wenjun Xie, Dr. Ning Fang, Dr. Jiyoung Lee, Guoxin Lu, Slavica Isailovic, Dr. Frank Li, Dr. Dragan Isailovic, Dr. Hungwing Li, Dr. Bob Hsin, and Dr. Seongho Kang. I specially thank to the mass spectrometry project team, Dr. Hui Zhang and Dr. Chanan Sluszny. I really enjoyed working with them. Besides our group members, my coworkers, Dr. Zhihong Song, Dr. Wenxu Zhou, Dr. Libuse Brachova, and Dr. Ksenia Jeftinija deserve thanks for their direct assistance to my research. In addition, I thank to my friends, Jeongyun Choi for helping Matlab programming and Dr. Insik Jeon for precious comments.

I would like to thank all my friends for their support and happy moments we've shared in Ames. Finally, I want to express my gratitude and love to my parents and all families for their love, endless support, advices and… everything. Specially thanks to my wife, Sang-Hee Shim for her support and love. You complete me.